Effect of Nanofillers on Thermo-Mechanical Properties of Polymers and Composite Laminates

AIDAH JUMAHAT

A Thesis Presented for the Degree of
Doctor of Philosophy

Department of Mechanical Engineering

Faculty of Engineering

University of Sheffield, UK

March 2011

Abstract

Carbon fibre reinforced polymer (CFRP) composites are high performance materials which are widely used in various applications, such as aircraft and aerospace structures, satellites, advanced marine vessels, fuel tanks, sports equipment, high-end automobile structures and many other strength/weight critical applications. It is well known that CFRP composites are stronger in tension (in the fibre direction) than in compression, typically 30-40% higher. This is due to the fact that the compressive strength depends on the properties of the matrix and quality of the laminate, such as alignment of the fibres embedded in the matrix and void content. In theory, stiffer, stronger and tougher matrices provide better support to the carbon fibres (better resistance to fibre instability or microbuckling), hence enhancing the compressive properties of the CFRP composites. The aim of this study is to improve the properties of the CFRP composite by carefully selecting and incorporating nanofillers in the epoxy resin. The nanomodified-epoxy is then combined with continuous carbon fibres, which results in better overall structural response.

The thesis is made up of two main parts i.e., examination of the thermal and mechanical properties of nanomodified-epoxies and investigation of mechanical properties of the nanofilled-CFRP composite with an emphasis on compressive behaviour.

In the first part, a systematic experimental investigation is conducted in order to identify the optimum content and dispersion of nanofillers in the resin systems to be used in the fabrication of CFRP composite laminates. The effect of silica nanospheres, carbon nanotubes and clay nanoplatelets on the compressive, tensile, flexural and fracture toughness properties of epoxy polymers were studied. Two types of epoxy resin were used: Epikote 828 and Cycom 977-20. In addition, the thermal properties of the nanomodified-epoxies compared to the neat systems were also investigated. The results showed that the addition of nanosilica into the epoxy significantly enhanced the compressive, tensile and flexural moduli. Additionally, strength and fracture toughness properties were also improved without any significant reduction in failure strain and thermal properties of the epoxy. It was found that the mechanical performance of nanosilica-modified Epikote 828 system was comparable to that of the commercial high-performance Cycom 977-20 polymer. The Halpin-Tsai model was modified to

include the effect of particle volume fraction on the shape factor ζ that appears in the equation for predicting the Young's modulus of the nanoreinforced-resin.

In the second part of the investigation, the effect of nanosilica on the compressive and in-plane shear properties of HTS40/828 CFRP composite was studied. A number of $[0]_8$ and $[\pm 45]_{2s}$ laminates were fabricated using dry filament winding, wet resin impregnation and vacuum bagging techniques. The quality of the laminate such as fibre distribution, fibre misalignment, void content, fibre and nanosilica volume fraction was examined and measured. Static uniaxial compression and tensile tests on $[0]_8$ and $[\pm 45]_{2s}$ laminates were performed. It was found that the compressive and in-plane shear properties of nanomodified CFRP were better than the neat system. For example, the addition of 7 vol% nanosilica improved the unidirectional (UD) compressive modulus and strength of the HTS40/828 composite by 40% and 54%, respectively. The compressive strength was also predicted using several analytical models based on fibre microbuckling and fibre kinking fracture mechanisms. One of the existing fibre microbuckling models was modified in this work to better account for the non-linear resin response. The predicted values showed that the UD nanomodified-FRP laminate exhibited a better compressive strength compared to that of the neat composite system. In addition, the results demonstrated that the performance of the nanosilica-filled HTS40/828 composite was comparable to that of the commercially available HTS40/977-2 system, which is currently used by the aircraft industry.

List of Publications

The following publications are based on the work within this thesis:

1. Jumahat A, Soutis C, Jones FR, Hodzic A. *Fracture mechanisms and failure analysis of carbon fibre/toughened epoxy composites subjected to compressive loading.* Composite Structures 2010;92(2):295-305.

2. Jumahat A, Soutis C, Hodzic A. *A graphical method predicting the compressive strength of toughened unidirectional composite laminates.* Applied Composite Materials 2011;18(1):65-83.

3. Jumahat A, Soutis C, Jones FR, Hodzic A. *Effect of silica nanoparticles on compressive properties of an epoxy polymer.* Journal of Materials Science 2010;45:5973-5983.

4. Jumahat A, Soutis C, Jones FR, Hodzic A. *Improved compressive properties of a unidirectional CFRP laminate using nanosilica particles.* Advanced Composites Letters 2010;19(6):204-207.

5. Jumahat A, Soutis C, Jones FR, Hodzic A. *Compressive behaviour of a nanoclay-modified aerospace grade epoxy polymer.* Accepted for publication in Plastic Rubbers and Composites Macromolecular Engineering. February 2011.

6. Jumahat A, Soutis C, Jones FR, Hodzic A. *The effects of nanosilica contents on thermal and mechanical properties of epoxy polymers.* Proceedings of the 10th SAMPE Europe International Conference (SEICO10), 12-14 April 2010, Paris France.

7. Jumahat A, Soutis C, Jones FR, Hodzic A. *Effect of clay nanoplatelets on compressive properties of an aerospace-grade epoxy Cycom 977-20.* Proceedings of the International Conference on Interfaces and Interphases in Multicomponent Materials (IIMM2010), 1–3 Sept. 2010, Sheffield UK.

8. Jumahat A, Soutis C, Jones FR, Hodzic A, Hayes SA. *Enhancement of compressive properties of unidirectional HTS40/828 CFRP composite using nanosilica-modified epoxy.* Proceedings of the International Conference on Interfaces and Interphases in Multicomponent Materials (IIMM2010), 1–3 Sept. 2010, Sheffield UK.

The following presentations were delivered as a result of the work within this thesis:

1. Jumahat A, Soutis C, Jones FR, Hodzic A. *Analysis of compressive failure of unidirectional carbon fibre/toughened resin composites.* 10th Conference of Deformation and Fracture of Composites (DFC10), 15-17 April 2009, Sheffield United Kingdom.

2. Jumahat A, Soutis C, Jones FR, Hodzic A. *Fracture mechanisms and failure analysis of carbon fibre/toughened epoxy composites subjected to compressive loading.* 15th International Conference on Composite Structures (ICCS15), 15-17 June 2009, Porto Portugal.

3. Jumahat A, Soutis C, Jones FR, Hodzic A. *Compressive properties of nanosilica-filled epoxy nanocomposites.* BSSM Seminar on New Approaches for Performance Definition of Composite Materials and Structures, 11 March 2010, London United Kingdom.

4. Jumahat A, Soutis C, Jones FR, Hodzic A. *The effects of nanosilica contents on thermal and mechanical properties of epoxy polymers.* 10th SAMPE Europe International Conference (SEICO10), 12-14 April 2010, Paris France.

5. Jumahat A, Soutis C, Jones FR, Hodzic A. *Polymer nanocomposites.* North Campus Annual Symposium 2010, 20 April 2010, Sheffield United Kingdom.

6. Jumahat A, Soutis C, Jones FR, Hodzic A. *Effect of clay nanoplatelets on compressive properties of an aerospace-grade epoxy Cycom 977-20.* International Conference on Interfaces and Interphases in Multicomponent Materials (IIMM2010), 1–3 Sept. 2010, Sheffield United Kingdom.

7. Jumahat A, Soutis C, Jones FR, Hodzic A, Hayes SA. *Enhancement of compressive properties of unidirectional HTS40/828 CFRP composite using nanosilica-modified epoxy.* International Conference on Interfaces and Interphases in Multicomponent Materials (IIMM2010), 1–3 Sept. 2010, Sheffield United Kingdom.

Acknowledgements

Praises to Allah for giving me guidance in life and strength to complete the thesis and also, peace be upon the beloved Prophet Muhammad.

I would like to thank my supervisor, Professor Constantinos Soutis, for his invaluable help, encouragement and direction throughout the duration of this project and my co-supervisors, Dr Alma Hodzic and Professor Frank R Jones, for many helpful discussions and advice.

I gratefully acknowledge both the Ministry of Higher Education Malaysia and Universiti Teknologi MARA for the PhD scholarship.

I would like to thank all members of the Composite Systems Innovation Centre (CSIC) University of Sheffield for their help and support with my work. In particular, I would like to thank Dr T Swait, Dr P Bailey, Dr S Hayes, Dr J Foreman, An Van, Austin, Vahid, Zurina, Galal, Akin, Carlos, Jack, Hong, Zheng and Suzeren.

I am grateful to the Departments of Mechanical Engineering and of Materials Science and Engineering for providing the facilities to carry out this project. I wish to thank all the staff of those departments for their help and support especially M Jackson, P Staton, D Smeadley, B Lane, C Grigson, M Renisson and R Kay. I would also like to thank C Hill from the Department of Biomedical Science and R Hanson from the Chemistry Department for their help with performing transmission electron microscopy and thermogravimetry analysis, respectively.

I gratefully acknowledge the Cytec Engineered Materials Ltd., for the supply of commercial aerospace grade epoxy resin Cycom 977-20, for providing the financial support for this work and for milling the nanoclay-filled epoxy. I would also like to acknowledge the nanoresins AG Geesthacht Germany for the supply of nanosilica (Nanopox F400), the nanocyl S.A. Belgium for the supply of Multi-wall carbon nanotubes (Epocyl NCR128), Nanocor for the supply of nanoclay (Nanomer I.28 and I.30) and the Toho Tenax Europe GmbH Germany for the supply of high tensile strength carbon fibre (HTS40 F13 12K 800 tex).

Finally, I would like to thank all my family members, especially my hubby Azuan Ahmad, my son Akmal Hakim, my daughter Amirah Afiqah, my mum Mosnah Lamri, my dad Jumahat Daim and my parents-in-law, who always support me and pray for my success in life and hereafter.

Contents

List of Figures

List of Tables

Abbreviations

ASTM	American Society for Testing and Materials
CAI	Compression after impact
CFRP	Carbon fibre reinforced plastics
CNF	Carbon nanofibres
CNT	Carbon nanotubes
CRAG	Composites Research Advisory Group
CT	Compact tension
CTE	Coefficient of thermal expansion
DGEBA	Diglycidylether of bisphenol A
DMTA	Dynamic mechanical thermal analysis
DSC	Differential scanning calorimetry
FRP	Fibre reinforced plastics
GFRP	Glass fibre reinforced plastics
ICL	Imperial College London
ILSS	Interlaminar shear stress
MMT	Montmorillonite
OHC	Open hole compression
PAN	Polyacrylonitrile
PES	Polyethersulphones
PTFE	Polytetraflouroethylene (Teflon)
RIM	Resin infusion moulding
RTM	Resin transfer moulding
SAMPE	Society for the Advancement of Material and Process Engineering
SEM	Scanning electron microscopy
SENB	Single-edge-notch bending
TEM	Transmission electron microscopy
TGA	Thermogravimetry analysis
TP	Thermoplastic
UD	Unidirectional
VARIM	Vacuum assisted resin infusion moulding
VARTM	Vacuum assisted resin transfer moulding
XRD	X-ray diffraction

Nomenclature

A	Cross-section area
A_f	Cross-section area of fibre
a_i	Major axial dimension of the cut fibre's elliptical surface
a	Initial crack length
b	Specimen tab length
d	Diameter
E	Young's modulus
E_m	Elastic modulus of the matrix
E_f	Elastic modulus of the fibre
F	Force
F_Q	Load to break
$f(a/w)$	Geometry calibration factor
G_{12}	Elastic shear modulus
G_{IC}	Critical energy release rate
G_m	Matrix shear modulus
h	Specimen thickness
I	Second moment of area
K_{IC}	Critical stress intensity factor
L	Length
m	Mass
N_i	Number of values within a class interval
n	Number of class interval
r_f	Fibre radius
s	Displacement
T	Temperature
Tg	Glass transition temperature
t	Specimen thickness
V_f	Fibre volume fraction
V_m	Matrix volume fraction
V_n	Nanoparticles volume fraction
V_o	Initial sinusoidal shape of amplitude
V_v	Void volume fraction
W_B	Energy to break
W_f	Fibre weight fraction
w	Specimen width

w	Kink band width
α	Coefficient of thermal expansion
β	Angle of kink band
δ	Displacement or deformation
ε	Normal strain
ε_f	Failure strain
Φ	Angle of the rotated fibres
ϕ_i	Angle of fibre misalignment
ϕ_o	Initial fibre misalignment
ϕ_{pc}	Sample intersection angle or plane-cut angle
$\phi(a/w)$	Energy calibration factor
γ	Shear strain
γ_y	Shear yield strain
λ	Fibre wavelength
ν_{12}	Longitudinal Poisson's ratio
θ_i	Precise angle of cut for each fibre
ρ	Density
σ	Standard deviation
σ	Normal stress
σ_y	Yield stress
σ_u	Ultimate stress
τ_{12}	In-plane shear stress
τ_y	Shear yield stress
τ_u	In-plane shear strength
ζ	Shape factor

Chapter 1

Introduction

1.1 Introduction

Fibre reinforced polymers (FRP) are composite material systems made of polymer matrices reinforced with continuous or discontinuous fibres. High strength, high modulus continuous carbon fibres of 5-7 μm filament diameter are the most versatile materials used in the development of modern FRP composite structures. Epoxies are well known thermosetting resins with excellent overall properties such as good adhesion characteristics with carbon fibres and good balance of physical, mechanical and thermal properties. The FRP composites, which are made of epoxy matrix reinforced with carbon fibre known as carbon fibre reinforced polymer (CFRP) composites, offer high strength and stiffness to weight ratios as well as good resistance to fatigue and corrosion. In addition, CFRP composites have extensively been used in the aircraft and high-end automobile constructions because of the ability to shape and tailor their structure to produce more aerodynamically efficient structural configurations [1,2].

However, the design of CFRP composite structures is often controlled by the compressive strength of the material. The compressive strength of currently used CFRP composites is usually 60% of the tensile strength, which minimises the potential of the CFRP composites. In addition, the compressive strength of the CFRP composite laminate can be reduced by more than 50% due to the presence of stress raisers, such as fastener holes, notches, fibre discontinuity caused by manufacturing defects or impact damage [1-6]. Furthermore, compressive loading and buckling can lead to instantaneous and catastrophic failure of the CFRP composite structure. In metals loaded in compression, yielding or plastic strain indicates fracture is about to occur while the CFRP composite system breaks in a more brittle manner. Therefore, compressive

response is one of the most important factors that should be taken into consideration when designing CFRP composite structures.

The compressive strength of unidirectional CFRP composites is primarily influenced by the in-plane shear properties and the initial fibre misalignment angle [1,3,7]. Since fibre waviness is difficult to avoid during the manufacturing processes (mainly due to mismatch of constituent thermal properties), in recent advanced composite systems attention is devoted to the development of a stiffer and tougher resin using nanofillers. A stiffer and tougher resin increases the lateral support provided to the fibre and extends the plastic hardening behaviour after shear yielding.

In theory, a stiffer and tougher resin provides a good load transfer and lateral support to the fibres, gives better resistance to fibre instability (microbuckling) and delays crack initiation and propagation. Therefore, by modifying the resin using nanofillers will improve the overall matrix-dominated properties such as in-plane shear, interlaminar shear and compressive strengths and fracture toughness. However, many factors affect the capability and performance of the nanomodified-resin. It primarily depends on the type and properties of the fillers along with their surface treatment, compatibility of the fillers to the epoxy and hardener, degree of dispersion of the fillers in the matrix and their interfacial adhesion, processing methods and curing conditions. Improper selection of resin, fillers and fabrication method leads to a significant reduction in the overall properties of the composite laminates; nanofillers may act as manufacturing defects.

This brief introduction highlights the need for improved compressive properties that can be achieved by optimisation of nanofiller content and dispersion in the selected polymer resin.

1.2 Aims of the thesis

Based on the problem statement discussed in the previous section, this research is aimed to:

i) develop a stiffer and tougher resin based on three types of nanofiller (silica nanospheres, multi-walled carbon nanotubes and clay nanoplatelets) and two types of epoxy (Epikote 828 and Cycom 977-20).

ii) evaluate the thermal and mechanical properties of the nanomodified-resins and compare those properties with that of the pure resins.

iii) select the best performance nanomodified-resin system for the fabrication of nanomodified-CFRP composites.

iv) investigate the effect of the selected nanofiller on the compressive and in-plane shear properties of CFRP laminates.

v) predict the compressive strength of the unidirectional laminate using existing models, compare to the measured values and modify if they differ.

Therefore, this work is intended to study and evaluate how much nanofillers influence the thermo-mechanical properties of the epoxy and contribute to the enhancement of the properties of the CFRP composite, especially the compressive response (stiffness, strength and strain to failure).

Chapter 2

Literature review

2.1 Summary

The aim of this chapter is to present a review of literature which is of relevance to the current study and justifies the need for this work. It focuses on the properties of epoxy-based fibre reinforced polymer (FRP) composite systems. First, various techniques for improving matrix-dominated properties of FRP laminates for the past two decades are reviewed. This is followed by a review of advanced polymer composite systems using nanofillers as the modifier to the epoxy and FRP laminates. The effects of nanosilica, carbon nanotubes (CNT) and nanoclay on the mechanical and thermal properties of epoxy polymers and FRP laminates (based on carbon or glass fibres) are discussed. The degree of reinforcement provided by the nanofillers is examined, along with important influence factors, such as type of nanofillers and their surface treatment, type of matrix and reinforcing fibres, nanofiller volume fraction, degree of dispersion and the particle-matrix interfacial properties.

2.2 Conventional FRP composites

The word "composite" describes a multi-phase material where its overall physical and mechanical properties are determined by the material interaction of the phases (or constituents) [8]. The reinforcing phase can take the form of fibres (either continuous or short, woven, aligned or randomly distributed), particle or flakes. Materials for this phase include glass, carbon, polymers, metals, or ceramics. Commonly used matrices include polymers, metals or ceramics. Continuous fibre reinforced polymer (FRP) composites are frequently regarded as advanced materials [1-10]. This is mainly due to high specific strength (strength/density) and specific modulus (elastic modulus/density)

that they possess. Nowadays, these materials are widely being used in various applications, such as aircraft and aerospace structures, satellites, advanced marine vessels, fuel tanks, sports equipment, high-end automobile structures, pipes and many other strength/weight critical applications [1-2,8-10].

The use of advanced composite materials in aircraft and aerospace structures required superior performance under extreme mechanical loadings and environmental conditions [1-2,8-10]. Carbon fibres of 5-7 μm diameter have 220-350 GPa Young's modulus and 2.3-3.7 GPa tensile strength [9]. Epoxy resins have several attractive features for composite applications that include good adhesion characteristics with carbon fibres, good physical and mechanical properties, chemical resistance and dimensional stability, ease of processing and low material cost [10]. A composite made of a high strength carbon fibre combined with a high performance epoxy matrix offers outstanding structural characteristics. For instance IM7/977-2 system has a tensile longitudinal elastic modulus of 142 GPa and a tensile strength of 2537 MPa [4-6]. Therefore the composites industries, especially for aircraft and aerospace structures, are dominated by carbon fibre reinforced polymer (CFRP) composite materials. This work mainly focuses on the properties of these FRP composite materials.

The first generation of composites introduced to aircraft construction in the 1960s employed brittle graphite/epoxy systems such as Thornel T300/Narmco 5208 CFRP composite [1,4-6]. This leads to laminated-structures with poor matrix-dominated properties, such low compressive strength, interlaminar strength, fracture toughness and impact resistance, and limits their potential to be used as aircraft primary structure that requires high damage resistance and damage tolerance. Several efforts have been devoted to improve these matrix-dominated properties [4-6,9-44], such as:

(i) developing high failure strain carbon fibres,
(ii) using a thin ply prepreg of 75 g/m^2,
(iii) applying thermoplastic film to the prepreg,
(iv) co-weaving and stitching the carbon fibre with thermoplastic fibre to produce hybrid woven fabrics,
(v) incorporating soluble thermoplastic powder into the epoxy,
(vi) adding thermoplastic veil onto the carbon fibre preform, and
(vii) modifying epoxy resins with toughening agents (elastomer, rubber, core shell and alumina particles, glass beads and others).

High strain carbon fibre has been developed to improve the mechanical performance of CFRP composite. However, attempts to improve failure strain and strength of the carbon fibre often lead to reduced stiffness and vice-versa. For instance, high strain carbon fibre has 230 GPa Young's modulus, 1.6% failure strain and 3.7 GPa tensile strength while high modulus carbon fibre has 340 GPa Young's modulus, 0.7% failure strain and 2.4 GPa tensile strength [9,10]. Yokozeki *et al.* [11] and Sihn *et al.* [12] introduced thin prepreg of 75 g/m^2 to produce laminates. The results showed a slight improvement (8-9%) of the open hole compression and compression after impact properties compared to that of standard laminates (using standard prepreg of 145 g/m^2). In addition, the manufacturing cost is increased by spreading fibre tows into thin-ply prepreg and layup process. The other method to improve matrix-dominated properties is using stitched or weaved fabrics for the fabrication of CFRP composite laminate [1,13-15]. A glass yarn is used for stitching or weaving. These operations maintain the alignment and orientation of the fibres during composite fabrication process. However, the compressive properties of the laminate were significantly reduced due to the presence of local fibre waviness, resin rich regions and fibre breakage created by the stitches [13-15]. Gary *et al.* [14] reported that the compressive strength of the composites was reduced by 50% compared to the unstitched composites.

In contrast to those systems, which have been discussed above, Vlasveld *et al.* [16-17] proposed alternative way by replacing epoxy matrix with thermoplastic (TP) polymer such as polyamide 6 (PA6). Although TP material provides a high fracture toughness and damage tolerance, it has low stiffness, strength, thermal stability and chemical resistance. In addition, the processing TP polymer needs high temperatures and pressures, which leads to higher production costs. Based on extensive literature work, Parlevliet *et al.* [18] showed that the TP composite laminates suffer from thermal residual stresses, which occur due to mismatch in thermal shrinkage. This induced microcracking and fibre waviness in the laminates and hence reduced their mechanical properties.

High performance TP materials, such as polyethersulphones (PES), polyetherketones (PEEK), polyimide and nylon, have been used as toughening agents for commercial CFRP composites [4-7,19-24,31-32] such as IM7/977-2, IM7/F655 and IM6/1808I systems. These TP materials exhibit high glass transition temperature and fracture toughness [25]. However, many of these polymers have a low resistance to attacks by solvents or chemicals and do not provide adequate dimensional stability at

high application temperatures [29]. Inclusion of TP material into the epoxy matrix to form two-phase morphology polymer exhibited better mechanical properties compared to the pristine polymer [25-30]. However, the rate of increase in viscosity of the epoxy-thermoplastic solution blend is much higher than the rate of increase in toughness of the resultant matrix [20,22,23,25,30]. The exponential increase in viscosity limits the process and handling characteristics of the matrix. For instance, the thermoplastic toughened epoxy Cycom 977-2 resin has a viscosity of more than 500 Pa.s at 65°C [22] while the Cycom 977-20, high molecular weight epoxy which has no thermoplastic, has a 0.5–1 Pa.s viscosity at the same temperature [23]. Therefore the optimum toughness is always sacrificed to maintain the processability of the resin. Due to the viscosity constrain, the TP powders, of 2-35 μm diameter, are mixed with epoxy resin and used for preparing prepreg [19]. During the curing process, the TP powder dissolves into the epoxy matrix. Nevertheless, dispersion is typically poor due to difficulty in controlling distribution of particles and non-uniform particle size. This influences the rate and degree of melting where large or agglomerated particles remain partially dissolved after curing and form thermoplastic rich regions [19].

One of the earliest techniques employed to improve fracture toughness of the CFRP composite system is to introduce undissolved thin thermoplastic film onto one side of the prepreg tape such as the IM6/1808I CFRP system [6,31]. When cured, the laminate has an interleaf approximately 12.7 μm thick between fibre plies. The film does not diffuse into the epoxy matrix hence reducing the capability of epoxy resin to support the carbon fibres. In compression, the specimens failed prematurely via longitudinal splitting due to poor interfacial bonding between resin and the fibres. The other way to add thermoplastic into a composite system is by stitching or weaving it directly to the carbon fibre [23,32]. Resin infusion technology (RIM) is used to cure the fibre preform. The stitching process using soluble polyester fibre yarn, causes damage to the carbon fibre and leads to reduced mechanical properties. Weaving the TP into the structural reinforcement fibres also increases the manufacturing cost. In addition, it disturbs the arrangement and straightness of the carbon fibres hence reduces the in-plane compressive properties of the laminate. LoFaro *et al.* [24] manufactured resin-soluble TP veil using PES fibres. The 8 mm chopped fibres are typically dispersed by hand on release film and pressed at 180°C for 1 hr to form a thin veil. Layers of carbon fabric were interleafed with non-woven fabrics to manufacture the composite using the resin transfer moulding method. The TP veil dissolved in 977-20 resin after curing. The

compressive strength and compression after impact strength were comparable to those prepared using 977-2 prepreg [22].

The other approach to improve matrix-dominated properties is by incorporating elastomeric particles into epoxy resin that form a compliant interleaf (approximately 20-40 μm thick) between fibre plies such as T800/F3900 and IM7/8551-7 system [4-6]. These particles are larger than the space between fibres therefore they are mostly confined to the interply region. Various types of elastomers or rubbers, which are commercially used in CFRP composites, are also reported in [33-35]. Rubbers or elastomers show ductility to some degree and are less rigid than the polymer matrix. These serve as excellent toughening agents in matrices. Rubbers tend to improve the toughness of the epoxy by preventing the propagation of cracks and boosting the strain capability. Rubber particles induce the formation of microvoids and activate the yielding processes of the matrix [36-38]. A substantial amount of energy is dissipated within the plastic zone near the crack tip. This contributes to the tougher matrix [36-38]. However, the increase in toughness of the epoxy-rubber matrix is accompanied by a reduction in elastic modulus, strength, creep resistance and the thermal stability of the composite [36-40]. Moreover, a low compressive strength of the CFRP system was observed in [4-6,40] due to the presence of a soft elastomer compliant interface, which minimised the capability of the epoxy to support the fibres against fibre microbuckling. In contrast, a stiffer matrix can be obtained by inclusion of rigid particulate fillers such as glass beads, glass flakes, mica flakes, alumina and titanium oxide [41-44]. These fillers enhance the elastic modulus of the polymer, however they often reduce the failure strain and strength. In other words, micron-sized fillers increase stiffness but damage the ductility of the polymer.

2.3 Advanced nanofilled-FRP composites

The overall performance of the FRP composites is mainly determined by the properties of the fibre, matrix and fibre-matrix interface [2,8-10]. In tension, the composite properties depend mainly on those of the continuous fibres and to lesser extend on fibre-matrix interface. While, in compression the properties depend on the properties of the resin, the fibre waviness and fibre-matrix interface [7,45-55]. Scanning electron micrographs revealed that the failure of unidirectional (UD) CFRP composite laminates was initiated by fibre microbuckling and subsequent plastic kinking of the material

[7,50]. Therefore the development of stiffer and tougher matrices is aimed at delaying fibre microbuckling, extending plastic hardening behaviour of the matrix and giving better resistance to crack initiation and propagation. As a result, this will improve the overall matrix-dominated properties of the CFRP composites, such as in-plane shear and compressive strength, compression after impact and open hole compression, leading to a less notch sensitive composite system. However, the conventional toughening epoxy systems, as discussed in the previous section, showed that attempts to enhance fracture toughness are frequently coupled with lower elastic modulus and thermal properties, and vice-versa [33-44]. This leads to a low compressive strength and reduces the overall performance of the CFRP composite.

The latest development in polymer composite technology is the enhancement of matrix-dominated properties and thermal stability of FRP composites by the inclusion of nanofillers in the epoxy matrix. In this thesis, this is called a nanofilled-FRP composite. The addition of nano-sized fillers into the epoxy (called nanomodified-epoxy) can lead to a number of desirable effects. The most practical reasons [56-61] are to:

(i) stiffen the matrix (increase elastic modulus) and make it more rigid,

(ii) enhance strength and failure strain,

(iii) improve resistance to crack initiation and propagation (fracture toughness), and

(iv) reduce the coefficient of thermal expansion, thermal shrinkage and enhance thermal stability of the neat polymer that could reduce thermal stresses and hence fibre waviness.

In order to achieve these, the selected nanofillers usually have higher elastic modulus and lower coefficient of thermal expansion than the matrix. There are several types of nanofillers commercially available and commonly used for developing nanomodified-epoxy, such as montmorillonite organoclay, nanosilica, carbon nanotubes (CNT) and carbon nanofibres (CNF). The incorporation of these nanofillers enhanced mechanical and thermal properties of the epoxy polymers that have been reported by numerous researchers [56-65,68-77,92-95,117-121].

Although the properties of nanomodified-epoxy polymers have widely been studied in various research fields [56-61], the research on nanofilled-FRP composites is

still in the early stages. This new generation of hybrid materials are very promising composites for use in commercial applications especially aircraft and aerospace structures. However, the use of nanomodified-epoxy resin systems for the fabrication of FRP composites has been a challenge. Several challenges that need to be overcome are:

(i) the selection of a processing method to uniformly disperse the nanoparticles in the epoxy matrix and in the FRP composites,

(ii) the viscosity increase with nanoparticle content, and

(iii) the selection of a nanomaterial which is compatible with the polymer matrix to create strong interfacial interaction between them. This includes type of surface treatment required.

Agglomerated nanoparticles in a matrix introduce local stress concentrations and a weak particle-matrix adhesion, reducing the capability of load transfer [56-61]. This leads to a premature failure of the polymer and thus reduces its strength and strain to failure. In addition, resin viscosity increases exponentially as the nanofiller content is increased [56-61]. This leads to process difficulties and a low quality FRP composite.

The following sections present and discuss some recent studies on nanomodified-epoxy resins and nanofilled-FRP composites, which are thought to be relevant to the present work.

2.3.1 Nanosilica-filled FRP composites

Silica nanospheres are used as a reinforcing filler for polymers because of their high elastic modulus (70GPa), high specific surface areas (50-380 m^2/g), high thermal stability (1200°C), low density (1.8 g/cm^3), low thermal expansion coefficient, good abrasion resistance and low material cost (USD $8.50/lb) [56,58,66-67,73]. The effect of nanosilica on mechanical and thermal properties of epoxy polymers has been investigated by several researchers [56,58,62-65,68-84]. Some of the results are listed in Tables 2.1 and 2.2.

Table 2.1: Thermal and mechanical properties of nanosilica-filled epoxy polymers prepared using direct mixing method reported in selected references.

Type of filler	Epoxy / Hardener	Effect	Refs.
14 nm silica Aerosil R202 (treated: polydimethysiloxane) (from: Degussa)	Cycom 977-3	DMTA: • 2 wt%: Tg ↑ 9%, E^* ↑ 100% • 5 wt%: Tg ↑ 3%, E^* ↑ 45%	[56]
12 nm silica Aerosil R805 (treated: octylsilane) (from: Degussa)	Cycom 977-3	DMTA: • 2 wt%: Tg ↑ 3%, E^* ↑ 47% • 5 wt%: Tg ↑ 0.4%, E^* ↑ 44%	[56]
15 nm silica pretreated with KH-560 coupling agent (from: Ming-Ri nanometer materials ltd.)	CYD-128/ JHB-590	DSC: • 3 wt%: Tg ↑ 40% • 5 wt%, Tg ↑ 17% Mechanical tests: • 3 wt%: TS ↑ 115%, TM ↑ 13%, IS ↑ 60% • 5 wt%: TS ↑ 11%, IS ↑ 10%	[62]
12 nm silica MEK-ST (from: Nissan chemical)	Epon 862 diglycidyl ether of bisphenol–F (DGEBF)/ Epicure-W	Mechanical tests: • 5 wt%: TS = 0%, TM ↑ 15%, K_{IC} ↑ 39%, G_{IC} ↑ 68% • 10 wt%: TS = 0%, TM ↑ 25%, K_{IC} ↑ 15%, G_{IC} ↑ 6%	[63]
7 nm silica Aerosil 380 (treated: 3-glycidyloxypropyltrimethoxy-silane) (from: Degussa)	MGS L135i diglycidyl ether of bisphenol–A DGEBA/ H137i amine	Mechanical tests: • 0.5 vol%: TS ↑ 3%, TM ↓ 4%, TFS ↑ 9%, K_{IC} ↑ 54%	[64]
12 nm silica Aerosil 200 (from: Degussa)	DGEBA/ Methyl hexahydrophthalic anhydride (MHHPA)	Mechanical tests: • 6 vol%: TS ↑ 8%, TM ↑ 17%, TFS = ↑ 15%, K_{IC} ↑ 48%, G_{IC} ↑ 85%	[65]

Note: Tg = Glass transition temperature, E^* = Dynamic elastic modulus, TS = Tensile strength, TM = Tensile modulus, IS = Impact strength, K_{IC} = Critical stress intensity factor, G_{IC} = Critical energy release rate, TFS = Tensile failure strain.

Table 2.2: Thermal and mechanical properties of nanosilica-filled epoxy polymers prepared using sol-gel technique reported in selected references.

Type of filler	Epoxy / Hardener	Effect	Refs.
12 nm silica ERL4221 (from: Hense Chemie)	Cyloaliphatic bisepoxide epoxy/ MHHPA	14 vol%: BS ↑ 40%, BM ↑ 37%, K_{IC} ↑ 58%	[58]
20 nm silica Nanopox E470 (from: Nanoresins)	DGEBA/ MHHPA	14 vol%: TS ↑ 20%, TM ↑ 44%, TFS ↓ 9%, K_{IC} ↑ 51%, G_{IC} ↑ 62%	[65]
20 nm silica XP22/0314 (from: Hense Chemie)	Cyloaliphatic epoxy UVA-CURE1500/ Albidur HE 600	14 vol%: Tg ↓ 7%, BS ↑ 4%, BM ↑ 37%, BFS ↓ 25%, K_{IC} ↑ 76%, G_{IC} ↑ 148%, IS ↓ 7%	[68]
20 nm silica XP22/0516 (from: Hense Chemie)	Araldite- F DGEBA/ Albidur HE 600	8 wt%: Tg ↑ 2%, TS ↑ 2%, TM ↑ 14%, BS ↑ 11%, BM ↑ 18%, K_{IC} ↑ 50%	[69]
25 nm silica Nanopox F520 (from: Nanoresins)	DGEBF/ Albidur HE 600	15 vol%: Tg ↓ 14%, TS ↑ 5%, TM ↑ 48%, TFS ↓ 38%, K_{IC} ↑ 77%, G_{IC} ↑ 114%	[70]
20 nm silica Nanopox F400 (from: Nanoresins)	DGEBA/ Albidur HE 600	20.2 wt%: K_{IC} ↑ 73%	[71]
	Bakelite EPR164 DGEBA/ Albidur HE 600	13.4 vol%: Tg ↓ 4%, TM ↑ 30%, K_{IC} ↑ 141%, G_{IC} ↑ 348%	[72-74]
	Araldite- F DGEBA/ Piperidine amine	5 vol%: Tg = 0%, CTE ↓ 49%, TS = 0%, TM ↑ 22%, TFS ↑ 4%, K_{IC} ↑ 72%, G_{IC} ↑ 141%	[75-76]
	Araldite- F DGEBA/ Jeffamine D230	20 wt%: TS ↑ 4%, TM ↑ 40%, K_{IC} ↑ 130%, G_{IC} ↑ 274%	[77]
	Araldite- F DGEBA/ diaminodihenyl sulfone (DDS)	20 wt%: TS ↑ 22%, TM ↑ 40%, K_{IC} ↑ 61%, G_{IC} ↑ 81%	[77]

Note: BS = Bending strength, BM = Bending modulus, BFS = Bending failure strain, TS = Tensile strength, TM = Tensile modulus, TFS = Tensile failure strain, K_{IC} = Critical stress intensity factor, G_{IC} = Critical energy release rate, IS = Impact strength, Tg = Glass transition temperature, CTE = Coefficient of thermal expansion.

Koo [56] studied the effect of two different types of nanosilica on glass transition temperature (Tg) and dynamic elastic modulus (E^*). The nanofillers were directly blended with the resin to prepare a series of nanocomposites. The specimens were tested using a dynamic mechanical thermal analysis (DMTA). In general all nanomodified-epoxy systems exhibited higher Tg and E^* compared to the neat Cycom 977-3 polymer, as summarised in Table 2.1. The TEM micrographs showed a distribution of agglomerated nanoparticles of 1, 2 and 5 wt% nanosilica in the matrix. The DMTA results showed that the addition of 2 wt% Aerosil R202 enhanced Tg and E^* by 9% and 100%, respectively. For Aerosil R805, the degree of reinforcement was slightly lower than those obtained using Aerosil R202. This is due to a strong interaction between the Aerosil R202 nanoparticles and the matrix. Koo [56] extended the study by fabricating prepregs using AS4-6K carbon fibre fabric and nanomodified-Cycom 977-3 resin of 2 wt% Aerosil R202 and 2 wt% Aerosil R805. The results of fracture toughness, tensile strength, interlaminar shear strength and flexural strength of nanomodified-AS4-6K/977-3 CFRP composite compared to the unmodified system were presented. However, the results obtained were disappointing where no significant improvement in tensile strength was observed for the nanomodified systems, and even worst the presence of agglomerated nanosilica reduced the fracture toughness, interlaminar shear strength and flexural strength. For instance, the inclusion of 2 wt% Aerosil R202 reduced the fracture toughness, interlaminar shear strength and flexural strength of the AS4-6K/977-3 CFRP composite by 39%, 7% and 6%, respectively. Therefore, the quality of the fabricated composite is one of the important factors along with the properties of the matrix, including the degree of nanofillers dispersion, void content, nanofillers volume fraction and interfacial bonding between the nanomodified-epoxy and the carbon fibre.

Agglomeration of nanosilica particles was also observed in [62-65] for various types of epoxy systems. At low nanosilica content, enhanced mechanical properties especially fracture toughness were observed. However, at high nanosilica content the nanocomposites failed prematurely due to weak interfacial bonding of agglomerated nanoparticles to the resin. Zheng *et al.* [62] fabricated glass fibre reinforced polymer (GFRP) composites using 1, 5 and 7 wt% nanosilica and epoxy system as given in Table 2.1. It was found that the addition of 7 wt% nanosilica into the GFRP composite improved the tensile strength, tensile modulus, bending strength, shear strength and compressive strength by 24%, 22%, 54%, 14% and 13%, respectively. They claimed

that these improvements were attributed to the strong adhesion of nanosilica particles to the surface of the glass fibres. Therefore, this promotes the stress transfer between the fibres and the matrix. However, the slight improvement in compressive strength indicated that uneven distribution of nanosilica in the laminate limits the capability of the resin to support the fibre against microbuckling.

In contrast to direct mixing methods applied in various nanomodified-epoxy systems as listed in Table 2.1, Hanse Chemie AG [66] and Nanoresins AG [67] produced a non-agglomerated and homogeneously dispersed nanosilica in epoxy using a sol-gel technique. These masterbatch nanosilica/epoxy products were used in various systems [58,65,68-84] to study the effect of nanosilica on thermal and mechanical properties of the epoxy polymers. Some results are listed in Table 2.2 based on the optimum formulation. It was found that the degree of reinforcement depends on the compatibility of the nanosilica with the resin systems. All results showed an agreement where the addition of homogeneously dispersed nanosilica enhances the fracture toughness of the polymer. A maximum of 141% and 348% increase in critical stress intensity factor K_{IC} and critical energy release rate G_{IC}, respectively, were reported by Johnsen *et al.* [73] for a 13 vol.% nanosilica-filled EPR164/HE600 epoxy polymer. Several types of toughening mechanisms such as crack pinning, crack deflection, immobilised polymer and plastic void growth were reviewed. The debonding of the nanoparticles and subsequent plastic void growth were considered as the major toughening mechanism responsible for the increase in fracture toughness [73].

Kinloch *et al.* [78] used the nanomodified-epoxy developed in [72-74] to investigate the effect of nanosilica on interlaminar fracture toughness of a CFRP composite. Friedrich *et al.* [58] showed that the viscosity of unmodified epoxy resin at room temperature was 0.075 Pa.s. The viscosity increased with nanosilica content. The maximum of 14 vol.% nanosilica increased the viscosity of the resin to about 0.33 Pa.s. At working temperature of 60°C, the viscosity was reduced to 0.01 Pa.s for the pure resin and 0.07 for the nanomodified-epoxy. Therefore, the addition of nanosilica contributed to a small increase in viscosity and retained ease of processing. The non-agglomerated and small particle size of 20 nm allows it pass through close meshed fabrics (no filtering effect). Therefore, a vacuum assisted resin transfer moulding (VARTM) manufacturing technique was employed by Kinloch *et al.* [78] in order to prepare a laminate using linen-weave 0/90 carbon fibre mat. The fibre volume fraction of the laminate was 26.5 vol.%. The result showed that the fracture toughness of the

unmodified CFRP was 439 J/m^2. However, the addition of 11.9 wt.% nanosilica showed no significant improvement on the fracture toughness of the CFRP (11 % increase). It was claimed in [78] that a 9 wt% carboxyl terminated butadiene-acrylonitrile (CTBN) rubber was added to the nanosilica-filled CFRP composite system and the fracture energy increase to 1320 J/m^2 (201% increase). The authors concluded that further work is needed to study the effect of adding rubber particles to the compressive properties of the laminate. This is due to the fact that a softer matrix reduces its capability to support the reinforcing fibre and leads to a lower compressive strength.

Kinloch and coworkers [79-83] extended the study to investigate the effect of nanosilica on fracture toughness and tensile fatigue behaviour of GFRP composites. Resin infusion technique was used to fabricate 10 wt% nanosilica-filled GFRP laminates based on UT-E500 glass fibres and LY556/HE600 epoxy resin. The results showed that the addition of nanosilica improves the fracture toughness by 208% [81-83]. The fracture surface of the nanomodified-UD laminate showed the presence of fibre bridging mechanism. This contributes to increase in fracture energy. The fatigue life of nanomodified-GFRP composite was 3-4 times higher than that of the unmodified system [79-80]. The reduced crack growth rate due to particle debonding and plastic void growth mechanisms contributed to an increase in fatigue life of the nanomodified system.

Uddin and Sun [84] took a further step to study the effect of nanosilica on tensile and compressive properties of GFRP composite laminates. A VARTM method was used to fabricate the unidirectional and off-axis laminates using E-LR-0908-14 E-glass fibre cloth and DGEBA/Cycloaliphatic amine resin. In order to minimise voids in the laminate, the nanomodified resin was degassed for an hour before it was diffused into the VARTM mould. Laminates with 42-50% fibre volume fraction (V_f) were fabricated. It was found that the addition of 15 wt% nanosilica into GFRP composite significantly improves the transverse tensile modulus and strength by 32% and 41%, respectively. The longitudinal tensile strength was increased by 11% while no improvement was recorded for the longitudinal tensile modulus. The longitudinal tensile properties depend on the properties of fibre while the transverse tensile properties depend on the properties of the matrix and fibre/matrix interface. Therefore, stiffer and tougher nanomodified matrix contributes to a significant improvement in the transverse tensile properties. The compression tests were conducted using ASTM D695 for rigid plastic materials rather than ASTM D3410 or D6641 compression test standards for composite materials. As a

result, the specimens failed due to brooming failure mode at the specimen's end near to the loading platens. Therefore, the longitudinal compressive strength was predicted using the off-axis compressive strength results. It was found that the compressive strength was improved by 81% and 61% for the nanomodified-laminate with V_f = 42% and 50%, respectively, but not physically measured.

Based on the literature study, it was found that the matrix dominated properties such as fracture toughness, transverse tensile strength and compressive properties primarily depend on the properties of the matrix. A stiffer and tougher matrix such as nanosilica-modified epoxy significantly improved these properties. However, further studies are needed to better understand the toughening mechanisms in newly developed nanomodified hybrid systems, especially where the reinforced fibres are carbon.

2.3.2 CNT-filled FRP composites

The remarkable physical and mechanical properties of carbon-based nanofibres render themselves an ideal class of reinforcing filler for polymeric materials. There are three types of fibrous nanoparticles:

(i) Single-walled carbon nanotubes (SWCNT) with diameter of about 1 nm [56],

(ii) multi-walled carbon nanotubes (MWCNT) with inner diameter of 2-10 nm and outer diameter of 20-70 nm [56], and

(iii) carbon nanofibres (CNF) such as cup-stacked carbon nanotubes (CSCNT) [88-89], vapour grown carbon nanofibres (VGNF) [56,90] and vertically-aligned carbon nanofibres (VACNF) [91]

SWCNT has low density (1.33-1.40 g/cm^3), high elastic modulus (1200 GPa), high tensile strength (2 GPa), high surface area (250-300 m^2/g), low coefficient of thermal expansion, high thermal stability (750°C) and high resilience in sustaining bending force [56,58-61,85-87]. MWCNT has tensile elastic modulus of 270-950 GPa, tensile strength of 11-63 GPa, bending elastic modulus of 1260 GPa and bending strength of 14 GPa [85-87]. CNF such as CSCNT has an outer diameter of 80-100 nm, inner diameter of 50-60 nm, length of 200 μm length, density of 2.1 g/cm^3, elastic modulus of 1400 GPa and tensile strength of 7 GPa [88-89]. The properties of CNF are comparable to that of

SWCNT. Therefore, the aim of adding CNT and CNF into epoxy polymers is to improve their mechanical and thermal properties.

The degree of reinforcement depends on the type of nanofiller and its surface treatment, processing method and type of resin system. Homogeneous dispersion of CNT in the resin and good interfacial adhesion between them are prerequisites for the improvement in mechanical properties [58-61,92-95]. In order to enhance the nanofibre/matrix interfacial adhesion, the surface of CNT or CNF is treated using several methods (similar methods used for the treatment of micron-sized carbon fibre [10]) as summarised in Figure 2.1. For instance, the influence of surface treatment of MWCNT on tensile properties of epoxy polymer (DGEBA YD128/amine TH432) was studied by Kim *et al.* [92]. The MWCNTs were purified using a 3:1 mixture of H_2SO_4/HNO_3 and then treated using Ar plasma. The addition of 1 wt% plasma treated CNT in the polymer enhanced the tensile modulus by 33%, tensile strength by 123% and failure strain by 124%. The field emission scanning electron (FESEM) micrographs showed good dispersion of CNT in the matrix. The fracture surface of the tensile specimens showed evidence of fibre breakage mechanisms rather than fibre pulled out. This indicates a strong interfacial adhesion between the CNT and matrix. A similar surface treatment technique was employed by Tseng *et al.* [93]. The results showed that the addition of 1 wt% plasma treated MWCNT increased the tensile modulus, strength and failure strain of epoxy polymer by 102%, 50% and 378%, respectively. In addition, the decomposition temperature of the nanomodified polymer was increased by 6% and the glass transition temperature was increased by 28%.

Although good dispersion of CNT in the epoxy resin was achieved, the problem still exists with resin viscosity, which limits the CNT content up to a maximum of 1-2 wt%. The viscosity of the resin was increased with an increase in CNT content. This reduced its processability at high CNT content especially for the fabrication of nanomodified-FRP composites. Therefore another challenge is to fabricate a good quality CNT-filled FRP composite, which has a low void content, good dispersion of CNT, optimum CNT content and high fibre volume fraction. Zhou [59] introduced pre-bind CNF onto glass fibre mat using a spray technique instead of a conventional mechanical mixing technique of CNT in epoxy. The surface-treated Pyrograf-III CNF (PR19-LHT-OX), with a diameter of 100-200 nm and length of 30-100 μm, was sprayed on UD QM6408 glass fibre mat. Vacuum assisted resin transfer moulding (VARTM) was used to impregnate the preform with unsaturated polyester resin Aropol

Q6585. The cured laminates had a fibre volume fraction of 48-51%. The results demonstrated that the addition of 3.5 wt% CNF improved the flexural modulus and strength of GFRP composite by 20% and 66%, respectively. However, SEM micrographs showed non-uniform distribution of CNF in the laminate.

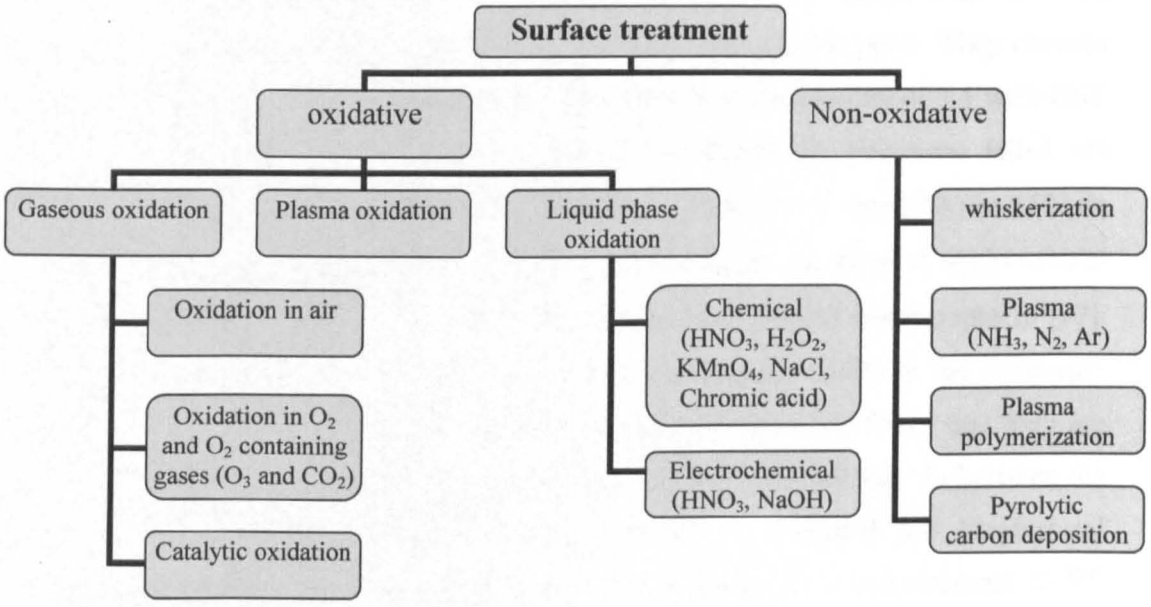

Figure 2.1: Summary of surface modification techniques of CNT/CNF based on surface modification technique for micron-sized carbon fibres [10].

A similar type of CNF was used by Rice *et al.* [90] to fabricate a nanomodified-IM7/862 CFRP composite using a wet-lay up technique. The impregnated carbon fibre was cured in the autoclave. The addition of 8 wt% Pyrograf III CNF into IM7/862 composite improved the interlaminar shear strength by 6%, in-plane shear modulus by 17%, in-plane shear strength by 15%, compressive modulus by 11%, compressive strength by 7%, which is similar to the coefficient of variation observed in compression tests. The optical micrographs showed that the CNF created ply interleaf in between the plies. A poor dispersion of CNF in the matrix minimised the capability of the matrix to support the fibre. Thus, the presence of CNF slightly improved the matrix-dominated properties of the composite. A similar type of CNF was also used by Koo [56] to fabricate a nanomodified-AS4-6K/Cycom 977-3 CFRP composite. The results showed that the inclusion of 2 wt% CNF in the CFRP laminate reduced the fracture toughness G_{IC} by 55% and flexural strength by 5% with slight improvement in interlaminar shear

strength (9%). This is perhaps due to a similar reason (poor dispersion of CNF in the matrix) observed in [90].

Quaresimin and Varley [96] used a ball milling technique with solvent to disperse Pyrograf III CNF into DER331/DEN431/XD5200 epoxy resin. The solution was then applied onto the UD carbon fibres Tenax-G30-700 12K HTA-7C using a paint brush. The impregnated carbon fibres were partially cured at room temperature to form prepregs. The manual lay-up prepreg was then cured using a hot press. They claimed that the fibre volume fraction was 65%. It was found that the addition of 7.5 wt% CNF enhanced the interlaminar shear strength by 19% where all specimens failed via delamination. The CNF-modified resin formed a ply interleaf of about 40 μm-150 μm between carbon fibre plies [90,96]. As received CNT are in the form of agglomerated particles (maximum about 50 μm diameter), as observed by SEM micrographs in [97]. Therefore, this shows evidence of agglomerated or entangled CNFs in the composite laminate where these particles are larger than the space between fibres and they are mostly confined to the interply region. Although a thick resin-rich layer in between the plies may enhance the interlaminar shear strength, it degraded the longitudinal compressive strength [96]. A similar result was observed in a conventional CFRP system as discussed previously in Section 2.2 (improving toughness using thermoplastic ply interleaf) where premature failure via longitudinal splitting in compression occurred because of poor interfacial bonding between the fibres and the matrix. Similar results were obtained for the other systems studied in [98-102] using CNF.

The other type of CNF, that is commercially available (from GSI Creos corporation) and currently used for developing nanomodified-epoxies, is cup-stacked carbon nanotubes (CSCNT) [88-89,103-104]. Yokozeki and co-workers [88-89,103] used a ball milling technique to disperse CSCNT in DGEBA EP827/dicyandiamide epoxy resin system. The prepreg was then prepared with T700SC-12K carbon fibre and the nanomodified resin. It was cured using an autoclave. TEM micrograph showed a good dispersion of CSCNT in the matrix. The mechanical tests showed that the incorporation of 5 wt% CSCNT into CFRP composite enhanced the matrix-dominated properties. The transverse tensile modulus and strength were improved by 6% and 13%, respectively. The fracture energy was also increased from 86 J/m^2 to 170 J/m^2. They claimed that fibre-bridging mechanism was visually observed during crack growth of the nanomodified CFRP composite. The SEM images illustrated a rough crack surface of the nanomodified system. The tension, compression, bending and compression-after-

impact tests were also conducted on quasi-isotropic $[0/90/45/-45]_{3s}$ laminates. The results demonstrated that the inclusion of 10 wt% CSCNT into the composite moderately increased the compressive stiffness and strength, bending stiffness and strength and compression after impact strength by 5%, 10%, 5%, 2% and 7%, respectively, while no improvements in tensile modulus and strength were recorded.

A moderate reinforcing effect was observed so far for the CNF-filled FRP system. For the CNT-filled FRP system, improvements in mechanical and thermal properties have been reported by several researchers [105-113]. Some selected results are summarised in Table 2.3. Qiu *et al.* [105] demonstrated significant enhancement of mechanical and thermal properties by incorporating 1 wt% functionalised MWCNT into GFRP composite laminate. The MWCNT was dispersed in the epoxy resin using ultrasonic technique. The nanomodfied-resin was then infused through the A1010 uni-warp knitting glass fibre fabric in the thickness direction using a vacuum assisted infusion method to produce a prepreg. The prepreg was then laid up and cured using VARTM. Thermal and mechanical properties of the nanomodified system compared to the unmodified system are summarised in Table 2.3. The results showed that the addition of 1 wt% into the GFRP composite significantly increased the tensile properties and reduced the CTE. A good dispersion of MWCNT in both inter-tow and intra-tow areas contributed to improved mechanical properties.

A modified-VARTM method, called injection and double vacuum assisted resin transfer moulding (IDVARTM), was designed by Fan *et al.* [106] to produce 2 wt% functionalised MWCNT in GFRP composite. This method successfully infused the MWCNT between fibres. A good dispersion of CNT in the matrix was revealed by the TEM. It was found that the interlaminar shear strength, which was measured using compression shear test device, of the 2 wt% MWCNT-filled GFRP composite was 33% higher than that of the unmodified GFRP system. The MWCNT content was limited to 2 wt% because of high viscosity of the nanomodified-resin.

Table 2.3: Thermal and mechanical properties of CNT-filled FRP composites reported in selected references.

Type of filler	FRP composite system	Effect	Refs.
MWCNT functionalised with acid oxidation (from: Sigma Aldrich)	A1010GF/ EPON862/ EPI-W	1 wt%: LTM ↑ 27%, LTS ↑ 16%, TTM ↑ 35%, TTS ↑ 18%, SM ↑ 11%, SS ↑ 8%, CTE ↓ 25%, Tg ↓ 10%	[105]
MWCNT functionalised with acid oxidation (from: ILJIN nanotech company)	Woven GF/ SC15	2 wt%: ILSS ↑ 33%	[106]
DWCNT-NH_2 amino functionalised (from: Nanocyl)	GF non-crimp fabric/ DGEBA L135i/ Amine H137i	0.3 wt%: ILSS ↑ 20%	[108]
MWCNT (from: Helix material solutions, Inc)	Woven fabric AS4 CF/ DGEBA GY6010/ DDS	0.5 wt%: Tg ↑ 19%, ILSS ↑ 15%, CS ↑ 39%,	[110]
MWCNT (from: ARKEMA)	CF/ Araldite LY564/ Aradur HY2954	0.5 wt%: CAIM ↑ 15%, CAIS ↑ 12-15%	[113]

Note: GF = Glass fibre, CF = Carbon fibre, LTM = Longitudinal tensile modulus, LTS = Longitudinal tensile strength, TTM = Transverse tensile modulus, TTS = Transverse tensile strength, SM = Shear modulus, SS = Shear strength, CTE = Coefficient of thermal expansion, Tg = Glass transition temperature, ILSS = Interlaminar shear strength, CS = compressive strength, CAIM = Compression after impact modulus, CAIS = Compression after impact strength.

Gojny and co-workers [107-109] used a three-roll mill machine to disperse CNTs by shear forces. The amino functionalised double-walled carbon nanotubes (DWCNT-NH_2) were milled with the epoxy resin and impregnated into the glass-fibre non-crimp fabric using a resin transfer moulding (RTM) technique. The addition of 0.3 wt% DWCNT into the GFRP composite increased the interlaminar shear strength by 33% (measured using short beam three-point bending test). The SEM observation of the fracture surface of the nanomodified system showed entangled CNTs in the matrix. No

filtering effect of agglomerated particles by the glass-fibre bundles was mentioned in the paper.

Cho *et al.* [110-111] claimed that a better dispersion of MWCNT was achieved using a solvent-dispersing technique. A solution of epoxy resin, solvent (Disperbyk-2150 dispersant) and MWCNT was prepared using rotary mixing and ultrasonication techniques. The 5-harness satin woven fabric with AS4 carbon fibre (AGP370-5H) was impregnated with the nanomodified-epoxy. The prepreg was then cured in an autoclave. The glass transition temperature of the nanomodified-CFRP composite was 19% higher than that of the unmodified system as measured using DMTA. The interlaminar shear strength was also increased by 15% by adding 0.5 wt% MWCNT into a CFRP composite. In addition, the compressive strength was significantly enhanced by 39%; no improvement in compressive modulus was recorded. It is interesting to note that the interlaminar shear and compressive strengths were increased simultaneously. They suggested that interfibre bridging and local microcracks, due to the presence of CNT, delayed the global failure of the composite. Other types of solvent that can be used to disperse CNT in epoxy are N,N-dimethylformamide (DMF), tetrahydrofuran (THF) and alcohols [112].

The effect of MWCNT on the compression after impact properties was studied by Kostopoulos *et al.* [113]. A good dispersion of 0.5 wt% MWCNT in the epoxy resin was achieved using a Torus mill where the high-speed rotating disc with zirconium dioxide beads generates high shear forces and reduces particle agglomeration. The resin was then impregnated to the carbon fibres. The prepregs were cured in the autoclave to produce quasi isotropic $[0/+45/90/-45]_{2s}$ laminates with approximately a 58% fibre volume fraction. It was found that the inclusion of MWCNT into the CFRP composite system, as given in Table 2.3, enhanced the compression after impact (CAI) modulus by 15% and CAI strength by 12-15%. They suggested that a tougher resin, due to the presence of CNT, contributes to higher energy absorption during compression.

The other method to prepare CNT-filled CFRP composites is by growing or grafting CNT onto the reinforcing carbon fibres [114-115] as illustrated in Figure 2.2c. Single-fibre fragmentation test results presented by Thostenson *et al.* [116] showed that the carbon fibre with nanotubes grown on the surface has a higher fibre/matrix interfacial strength compared to the conventional carbon fibre system. The presence of local grown CNT on the fibre surface improved interfacial load transfer due to local

stiffening of the polymer matrix near the fibre/matrix interface. Therefore, the purpose of fabricating CNT-modified CFRP using this CNT grown CF is to improve the interlaminar shear or matrix-dominated properties. A significant enhancement of interlaminar shear modulus and strength was reported in [114-115]. In terms of commercialisation purposes, this kind of fabrication method needs to be further investigated.

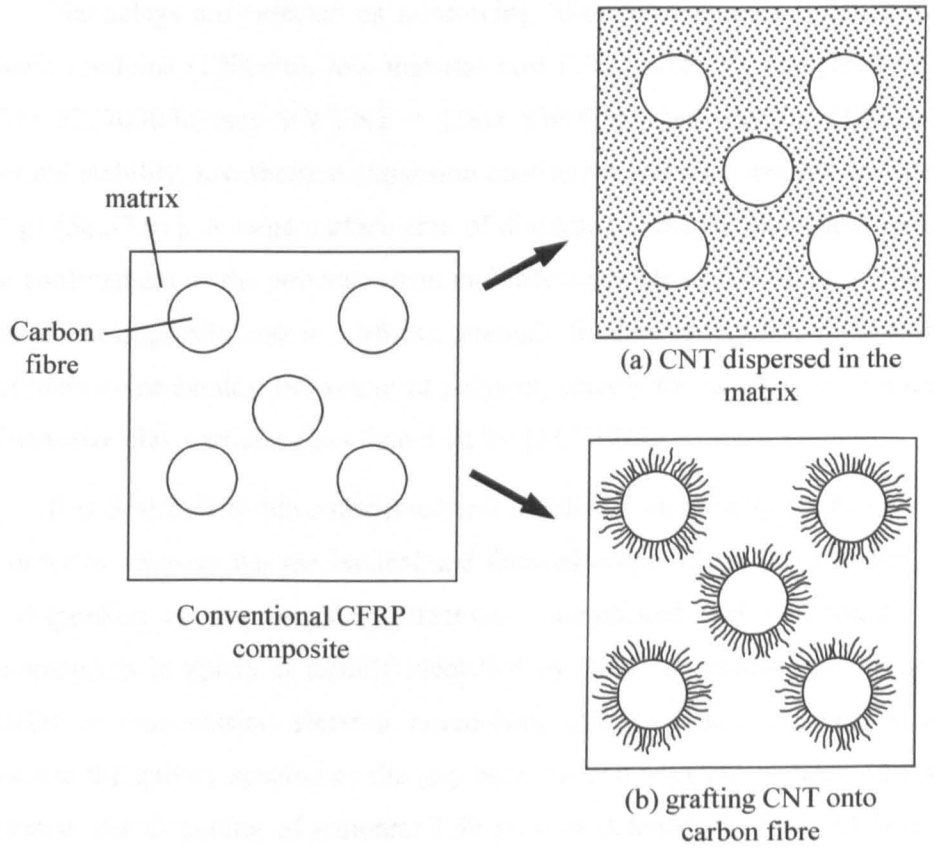

Figure 2.2: Schematic illustration of CNT-filled CFRP composites using two different routes: (a) dispersing CNT throughout the composite matrix and (b) attaching CNT directly onto the carbon fibre; based on [114]. (CNT dimensions are not to scale)

2.3.3 Nanoclay-filled FRP composites

Clay nanoplatelet is one of the most widely investigated nanofillers in a variety of different polymer matrices for a wide range of applications [57]. The origin of the natural clay (such as montmorillonite (MMT)) is commonly formed from the alteration

of volcanic ash or rocks [56]. The dominant constituent of the MMT clays, which are used in current work, is silica and alumina [57]. The chemical structure of the MMT clay consists of tetrahedral silicate and octahedral alumina layers where the two tetrahedral layers sandwich the octahedral layer to form one clay sheet (which has thickness of 1 nm) [57]. Layered silicates are hydrophilic materials while most polymers are hydrophobic materials. Therefore, organic treatment on the MMT clays is carried out to ensure compatibility with the polymers.

Nanoclays are selected as reinforcing filler for polymers because of their high elastic modulus (170GPa), low material cost (USD $3.50/lb; compared to SWCNT = USD $227000/lb and MWCNT = USD $3000/lb), low density (1.71 g/cm^3), high thermal stability, low thermal expansion coefficient and high specific surface areas (750 m^2/g) [56,57,61]. A large surface area of dispersed nanoclay plays an important role in the confinement of the polymer chain mobility under stress [59,61,117-118]. These give significant improvements in stiffness, strength, fracture toughness, dimensional stability and thermo-mechanical behaviour of polymer, usually for an addition of a small amount of nanosize clay particles (less than 5 wt.%) [117-121].

It is desirable to have dispersed and exfoliated organoclay in the nanocomposites in order to improve the mechanical and thermal properties of the polymer. The degree of dispersion or microstructure (tactoids, intercalated and exfoliated) of the clay nanoplatelets in epoxy is usually identified by wide- or small-angle X-ray diffraction (XRD) or transmission electron microscopy (TEM). These techniques are used to measure the gallery spacing or the gap between two adjacent platelets (d-spacing). For instance, the d-spacing of nanomer I.30 powder determined using XRD is about 2.3-2.37 nm [118-120].

Schematic illustrations of the microstructures (a) tactoids, (b) intercalated, (c) exfoliated with ordered structure and (d) fully exfoliated with random orientation polymer-clay nanocomposites are shown in Figure 2.3. An intercalated type nanocomposite has gallery spacing of 2.37-8 nm [119]. Polymer chains diffuse into the galleries between the clay platelets and increase the d-spacing as shown in Figure 2.3b. For an exfoliated structure nanocomposite (Figure 2.3c-d), more polymer molecules enter the galleries of the platelets and push the platelets further apart. The d-spacing for exfoliated structure is more than 8 nm [119]. Whereas for tactoids, the clay platelets are still aggregated together, and no polymer molecule moves into the galleries of the

adjacent platelets (Figure 2.3a). The degree of exfoliation depends on the type of clay and its surface treatment, type of epoxy and hardener (including viscosity of the resins), resin-clay interaction, clay content and processing method. To date, a processing technique that produces complete dispersion and exfoliation of silicate layers in the polymer matrix is still a technical challenge.

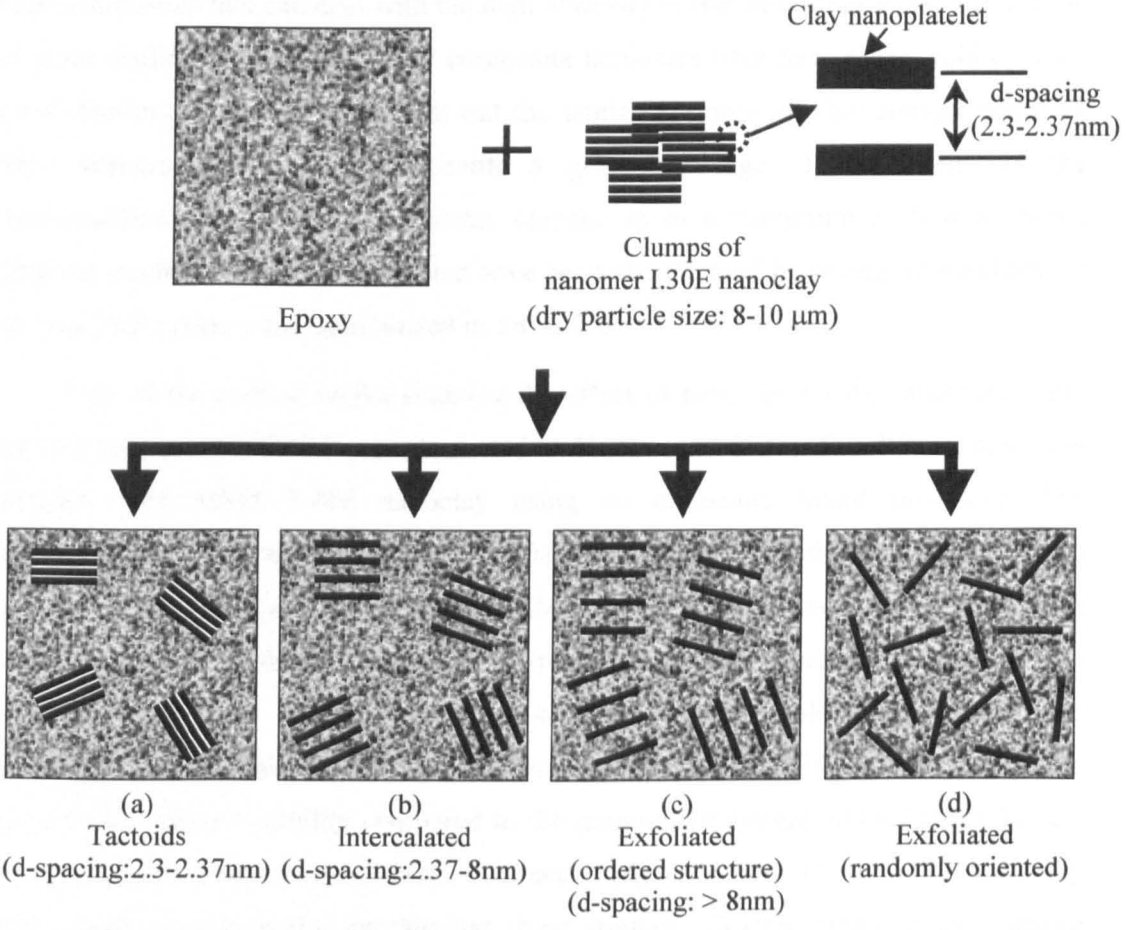

Figure 2.3: A schematic diagram of morphologies that can be observed in epoxy-clay nanocomposites (Based on [56]). In the current work, MMT clay nanomer I.30E was used. The nanoparticle size and d-spacing between platelets are also shown.

The most widely used manufacturing methods for polymer nanocomposites are direct mechanical stirring, in-situ polymerisation, high shear mixing, melt blending, high-pressure mixing, sonication and combination of these (for example studied in

[56,57,59,117-121]). Yasmin *et al.* [117] reported that high shear mixing using a three-roll mill machine was the best method to exfoliate the stacked layers of silicate clay in the epoxy matrix. This method applies external shear forces generated between the adjacent rollers to increase the d-spacing of the silicate platelets.

Although good dispersion and exfoliated state of nanoclay in the epoxy resin was achieved, the problem still exists with selecting an appropriate fabrication method for FRP composites that can deal with the high viscosity of nanomodified-resin. Fabrication of good quality nanomodified-FRP composite laminates (that have a low void content, good dispersion/exfoliation through out the laminate, optimum clay content and high fibre volume fraction) stills presents a great challenge. The viscosity of the nanomodified-resin limits the nanoclay content up to a maximum of 5 wt%. Some selected results and achievements that have been documented by several researchers for various FRP systems are summarised in Table 2.4.

One of the earliest works studying the effect of nanoclay on the mechanical and thermal properties of GFRP was conducted by Haque *et al.* [122]. The SC-15 epoxy was blended with MMT I.28E nanoclay using an ultrasonic liquid processor. The nanomodified-resin was infused into a plain weave glass fabric using the vacuum assisted resin infusion molding (VARIM) manufacturing technique. The TEM micrographs showed that the nanomodified-resin has an intercalated microstructure with occasional presence of tactoids; this suggests an incomplete dispersion. The thermogravimetry analysis (TGA) results showed that nanomodified-GFRP composite has a better thermal stability compared to the unmodified system where higher Tg and decomposition temperatures were obtained. The addition of 1 wt% nanoclay significantly improved the interlaminar shear strength, flexural strength and fracture toughness of the GFRP composite (see Table 2.4). This is due to the enhanced fibre/matrix interfacial bonding where the SEM micrographs revealed a rough surface of glass fibre due to a strong bonding to the nanomodified-matrix compared to a smooth glass fibre surface for the unmodified system. The addition of more than 1 wt% nanoclay, severely degraded the properties of the laminate due to the increased amount of agglomerated nanoparticles. Lin *et al.* [123] employed a similar technique to disperse the Cloisite 15A in the epoxy resin (YD-128/JeffamineD-230). The nanomodified-GFRP composite based on UD GF T800 was prepared using a vacuum assisted resin transfer moulding (VARTM) technique. Intercalated nanocomposite structures were also observed. No significant improvement in flexural properties was documented.

Moreover, the filtering effect of the cured laminate can be clearly observed by the density of the nanoclay at the resin inlet region that was higher than that of the resin outlet region. Non-uniform distribution of nanoclay in the laminate contributes to a large variation in mechanical properties.

In order to avoid the problem of nanoclay being filtered by the fibres, Arun and Sun [124] impregnated the resin to the fibre manually using a wet-lay up technique. The wetted fibre was then cured using the VARTM mould without the resin inlet tube. This technique produced a laminate with fibre volume fraction of 35-37%. In order to study the effect of nanoclay on the UD compressive strength of GFRP composite, the laminates were cut at off-axis angles 5°, 10° and 15°. The prismatic blocks were tested in compression. The UD compressive strength was calculated based on the off-axis compressive strength. The addition of 5 wt% nanoclay enhanced the UD compressive strength by 36%. Although the measurements did not follow the standard testing method for composite laminates (ASTM D3410 or D6641), the result gave a good indication of the enhanced compressive properties by adding nanoclay into the matrix. Arun and Sun [125] extended the study to determine the effect of nanoclay on the fracture toughness. The results showed that the addition of 5 wt% nanoclay reduced the critical strain energy release rate G_{IC} by 40%. This contradicts that observed in [122]. A similar fabrication technique as in [124-125] was employed by Tsai and Wu [119,126]. Table 2.4 shows that the fracture toughness of nanomodified-GFRP was 35% less than the unmodified system. This is consistent with the result obtained in [125]. In addition, increased in-plane shear strength contributed to an increase in compressive strength as observed in [124]. The SEM observation on the fracture surface showed evidence of agglomerated nanoclay in the laminate. Although the addition of nanoclay increases the matrix stiffness, poor bonding between the clay platelets (because of the agglomeration) has a detrimental effect on its fracture toughness due to cracks that can easily penetrate into the agglomerated nanoparticles and propagate between the clay platelets. This reduces the fracture energy.

Table 2.4: Thermal and mechanical properties of nanoclay-filled GFRP and CFRP composites reported in selected references.

Type of filler	FRP composite system	Effect	Refs.
MMT I.28E (from: Nanocor)	Plain weave S2-glass fabric/ SC-15 (DGEBA/DGEBF blend)/ Cyclo aliphatic amine	1 wt%: Tg ↑ 3%, ILSS ↑ 44%, BS ↑ 24%, BM ↑ 14%, K_{IC} ↑ 23%	[122]
MMT I.30E (from: Nanocor)	E-LR 0908-14 stitched UD E-glass fibre cloth/ Epoxy vinyl ester resin	5 wt%: LCS ↑ 36%, G_{IC} ↓ 40%	[124, 125]
MMT I.30E (from: Nanocor)	E-LR 0908-14 stitched UD E-glass fibre cloth/ DGEBA EPON828/ JeffamineD-230	5 wt%: LTM ↑ 6%, LTS ↓ 12%, TTM ↑ 54%, TTS ↑ 46%, SS ↑ 16%, LBS ↑ 2%, TBS ↑ 50%, G_{IC} ↓ 35%, TCS ↑ 24%	[119, 126]
Somasif ME-100 treated with octadecylamine (CO-OP Ltd.)	Satin GF mat EC9-204/ Araldite CY225/ Araldite HY925	10 wt%: BS ↑ 27%, BM ↑ 6%, BFS ↑ 24%, E^* ↑ 10%, Tg ↓ 12%	[127]
MMT Cloisite 30B (from: Southern clay)	Satin weave carbon fabric/ EPON 815C/ Epicure W	2 wt%: BS ↑ 24%, BM ↑ 32%, ILSS ↓ 11%	[134]
MMT I.28E (from: Nanocor)	Plain weave CF/ SC-15 (DGEBA/DGEBF blend)/ Cyclo aliphatic amine	2 wt% (VARIM): V_f = 56% , V_v = 6% BS ↑ 25%, BM ↑ 14%, E^* ↑ 49%, Tg ↑ 13%, ILSS ↑ 30%	[135]
		2 wt% (Hand-layup and vacuum bagging): V_f = 55% , V_v = 3% BS ↑ 25%, BM ↑ 22%, E^* ↑ 24%, Tg ↑ 1%	[138]
K-10 MMT (from: Sigma Aldrich)	Plain weave CF/ SC-15 (DGEBA/DGEBF blend)/ Cyclo aliphatic amine	2 wt%: BS ↑ 14%, BFS ↑ 8%, E^* ↑ 8%, Tg ↑ 5%	[139]
MMT I.30E (from: Nanocor)	Plain woven CF T1101/ DGEBA EPON828/ Phenylenediamine (mPDA) Methylenedianaline (MDA)	3 wt%: BS ↓ 11%, BM ↑ 5%	[140]

Note: Tg = Glass transition temperature, ILSS = Interlaminar shear strength, BS = Bending strength, BM = Bending modulus, BFS = Bending failure strain, K_{IC} = Critical stress intensity factor, G_{IC} = Critical energy release rate, LCS = Longitudinal compressive strength, TCS = Transverse compressive strength, LTM = Longitudinal tensile modulus, LTS = Longitudinal tensile strength, TTM = Transverse tensile modulus, TTS = Transverse tensile strength, SS = In-plane shear strength, LBS = Longitudinal bending strength, TBS = Transverse bending strength, E^* = Dynamic elastic modulus, V_f = Fibre volume fraction, V_v = Void volume fraction.

A GFRP composite laminate with higher nanoclay content was fabricated by Kornmann *et al.* [127]. At first, the nanoclay was treated with octadecylamine and dispersed in the epoxy resin using mechanical stirring technique. The prepregs were then fabricated and cured in a vacuum bag using a hot-press. The laminates have a 54-55% fibre volume fraction. The TEM showed a predominantly intercalated structure of nanoclay in the polymer with an average spacing between silicate layers of 9 nm. As shown in Table 2.4, the addition of 10 wt% nanoclay into the GFRP composite moderately improved the flexural strength and modulus without reducing its failure strain. SEM micrographs showed the evident of agglomerated nanoparticles. Thus this perhaps limits the degree of reinforcement offered by the nanoclay.

Based on a study conducted by Hamidi *et al.* [128] the viscosity of the resin increased exponentially with the nanoclay content. The viscosity of neat EPON815C/EPICURE3282 epoxy resin increases from 0.65 Pa.s to 1.12 Pa.s by adding 5 wt% Closite 25A nanoclay. For 10 wt% nanoclay, the density of the resin reaches 3.69 Pa.s. As a result, the void content in the laminate increases with nanoclay content due to difficulties in removing the entrapped air. For instance, Bozkurt *et al.* [129] found that the addition of 10 wt% MMT clay increased the void content in the laminate by 78%. This degraded the overall performance of the GFRP laminate.

As discussed earlier, the effect of nanoclay on the properties of GFRP composites primarily depends on the type of nanoclay and its surface treatment, resin system, mixing method, degree of exfoliation and intercalation, fabrication method of the laminate, volume content of fibre, nanoclay and voids in the laminate. For CFRP composite systems, these factors obviously contribute to inconsistent results achieved by several researchers. The presence of nanoclay significantly degraded the properties of CFRP composite have been reported in [56,96,130]. For instance, the addition of 2 wt% cloisite 10A MMT nanoclay into the AS4-6K/Cycom 977-3 CFRP composite reduced the fracture toughness G_{IC} by 61%, tensile strength by 8% and interlaminar shear strength by 19% with slight improvement in flexural strength (6%) [56]. Quaresimin and Varley [96] reported that the agglomerated Cloisite 30B MMT clay act as a defect that induced local stress concentration in the laminate. This provides points of weakness rather than reinforcement, which leads to premature failure. SEM micrographs showed that the agglomerated particles were filtered out by the fibres and formed a thin strip of a resin rich layer in between the carbon fibre tows. Although this layer often contributes to higher interlaminar shear strength for the case of CNT-filled

CFRP composites, in nanoclay-filled CFRP composites it contributes to a low interlaminar shear strength. This is due to a weak interfacial bonding between silicate platelets in the agglomerated nanoclay, which leads to no resistance to either crack initiation or crack propagation. This is consistent with the results obtained in [96] where the addition of 5 wt% nanoclay reduced the interlaminar fracture toughness (fracture energy G_{IC}) by 55% at crack initiation and 70% at crack propagation.

A better dispersion or exfoliation of nanoclay in the epoxy resin and throughout the laminate was achieved as reported in [131-143] particularly at low clay content (2-3 wt%). Exfoliated structures provide strong interfacial bonding between clay platelets and the epoxy resin, thus contributing to better mechanical properties of nanomodified-FRP composites compared to those of the unmodified system. Some of the results are presented in Table 2.4. Dean *et al.* [134] studied the silicate interlayer distance (d-spacing) using an XRD. At small clay content (2 wt% Cloisite 30B), a good dispersion and exfoliation (d-spacing more than 9 nm) was achieved. The density of the nanomodified resin was measured using a Rheometer. It was found that as the clay content increases the viscosity increases significantly. The viscosity of the pure resin (1 Pa.s) increases to 7 Pa.s with the addition of 4 wt% nanoclay. They suggested that, for a viscosity less than 10 Pa.s, VARIM still could be used for the fabrication of FRP laminates. Therefore, the nanomodified CFRP laminate with 2 wt% nanoclay was manufactured using VARIM. The results showed that the flexural modulus and strength were significantly increased however 11% reduction in interlaminar shear strength was recorded. Chowdhury *et al.* [135] employed a similar fabrication technique to produce 2 wt% MMT I.28E nanoclay-filled CFRP composites. It was found that although a high fibre volume fraction (56%) was achieved, the void content in the laminate was high (6%). Low quality laminates and weak interfacial bonding of Cloisite 30B with epoxy resin perhaps contribute to reduced interlaminar shear strength as observed by Dean *et al.* [134]. Chowdhury and co-workers [135,138] extended the study to fabricate a better quality of laminate using a hand lay-up and vacuum bagging technique. A laminate with a lower void content (3%) was produced. The results showed that the addition of 2 wt% I.28 MMT improved the flexural, thermal and impact properties [135-138], see Table 2.4. The nanomodified-CFRP prepared using VARTM [139] was also showed a similar degree of reinforcement as those obtained using a hand lay-up technique.

A hand-layup technique was also used by Siddiqui *et al.* [140], Khan *et al.* [141-142] and Iqbal *et al.* [143]. The prepreg was cured using a vacuum hot press. It was

found that, the incorporation of 3 wt% I.30 MMT nanoclay into the CFRP laminate enhanced the flexural, interlaminar fracture toughness G_{IC}, impact properties, fatigue life and tensile properties.

Based on a review of literature on the properties of nanoclay-modified FRP composites conducted in the past 10 years, it can be concluded that effectiveness of using nanoclay-modified epoxy in current fabrication methods needs to be further investigated. Low quality of laminates due to inadequate dispersion (agglomerated nanoclay) and high void content indicate that the processing and fabrication methods still need to be improved and, at the moment, the usage of nanoclay-filled epoxy still remains uncertain for commercial applications.

2.4 Concluding remarks

FRP composites are versatile materials that are being used widely in advanced applications due to their high stiffness/weight and high strength/weight properties. However, their brittleness (primarily caused by the low stiffness and fracture toughness of epoxy) contributes to low matrix-dominated properties such as fracture toughness, interlaminar shear strength, impact strength, compressive strength and in-plane shear strength. Much effort has been devoted to improve the matrix-dominated properties of the FRP composites. However, attempts to increase the interlaminar shear strength and fracture toughness frequently accompany a reduction in compressive strength due to low stiffness of the matrix. Recently, the concept of forming hybrids using nanofillers has received significant attention. This is because nanomodified-epoxy has high stiffness and high fracture toughness properties that can improve the matrix-dominated properties of the FRP composites. It has been shown that the use of nanomodified-epoxy resin systems for the fabrication of FRP composites has been a challenge. Several difficulties that need to be overcome are:

(i) the selection of nanofiller which is compatible to the resin system (includes type of nanofilers and their surface treatment) that can create a strong interfacial bonding between nanofiller and the matrix,

(ii) the selection of a suitable mixing method that can homogeneously disperse the nanofiller in the epoxy resin, especially with a high nanofiller content,

(iii) the selection of a suitable fabrication method of FRP laminates that can deal with high viscosity nanomodified-resins and produce a laminate with low void content (less than 1%), high fibre volume fraction (55-65%), high nanofiller content (to fully utilise its properties) and good fibre alignment in the matrix (low fibre waviness).

This thesis will focus first on the development of homogeneously dispersed nanomodified-resins. The thermal and mechanical properties of the nanomodified-resins will be evaluated to study the reinforcement effect provided by the nanofillers to the epoxy polymers. The optimum formulation will be selected to prepare the nanofilled-CFRP laminates. Based on the literature review that has been conducted, the investigation on compressive properties is very limited. In practice, reliable and repeatable compressive strength data of composite laminates are very difficult to achieve due to several factors, such as Euler buckling, specimen misalignment, improper tabbing and 3-D stress fields introduced on the specimens by the test machine or fixtures. Therefore, the aim of this thesis is to study the compressive response of nanomodified-CFRP composite laminate. The benefit offered by the nanofillers will be used to improve compressive and in-plane shear properties of FRP composites. In addition, several analytical models will be presented where fracture mechanisms are carefully studied and parameters that influence compressive strength are identified.

Chapter 3

Experimental details

3.1 Summary

This chapter reports on materials and fabrication methods of (i) nanoparticle-filled epoxy nanocomposites and (ii) nanoparticle-filled CFRP composites. The experimental procedures for the evaluation of physical, thermal and mechanical properties of the pure and nanomodified epoxies and CFRP composites are explained. The characterization of epoxy polymers involved several techniques including transmission electron microscopy (TEM), density measurement, thermogravimetry analysis (TGA), thermomechanical analysis (TMA), differential scanning calorimetry (DSC), compression, tensile, flexural and fracture toughness tests. The performance of CFRP polymer composites was evaluated using unidirectional compression and in-plane shear tests. In addition, the quality of the laminates was evaluated using an image analyser. The experimental procedures for the measurement of constituents content and fibre misalignment in the composite laminate are also described. In order to correlate the mechanical properties with the mode of failure, the fractured specimens were examined using optical and scanning electron microscopy. The details of the materials used, fabrication processes, testing and subsequent damage evaluation techniques are described in the following sections.

3.2 Materials

Two types of resin systems were used: (i) Epikote 828 epoxy, a diglycidyl ether of bisphenol-A (DGEBA), cured with an alicyclic anhydride hardener and (ii) Cycom 977-20 epoxy with aromatic amine curing system. Even though DGEBA is widely used in various applications, most aerospace and other high performance applications require

epoxies of higher functionality such as Cycom 977-20. Cycom 977-20 has higher mechanical and thermal properties compared to the conventional DGEBA resin system. In this study, these thermosetting resins were modified with nanofillers to produce polymer nanocomposites. Three types of nanofillers were used: (i) clay nanoplatelets (nanoclay), (ii) silica nanospheres (nanosilica) and (iii) carbon nanotubes (CNT) as shown in Figure 1. The general properties of the materials used in this study, which were available in manufacturer's datasheet, are summarised in Table 3.1.

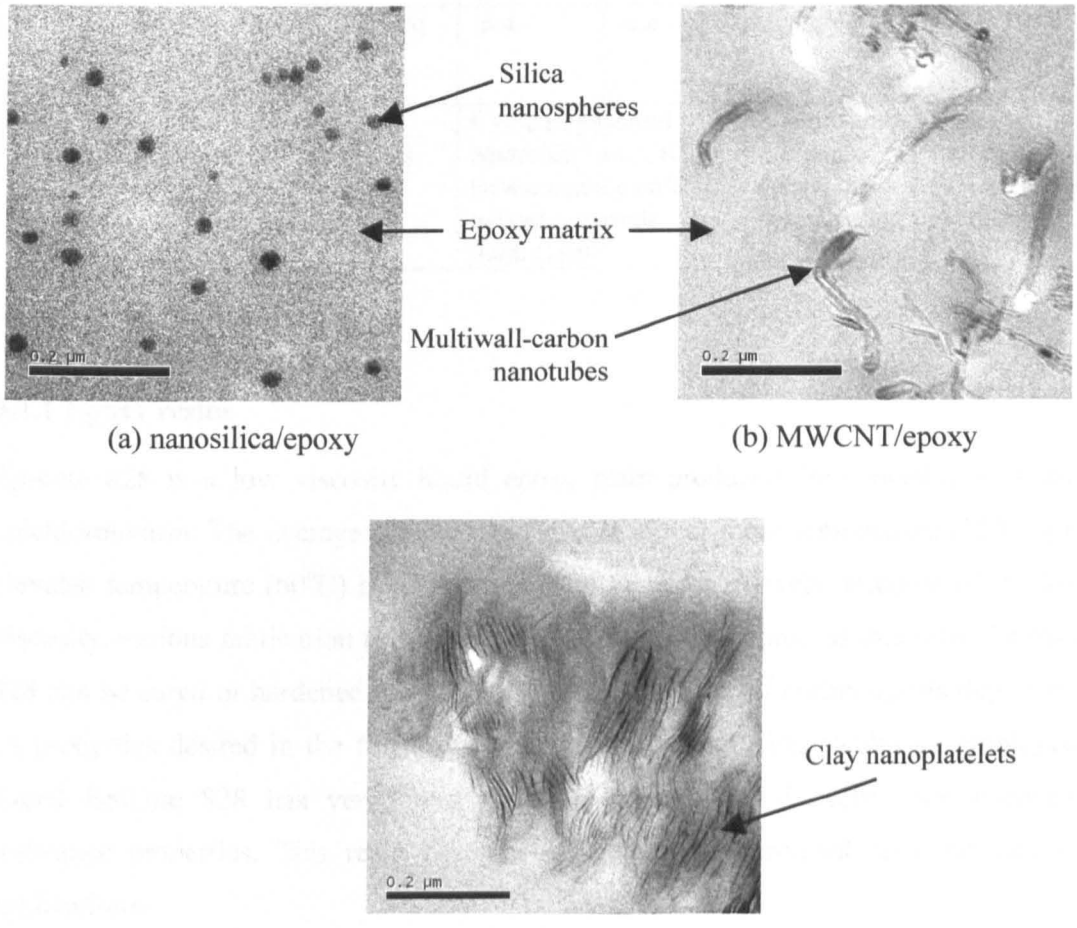

(a) nanosilica/epoxy

(b) MWCNT/epoxy

(c) nanoclay/epoxy

Figure 3.1: TEM images showing nanoparticle-modified epoxy nanocomposites prepared using (a) nanosilica, (b) multiwall-carbon nanotubes (CNT) and (c) nanoclay.

Table 3.1: Summary of general properties of the resins and nanomaterials obtained from manufacturer's datasheet.

Material properties	Epikote 828	NMA	Cycom		F400 (nanosilica)	NCR128-02 (CNT)
			977-20	977-2		
Appearance and colour	Clear liquid	Light yellow liquid	Yellow liquid	Solid, brown	Opaque liquid	Black paste liquid
Density	1.16 g/ml	1.232 g/ml	-n.a-	-n.a-	1.4 g/ml	1.15 – 1.2 g/ml
Viscosity (at 25°C)	13 Pa.s	0.18-0.2 Pa.s	-n.a-	1000-5000 Pa.s	60 Pa.s	300-500 Pa.s
Viscosity (at 65°C)	≈ 0.18 Pa.s	-n.a-	0.4 - 1 Pa.s	500 – 1000 Pa.s	-n.a-	-n.a-
Epoxy equivalent weight	184 – 192 g/eq	178 g/eq	-n.a.-	-n.a.-	295 g/eq	190 – 198 g/eq
Manufacturer/Supplier	Robnor Resins, UK (www.robnor.co.uk)		Cytec Engineered Materials Ltd.,UK (www.cytec.com/engineered-materials/index.htm)		Nanoresins, Germany (www.nanoresins.ag/index.php)	Nanocyl, Belgium (www.nanocyl.com)

3.2.1 Epoxy resins

Epikote 828 is a low viscosity liquid epoxy resin produced from bisphenol A and epichlorohydrin. The average viscosity of Epikote 828 at room temperature (25°C) and elevated temperature (60°C) is 13 Pa.s and 0.24 Pa.s, respectively. Because of the low viscosity, various fabrication techniques can be employed to process this resin. Epikote 828 can be cured or hardened or cross-linked with a variety of curing agents depending on properties desired in the finished product and the processing conditions employed. Cured Epikote 828 has very good mechanical, adhesive, dielectric and chemical resistance properties. This resin becomes a standard conventional resin for various applications.

Cycom 977-20 is designed and supplied by Cytec Engineered Materials Ltd. This new type of resin is formulated from a commercial Cycom 977-2 thermoplastic-toughened prepreg resin. It has already been mixed with aromatic amine hardener. Cycom 977-2 has been used widely in many aerospace applications including primary and secondary aircraft structures, space and ballistic structures, or any application requiring excellent impact resistance. It is in a solid form at room temperature because of the presence of thermoplastic filler. Incorporation of polyaromatic thermoplastic

polymer into thermosetting resin offers significantly increased fracture toughness, without reduction in elastic modulus, compared to unmodified epoxy [29,144-145,146-147]. However, the viscosity of the resin increases exponentially with increasing thermoplastic content, hence causes processing difficulties. Cycom 977-2 is not suitable for wet layup or resin transfer moulding (RTM) processing techniques. Therefore in this project the nanomodified resin was developed using Cycom 977-20.

3.2.2 Nanosilica

The spherical silica nanoparticles (Nanopox F400) were supplied as a colloidal sol (40 wt%) in epoxy by nanoresins AG, Geesthacht, Germany. Nanopox F400 is nanosilica reinforced bisphenol A based epoxy resin for the use in fibre composites. The nanosilica particles had a mean particle size of about 20 nm. The silica phase consists of surface-modified synthetic SiO_2 nanospheres of very small size (average diameter of 20 nm and the maximum diameter of 50 nm) as shown in Figure 3.1a. Ma et al [77] reported that the curing agents gave a significant influence on the mechanical properties of the nanosilica filled epoxy polymers. In this study anhydride curing agent was used as the hardener. The general properties of Nanopox F400 resin, provided by the manufacturer, are summarised in Table 3.1.

Thermogravimentry analysis (TGA) was conducted to confirm the weight fraction of the spherical silica nanoparticles in the Nanopox F400 resin using a Perkin Elmer TGA equipment. A sample mass of 10 to 15 mg of Nanopox F400 resin was heated from room temperature to 900°C at 10°C/min heating rate in Nitrogen gas at 50 ml/min. Data was collected using TGA PYRIS software. The TGA curve plot, as shown in Figure 3.2, shows the percentage of weight loss and rate of weight loss as a function of sample temperature. TGA results identified the rapid decomposition temperatures of the DGEBA matrix constituent occurred at temperature range of 200 to 500°C. The TGA profile illustrates three decomposition mechanisms. Stage (A), as the material is heated from room temperature up to 200°C, shows that the initial weight loss of about 1.5 wt% occurred due to solvent or water vaporization. When the sample temperature is increased up to 550°C, Stage (B) illustrates the decomposition of epoxy resin of about 57.5 wt%. The temperature of 550°C is selected as the optimum temperature to burn off the low molecular weight epoxy resin as suggested in ASTM standard E1131 [148]. In

stage (C), the remaining residue of about 41 wt% at temperature of 550°C confirmed the average weight fraction of the silica nanoparticles in the epoxy resin is about 40 wt%.

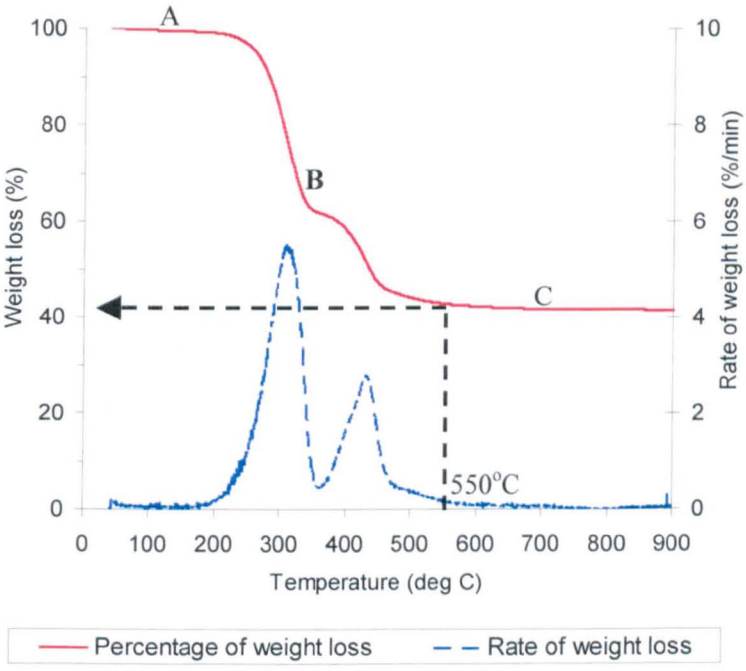

Figure 3.2: Percentage of weight loss and rate of weight loss as a function of sample temperature.

3.2.3 Carbon nanotubes (CNT)

The Epocyl NCR128, which is supplied by nanocyl S.A Belgium, is a masterbatch based on liquid Bisphenol-A epoxy resin containing a high concentration of multiwall carbon nanotubes (CNT). The Epocyl NCR128 has an average of 3 wt% of multiwall CNTs in the DGEBA epoxy. The material is specifically developed to enhance the mechanical properties of fibre reinforced polymer composite materials. The multiwall CNTs are produced via the catalytic carbon vapor deposition (CCVD) process. The multiwall CNTs are treated and pre-dispersed in the epoxy matrix. The masterbatch of Epocyl NCR128 was diluted into the epoxy matrix and hardener to produce 0.5 and 1 wt% CNT/epoxy nanocomposite. The multiwall CNT, as shown in Figure 3.1b, has an average diameter of 9.5 nm, average length of 1.5 μm and large surface area of 250-300 m^2/g. The general properties of Epocyl NCR128 resin, available in manufacturer datasheet, are summarised in Table 3.1.

3.2.4 Nanoclay

Clay nanoplatelets are the most widely investigated nanoparticles in a variety of different polymer matrices for a wide range of applications [57] where the origin of the natural clay is most commonly formed from the alteration of volcanic ash or rocks. The dominant constituent of the montmorillonite (MMT) clays, which is used in this study, is silica and alumina. The chemical structure of the MMT clay consists of tetrahedral silicate and octahedral alumina layers [57]. The two tetrahedral layers sandwich the octahedral layer to form one clay sheet which has thickness of 1 nm as shown in Figure 3.1c. Layered silicates are hydrophilic materials while most polymers are hydrophobic materials. Therefore, organic treatment on the MMT clays is carried out to ensure compatibility with the polymers used. In this study, MMT clays type nanomer I.30 and nanomer I.28 (supplied by Nanocor Inc. USA) were used as fillers in the Cycom 977-20 and Epikote 828 epoxy resins, respectively. The surface of the MMT clay is modified with 25–30 wt% of Octadecylamine to produce the Nanomer I.30 while the MMT clay surface is modified with 25–30 wt% of trimethyl stearyl ammonium to produce nanomer I.28. The onium ion surface modified MMT mineral Nanomer I.30 and Nanomer I.28 nanoclays are designed to be dispersed into amine-cured epoxy resins and anhydride-cured epoxy resins, respectively, to form nanocomposites. Nanomers I.30 and I.28 are supplied as a white powder that has a mean dry particle size of 8 – 10 μm and density of 1.71 and 1.9 g/cm^3, respectively.

3.2.5 HTS40 Carbon fibres

The carbon fibres type Tenax E HTS40 F13 I 12K 800 tex (supplied by Toho Tenax Europe GmbH Germany), as shown in Figure 3.3, were used to fabricate CFRP composite laminates. HTS40 is a high tensile strength and standard modulus carbon fibres, which is used as reinforcement in high performance composite structures. These fibres are produced from poly-acrylonitrile (PAN) precursor and are surface treated to promote adhesion to organic matrix polymers. Sizing materials for this type of carbon fibre is based on polyurethane. The characteristics of HTS40 carbon fibre, which are given in the manufacturer's datasheet, are summarised in Table 3.2.

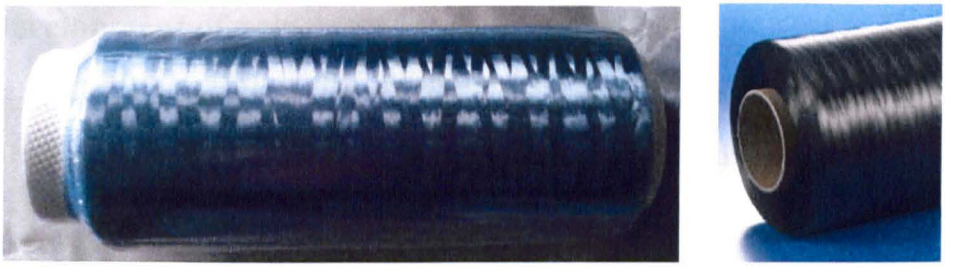

Figure 3.3: HTS40 F13 carbon fibre.

3.2.6 Commercial prepreg HTS40/977-2

The HTS40/977-2 laminates were fabricated from carbon fibre/epoxy pre-impregnated tapes of 0.27 mm thick and 300 mm tow width. The prepreg was made of unidirectional continuous high tensile strength carbon fibres (Toho Tenax HTS40 12K 800tex) pre-impregnated with Cycom®977-2 thermoplastic toughened epoxy resin. The properties of these materials are presented in Table 3.2. The HTS40/977-2 prepreg tapes are commercially available and supplied by Cytec Engineered Materials Ltd, UK.

Table 3.2: Characteristics of carbon fibre and cured Cycom 977-2 epoxy resin.

Property	Tenax E HTS40 F13 12K 800 tex	Cycom®977-2 toughened epoxy resin
Tensile modulus (GPa)	240	3.52
Tensile strength (MPa)	4300	81.40
Failure strain (%)	1.80	- n.a. -
Density (g/cc)	1.77	1.31
Filament diameter (μm)	7	-
Specific heat capacity (J/kgK)	710	-
Thermal conductivity (W/mK)	17	-
Coefficient of thermal expansion (10^{-6}/K)	-0.1	-
Flexural Modulus (GPa)	-	3.45
Flexural Strength (MPa)	-	197
G_{1c} (J/m^2)	-	478
K_{1c} (MPa$\sqrt{m}$)	-	1.34
T_g (°C)	-	212
Supplier	Toho Tenax Europe GmbH (www.tohotenax-eu.com/en/home.html)	Cytec Engineered Materials Ltd.,UK (www.cytec.com/engineered-materials/index.htm)

3.3 Development of polymer nanocomposites

Four nanomodified epoxy systems were developed based on Epikote 828 and Cycom 977-20 epoxies, i.e., nanosilica/828, CNT/828, nanoclay/828 and nanoclay/977-20.

3.3.1 Pure Epikote 828 polymer

The polymer matrix used was an epoxy resin consisting of Epikote 828, a diglycidyl ether of bisphenol A (DGEBA), cured with 90 parts per hundred of resin (phr) Aradur HY906, a hardener consisting of 1-methyl-5-norbornene-2,3-dicarboxylic anhydride (NMA), and 1 phr DY062, an accelerator consisting of benzyldimethylamine (BDMA). Before mixing, the Epikote 828 and NMA hardener were heated to 80°C to reduce the viscosity of the resins. 100 parts of Epikote 828 was mixed with 90 parts of anhydride curing agent NMA and 1 part of BDMA accelerator. The mixtures were stirred for 30 min in a heated oil bath of 80°C.

At the same time, the silicon moulds were preheated in the vacuum oven to 80°C. The silicon rubber moulds of various shapes (dogbone, cylindrical, cubic, trapezium, rectangular block and plate) were prepared to produce near net shape samples for various types of testing. In order to prepare the silicon rubber moulds, a high performance silicon rubber RTV 3450A was mixed with the curing agent RTV 3450B (supplied by Bentley chemicals) with the proportion of 100:11 in a glass beaker. The mixtures were stirred completely and poured into a ceramic mould. It was degassed in a vacuum oven at room temperature for 10 min. It was then cured at room temperature for 48 hr.

After mixing, the Epikote 828/NMA/BDMA formulations were degassed in the vacuum oven at 80°C for 20 min. After degassing, the resin was poured into the preheated release agent-coated rubber moulds. The resin was returned to the vacuum oven for further degassing at 80°C for 20 min. Before curing in the conventional oven, PTFE bleed out fabric and glass plate (wrapped with PTFE release film) were placed on the mould to produce flat and near-net shape specimens. The curing schedule consists of pre-cure at 80°C for 2 h, cure 120°C for 3 h, post-cure at 150°C for 4 h, with ramp rates of 1°C/min as illustrated in Figure 3.4. After curing, the specimens were carefully machined on a lathe, ground and polished to achieve the required dimensions with accuracy of 0.01 mm for several types of testing as discussed in Section 3.6.

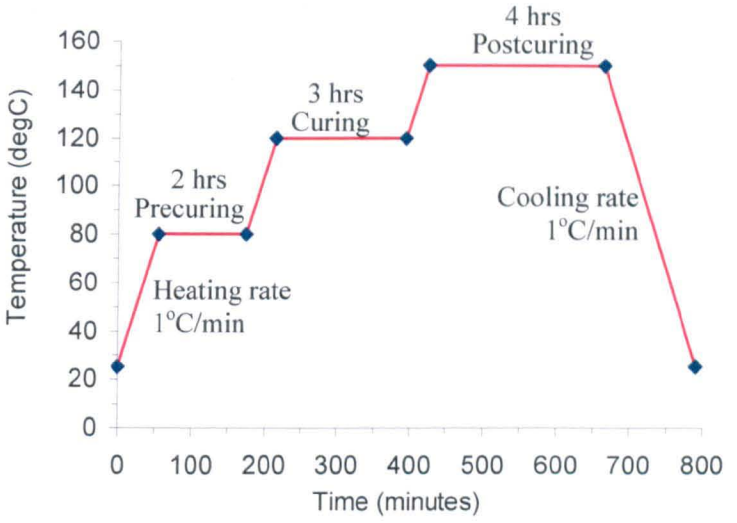

Figure 3.4: Curing cycle for Epikote 828 resin system.

3.3.2 Pure Cycom®977-20 polymer

The resin was preheated to 80°C to reduce the viscosity. The resin was degassed in a glass beaker for 1 hr at 85°C. The resin was then poured into the preheated release agent-coated rubber moulds with various cavity dimensions. The resin was returned to the vacuum oven for further degassing at 85°C for 1 hr. Before curing in the conventional oven, PTFE bleed out fabric and glass plate (wrapped with PTFE release film) were placed on the mould to produce flat and near-net shape specimens. After that, the resin was subjected to a curing schedule of 3 h at 177°C, ramping at 1°C/min. It was then brought down to room temperature at a rate of 2°C/min as illustrated in Figure 3.5. After curing, the specimens were carefully machined to have the required dimensions with accuracy of 0.01 mm for mechanical testing, see Section 3.6.

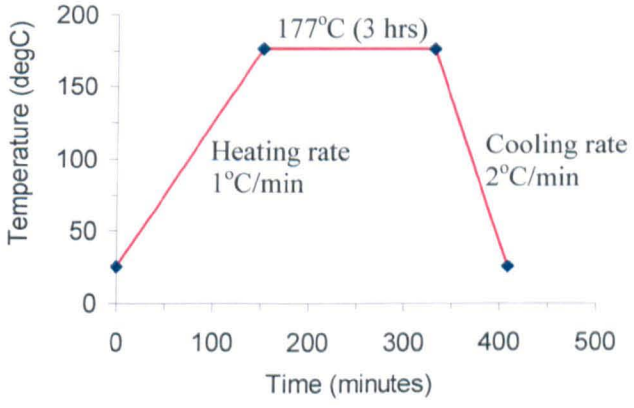

Figure 3.5: Curing cycle for Cycom 977-20 resin system.

3.3.3 Nanoparticle-filled Epikote 828

In order to prepare a series of nanocomposites with 5-25 wt% nanosilica content, the Epikote 828 resin was mechanically mixed with a specific amount of Nanopox F400 nanosilica/DGEBA masterbatch in a heated oil bath of 80°C for 1 h at 400 rpm. The mixture was completely degassed in a vacuum oven at 80°C to remove the entrapped air.

CNT/828 nanocomposite was prepared using the Epikote 828 resin and the master batch of epoxy/CNTs (Epocyl NCR128). The Epikote 828 was mechanically mixed with a specific amount of the Epocyl NCR128 at 400 rpm in a heated oil bath of 80°C for 2 h to produce a nanocomposite with 0.5 and 1 wt% CNT. The mixture was completely degassed in a vacuum oven at 80°C to remove the entrapped air.

A series of nanocomposites with 1, 3 and 5 wt% nanoclay was prepared using a mechanical stirrer. The nanomer I.28 nanoclay was dried at 60°C for 24 h under vacuum before sample preparation. The Epikote 828 was preheated to 80°C in a vacuum oven to reduce the viscosity of the resin. A specific amount of nanoclay was added into the Epikote 828 and mechanically stirrer at 400 rpm in a heated oil bath of 80°C for 2 h. The mixture was completely degassed in a vacuum oven at 80°C to remove the entrapped air.

After degassing, the mixture was blended with the appropriate stoichiometric amounts of NMA hardener and BDMA accelerator (based on the proportion of DGEBA:NMA:BDMA=100:90:1) in a heated oil bath of 80°C for 20 min. The resin was then poured into the preheated release-coated silicon moulds and degassed for another 1 hr. After the degassing process was completed, the PTFE bleed out fabric and glass plate (wrapped with PTFE release film) were placed on the mould to produce flat and near-net shape specimens. The resins were cured using a similar schedule explained in Section 3.3.1.

3.3.4 Nanoclay-filled Cycom 977-20

The nanomer I.30 nanoclay was dried at 60°C for 24 h under vacuum before sample preparation. The nanocomposite samples, with different clay contents, were prepared using two different methods; (i) mechanical stirring and (ii) 3-roll mill.

3.3.4.1 Mechanical stirring

A specific amount of nanoclay was mixed with the epoxy resin using a mechanical stirrer at 400 rpm in a heated oil bath of 80°C for 1 hr. This was followed by degassing in a vacuum oven for 1 hr at 85°C to remove any entrapped air in the mixture. The mixture was then poured into a preheated silicon mould (pre-treated with mould-release agent) with various shape cavities. It was returned into the vacuum oven for another 1 hr. After degassing, it was covered with a PTFE bleed out fabric and a glass plate (wrapped with PTFE release film) to produce a flat and near net shape specimens. Finally, the resin system was cured at 177°C for 3 h with a heating rate of 1°C/min followed by cooling down to room temperature at 2°C/min.

3.3.4.2 Three roll mill

The desired weight fraction of clay particles was pre-dispersed into the resin using a mechanical stirrer in a heated oil bath at 80°C for 15 min. The epoxy resin became viscous and opaque due to the presence of the clay particles. The mixture was then milled using an Exakt three roll mill machine, as shown in Figure 3.6a, to produce nanocomposites. In Figure 3.6b a schematic of the machine is presented that illustrates the three rollers and the flow direction of the material during processing. The dispersion was achieved by the shear forces generated between the adjacent rollers. At the beginning of the milling process, the machine was programmed into a gap mode where the feed and apron rollers were set close to the centre roller with approximate feeder-centre roller and apron-centre roller spacing of 15μ and 5μ, respectively. The milling process was carried out at 60°C temperature by pouring the clay-epoxy mixtures in between the feed and the centre rollers. The mixture, which was stuck to the bottom of the centre roller, was then transported into the second gap, see Figure 3.6b. Since the three roll mill mixing was not a continuous process, the material from the apron was collected and fed back into the feed and centre rollers after each complete pass of the material. It is assumed that, using the gap mode setting, the external shear forces generated between the adjacent rollers dispersed the particles into smaller tactoids. The machine was then set into a force mode programme where the feeder gap was about 5μ and the apron gap was approximately 0-1μ. In this step, the combined shear and diffusion processes facilitated the separation and penetration of the polymer between the clay platelets to form an intercalated and/or exfoliated structure. After this process, a clear or transparent solution was produced indicating that the dispersion was completed.

The processing time was limited to 1 hr due to the presence of the hardener. The mixture was then poured into a preheated silicon mould and degassed in a vacuum oven before a similar curing process (as discussed earlier) took place.

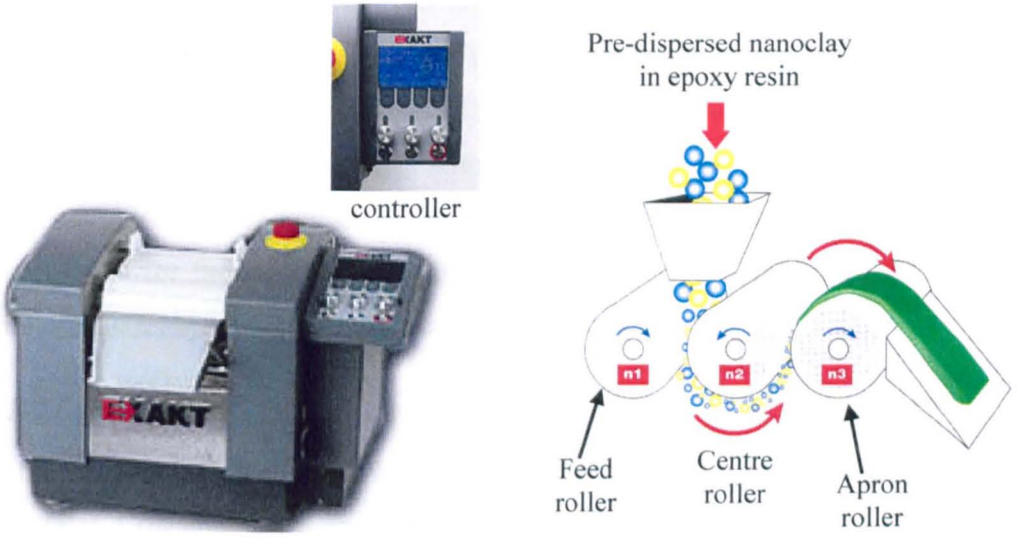

(a) (b)

Figure 3.6: (a) The EXAKT 120E Three roll mill machine with dimensions 820 mm width x 650 mm depth x 740 mm height and (b) Schematic of the three-roll mill machine showing the material flow direction with roller speed ratio n1:n2:n3 of 9:3:1. (Source: EXAKT technical brochure, www.exakt.de)

3.4 Fabrication of CFRP composite laminates

3.4.1 HTS40/828 CFRP composite

3.4.1.1 Winding of fibres

A $[0_2/90]_s$ CFRP laminate was prepared using a HTS40/977-2 prepreg. The cured panel was cut into 250 x 10 mm^2 strips. These strips were glued to prepare square frames. The HTS40 carbon fibres were wound onto the 250 mm x 250 mm CFRP frame using a dry filament winding technique as shown in Figure 3.7. The frame rotates at 12 rpm while the carriage moves horizontally across the frame at 34.43 mm/min laying down fibre

onto the frame. The fibres were wound into two different configurations: (i) $[0]_{4s}$ and (ii) $[0/90]_{2s}$ for the fabrication of compression and in-plane shear test specimens. The unidirectional (UD) and cross-ply carbon fibre panels were then dried in a vacuum oven at 100°C for 15 min before resin impregnation process took place.

3.4.1.2 Resin impregnation

In order to prepare UD and cross-ply HTS40/828 laminates, the pure resin, which was developed in Section 3.3.1, was used. The mixture of Epikote 828/NMA/BDMA was poured into a ceramic tray (wrapped with PTFE release film) and degassed for 20 min. After that, the frame of wound fibres was immersed in the resin and returned to the vacuum oven for further degassing. Overall the mixed resin spent 1 hr 30 min under vacuum at 80°C, by which time the viscosity started to increase.

3.4.1.3 Curing process

The frame of wound fibres was removed from the resin bath and placed in between flat glass plates. Consumables were added to form a vacuum bag as in Figure 3.8. All films, fabrics and other consumables were supplied by Tygavac, UK. The resin-impregnated fibres were cured in an oven. The cure schedule comprised a 2 hr, 80°C gel period, a 3 hr, 120°C cure period and a 4 hr, 150°C post cure period, followed by a ramp section down to room temperature. Each dwell period was separated by a 1°C/min ramp rise, the final ramp to room temperature was also 1°C/min, see Figure 3.4. After curing the frames were cut away to leave the composite panels.

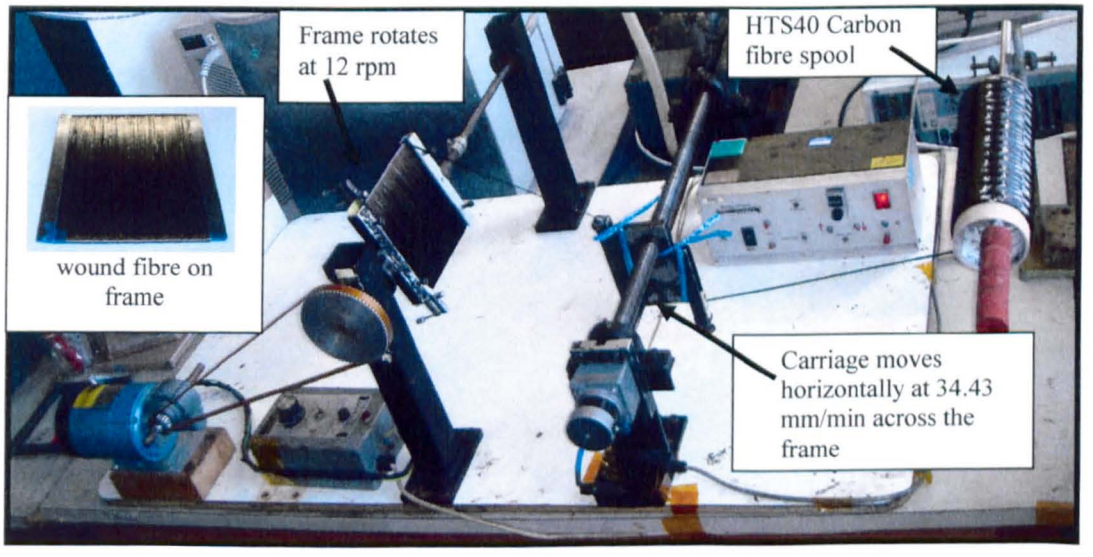

Figure 3.7: Filament winding experimental set-up.

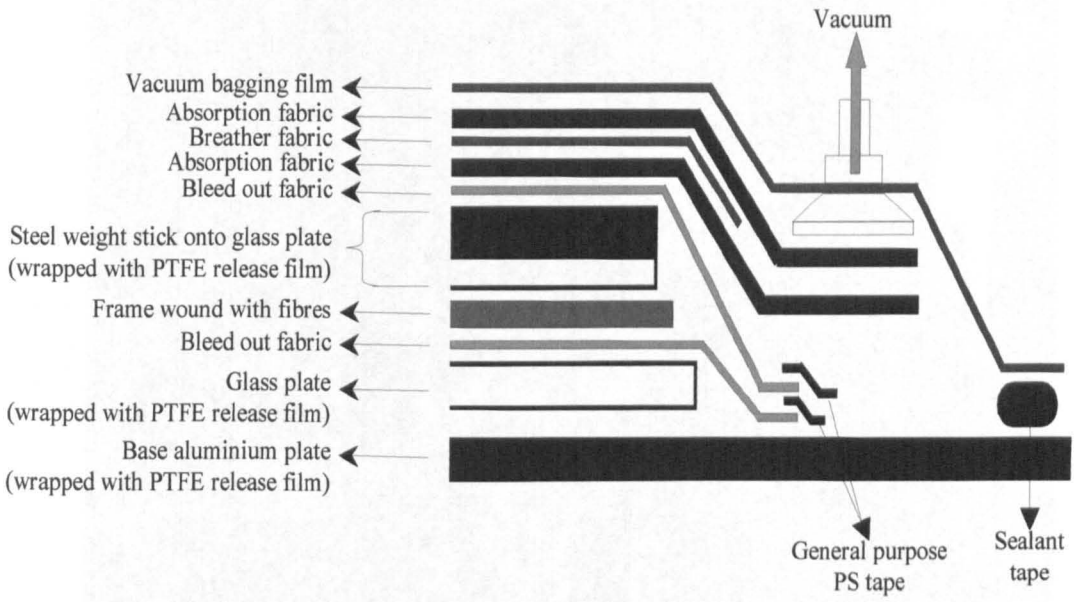

Figure 3.8: A schematic diagram of the vacuum bagging arrangement.

3.4.2 Nanosilica-filled HTS40/828 CFRP composite

A series of nanomodified CFRP composite was fabricated using 5 – 25 wt% nanosilica-modified Epikote 828 epoxy resin. The laminates were prepared using similar steps discussed in Section 3.4.1. The frame of wound fibres was immersed in the nanomodified resin which was prepared in Section 3.3.3. The processing time and curing cycle used were similar to those used in Section 3.4.1.

3.4.3 Commercial CFRP composite HTS40/977-2

The HTS40/977-2 prepreg was cut into 300mm length and laid up by hand into $[0]_{4s}$ and $[0/90]_{2s}$ designs. The laminates were cured in an autoclave, as shown in Figure 3.9, using the curing cycle illustrated in Figure 3.5.

Figure 3.9: An autoclave used to cure HTS40/977-2 laminates.

3.5 Physical and thermal tests

3.5.1 Transmission electron microscopy (TEM)

The degree of dispersion of the nanosilica, nanoclay and CNT in the epoxy matrices was investigated using Transmission Electron Microscopy (TEM). The nanomodified resins were cured into trapezium shape specimens, see Figure 3.10a. The cured resins were then cut using a Leica UC2 Ultra-microtome machine, see Figure 3.10b, at room temperature. After cutting, sections were collected on 200-mesh copper grids. The TEM samples with a thickness of 85 nm, see Figure 3.10c, were examined using a FEI Tecnai Transmission Electron Microscope, see Figure 3.10d, at an accelerating voltage of 80 kV. The images were captured using a Gatan MS600CW high resolution digital camera and collected using Gatan digital micrograph software at several magnifications such as 22500x, 34000x, 115000x, 170000x and 225000x.

(a)

(b)

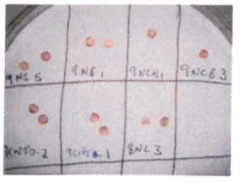

(c)

(d)

Figure 3.10: Preparation of TEM samples to be examined under the FEI Tecnai TEM.

3.5.2 Density measurement

Density of the cured epoxy and CFRP composite was measured using a density balance based on the Archimedes principle in distilled water. The measurement and calculation were conducted in according to ASTM D792 [149]. Three specimens were measured for each system. The calculation of the density is obtained by:

$$\rho_c = \frac{m_1}{m_1 - m_2} \times \rho_{water} \tag{3.1}$$

where m_1 = mass of dry sample, m_2 = mass of sample in water, $m_1 - m_2$ = mass of water displaced = up-thrust or apparent loss in weight, $\frac{m_1 - m_2}{\rho_{water}}$ = volume of water displaced = volume of the sample, ρ_{water} = density of water at room temperature (20°C) = 0.9982 g/cm^3 and ρ_c = density of the composite = $\frac{m_1}{\text{volume of the sample}}$.

3.5.3 Thermogravimetry analysis (TGA)

TGA is a technique to measure the weight change of a solid or liquid as it is heated at a controlled rate and in a controlled environment. The test is conducted according to ASTM Standard E1131 [148]. The tests were performed using a Perkin Elmer TGA, as shown in Figure 3.11a, to measure the constituent volume fraction of the nanocomposites and CFRP composites. TGA was also used to identify the rapid decomposition temperature of the constituent and to monitor the rate of degradation at a specified temperature.

(a)

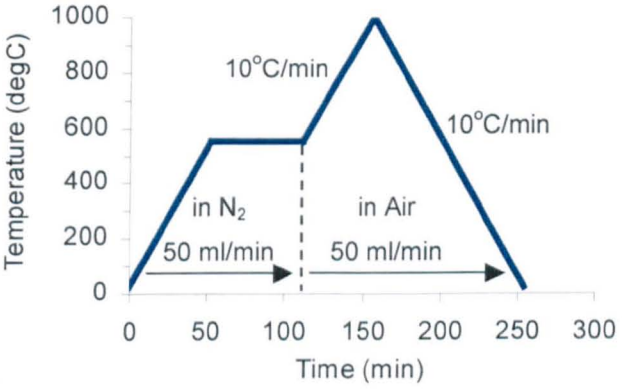

(b)

Figure 3.11: Perkin Elmer TGA.

A sample mass of 15 to 30 mg was heated from 25°C to 900°C at 10°C/min heating rate. The TGA programme is shown in Figure 3.11b. The sample is burnt in two stages. At first, it was heated from 25°C to 550°C at 10°C min^{-1} heating rate in nitrogen at 50 ml/min. The temperature was then kept at 550°C for 1 hour to decompose the epoxy resin. In stage two, the N_2 gas supply was then switched to air and the temperature was increased to 1000°C to decompose the carbon residue and/or graphite fibres. Data were collected using TGA PYRIS software. The TGA curve plots showed the percentage weight change against the material's decomposition temperature. The isothermal temperature of 550°C is selected as the optimum temperature to burn off the epoxy resin. For SEM evaluation, some of the residue (char) after isothermal temperature 550°C was collected.

3.5.4 Determination of constituent volume fraction

3.5.4.1 TGA

The weight fraction of the constituents in the composite obtained from TGA was used to determine the fibre, resin, nanoparticles and void volume fractions. The basic equations were given in ASTM Standard D3171-99 [150] were used to calculate the constituent content of nano-filled composite materials as the following:

(i) The fibre volume fraction:

$$V_f = \left(\frac{m_f}{m_c}\right) \times \left(\frac{\rho_c}{\rho_f}\right) \times 100 \tag{3.2}$$

where m_f = mass of the fibre, m_c = mass of the composite or initial mass of the specimen, ρ_f = density of the fibre and ρ_c = density of the composite

(ii) The resin volume fraction:

$$V_m = \left(\frac{m_m}{m_c}\right) \times \left(\frac{\rho_c}{\rho_m}\right) \times 100 \tag{3.3}$$

where m_m = mass of the epoxy and ρ_m = density of the epoxy resin

(iii)The nanoparticles volume fraction:

$$V_n = \left(\frac{m_n}{m_c}\right) \times \left(\frac{\rho_c}{\rho_n}\right) \times 100 \tag{3.4}$$

where m_n = mass of the nanoparticles or the final mass of the specimen after combustion and ρ_n = density of the nanoparticles

(iv) The void volume fraction:

$$V_v = 100 - (V_f + V_m + V_n) \tag{3.5}$$

or volume fraction of voids can be determine using the following equation:

$$V_v = \frac{\rho_t - \rho_c}{\rho_t} \tag{3.6}$$

where ρ_t is the theoretical composite density obtained from the rule of mixture

$$\rho_t = V_f \rho_f + V_m \rho_m + V_n \rho_n \tag{3.7}$$

The weight fraction of the constituents to the composites, $\left(\frac{m_f}{m_c}\right), \left(\frac{m_m}{m_c}\right), \left(\frac{m_n}{m_c}\right)$, was obtained from TGA results.

3.5.4.2 Image analyser technique

The volume fraction of the fibre can also be measured using an image analyser technique. This technique requires the use of metallographic specimen preparation equipment, a reflected light microscope with a magnification of at least 400 times, which has the capability of porting the image to a digital camera, a computer with image acquisition card and image analysis software. Figure 3.12a shows a Polyvar B-Met optical microscope with the image analyzer apparatus.

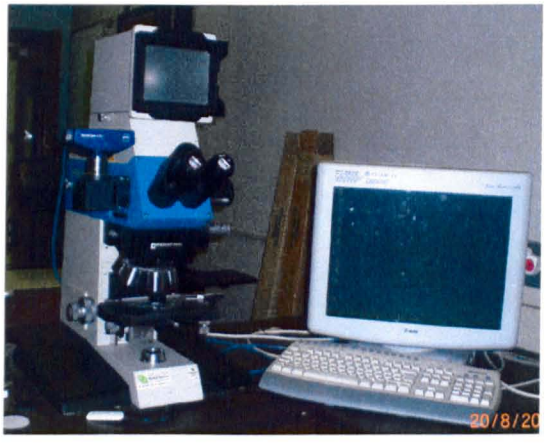

(a)

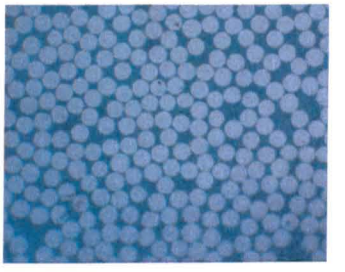

(b)

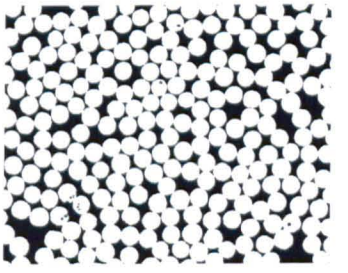

(c)

Figure 3.12: (a) Image Analyzer Apparatus and typical (b) greyscale and (c) binary fibre images of UD HTS40/977-2 laminate at magnification of 1000x; fibre diameter is approximately 7 μm.

A small section of laminate was prepared using a standard metallographic technique. The composite panels were sectioned perpendicular to the fibre axis. At least five different locations were taken and then cast in epoxy resin. The specimens were carefully ground and polished using a PHOENIX 4000 Automatic Grinding and Polishing machine. The procedure followed during the grinding and polishing processes are shown in Table 3.3. The surface of the polished specimen should display a clear delineation between the fibres and the matrix as shown in Figure 3.12b. In order to achieve a focused view, the coupon has to be level with the microscope lens. The computer package KSRUN version 3.0 ZEISS allows the camera view to be displayed

and analysed. The greyscale image, in Figure 3.12b, was converted into binary image where the pixels with values greater than the threshold value were presented as black, while the pixels with values less than the threshold value were presented as white as shown in Figure 3.12c. The KSRUN version 3.0 ZEISS software automatically calculates the fibre volume percentage based on the proportion of total field area to the total frame area.

Table 3.3: Regime followed for grinding and polishing of optical microscopy specimens.

	grain size	Time (s)	Pressure (N)	Speed (rpm)
Grinding (using SiC cloth)	600	150	18	200
	800	150	18	200
	1200	150	18	200
Polishing (media: diamond)	6μ	180	18	150
	1μ	180	18	150

3.5.5 Thermomechanical Analysis (TMA)

A Perkin Elmer Diamond TMA instrument, as shown in Figure 3.13a, was used to study the thermal stability of the cured resins such as thermal strain, coefficient of thermal expansion (CTE) and glass transition temperature (Tg) of the materials. The test and measurements of CTE and Tg were performed according to British standard BS ISO 11359-2:1999 [151]. The cured resins were cut into rectangular specimens of about 5 mm length, 5 mm in width and 1-2 mm in height, as shown in Figure 3.13b. All specimens were tested in an Argon atmosphere, which was supplied at 50 ml/min. A static load of 100 mN was applied via the TMA expansion probe. Therefore the probe rests on the surface of the test specimen under low loading conditions and the thermal response of the material was monitored by the sensitive displacement devices of the TMA instrument as illustrated in Figure 3.13c. All data were recorded and analysed using Diamond TMA PYRIS software.

In this study, the specimens were heated in two cycles as shown in Figure 3.14a for Epikote 828 resin systems and Figure 3.14b for Cycom 977-20 resin systems. The first heating cycle eliminates any thermal-memory effects in the specimen. The thermal

properties, such as thermal strain, CTE and Tg, were calculated based on the second heating where the specimens were heated from 25°C to 180°C for Epikote 828 resin systems and to 350°C for Cycom 977-20 resin systems at 5°C/min heating rate. At least three specimens for each resin system were tested. The CTE α is obtained from the TMA curve using the following equation:

$$\alpha = \frac{dL}{dT} \times \frac{1}{L_o} \tag{3.8}$$

where L_o is the length of the specimen at room temperature, L is the length of the specimen at temperature T.

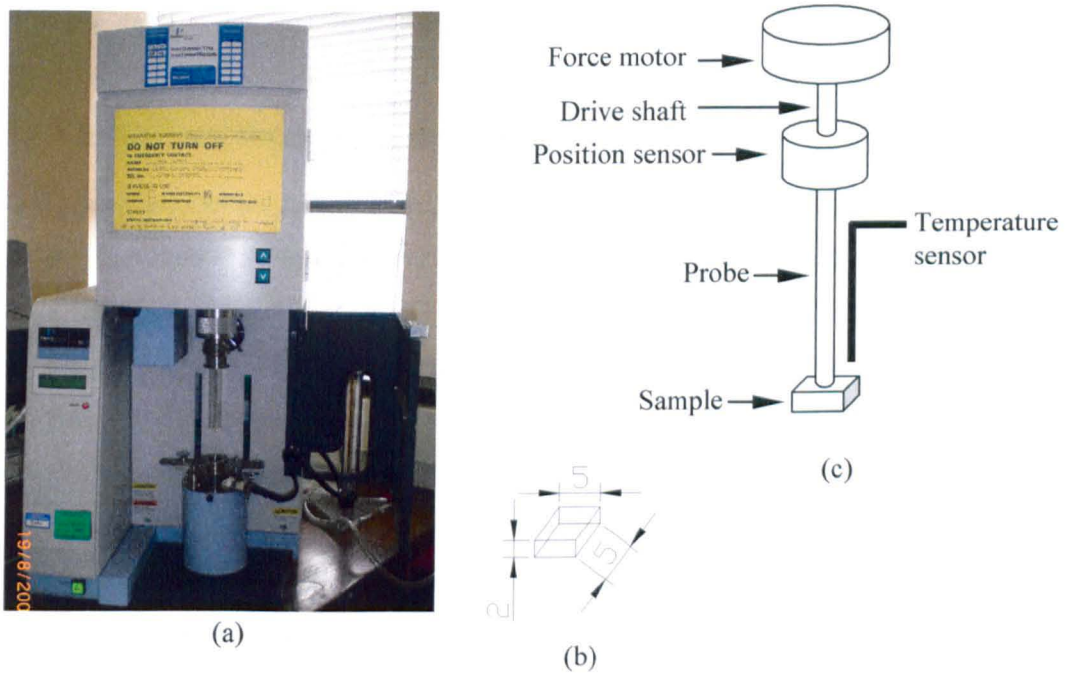

Figure 3.13: (a) Perkin Elmer Diamond TMA instrument, (b) specimen dimensions and (c) illustration of load, displacement and temperature monitoring devices.

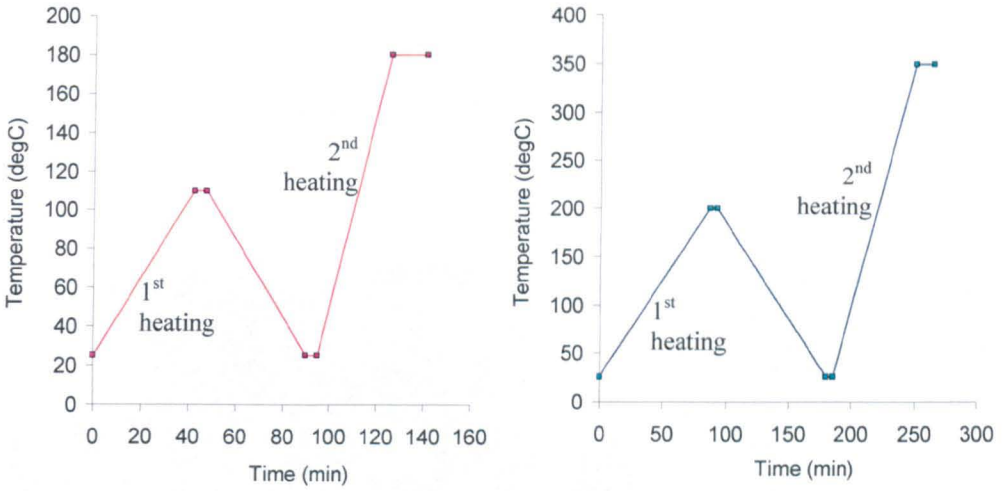

Figure 3.14: TMA program for (a) Epikote 828 and (b) Cycom 977-20 resin systems.

3.5.6 Differential Scanning Calorimetry (DSC)

DSC was used in conjunction with TMA to determine the glass transition temperature of the materials. The test and measurement of Tg were performed according to British standard BS ISO 11357-2:1999 [152] using a Perkin Elmer DSC7 instrument as shown in Figure 3.15a. DSC measures the difference between the heat flow rate into the specimen and that into the reference as a function of temperature and/or time while the specimen and the reference are subjected to the same controlled temperature program under a specified atmosphere [152]. The basic principle of heat-flux DSC technique is that when the physical transformation happens in the specimen more or less heat will be necessary to maintain both sample and reference at the same temperature. The amount of the heat flowing to the specimens depends on whether the process is exothermic (releases heat) or endothermic (absorbs heat). The glass transition can be defined as the change in the heat capacity as the polymer goes from the glass state to the rubber state. It can be determine using the DSC curve of heat flow verses temperature.

The cured resins were cut into small pieces of 10-20 mg weight. The specimen is placed in an aluminium pan. The sample and the reference (empty pan) were put into the holders, as shown in Figure 3.15b, and heated in two cycles as shown in Figure 3.16. The first heating cycle eliminates any thermal-memory effects in the specimen. The Tg was determine based on the heat flow rate versus temperature curve from the second heating cycle where the specimens were heated from 25°C to 180°C for Epikote 828

resin systems and 350°C for Cycom 977-20 resin systems at 10°C/min heating rate. All specimens were tested in an Argon atmosphere, which was supplied at 20ml/min. All data were recorded and analysed using DSC7 PYRIS software. At least three specimens for each resin system were tested.

(a) (b)

Figure 3.15: (a) Perkin Elmer DSC7 instrument with a cooling system using nitrogen gas and (b) holders for specimen in an aluminium pan and empty pan.

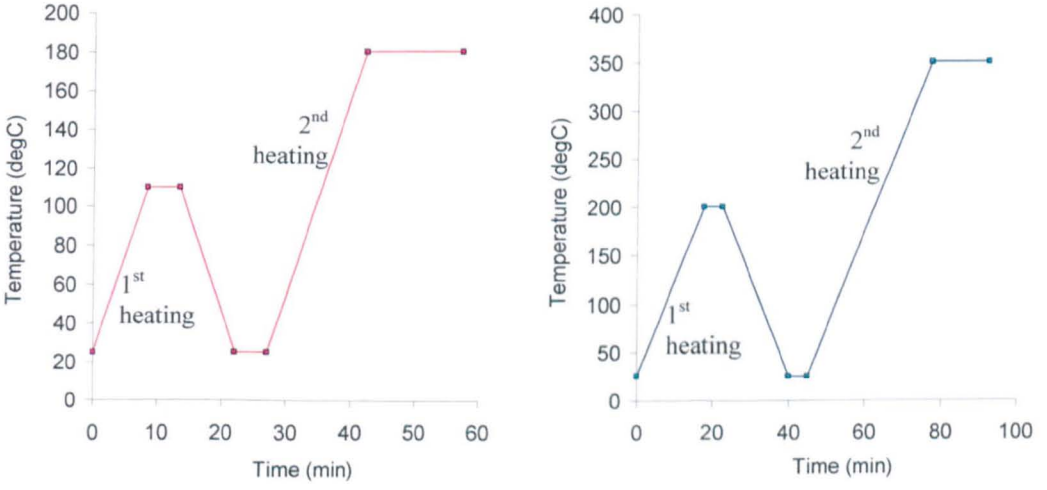

(a) (b)

Figure 3.16: DSC program for (a) Epikote 828 and (b) Cycom 977-20 resin systems.

3.5.7 Determination of fibre misalignment

The in-plane fibre waviness of long-fibre composites was characterised and quantified using a method proposed by Yugartis [153]. This method assumes that (1) the fibres are straight over short distances (at least twenty fibre diameters) and (2) all fibres have the same circular diameter. The determination of fibre misalignment involves several procedures:

(i) The composite panels were sectioned at an angle of approximately 5° to the nominal fibre direction 0° in agreement with Yugartis's work. At least five different locations were taken and then cast in epoxy resin. The specimens were ground and polished followed the procedure discussed in Section 3.5.4.2. Figure 3.17 illustrates a typical micrograph taken from a specimen (HTS40/977-2 $[0]_{2s}$) sectioned at an angle of approximately 5° from the 0° direction.

(ii) The major axial dimension of the cut fibre's elliptical surface and fibre diameter were directly measured using the KSRUN version 3.0 ZEISS programme. 400 data per specimen were collected. At least 5 specimens were analysed for each CFRP systems.

(iii) The precise angle of cut for each fibre, θ_i, is calculated using the following equation:

$$\theta_i = \sin^{-1}\left(\frac{d_f}{a_i}\right) \tag{3.9}$$

where a_i is the major axial dimensions of the cut fibre's elliptical surface, as shown in Figure 3.18b, and d_f is the fibre diameter. The subscript i refers to the i^{th} fibre. The HTS40 carbon fibre has 7 μm diameter.

(iv) The angle of cut was sorted into the class interval width at the angle of half a degree.

(v) The fibre volume fraction of the total fibre at angle θ_i is calculated using the following equation:

$$f_v(\theta_i) = \frac{\left(\frac{N_i}{\tan\theta_i}\right)}{\sum_1^n \frac{N_i}{\tan\theta_i}} \tag{3.10}$$

where θ_i is the class interval mean, N_i is the number of values within a class interval and n is the total number of class interval.

(vi) The average angle that represents the mean of distribution, $\bar{\theta}$, is calculated using the following equation:

$$\bar{\theta} = \sum_{i=1}^{n} f_v(\theta_i)\theta_i \tag{3.11}$$

(vii) The angle of intersection of each individual fibre, ϕ_i (see Figure 3.18) is calculated using the following transformation:

$$\phi_i = \theta_i - \phi_{pc} \tag{3.12}$$

where the plane-cut angle ϕ_{pc} is the mean of distribution angle $\bar{\theta}$.

(viii) Finally, in order to characterise the form of distribution, standard deviation, σ, is calculated based on the following equation:

$$\sigma = \left(\sum_{i=1}^{n} f_v(\theta_i)(\theta_i - \bar{\theta})^2\right)^{\frac{1}{2}} \tag{3.13}$$

A large standard deviation indicates poor overall alignment whereas a smaller one would characterise a more narrow angle distribution.

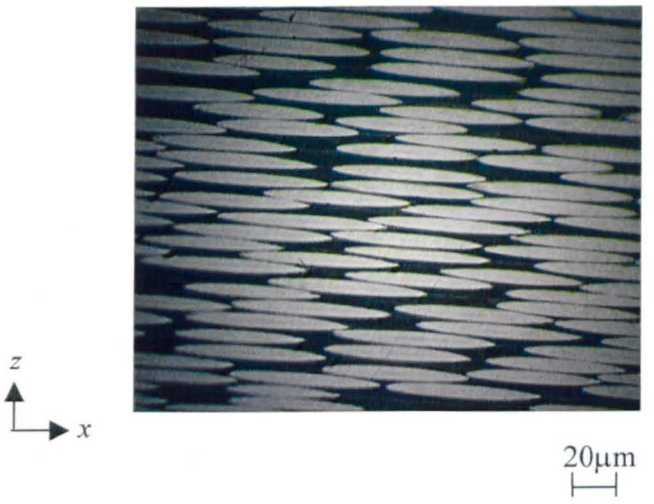

Figure 3.17: A typical optical micrograph taken from a $[0]_8$ HTS40/977-2 specimen sectioned at an angle of approximately 5° to the fibre axis.

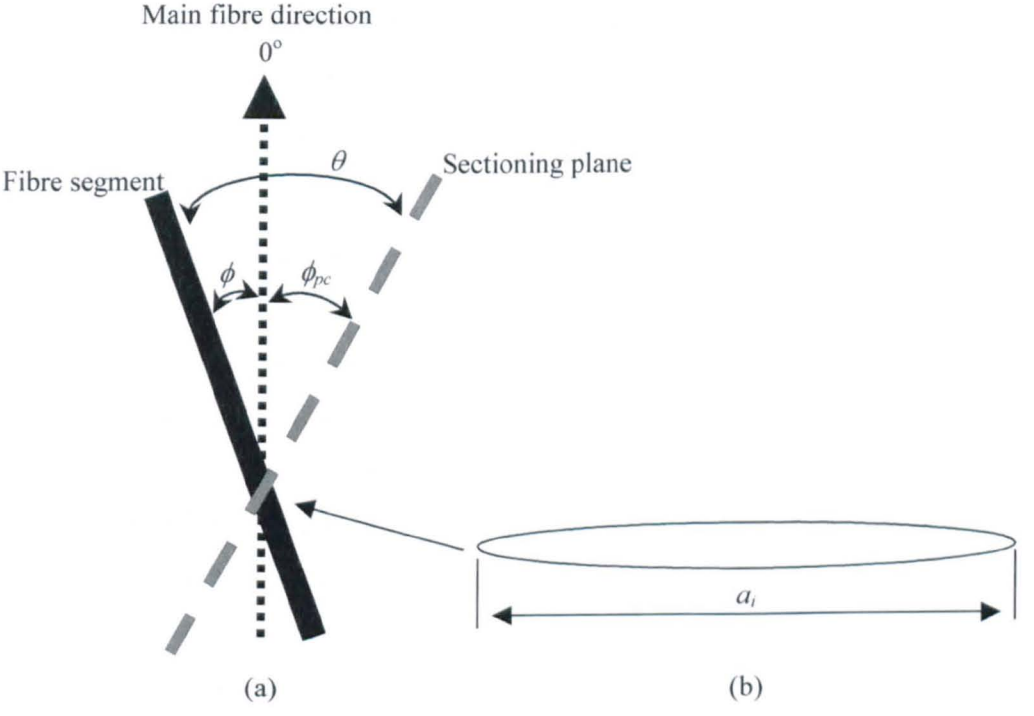

Figure 3.18: (a) Definition of fibre angle ϕ_i in a sectioned composite sample and (b) cross-section of the fibre sectioned at angle θ_i.

3.6 Mechanical tests

3.6.1 Compressive response of epoxy polymers

3.6.1.1 Test specimens and test procedures

The cured resins with dimension of 1:1 length to diameter (L/D) ratio (10 mm/10 mm), as recommended in [154], were fabricated for the uniaxial compression test. This helped to avoid buckling, reduce friction due to small cross-section area, avoid premature failure due to sharp corners (found in prismatic shape specimens) and prevent self-reaction of the epoxy resin during curing. Cured resin had a darker appearance for thick specimens (>10 mm), see Figure 3.19a, due to exothermic reaction. In order to have smooth parallel ends perpendicular to the cylindrical axis, the cast specimens were machined on a lathe and polished to an accuracy of 0.01 mm (measured with a micrometer). All specimens were prepared carefully with no bubbles, visible flaws, scratches or any imperfections, which may result in premature failures. Examples of these specimens are shown in Figure 3.19a. All specimens were dried in a vacuum oven before being kept in vacuum at room temperature. Compression tests were also conducted on the 12.5x12.5x25.4 mm^3 cube specimens (according to ASTM standard D695-96 [155]) to study the effect of specimen geometry and dimensions on the compressive stress-strain response and their failure mechanisms. At least five specimens were tested for each system.

Static uniaxial compression tests were carried out on the cubic and cylindrical specimens using a Hounsfield universal testing instrument, as shown in Figure 3.19b, with a crosshead speed of 1 mm/min. In order to minimize the frictional forces between test machine platen and specimen loaded surfaces especially at circumference edges where barrelling may be triggered, the specimen ends were smeared with petroleum jelly. The compliance of the testing machine for compression, based on a technique proposed in [156], was performed to calculate the actual displacement of the specimen. In the 'direct technique' demonstrated by Kalidindi *et al* [156], the load-displacement relationship for the machine was measured without any specimen between the compression bars. The actual deformation of the sample can then be calculated by subtracting the non-sample displacement of the testing fixture from the total displacement recorded by the actuator. This load-displacement relationship for the machine can be used to correct the recorded load–displacement data for any specimen tested under uniaxial compression by the testing machine at the same crosshead speed.

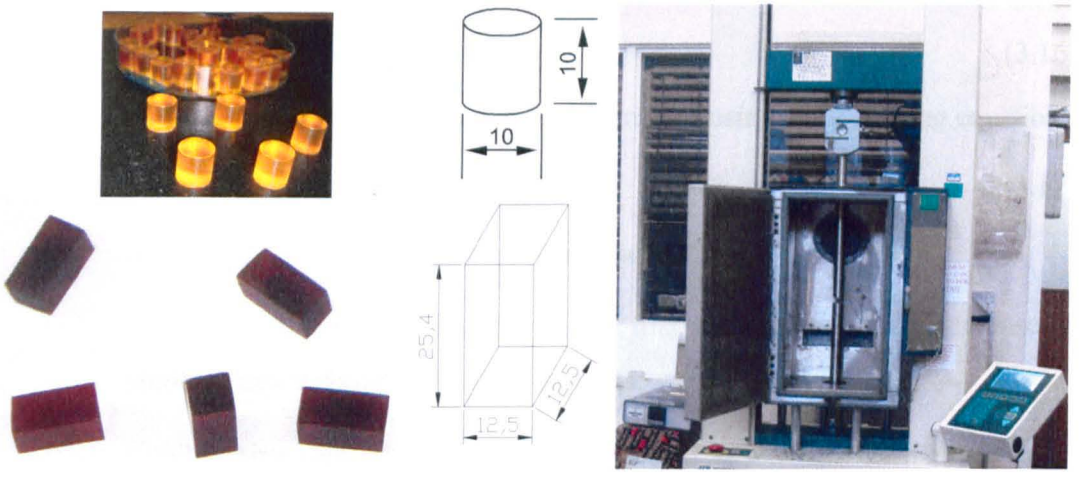

(a) (b)

Figure 3.19: (a) Examples of the uniaxial compression test specimens of cylindrical and cubic shapes with their dimensions and (b) Hounsfield universal testing machine with the compression bars and fan-assisted oven mounted apparatus.

3.6.1.2 Data analysis

The compression tests were conducted based on British standard BS EN ISO 604:2003 [157] and ASTM standard D695-96 [155]. The compressive properties obtain from the test are as follows:

(i) Engineering compressive stress, σ_e, is defined as compressive load, F, per unit area, A, of the original cross-section of the test specimen.

$$\sigma_e\,(\text{MPa}) = \frac{F}{A} \tag{3.14}$$

(ii) Engineering compressive strain, ε_e, is decrease in length, ΔL, per unit original length, L_o, of the test specimen

$$\varepsilon_e = \frac{\Delta L}{L_o} \tag{3.15}$$

(iii) The change in cross-sectional area is significant when calculating stress of a polymer loaded in compression. The stress was calculated using the current cross-sectional area (true stress) instead of the initial cross-sectional area

(engineering stress). The true compressive stress can be determined using the following equation:

$$\sigma_{true} = (1 - \varepsilon_e)\sigma_e \tag{3.16}$$

(iv) The true compressive strain can be determined using the following equation:

$$\varepsilon_{true} = \ln(1 + \varepsilon_e) \tag{3.17}$$

(v) True compressive stress-strain (σ-ε) response.

(vi) Compressive stress at yield, σ_y, is the first stress at which an increase in strain occurs without an increase in stress.

(vii) Compressive yield strain, ε_y, is the strain corresponding to the compressive stress at yield.

(viii) Compressive strength, σ_u, is a maximum compressive stress sustained by the test specimen during a compressive test.

(ix) Compressive stress at break (rupture), σ_f, is the compressive stress at break of the test specimen

(x) Compressive strain at break, ε_f, is the strain at break of the test specimen.

(xi) Compressive modulus, E, is the ratio of the stress difference (σ_{i+1} minus σ_i) to the corresponding strain difference values (ε_{i+1}=0.025 minus ε_i=0.010) on the true stress-strain curve. With computer aided equipment, the compressive modulus was determined using a linear regression procedure on the part of the compressive stress-strain curve between these mentioned points.

$$E(\text{MPa}) = \frac{\sigma_{i+1} - \sigma_i}{\varepsilon_{i+1} - \varepsilon_i} \tag{3.18}$$

(xii) Statistical analysis was performed to obtain the standard deviation and standard error of the mean of a particular data set. The following equations were used:

$$X = \overline{X} \pm a \tag{3.19}$$

$$a = \frac{SD}{\sqrt{n}} \tag{3.20}$$

where $\overline{X}$ is the mean value of a set of measurements, X is the individual measurement, SD is the standard deviation, a is the standard error of the mean and n is the number of measurements.

3.6.2 Tensile response of epoxy polymers

3.6.2.1 Test specimens and test procedures

The dogbone shape specimens with a gauge length/width/thickness of 33mm/10mm/2mm were adhered with 1.5 mm thick glass fibre reinforced polymer (GFRP) composite end-tabs. This is to prevent a premature failure at grips. The dimensions of the specimen and examples of the specimens are illustrated in Figure 3.20. At least five specimens were tested for each system. Prior to testing, the actual width and thickness of the coupon at the gauge length was measured at 3 different points using a digital electronic Vernier calliper. The cross sectional area of the specimens was calculated by multiplying the mean width by the mean thickness. A Hounsfield Universal Testing machine with wedge type grips, as shown in Figure 3.21, was used for the tensile testing at a crosshead speed of 1 mm/min. A 10 kN load cell and a 25 mm gauge length clip-on extensometer were used to record the applied load and elongation data. These data were logged to a computer for analysis.

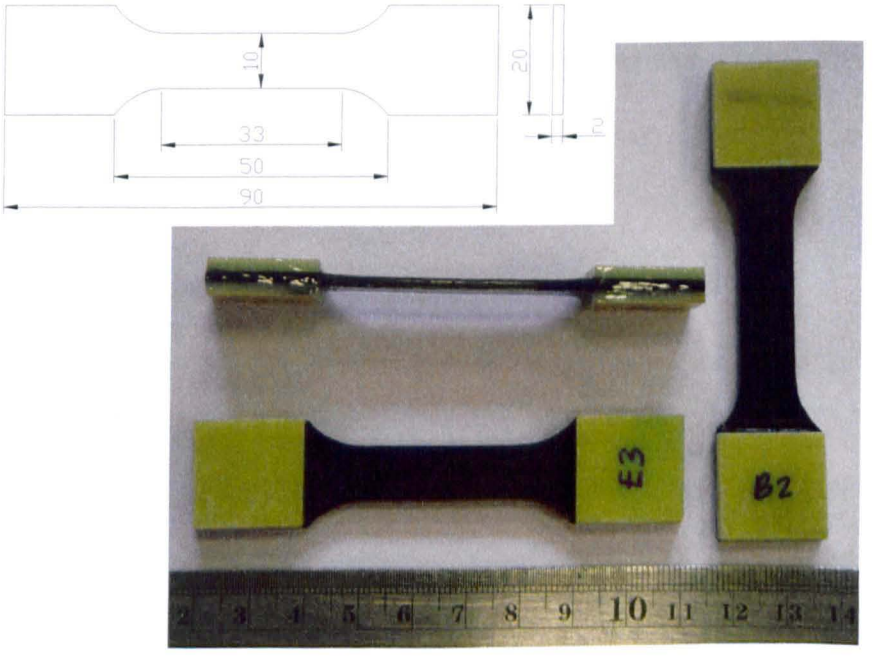

Figure 3.20: Dimensions and examples of the dogbone shape specimens.

Figure 3.21: A Hounsfield universal testing machine with wedge type grips for tensile test.

3.6.2.2 Data analysis

The tensile tests were conducted based on British standard BS EN ISO 527-1 and -2 :1996 [158]. The tensile properties obtain from the test are as the following:

(i) Tensile stress, σ, is defined as tensile force, F, per unit area, A, of the original cross-section within the gauge length.

$$\sigma\,(\text{MPa}) = \frac{F}{A} \tag{3.21}$$

(ii) Tensile strain, ε, is an increase in length, ΔL_o, per unit original length, L_o, of the gauge

$$\varepsilon\,(\%) = \frac{\Delta L_o}{L_o} \times 100 \tag{3.22}$$

(iii) Tensile stress-strain (σ-ε) response.

(iv) Tensile strength, σ_u, is a maximum tensile stress sustained by the test specimen during a tensile test

(v) Tensile strain at break, ε_f, is the tensile strain at break of the test specimen

(vi) Modulus of elasticity in tension (Young's modulus), E, is the ratio of the stress difference σ_{i+1} minus σ_i to the corresponding strain difference values ε_{i+1}=0.0025 minus ε_i=0.0010. With computer aided equipment, the Young's

modulus was determined using a linear regression procedure on the part of the tensile stress-strain curve between these mentioned points.

$$E(\text{MPa}) = \frac{\sigma_{i+1} - \sigma_i}{\varepsilon_{i+1} - \varepsilon_i} \tag{3.23}$$

3.6.3 Flexural response of epoxy polymers

3.6.3.1 Test specimens and test procedures

The tests were conducted based on the British Standard BS EN ISO 178:2003 [159]. The cured resins of 80 mm length x 10 mm width x 4 mm thickness were bent under three-point bend configuration. The dimensions and examples of the flexural test specimens are illustrated in Figure 3.22. At least five specimens were tested for each system. Prior to testing, the actual width and thickness of the specimens were measured at 3 different points using a digital electronic Vernier calliper. The average width and thickness data were calculated and recorded. The test specimen was placed symmetrically on the two supports of span=60 mm. A Hounsfield Universal Testing machine with the three-point bending fixtures, as shown in Figure 3.23, was used to apply force at midspan at a crosshead speed of 2 mm/min. A 10 kN load cell was used to record the applied load and the corresponding deflection of the specimen during the test was recorded using the crosshead displacement of the machine. These data were logged to a computer for analysis.

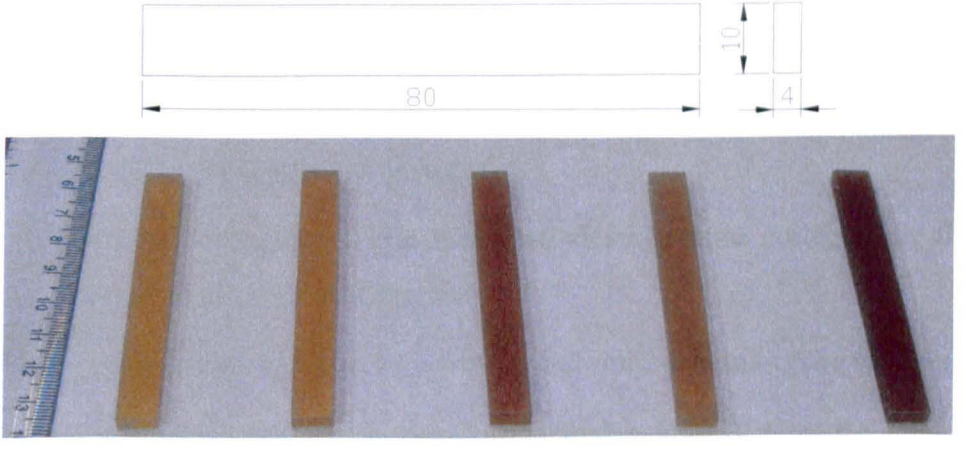

Figure 3.22: Dimensions and examples of the test specimens used in three point bending tests.

Figure 3.23: A Hounsfield universal testing machine with three point bending test fixtures and the test set-up.

3.6.3.2 Data analysis

The properties of the materials obtained from the flexural test were as follows:

(i) Flexural stress, σ

$$\sigma\,(\text{MPa}) = \frac{3FL}{2bh^2} \tag{3.24}$$

where F is the applied force (in N), L is the span=60 mm, b is the width (in mm) of the specimen and h is the thickness (in mm) of the specimen.

(ii) Flexural strain, ε

$$\varepsilon = \frac{6sh}{L^2} \tag{3.25}$$

where s is the deflection (in mm), h is the thickness (in mm) and L is the span (in mm).

(iii) Flexural stress-strain (σ-ε) response.

(iv) Flexural strength, σ_u, is a maximum flexural stress sustained by the test specimen during a bending test

(v) Flexural strain at break, ε_f, is the flexural strain at break of the test specimen

(vi) Modulus of elasticity in flexure (Flexural modulus), E, is the ratio of the stress difference σ_{i+1} minus σ_i to the corresponding strain difference values ε_{i+1}=0.0025 minus ε_i=0.0010. With computer aided equipment, the Flexure

modulus was determined using a linear regression procedure on the part of the flexural stress-strain curve between these mentioned points.

$$E(\text{MPa}) = \frac{\sigma_{i+1} - \sigma_i}{\varepsilon_{i+1} - \varepsilon_i} \tag{3.26}$$

3.6.4 Fracture toughness of epoxy polymers

3.6.4.1 Test specimens and test procedures

The tests were conducted based on the British Standard BS ISO 13586:2000 [160]. The cured rectangular blocks (of size 33 x 26 x 14 mm^3 and 80 x 10 x 4 mm^3) were machined according to the dimensions as shown in Figure 3.24. Examples of the specimens are illustrated in Figure 3.25. The notch was sharpened by sliding a razor blade across the notch. A new razor blade was used for each test specimen. There are two types of specimens. The compact tension (CT) test specimens, with 9 mm initial crack length, were used to determine the fracture toughness properties of Epikote 828 epoxy systems while single-edge-notch bending (SENB) samples, with 4.5 mm initial crack length, were used to determine the fracture properties of Cycom 977 epoxy systems. Cycom 977 systems could not be cast into a thick block due to exothermic reaction during curing. The resins were overheated and darkened when moulded and cured into thick specimens.

At least five specimens were tested for each system. Prior to testing, the actual width, thickness and crack length for each specimen were measured at 3 positions using a digital electronic Vernier calliper. The average values were calculated and recorded. The fracture toughness test on the CT specimens was conducted using a Hounsfield Universal Testing machine mounted with fracture toughness test fixtures as shown in Figure 3.26a. The specimens were loaded at 10 mm/min test speed (in accordance to British standard 13586). A 5 kN load cell was used to record the applied load. The specimen was loaded by means of two pins in holes in the specimen. The displacement of the load points during the test was recorded using the movement of the crosshead of the machine. These force and displacement data were logged to a computer for analysis. The compliance of the testing machine was performed to calculate the actual displacement of the specimen. A hardened steel block was machined to have dimensions similar to that of the actual CT specimen but unnotched. The steel block was tested using a similar configuration and test speed for CT specimens. The

displacement δ verses force F (up to 500N) graphs were plotted and the δ-F relationship obtained from the graphs were the displacement of the test fixtures. In this study, $\delta = 0.0005F + 0.015$ was used. The actual deformation of the sample can then be calculated by subtracting the displacement of the test fixtures from the total displacement recorded by the actuator. This load-displacement relationship for the machine can be used to correct the recorded load–displacement data for any CT specimen tested by the machine at the same crosshead speed.

The SENB samples were tested using the three point bending test fixtures as shown in Figure 3.26b. The test specimen was placed symmetrically on the two supports of span=40 mm. A force is applied at midspan with a crosshead speed of 1 mm/min. This test speed was chosen because the SENB specimens usually fail at a very small load (<100N) due to small dimensions and brittle behaviour of the materials. A 5 kN load cell was used to record the applied load and the corresponding deflection of the specimen during the test was recorded using the crosshead displacement of the machine. These data were logged to a computer for analysis.

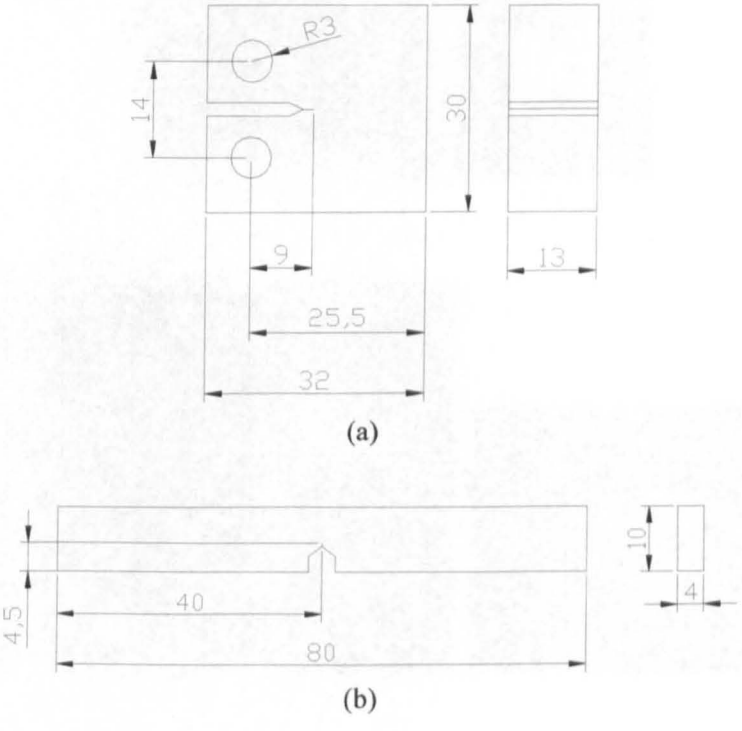

Figure 3.24: Dimensions of (a) compact tension test specimen for fracture toughness test of Epikote 828 resin systems and (b) single-edge-notch bending specimen (three-point-bending) for fracture toughness test of Cycom 977-20 resin systems.

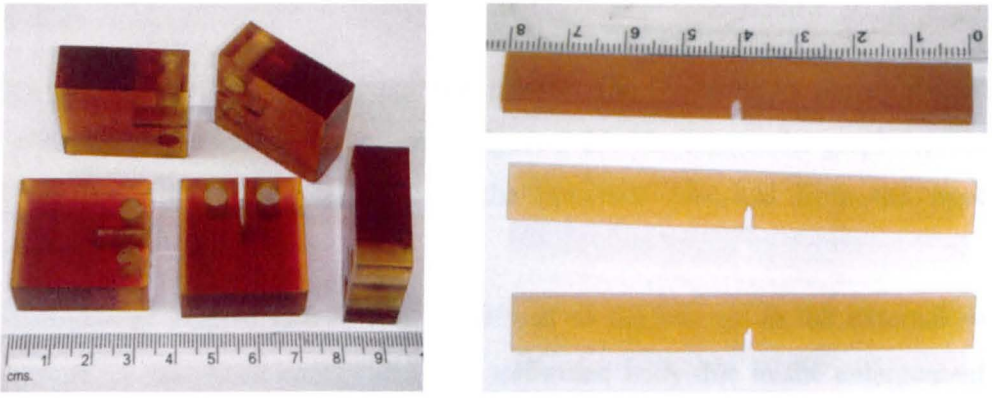

(a) (b)

Figure 3.25: Examples of the test specimens for the fracture toughness test (a) compact tension test specimens and (b) single-edge-notch bending specimens.

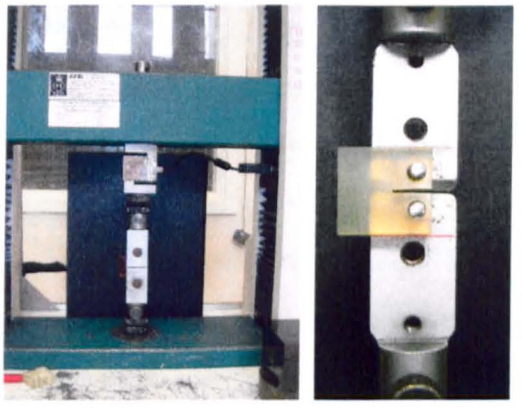

(a)

(b)

Figure 3.26: A Hounsfield universal testing machine with (a) compact tension test set-up and (b) three-point bending test set-up for measuring fracture toughness of Epikote 828 and Cycom 977-20 resin systems, respectively.

3.6.4.2 Data analysis

The force (F) vs displacement (s) curve was plotted. The F-s curve for most polymers is linear due to brittle behaviour as shown in Figure 3.27. The area under graph represents energy to break W_B. The properties of the materials obtained from the fracture toughness test were as follows:

(i) Energy release rate G can be defined as the change in the external work δU_{ext} and strain energy δU_S of a deformed body due to the enlargement of the cracked area δA

$$G(\mathrm{J/m^2}) = \frac{\delta U_{ext}}{\delta A} - \frac{\delta U_S}{\delta A} \tag{3.27}$$

Critical energy release rate G_{IC} is the value of the energy release rate G in a pre-cracked specimen under plane-strain loading conditions when the crack starts to grow. G_{IC} can be calculate from the energy W_B up to the instant of crack growth initiation, where the load is F_Q (the applied load at the initiation of crack growth) and the original crack length is a:

$$G_{IC}(\mathrm{J/m^2}) = \frac{W_B}{h \times w \times \phi(a/w)} \tag{3.28}$$

where W_B is the energy to break (the input energy when crack growth initiates), h is the test specimen thickness, w is the test specimen width and $\phi(a/w)$ is the energy calibration factor depending on the initial crack length a. The calibration factor $\phi(a/w)$ can be obtained from Table A.1 and Table A.2 in BS ISO 13586:2000 for SENB and CT specimens, respectively. For example, the $\phi(a/w)=\phi(0.45)=0.275$ and $\phi(a/w)=\phi(0.35)=0.213$ for SENB and CT specimens, respectively.

(ii) Stress intensity factor is the limiting value of the product of the stress $\sigma(r)$ perpendicular to the crack area at a distance r from the crack tip and the square root of $2\pi r$. For small value of r

$$K(\mathrm{Pa}.\sqrt{\mathrm{m}}) = \lim_{r \to 0} \sigma(r) \times \sqrt{2\pi r} \tag{3.29}$$

Critical stress intensity factor K_{IC} is the value of the stress intensity factor when the crack under load actually starts to enlarge under a plane strain loading condition around the crack tip. K_{IC} can be calculated from the load F_Q at crack growth initiation and the original crack length a:

$$K_{1C}\left(\text{Pa}.\sqrt{\text{m}}\right)= f(a/w)\frac{F_Q}{h\sqrt{w}} \tag{3.30}$$

where F_Q is the load at crack growth initiation, h is the test specimen thickness, w is the test specimen width and $f(a/w)$ is the geometry calibration factor depending on the initial crack length a. The calibration factor $f(a/w)$ can be obtained from Table A.1 and Table A.2 in BS ISO 13586:2000 for SENB and compact tension specimens, respectively. For example, the $f(a/w)=f(0.45)=9.14$ and $f(a/w)=f(0.35)=6.39$ for SENB and CT specimens, respectively.

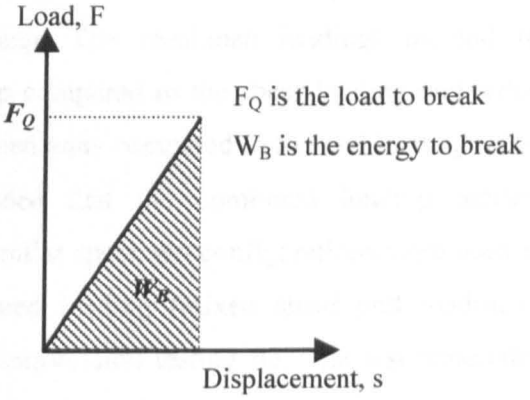

Figure 3.27: A load displacement (F-s) curve for a notched test specimen.

3.6.5 Compressive response of CFRP laminates

Compression tests were conducted on unidirectional (UD) laminates to determine ultimate compressive strength, strain-at-failure, compressive modulus and Poisson's ratio. Several test methods have been used by previous researchers to study how the composite materials respond to compressive loading. In practice, reliable and repeatable compressive strength data of composite laminates are very difficult to achieve because these data rely on various parameters. The most significant contributors to the variations in compressive properties include selection of test method, fabrication practices and Euler buckling, control of fibre alignment, inaccurate specimen machining, improper

tabbing procedures, poor quality of the test fixture, improper placement of the specimen in the test fixture, improper placement of the fixture in the testing machine, and improper test procedure [161-163].

The compression test methods can be classified into three groups; (1) the load is introduced into the specimen through direct compression called direct end loading such as in ASTM D695 [155], (2) the load is introduced into the specimen through shear such as in ASTM D3410 [164] and (3) the combined loads are introduced into the specimens through both end loading and shear such as Imperial College London (ICL) test fixture used in [163, 165]. The effect of compression loading methods has been investigated by Xie and Adams [162]. The results showed that the shear loading method yielded to more severe stress concentrations at the tab tip of the tabbed specimen, which caused a sudden change in specimen geometry and the presence of through thickness shear stress. Therefore the specimen has a very high tendency to fail near the geometry change caused by the end tabs. Meanwhile the end loading method yielded high stress concentrations at the specimen ends which lead to premature failure at the specimen ends due to local crushing. The combined loadings method reduced the stress concentration at the tab tip compared to the shear loading and reduced also the stress concentration at the specimen ends compared to the end loading method. Therefore Xie and Adams [162] concluded that the combined loading method yielded higher compressive strengths if similar specimen configurations were used in all test methods. In this study, the combined loading (mixed shear end loading) test method was employed using the ICL compression testing rig. The test materials, specimen design and fabrication processes, test programme and testing equipment are described in the following subsections.

3.6.5.1 Preparation of compression test specimens

The composite panels, prepared in Section 3.4, were cut into 112 mm long x 10 mm width strips. The specimen geometry was recommended by the CRAG test method [166] and the ASTM Standard D3410 [164]. A short gauge-length specimen of 10 mm to 12 mm was used. The specimen dimensions are illustrated in Figure 3.28. The specimen was bonded with 50 mm long woven glass fibre reinforced polymer (GFRP) composite end-tabs. Glass fibre laminate tabs were sand blasted and bonded onto the sand blasted CFRP coupon surfaces using Araldite adhesive. A jig was used to align the end tabs and apply mechanical pressure while the adhesive cured at room temperature

overnight. The adhesive was then post cured at 60°C for 2 hours. After tabbing, individual specimens were machined to final tolerance by grinding the specimen ends and tab surfaces parallel within 0.025 mm.

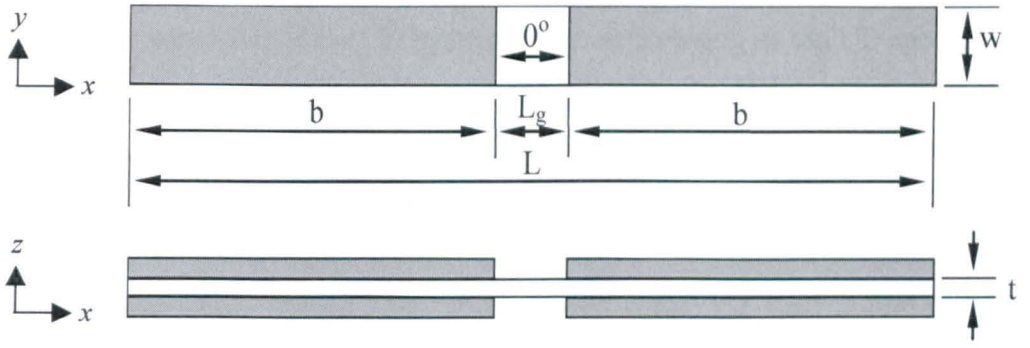

Figure 3.28: Compression test specimen drawing. Specimen dimensions: L = Total specimen length = 112 mm, L_g = Gauge length = 12 mm, b = Tab length = 50 mm, w = Specimen width = 10 mm, t = Specimen thickness ≈ 2.16 mm, GFRP tab dimensions = 50 mm length x 10 mm width x 1.5 mm thickness.

120Ω strain gauges were attached on both faces of five specimens to be tested in order to monitor the degree of Euler bending and measure axial strain and, hence, axial modulus. The test was considered invalid if there was a big difference in signals from the gauges on both faces of the specimen, which indicated that the specimen had undergone bending. In addition, another three specimens were prepared to measure the Poisson's ratio where a pair of longitudinal and transverse strain gauges was bonded on the gauge length. Examples of the specimens are illustrated in Figure 3.29.

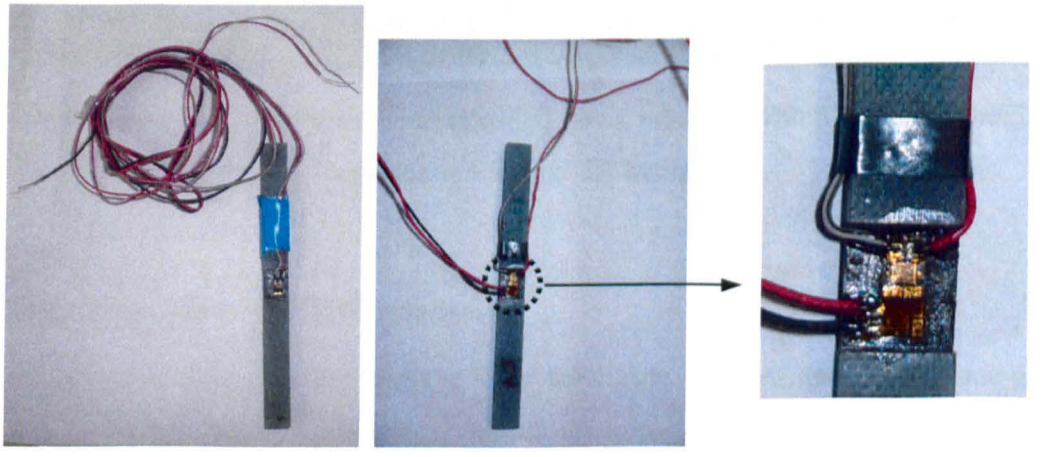

Figure 3.29: Examples of the UD compression test coupons attached with strain gauges.

3.6.5.2 Test machine and programme

The compression test was conducted in accordance to the CRAG test method [166] and the ASTM Standard D3410 [164]. A 250 kN servo-hydraulic machine with the ICL test fixture design [163,165], as shown in Figure 3.30, was used to determine the compressive behaviour of the UD laminate. The compression on the UD specimens was performed at a constant compression rate of 1 mm/min. The ICL testing fixture consists of upper and lower blocks, which grip the test specimen and prevent debonding of the tabs from the specimen end. All data were recorded by the computer via data acquisition system such as applied load, plunger displacement, back-to-back longitudinal strains and transverse strain. Several tests were stopped before the final failure occurred in order to examine the initial failure mode. The fractured specimen was prepared using the standard metallographic technique and observed under the optical microscope at 50x to 1000x magnification. The post-failure surfaces of the compression specimens were also observed using Scanning Electron Microscopy (SEM) to identify the failure mechanisms involved during compression.

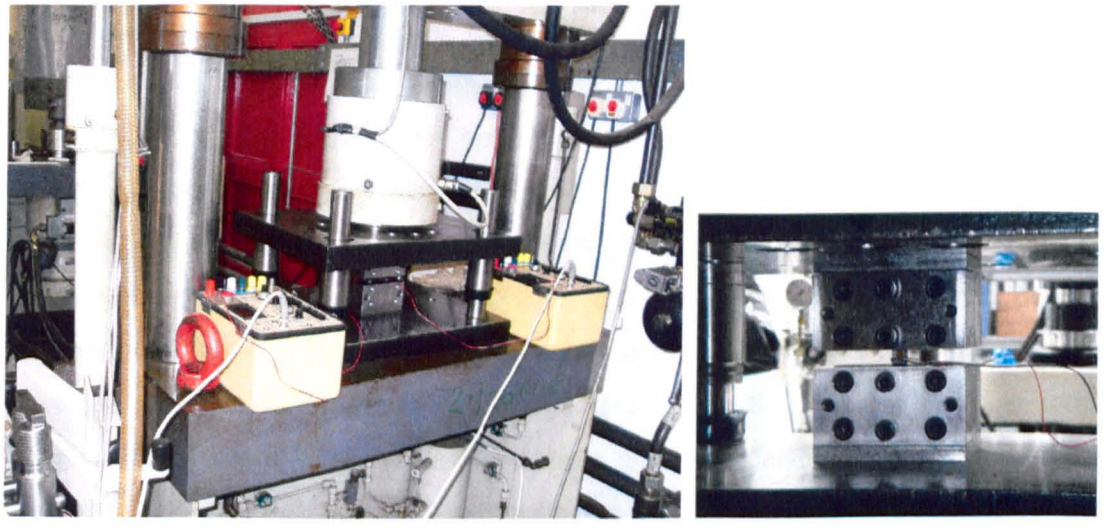

Figure 3.30: 250 kN compression servo-hydraulic machine with ICL test fixture for compression test of UD laminate.

3.6.6 In-plane shear of CFRP composites

The objectives of conducting in-plane shear tests were to determine the in plane shear strength, failure shear strain, shear chord modulus of elasticity and offset shear properties. On top of that, the shear stress versus shear strain response were plotted in

order to understand the behaviour of [±45°] CFRP laminate under tensile loading and the failure mechanisms involved during the test. The determination of in-plane shear properties is one of the most difficult areas of mechanical property testing. The most challenging is the determination of shear strength because the capability of the test method to produce a perfectly pure shear stress condition to failure for every material system is still questionable. The under- or over- estimate shear strength results depend on several identified parameters such as the presence of edge effects, material coupling effects, nonlinear behaviour of the matrix or the fibre/matrix interface, imperfect stress distributions, and the presence of normal stresses.

3.6.6.1 Preparation of in-plane shear test specimens

The cross ply laminates ($[0/90]_{2s}$) prepared in Section 3.4, were cut at 45° angle to produce a [±45°] CFRP composite panels. Due to the constrain imposed by the size of the CFRP panels which could be cured using wet-lay up method, it was not possible to produce specimens with dimensions recommended in the CRAG test method [166] or the ASTM Standard D3518 [167]. In order to study the effect of specimen size, in-plane shear specimens with a standard size were prepared using the commercial CFRP composite HTS40/977-2. The results were compared to the non-standard design used throughout this project. Table 3.4 and Figure 3.31 show the differences in geometry between standard and non-standard specimens.

The specimen was bonded with woven glass fibre reinforced polymer (GFRP) composite end-tabs or Aluminium end-tabs. The tabs were sand blasted and bonded onto the sand blasted CFRP coupon surfaces using Araldite adhesive. A jig was used to align the end tabs and apply mechanical pressure while the adhesive cured at room temperature overnight. The adhesive was then post cured at 60°C for 2 hours. After tabbing, individual specimens were machined to final tolerance by grinding the specimen ends and tab surfaces parallel within 0.025 mm. In order to determine the shear modulus, the strains parallel and perpendicular to the specimen axis were measured. The direction parallel to the specimen longitudinal axis is the x-direction and the direction perpendicular to it is the y-direction. The fibres are oriented at ± 45° to these directions as shown in Figure 3.31. A pair of longitudinal and transverse strain gauges was bonded onto the face of five specimens to measure the longitudinal and transverse normal strain. An example of the specimen is illustrated in Figure 3.32.

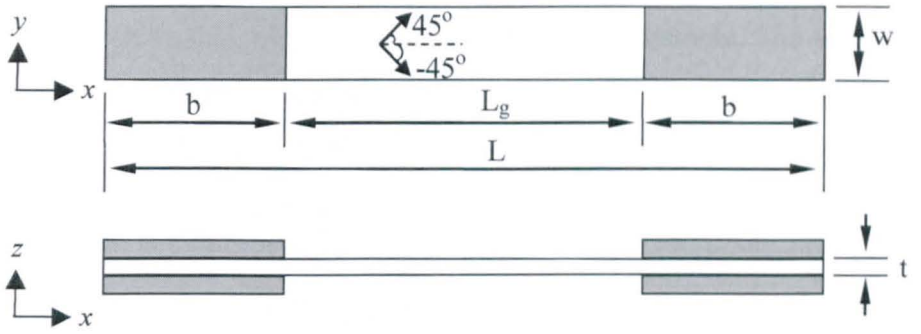

Figure 3.31: In-plane shear test specimen drawing.

Table 3.4: Differences between ASTM D3518 and specimen geometry used in this project.

Dimensions in mm	**ASTM D3518**	**Non-standard**
Total specimen length, L	200	110
Gauge length, L_g	100	60
Tab length, b	50	25
Specimen width, w	25	20
Thickness, t	2	2
Tab dimensions (length x width x thickness)	50 x 25 x 1.5	25 x 20 x 1.5

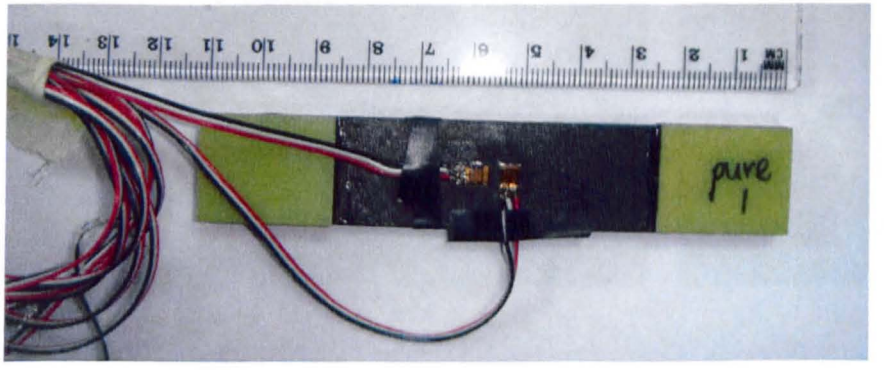

Figure 3.32: The example of the in-plane shear test coupon attached with strain gauges.

3.6.6.2 Test machine and programme

The in-plane shear test is a tensile test of a ±45° laminate. The test was performed in accordance with the CRAG test method [166] and the ASTM Standard D3518 [167]. The ASTM Standard D3039 [168] was also referred for the tensile test procedure and apparatus needed. Figure 3.33 shows the Mayes 100kN dynamic fatigue load frame and test fixtures which was used to determine the tensile properties of ±45° laminate. The test fixture was designed to grip the specimen and transfer the tensile load to the specimen. Specimens were carefully aligned in the test machine gripper to avoid induced specimen bending. The tensile load was increased uniformly, at 5 mm/min crosshead speed, to cause failure within 30-60 seconds. The tensile machine was connected to the data acquisition system. Therefore, all data such as load, plunger displacement, longitudinal strain and transverse strain, were directly recorded by the computer. The in-plane shear stress in the material coordinate system was directly calculated from the applied axial load meanwhile the related shear stress was determined from longitudinal and transverse normal strain data collected by the strain gauges.

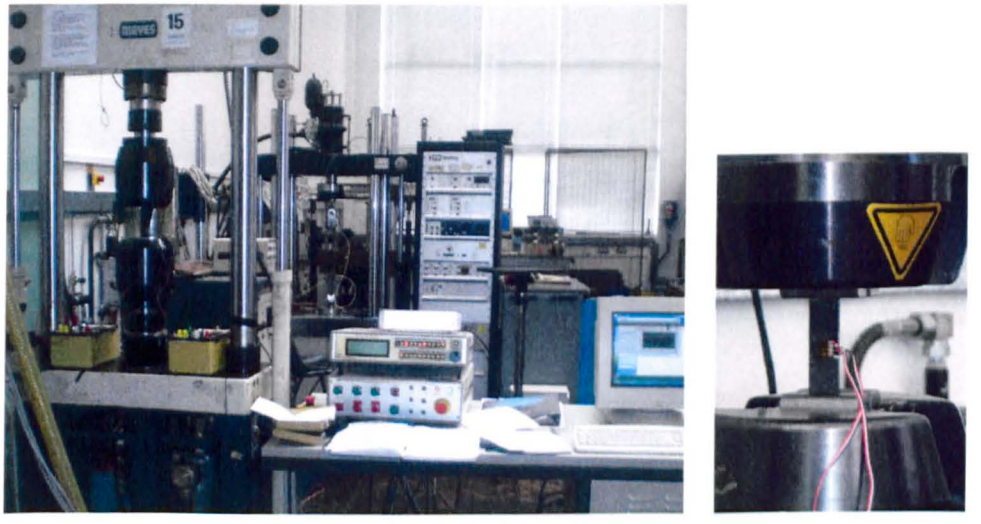

Figure 3.33: Mayes 100 kN dynamic fatigue load frame with pneumatic wedge grips fixtures for in-plane shear test of CFRP composite laminate.

3.7 Damage evaluation techniques

3.7.1 Optical microscopy

The optical microscopy technique was used to characterise the failure modes of composite materials. Primary information such as the origin of fracture, crack propagation direction or a general view of fracture surface can be gained. Figure 3.34 illustrates the process of the sample preparation for optical microscopy. The area of interest was cut from the specimen using a diamond saw and mounted into plastic clip for holding, as shown in Figure 3.34b. This sample was then placed in a pot and covered with a mixture of epoxy resin and hardener and left to cure overnight, as shown in Figure 3.34c. When cured, the sample was removed from the pot and was then ground and polished using PHOENIX 4000 grinding and polishing machine. The regimes followed during the grinding and polishing processes were discussed in Section 3.5.4.2. Examples of cured and polished samples are shown in Figure 3.34d. The polished coupons must be handled with care at all times so that the polished surface does not become scratched. The specimens were examined using a Polyvar B-Met optical microscope and all images were captured and analysed using a KSRUN version 3.0 ZEISS software.

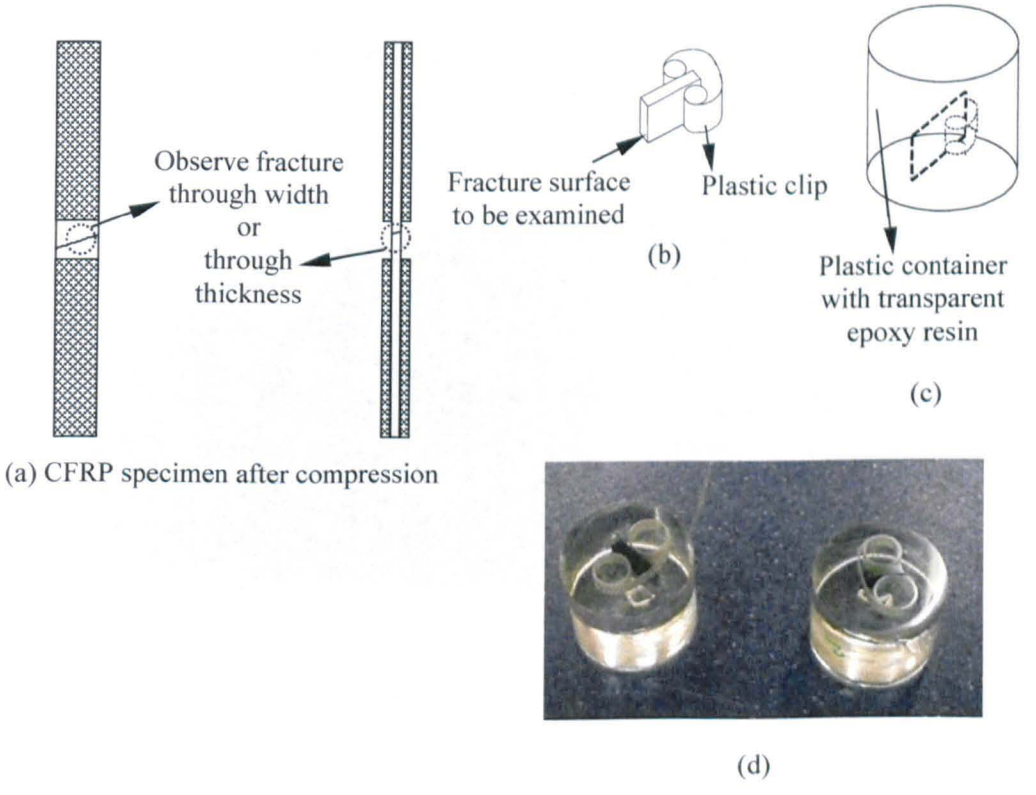

Figure 3.34: Specimen preparation for optical microscopy.

3.7.2 Scanning electron microscopy (SEM)

SEM is one of the advanced techniques in damage monitoring programme used to provide insight into the type and extent of damage the polymer composite experiences at extreme loads. In this study, this technique was used to examine the fracture surface of epoxy polymer and CFRP composite materials after mechanical testing. Examination of fracture surfaces is important to characterise the type of failure modes involved during the test. The fracture surfaces perpendicular to the loading direction or the longitudinal splits were observed by sectioning the area of interest and mounted onto suitable holders. Sections were mounted onto aluminium stubs using a carbon adhesive patch. The unwanted and non-conductive areas were painted with a silver die. The specimens were then coated with a thin layer of gold using a Sputter Coater Unit EMSCOPE SC500 A, as shown in Figure 3.35a, at 20 mA current and 0.05 torr pressure for 3 min. A coating of gold was applied to provide conducting film and enhance the electron emission from the sample surface. Figure 3.35b shows the examples of the SEM samples. The specimen was then placed into the vacuum chamber of the scanning electron microscope at accelerating voltage 10 kV and resolution 5 to allow effective examination. A variety of magnifications were used. Three types of scanning electron microscopes, as shown in Figure 3.36, were used throughout the project, i.e. (i) CAMSCAN SEM, (ii) Joel JSM6400 SEM and (iii) Inspect F Philip FEG-SEM. The selection on the microscope depends on the type of sample, holder and magnification used for imaging process and also the availability of the machine.

(a) (b)

Figure 3.35: (a) Sputter Coater Unit EMSCOPE SC500 A and (b) Examples of SEM samples.

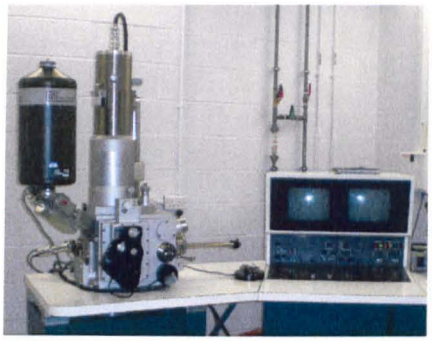

(a)

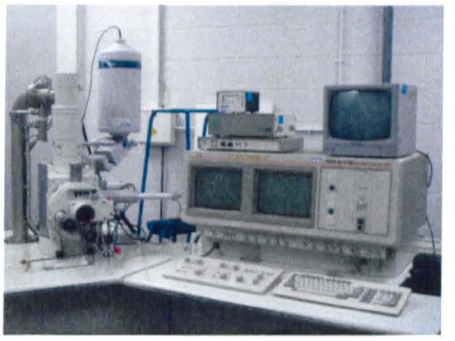

(b)

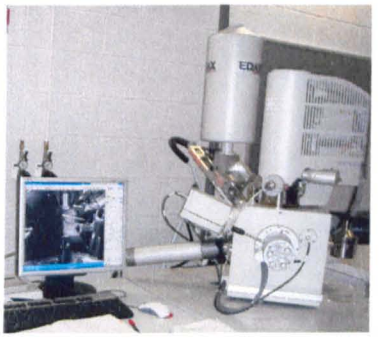

(c)

Figure 3.36: Scanning Electron Microscopy; (a) CAMSCAN, (b) Joel JSM6400 and (c) Inspect F.

3.8 Concluding remarks

This chapter describes the experimental procedures that were used to collect the data. The nanomodified-resins were developed based on nanosilica, CNT and nanoclay. The performance of these systems was evaluated through physical, thermal and mechanical testing. The best resins were selected, based on their performance, for the fabrication of nanomodified-CFRP composite using a wet lay-up technique. The laminates were tested in compression and in-plane shear to study their properties compared to the neat system. The quality of the laminates was evaluated based on fibre volume fraction and fibre misalignment. Finally the post failure analysis was conducted using optical microscopy and SEM techniques to study the fracture mechanisms involved during mechanical testing. The data produced from the physical, thermal and mechanical testing and post failure analysis of neat and nanomodified epoxy polymers are presented in Chapters 4 and 5. The effect of nanofillers on the mechanical properties of CFRP composites is reported in Chapter 6.

Chapter 4

Characterisation of neat epoxy polymers

4.1 Summary

Neat Epikote 828 and Cycom 977-20 epoxy polymers were characterised using several types of testing for reference. The thermal properties of these pure systems were investigated using TGA, TMA and DSC. The results of mean and differential coefficient of linear thermal expansions (CTE), thermal strain, glass transition temperature (Tg) and thermal stability of the materials are presented. The mechanical performance of the neat resins was determined using compression, tensile, flexural and fracture toughness tests. Mechanical properties, such as elastic modulus, strength, failure strain, yield strength and toughness, are reported. All results are discussed in the following sections.

4.2 Pure Epikote 828 polymer

4.2.1 Density and constituent volume fraction

The measured density of neat Epikote 828 epoxy polymer using a density balance equipment was 1.2210 ± 0.0001 g/cm^3.

The thermal stability of pure Epikote 828 was studied using TGA technique outlined in Section 3.5.3. This information is important for the evaluation of nanofiller and carbon fibre contents in the following chapters. Figure 4.1 shows that the Epikote 828 starts to degrade at about 250°C and ends at about 680°C. This TGA profile can be divided into four different stages. These four decomposition mechanisms were marked A, B, C and D in Figure 4.1. Stage A shows that the initial weight loss of 0.1 wt% occurred due to moisture content or water vaporization. Stage B represents

decomposition of the resin in nitrogen. The weight loss gradually increased from 380°C to 550°C with a total mass loss of 81.4 wt%. After holding at 550°C for 1 hr, the purge gas flowing over the sample was automatically switched to oxygen. The resin residue was burnt off starting from 565°C and finished at 680°C with a mass loss of 18.5 wt%, see Stage C. The maximum degradation temperature of 440°C and 615°C of the epoxy resin and its residues, respectively, was identified by the peak of the rate of weight loss versus sample temperature curve (see Figure 4.1(i) and (ii)). Stage D shows that there is no material remaining behind after exposing the resin residue to oxygen. This suggests no contamination of the resin.

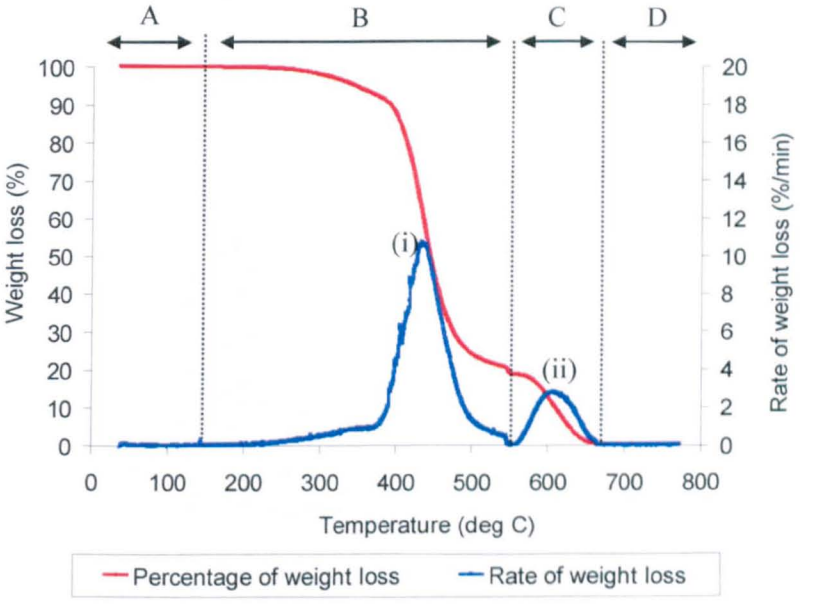

Figure 4.1: A typical TGA profile showing thermal degradation of pure Epikote 828 polymer. The heating program consists of heating from 25°C to 550°C in N_2 and then kept at 550°C for 1 hr, followed by heating to 800°C in air. An isothermal temperature of 550°C is applied to achieve a constant residual weight of the epoxy.

The thermal degradation behaviour of the resin was also studied by burning in air (see Figure 4.2a) and nitrogen (see Figure 4.2b). By exposing to air, the maximum degradation temperature for epoxy resin occurred at 421°C, which was about 20°C lower than that of burning in nitrogen as shown in Figure 4.1, with a total mass loss of 73.3 wt% and for the resin residue occurred at 610°C with a total mass loss of 26.6 wt%. It can be seen that the mixture of epoxy and its residue occurred at a temperature of 530-550°C. This contributes to a higher amount of resin residue when burning the epoxy

in air (see Figure 4.1) compared to that of burning in Nitrogen (see Figure 4.2a). This is the reason why the isothermal temperature of 550°C was employed in this study. A constant residual weight of the epoxy was achieved by burning it in nitrogen from 25°C to 550°C and keeping the temperature at 550°C for 1 hr. Therefore the actual amount of epoxy and resin residue can be calculated.

The amount of resin residue obtained in Figure 4.1 was confirmed by heating the resin in N_2 from 25°C to 800°C. The TGA result shows almost constant residual weight of about 18 wt% between 600-700°C, see Figure 4.2b. This is similar to that obtained in Figure 4.1. Three samples have been tested for each condition. Table 4.1 shows the summary of the TGA results.

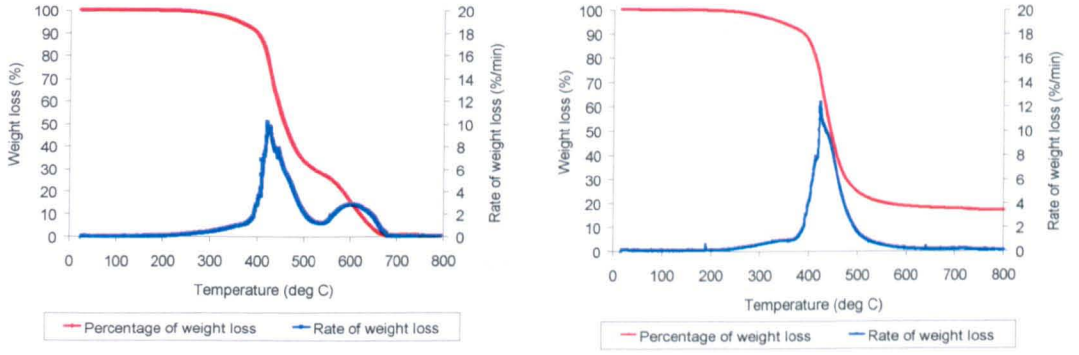

Figure 4.2: Typical TGA profiles showing thermal decomposition of pure Epikote 828 polymer in two different conditions: (a) burn in air from 25°C to 800°C and (b) burn in nitrogen from 25°C to 800°C.

Table 4.1: Constituent content and degradation temperature of Epikote 828 resin based on TGA results.

Heating program	**Weight fraction (wt%)**		**maximum degradation temperature (°C)**	
	Epoxy resin	**Resin residue**	**Epoxy resin**	**Resin residue**
Heating from 25°C to 550°C in N_2 and then kept at 550°C for 1 hr, followed by heating to 800°C in air	81.33 ± 0.17	18.29 ± 0.15	438.61 ± 2.20	609.67 ± 4.02
Burn in air from 25°C to 800°C	73.02 ± 0.59	26.83 ± 0.64	424.34 ± 1.81	605.69 ± 2.09
Burn in nitrogen from 25°C to 800°C	81.60 ± 0.25	18.32 ± 0.23	430.17 ± 3.90	-

4.2.2 Dimensional stability and glass transition temperature

The thermal response of cured resins is measured using the TMA expansion probe. As the sample expands during heating or contracts during cooling, the probe is moved up or down and the resulting expansion or contraction of the sample is measured. Figure 4.3 displays a typical TMA result of a cured pure Epikote 828 sample, which was tested using a two heating cycle program (as shown in Figure 3.14a, Section 3.5.5). The coefficient of thermal expansion (CTE) and glass transition temperature (Tg) were determined based the 2nd heating cycle curve.

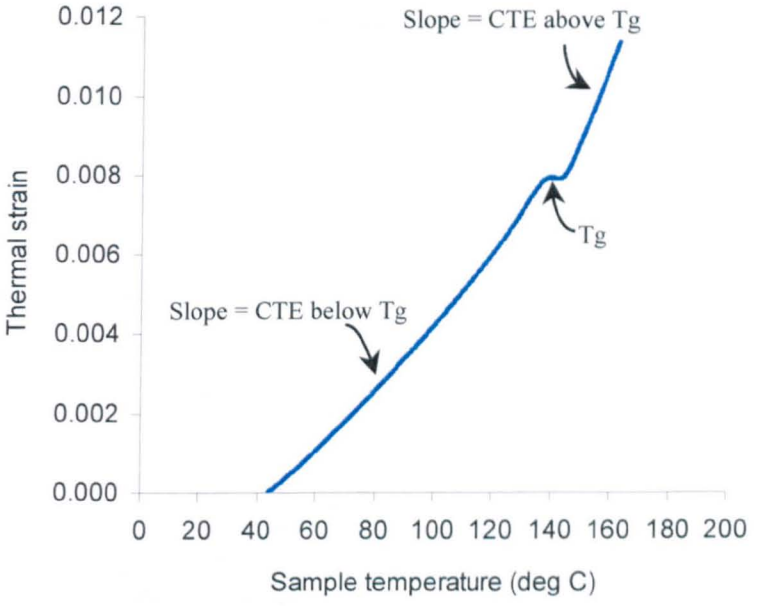

Figure 4.3: A typical TMA result of pure Epikote 828 polymer, which was heated from 25°C to 180°C at 5°C/min in Argon.

CTE is defined as the fractional increase in length per unit rise in temperature [151]. There are two different coefficients of thermal expansion that can be determined from the TMA thermal response [151]; (a) the mean coefficient of linear thermal expansion and (b) the differential coefficient of linear thermal expansion. The mean CTE is calculated using the following expression:

$$\overline{\alpha} = \frac{\Delta L}{\Delta T} \times \frac{1}{L_0} \tag{4.1}$$

where ΔL is the change in length of the test specimen between two temperatures T_1 and T_2, L_0 is the reference length of the test specimen at room temperature, and ΔT is the change in temperature equal to T_1- T_2. The differential CTE can be defined as:

$$\alpha = \frac{(dL)_p}{(dT)_p} \times \frac{1}{L_0} = \frac{(dL/dt)_p}{(dT/dt)_p} \times \frac{1}{L_0} \tag{4.2}$$

where L_0 is the reference length at room temperature, L is the length at temperature T, dL is the change in length over the time interval dt at a constant pressure p, and dT is the change in temperature over the time interval dt at constant pressure p. In this study, Pyris-series Diamond TMA software was used to analyse all TMA results. This software was used to determine both mean and differential CTE. Figure 4.4 shows an example of thermal analysis of Pure Epikote 828 polymer sample.

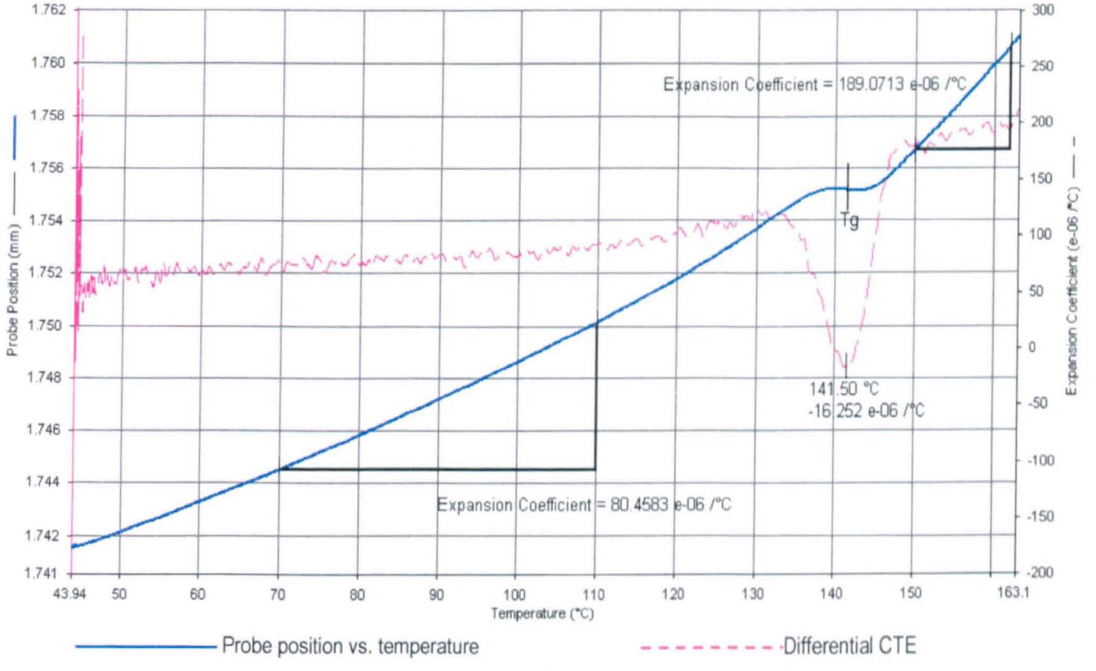

Figure 4.4: A typical TMA result of pure Epikote 828 polymer, which was analysed using Pyris-series Diamond TMA software.

The differential CTE curve in Figure 4.4 shows an increasing CTE value from 25°C to 138°C with a mean CTE value of 80.46 με/°C. At the glass transition event, from 138 to 145°C, the expansion of the material is no longer proportional to the heating temperature. Therefore, the epoxy matrix exhibits a significant change in slope due to an increase in its rate of expansion. The temperature of this change in expansion

behavior is the Tg of the resin which occurs at 141.5 °C, see Figure 4.4. Above Tg, the materials expand at more than twice the rate of expansion before Tg, due to a lowering of the elastic modulus of the material. The CTE increases from 145 to 180 °C with a mean CTE value of 189.07 με/°C. Three samples were tested for the pure Epikote 828 polymer. The mean CTE below Tg was measured from the initial linear slope of the TMA curve at temperature between 70 to 110°C while the CTE above Tg was measured from the second linear slope of the curve between 150-180°C. The average CTE below Tg was 79.78 ± 0.47 με/°C and CTE above Tg was 187.76 ± 3.59 με/°C while the average Tg was 139.52 ± 1.02 °C.

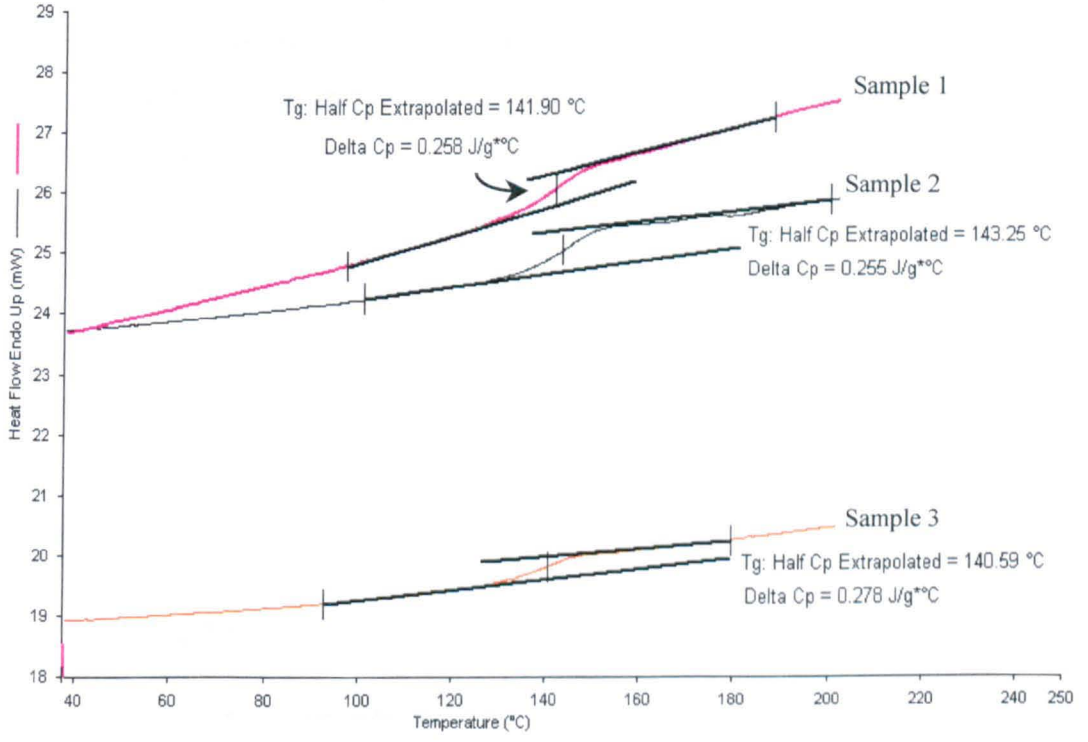

Figure 4.5: DSC results of pure Epikote 828 polymer, which were analysed using Pyris-series DSC 7 software.

Glass transition temperature is one of the most important characteristics for polymeric materials. Tg is often used to determine the upper use temperature of the polymer or composite since the matrix stiffness decreases above Tg and the matrix no longer functions effectively to transfer load. In addition to TMA, DSC was also conducted to determine the Tg of the pure Epikote 828 polymer. DSC is used because the heat capacity of a composite material changes at the glass transition. It is marked as

a shift in the heat flow versus temperature curve as shown in Figure 4.5. From the analysis using Pyris-series DSC 7 software on three samples as shown in Figure 4.5, the average Tg for pure Epikote 828 polymer is 141.91 ± 0.77 °C. This value is close to that obtained using TMA.

4.2.3 Compressive properties

The change in cross-sectional area is significant when calculating stress of polymer material loaded in compression. The stress was calculated using the current cross-sectional area (true stress) instead of the initial cross-sectional area (engineering stress). The true and engineering compressive stress-strain curves were compared in Figure 4.6. The cross sectional area of the specimen increases with the compressive strain and therefore the true stress-strain curve plot shows lower values than the engineering curve as shown in Figure 4.6.

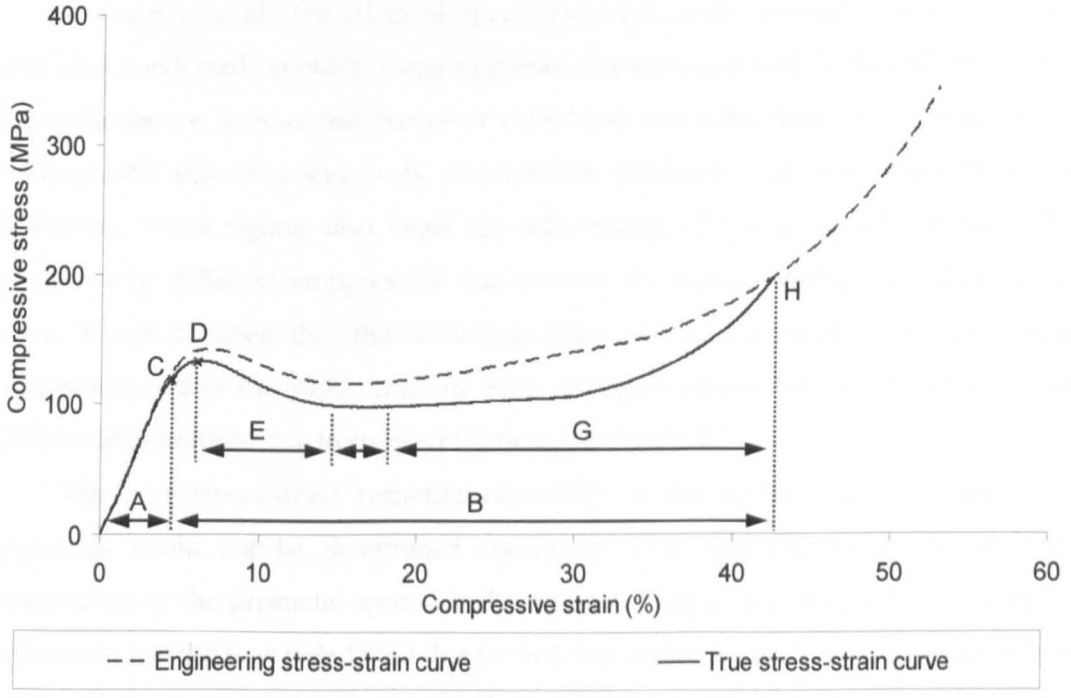

Figure 4.6: Typical engineering and true stress-strain curves of a cylindrical specimen of pure Epikote 828 loaded in static uniaxial compression. A, B, C, D, E, F, G and H are the elastic region, plastic region, elastic limit, yield point, plastic strain softening region, plateau region, plastic strain hardening region and ultimate stress, respectively.

The true stress-strain curve, as illustrated in Figure 4.6, shows that epoxy undergoes elastic (region A) and plastic (region B) behaviour before rupture. The stress initially increases proportionally to the strain, obeying Hooke's law, until it reaches an elastic limit (point C). The compressive modulus of the epoxy was calculated at 1% to 3% compressive strain. With an increase in load beyond the proportional limit, the strain begins to increase more rapidly for each increment in stress until it reaches yield stress (point D) where the material deforms without an increase in the applied force. After yielding, the shortening increases with decrease in the applied load, known as the plastic softening mechanism (region E), until the graph plateaus (strain increases with no noticeable increase in the compressive stress; see region F). As the material undergoes large softening strains, the cross-sectional area is continues to increase, resulting in increased resistance of the material to further deformation. Thus after region F, additional deformation requires an increase in the compressive load, known as plastic hardening mechanism (region G), until it reaches maximum load where the material rupture occurs (known as ultimate stress, point H).

In order to study the effect of specimen shape, static uniaxial compression tests were also conducted on cubic shape specimen (as recommended in ASTM D695). The true compressive stress-strain curves of cylindrical and cubic specimens are illustrated in Figures 4.7 and 4.8, respectively. At least five specimens were tested for each type of specimens. These figures also show the deformation of typical cylindrical and cubic specimens at different compressive strains over the corresponding true stress–strain curve. It can be seen that the barrelling effect of the cylindrical specimen during compression (after the yield strain or even at higher strains before the fracture) was effectively minimised due to reduced friction, see Figure 4.7.

The true stress-strain response especially in the plastic region of the cubic specimens could not be determined accurately. This was due to the non-uniform deformation of the prismatic specimen during compression, which results in a complex stress state and the materials failed due to buckling and/or shear deformation. Shear type failure mode occurred due to the ineffective height to width ratio of 2:1 for epoxy polymer. In theory, the specimen subjected to compression would get shorter and expand uniformly along its length (see Figure 4.9a). However, this could be achieved if there was zero friction between the flat ends of the specimen and the compression platens. In practice, it is difficult to completely eliminate friction. This results in barrelling formation where the ends of the specimen do not expand as much as its

central region (see Figure 4.9b). Compression tests on cylindrical specimens, Figure 4.7, developed less barrelling deformation in addition to lower stress concentration near the loading ends when compared to prismatic ones, Figure 4.8. These two effects resulted in higher failure loads for the cylindrical specimens, Figure 4.7. The prismatic specimens failed prematurely due to buckling, which was triggered by longitudinal cracking that formed at specimen's edges (sharp corners) near the loaded ends, see Figure 4.8.

The compressive properties such as elastic modulus, strength, failure strain, yield strength and strain at yield point, were determined based on ASTM standard D695. Table 4.2 shows the comparison between the compressive properties of cylindrical and cubic specimens. It was found that both have a similar Young's modulus, however, the measured compressive strength and failure strain of the cube type specimens were significantly lower than those of the cylindrical specimens, Table 4.2. This is due to the high localised stresses developed in the specimens during compression which leads to premature failure.

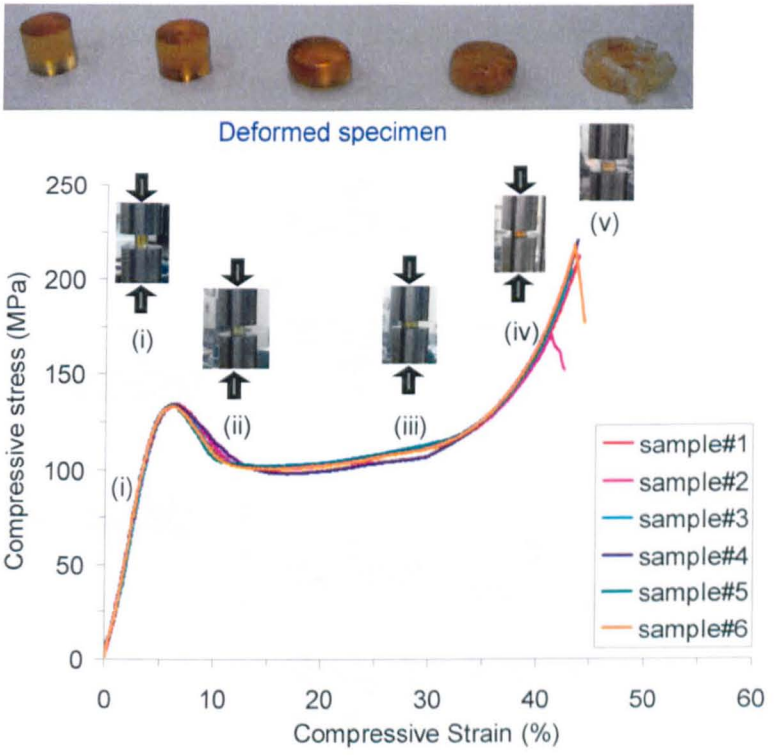

Figure 4.7: Typical true stress-strain curves of cylindrical specimens loaded in static uniaxial compression. Six specimens were tested and the compressive properties were summarised in Table 4.2. (i), (ii), (iii), (iv) and (v) show the deformation of a typical specimen in between the compression rods at different compressive strains.

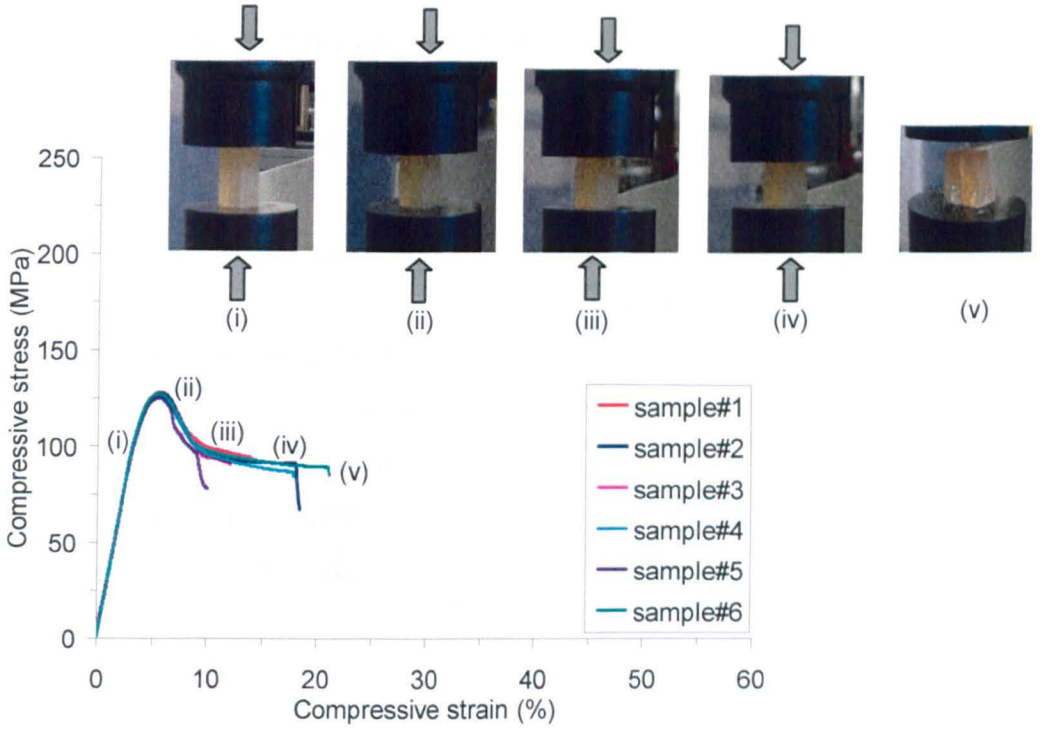

Figure 4.8: Typical true stress-strain curves of cubic specimens loaded in static uniaxial compression. (i), (ii), (iii), (iv) and (v) show the deformation of a typical specimen at different compressive strains.

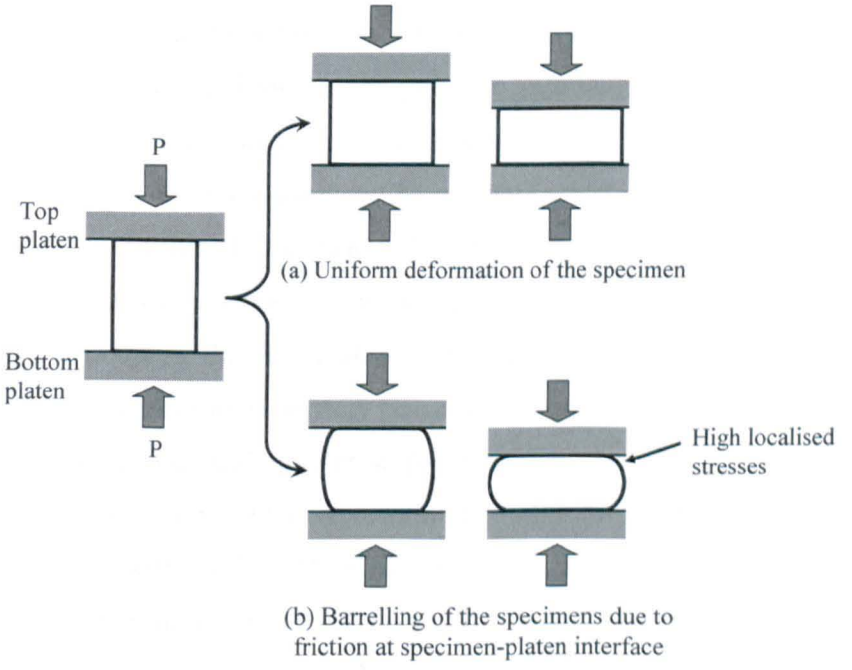

Figure 4.9: Schematic diagram of epoxy polymer specimen loaded in compression showing (a) uniform and (b) non-uniform deformations; high localised stresses can develop leading to early damage and hence premature failure.

Table 4.2: A summary of compressive properties of pure Epikote 828 polymer showing the effect of specimen shape; Cylindrical specimen of 10 mm diameter x 10 mm length and cubic specimen of 12.5 mm width x 12.5 mm thickness x 25.4 mm length.

Compressive property	Specimen type	
	Cylindrical	Cubic
Compressive modulus, E (GPa)	3.02 ± 0.06	3.12 ± 0.02
Compressive stress at yield, σ_y (MPa)	132.99 ± 0.20	126.59 ± 0.39
Compressive strain at yield point, ε_y (%)	6.50 ± 0.05	5.53 ± 0.03
Compressive strength, σ_u (MPa)	211.47 ± 3.17	126.59 ± 0.39
Compressive strain at break, ε_f (%)	42.66 ± 0.65	16.49 ± 1.56

4.2.4 Tensile properties

Figure 4.10 shows the stress-strain diagram of pure Epikote 828 polymer loaded in tension. All tested specimens were adhered with GFRP composite end-tabs to prevent failure at the grips as shown in Figure 4.10(ii). Epoxy polymers are classified as brittle material because these materials usually fail in tension at relatively low values of strain. Figure 4.10 shows that the Epikote 828 polymer fails with small elongation (of about 3% average failure strain) after the proportional limit (point A) is exceeded and the fracture stress (point B) is the same as the ultimate stress. The diagram begins with a straight line where in this elastic region, the stress and strain are directly proportional. The tensile modulus of the material was measured from the slope of 0.1 to 0.25% tensile strain. Beyond point A, the deformation of the materials becomes permanent and the strain begins to increase more rapidly for each increment in stress. The stress-strain curve then has a smaller and smaller slope until it reaches point B then the material ruptures. The tensile properties were determined based on Figure 4.10 using equations given in British standard 527-1. The elastic modulus, tensile strength and failure strain of pure Epikote 828 polymer were 2.75 ± 0.02 GPa, 70.84 ± 1.08 MPa and 3.28 ± 0.08%, respectively.

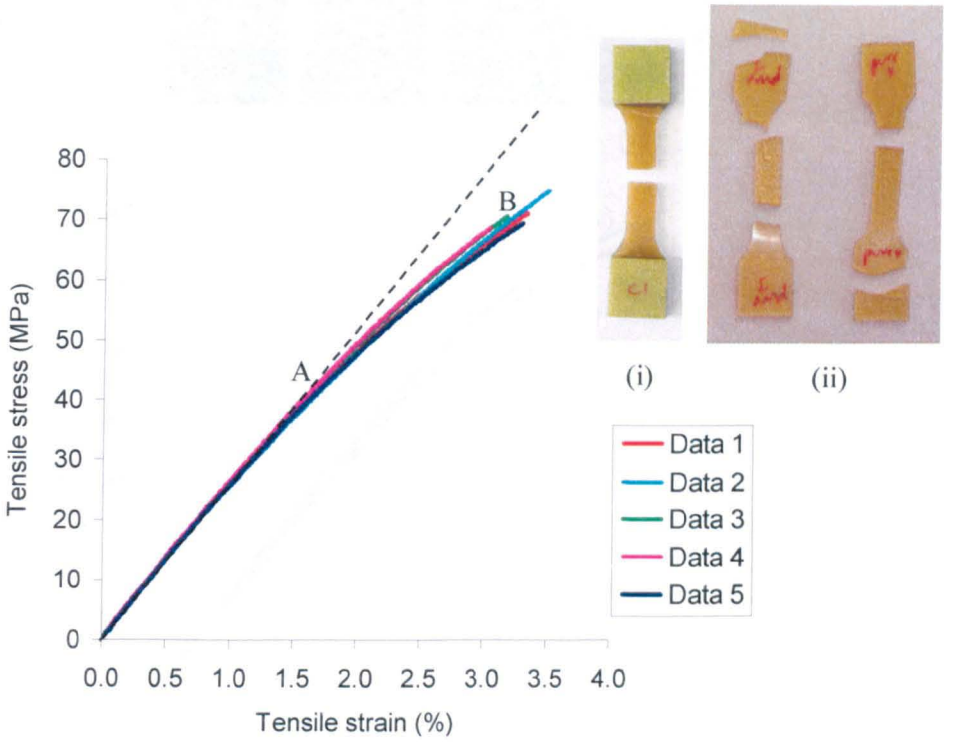

Figure 4.10: Stress-strain curves of five dogbone shape specimens loaded in tension. All tested samples were adhered with GFRP composite end-tabs to prevent failure at grips. (i) and (ii) show examples of broken specimens; with tabs the specimen fails at gauge length and without tabs the specimen fails at grip.

4.2.5 Flexural properties

Figure 4.11 shows the flexural stress-strain curves of pure Epikote 828 polymer. These curves provide useful information on flexural modulus, ultimate strength and strain at failure. These properties were determined using the technique described in British standard 178:2003. Five specimens were tested and the average flexural modulus, flexural strength and failure strain of pure Epikote 828 polymer were 2.88 ± 0.03 GPa, 117.73 ± 8.70 MPa and 4.84 ± 0.61%, respectively. Figure 4.11 shows that the stress initially increases proportionally to the strain, obeying Hooke's law, until it reaches the proportional limit at about 3.5% flexural strain (see point A). The bending stiffness of the epoxy was calculated based on the slope at 0.1 to 0.25% strain. Beyond proportional limit, the strain begins to increase more rapidly for each increment in stress until failure at point B.

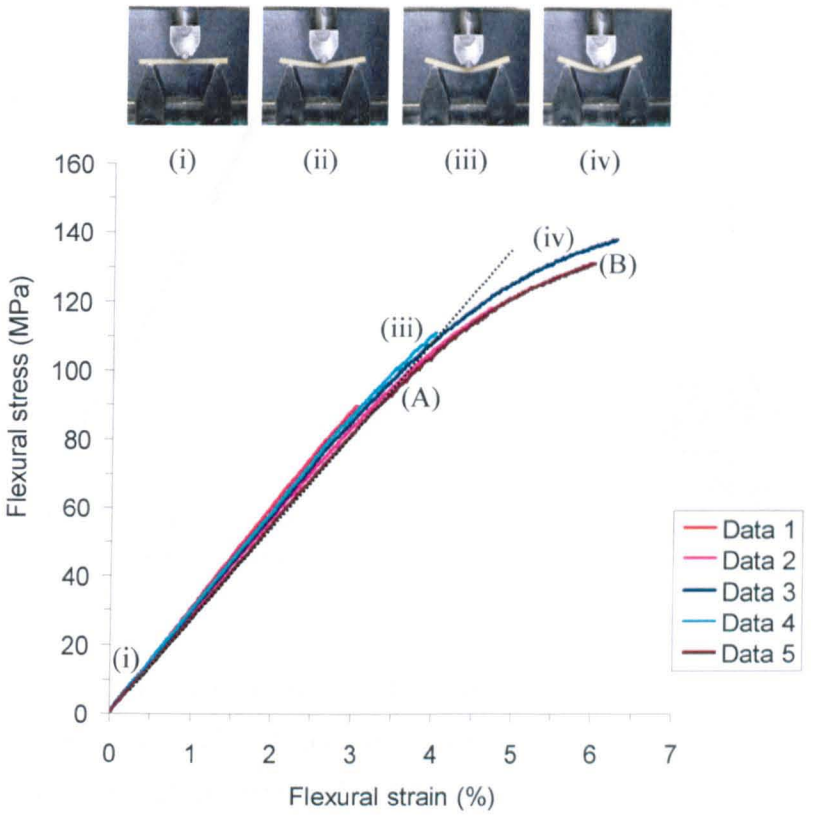

Figure 4.11: Flexural stress-strain response of five samples tested using a three-point bending test fixture. (i), (ii), (iii) and (iv) show the deflection of a typical specimen at different flexural strains.

4.2.6 Fracture toughness properties

Figure 4.12a shows typical force-crack opening displacement curves of compact tension (CT) specimens tested at 10 mm/min crosshead speed. The curves are essentially straight lines with failure occurring before any yielding or plastic deformation takes place. In other words, the material fails in a brittle manner. The average of load at crack growth initiation was 217.35 ± 7.43 N. The fracture toughness test was also conducted on the single-edge-notch bending specimen (SENB) for comparison purposes. The load was applied at 1 mm/min crosshead speed due to a small crack area and the corresponding typical force-crack opening displacement curves were illustrated in Figure 4.13a. The average load at crack growth initiation was 32.39 ± 4.48 N. Figures 4.12b and 4.13b show the examples of fractured specimens after fracture toughness tests.

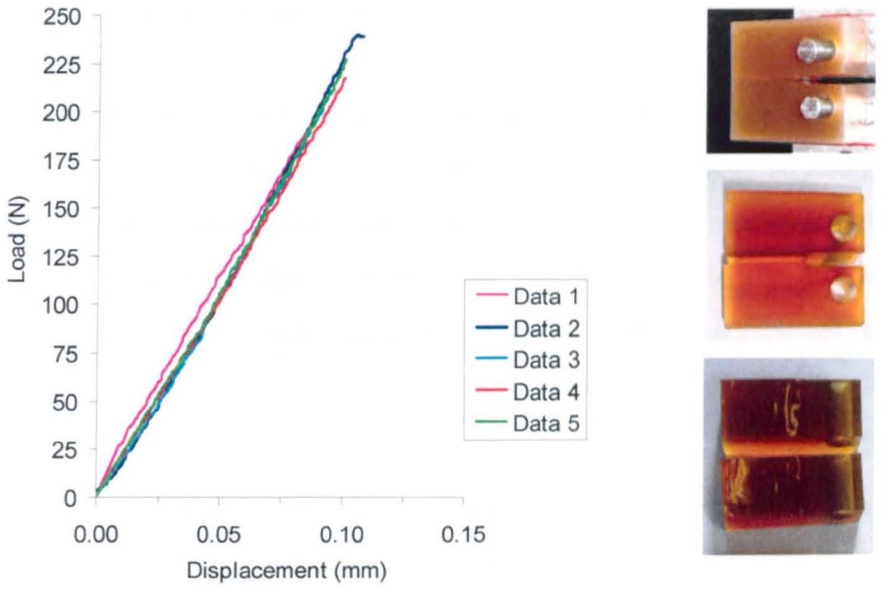

(a) (b)

Figure 4.12: (a) Typical load – displacement curves of compact tension specimens pulled at 10 mm/min strain rate for the measurement of fracture toughness of pure Epikote 828 polymer and (b) examples of broken specimens.

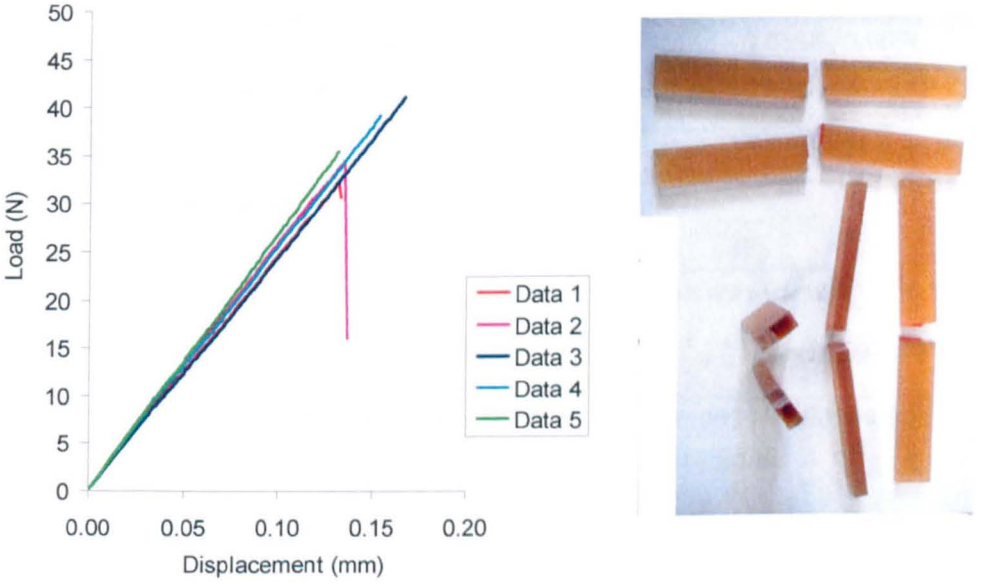

(a) (b)

Figure 4.13: (a) Typical load – displacement curves of single end notch bending specimens loaded at 1 mm/min strain rate for the measurement of fracture toughness of pure Epikote 828 polymer and (b) examples of broken specimens.

Table 4.3 shows the summary of the critical energy release rate G_{IC} and critical stress intensity factor K_{IC} of CT and SENB specimens, which were calculated based on British standard 13586. Table 4.3 shows that the SENB samples, test at 1 mm/min, have higher G_{IC} and K_{IC} compared to those of the CT specimens test at 10 mm/min. For CT specimens, an instantaneous and catastrophic failure occurred at a very high strain rate therefore the number of data collected were less compared to those collected using SENB specimens where 1 mm/min strain rate allowed an extra time for the failure to occur.

Table 4.3: A summary of critical energy release rate G_{IC} and critical stress intensity factor K_{IC} of pure Epikote 828 polymer for CT and SENB specimens.

Fracture toughness	**Specimen type**	
	CT	**SENB**
Critical stress intensity factor, K_{IC} (MPa.$\sqrt{\text{m}}$)	0.67 ± 0.02	0.84 ± 0.17
	Calculation: $K_{1C} = f(a/w)\frac{F_Q}{h\sqrt{w}}$ $= (6.39)\frac{217.35}{0.0129\sqrt{0.0255}}$ $= 0.67$ MPa.$\sqrt{\text{m}}$	Calculation: $K_{1C} = f(a/w)\frac{F_Q}{h\sqrt{w}}$ $= (9.64)\frac{32.39}{0.0038\sqrt{0.0096}}$ $= 0.84$ MPa.$\sqrt{\text{m}}$
Critical energy release rate, G_{IC} (J/m^2)	152.73 ± 10.84	244.50 ± 41.90
	Calculation: $G_{1C} = \frac{W_B}{h \times w \times \phi(a/w)}$ $= \frac{\left(\frac{1}{2} \times 217.35 \times 0.098 \times 10^{-3}\right)}{0.0129 \times 0.0255 \times 0.213}$ $= 152$ J/m^2	Calculation: $G_{1C} = \frac{W_B}{h \times w \times \phi(a/w)}$ $= \frac{\left(\frac{1}{2} \times 32.39 \times 0.146 \times 10^{-3}\right)}{0.0038 \times 0.0096 \times 0.265}$ $= 244.5$ J/m^2

4.3 Pure Cycom 977-20 polymer

4.3.1 Density and constituent volume fraction

The measured density of neat Cycom 977-20 epoxy polymer using a density balance was 1.2970 ± 0.0002 g/cm^3.

The thermal stability of Cycom 977-20 was studied using the TGA heating program provided in Section 3.5.3. The heating program consists of heating the specimen from 25°C to 550°C in N_2 and then kept at 550°C for 1 hr, followed by heating to 800°C in air. The isothermal temperature of 550°C was applied to achieve a constant residual weight of the epoxy. Figure 4.14 shows the TGA profile result. The thermal degradation of Cycom 977-20 starts at about 340°C and ends at about 770°C. The thermal degradation temperature of this system is higher than that of the Epikote 828 system therefore, this system is used for high-end applications such as aerospace components.

The TGA profile can be divided into four different stages, which were marked as A, B, C and D in Figure 4.14. Stage A shows that the initial weight loss of about 0.05 wt% occurred due to moisture content. Stage B represents decomposition of the resin in nitrogen. The weight loss gradually increased from 390°C to 550°C with a total mass loss of about 70 wt%. After holding at 550°C for 1 hr, the purge gas flowing over the sample was automatically switched to oxygen. The resin residue was burnt off started from 570°C and ended at 770°C with a mass loss of about 29 wt%, see Stage C. The maximum degradation temperature of 430°C and 646°C of the epoxy resin and its residues, respectively, was identified by the peak of the rate of weight loss versus sample temperature curve (see Figure 4.1(i) and (ii)). Stage D shows that there is no material remained behind after exposing the resin residue to oxygen suggested no contamination of the resin.

In addition, the resin was heated in N_2 from 25°C to 800°C to confirm the amount of resin residue obtained in Stage C of Figure 4.14. The TGA result shows almost constant residual weight of about 27 wt% between 550-650°C, see Figure 4.15. This confirms the result obtain in Figure 4.14. Three samples were tested for each condition and the average values were presented in Table 4.4.

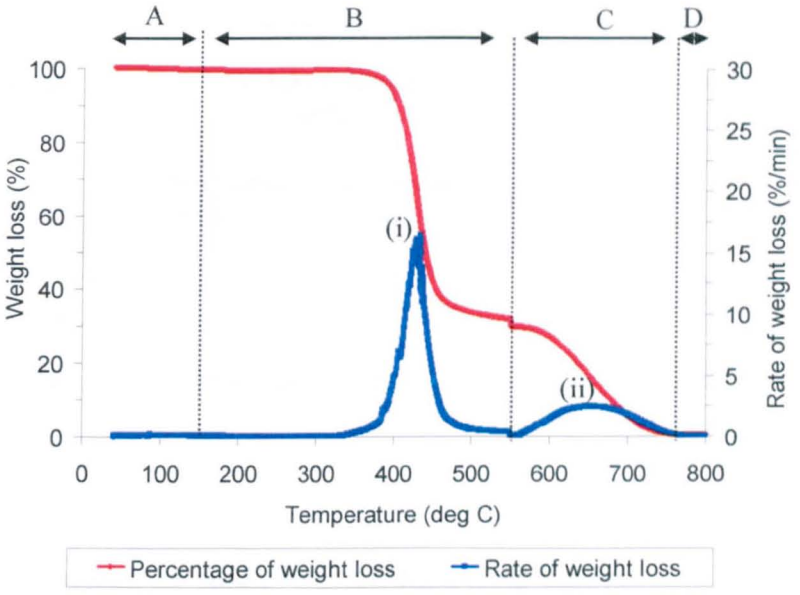

Figure 4.14: A typical TGA profile showing thermal degradation of Cycom 977-20 polymer. The heating program consists of heating from 25°C to 550°C in N_2 and then kept at 550°C for 1 hr, followed by heating to 800°C in air.

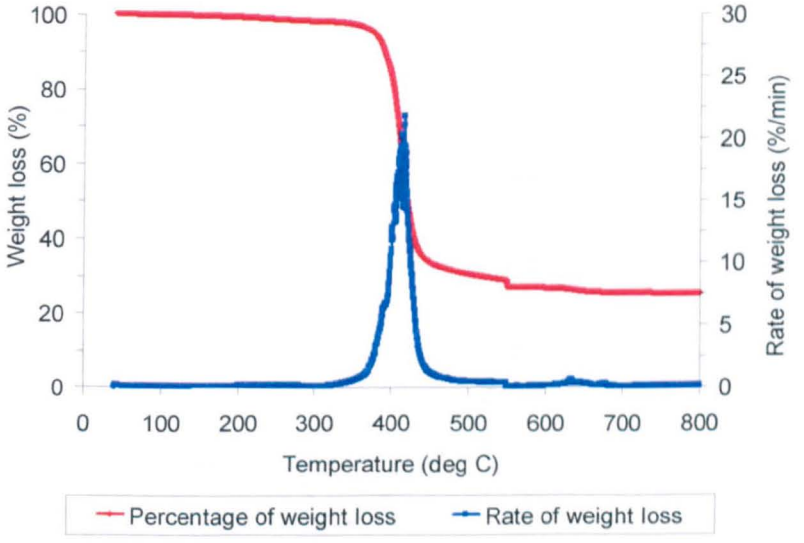

Figure 4.15: A typical TGA result showing thermal decomposition of pure Cycom 977-20, which was burnt in nitrogen from room temperature to 800°C.

Table 4.4: Constituent content and degradation temperature of Cycom 977-20 resin based on TGA results.

Heating program	Weight fraction (wt%)		maximum degradation temperature (°C)	
	Epoxy resin	Resin residue	Epoxy resin	Resin residue
Heating from 25°C to 550°C in N_2 and then kept at 550°C for 1 hr, followed by heating to 800°C in air	70.18 ± 1.11	29.67 ± 0.59	427.17 ± 3.71	645.80 ± 1.40
Burn in nitrogen from 25°C to 800°C	72.73 ± 0.68	27.20 ± 0.69	421.00 ± 4.93	-

4.3.2 Dimensional stability and glass transition temperature

Figure 4.16 displays a typical TMA result of cured pure Cycom 977-20 sample, which was tested using the two heating cycle program (as shown in Figure 3.14b, Section 3.5.5). The coefficient of thermal expansion (CTE) and glass transition temperature (Tg) were determined based the 2nd heating cycle curve. Mean CTE below and above Tg, differential CTE curve and Tg were determined using the Pyris-series Diamond TMA software. Figure 4.17 shows an example of thermal analysis of Pure Cycom 977-20 polymer sample.

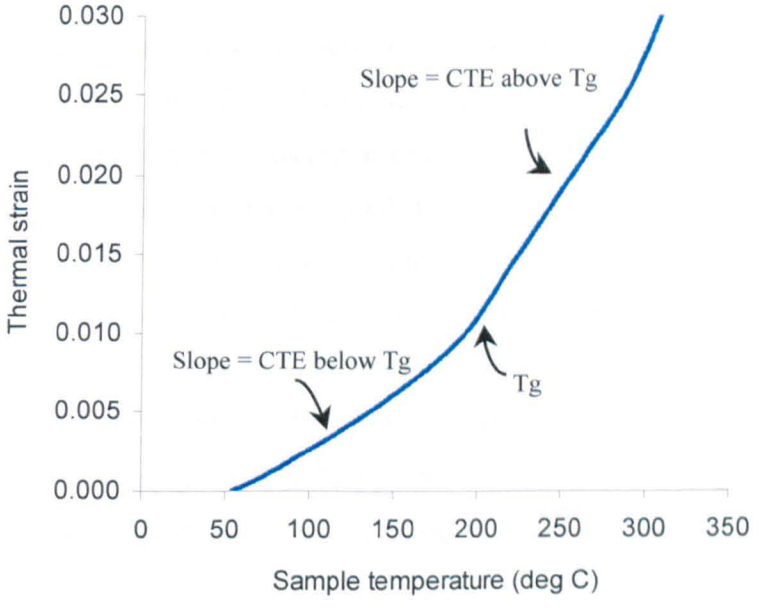

Figure 4.16: A typical TMA result of pure Epikote 828 polymer, which was heated from 25°C to 350°C at 5°C/min in Argon.

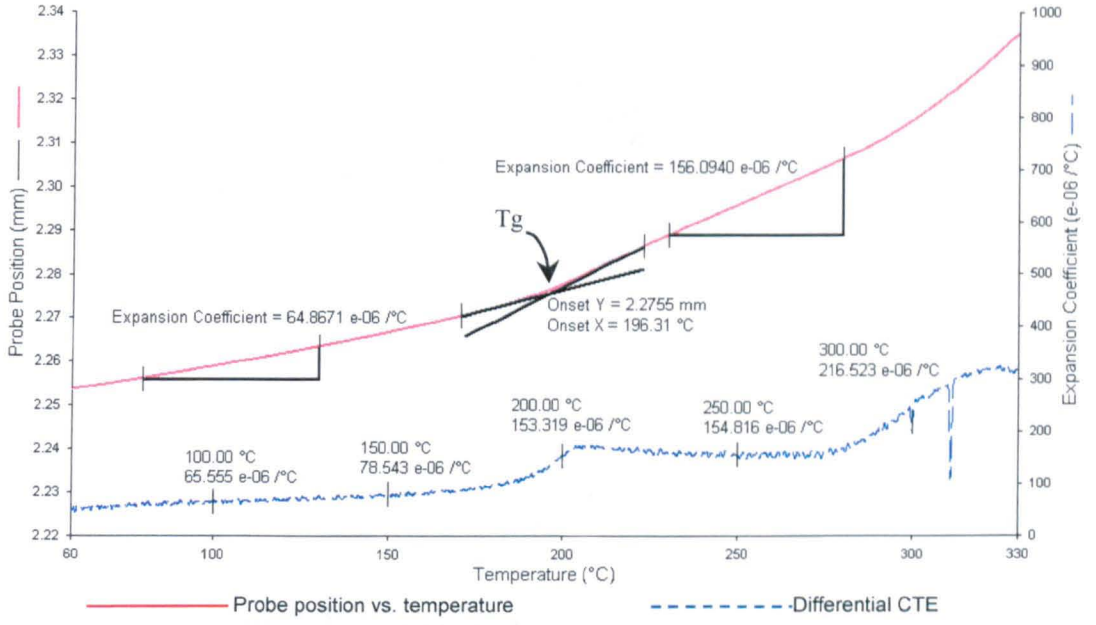

Figure 4.17: A typical TMA result of pure Cycom 977-20 polymer, which was analysed using Pyris-series Diamond TMA software.

The sample expands when it is heated. It can be seen from the differential CTE curve in Figure 4.17 that CTE value increases linearly with temperature until it reaches glass transition event where the epoxy matrix exhibits a significant change in slope due to an increase in its rate of expansion. The onset temperature of this change in expansion behavior is the Tg of the resin, which is at 196.31 °C. Above Tg, the CTE value keeps increasing with temperature and the linear CTE is more than twice as high as that of the CTE below Tg. The material starts to degrade at temperature above 300°C.

Three samples were tested for the pure Cycom 977-20 polymer. The mean CTE below Tg was measured from the initial linear slope of the TMA curve at temperature between 80 to 130°C while the CTE above Tg was measured from the second linear slope of the curve between 230-280°C. The average CTE below Tg was 64.62 ± 0.24 με/°C and CTE above Tg was 156.21 ± 1.18 με/°C while the average Tg was 200.19 ± 1.94 °C. In addition, DSC was also conducted to determine the Tg of the pure Cycom 977-20 polymer.

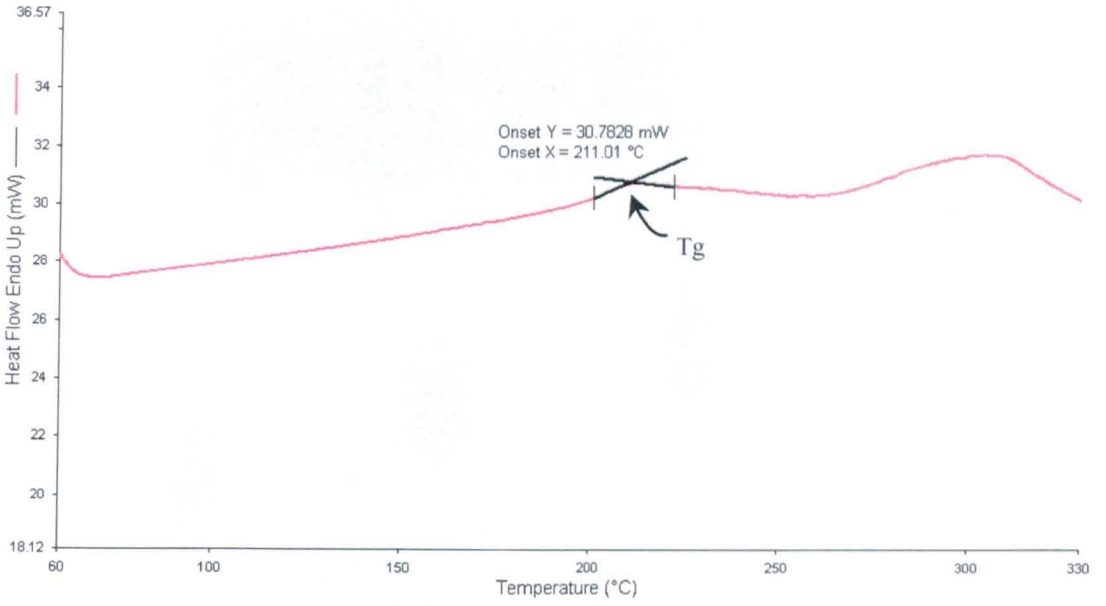

Figure 4.18: A typical DSC result of pure Cycom 977-20 analysed using a Pyris-series DSC 7 software.

Figure 4.18 shows a typical DSC result of heat flow verses sample temperature. The Tg of the sample was determined using Pyris-series DSC 7 software as shown in Figure 4.18. Three samples were tested and the average Tg for pure Cycom 977-20 polymer was 210.33 ± 0.85 °C. This value is slightly higher than that obtained using TMA because TMA is significantly more sensitive than DSC for the measurement of Tg of crosslinked polymer.

4.3.3 Compressive properties

The true and engineering compressive stress-strain curves were compared in Figure 4.19 for pure Cycom 977-20 polymer. The cross sectional area of the specimen increases with the compressive strain and therefore stress was calculated using the current cross-sectional area (true stress) instead of the initial cross-sectional area (engineering stress). The true stress-strain curve plot shows lower values than the engineering curve as shown in Figure 4.19. This true stress-strain curve was used to determine the compressive properties of epoxy polymer. Figure 4.19 also shows the deformation of a typical specimen at different compressive strains over the corresponding true stress–strain curve. It can be seen that the material deformed uniformly and barrelling effect was effectively minimised.

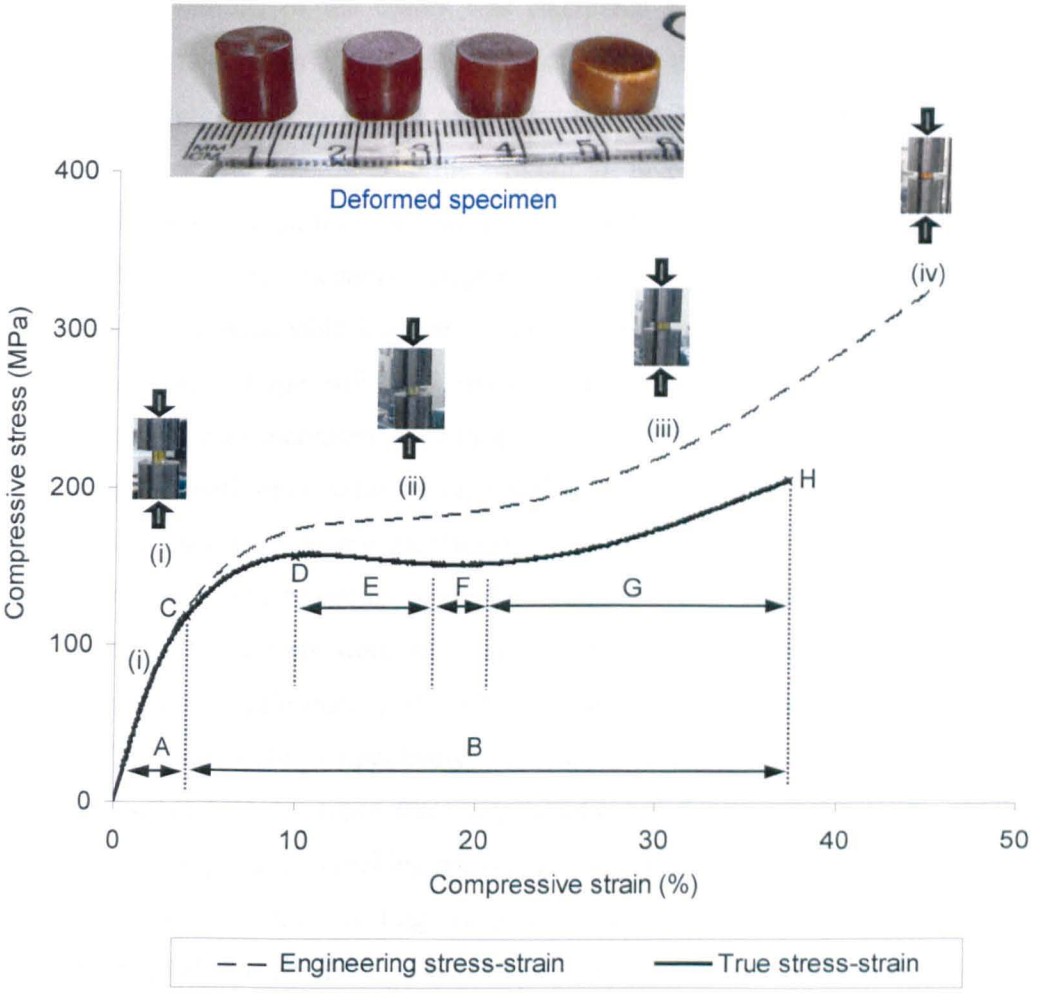

Figure 4.19: Typical engineering and true stress-strain curves of a cylindrical specimen of pure Cycom 977-20 epoxy loaded in static uniaxial compression. (i), (ii), (iii) and (iv) show the deformation of a typical specimen in between the compression rods at different compressive strains. A, B, C, D, E, F, G and H are the elastic region, plastic region, elastic limit, yield point, plastic strain softening region, plateau region, plastic strain hardening region and ultimate stress, respectively.

In tension, epoxy resin usually fails at a very low tensile strain, at about 2-3% strain at failure. However, in compression it exhibited a large plastic deformation. Pure Cycom 977-20 failed at about 38% failure strain as shown in Figure 4.19. The true compressive stress-strain curve shows that epoxy undergoes elastic (region A) and plastic (region B) behaviour before rupture. The stress initially increases proportionally to the strain, obeying Hooke's law, until it reaches an elastic limit (point C). The

compressive modulus of the epoxy was calculated based on the slope at 1 to 3% compressive strain. With an increase in load beyond the proportional limit, the strain begins to increase more rapidly for each increment in stress until it reaches yield stress (point D) where the material deforms without an increase in the applied force. After yielding, the deformation increases with a slightly decrease in the applied load, known as the plastic softening mechanism (region E), until the graph plateaus, where the strain increases with no noticeable increase in the compressive stress (see region F). As the material undergoes large softening strains, the cross-sectional area is continues to increase, resulting in increased resistance of the material to further deformation. Thus after region F, additional deformation requires an increase in the compressive load, known as the plastic hardening mechanism (region G), until it reaches maximum load where the material rupture occurs (known as ultimate stress, point H).

In addition, the tests were also conducted on cubic shape specimens. The true compressive stress-strain curves of cylindrical and cubic specimens were illustrated in Figures 4.20a and 4.20b, respectively. Five specimens were tested for each type of specimen. Figure 4.21 illustrates that the prismatic specimens failed prematurely due to barrelling and longitudinal cracking triggered at sharp corners near the loaded ends and also end crushing at high loading. High localised stresses due to the non-uniform deformations lead to early damage and hence premature failure. This is the reason why the compressive stress of cylindrical specimens was higher than that of the cubic specimens at the same compressive strain. In addition, the non-uniform deformation of the material under compression results in a complex stress state induced in the cubic specimen. Hence, the true stress-strain response especially in the plastic region cannot be determined accurately. The compressive properties such as elastic modulus, strength, failure strain, yield strength and strain at yield point, were determined based on ASTM standard D695. Table 4.5 shows the comparison between the compressive properties of cylindrical and cubic specimens. It was found that both have a similar Young's modulus, however, the measured compressive strength and failure strain of the cube type specimens were significantly lower than those of the cylindrical specimens.

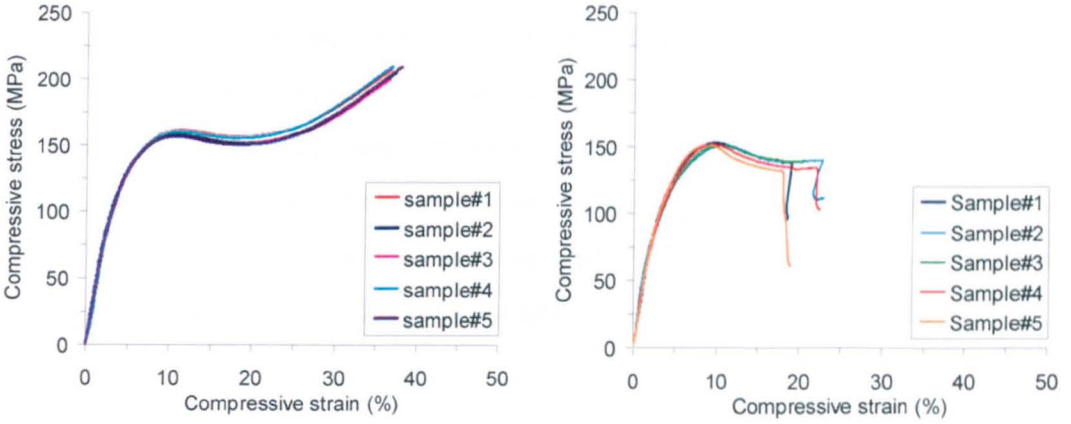

Figure 4.20: Typical true stress-strain curves of (a) cylindrical and (b) cubic specimens loaded in static uniaxial compression.

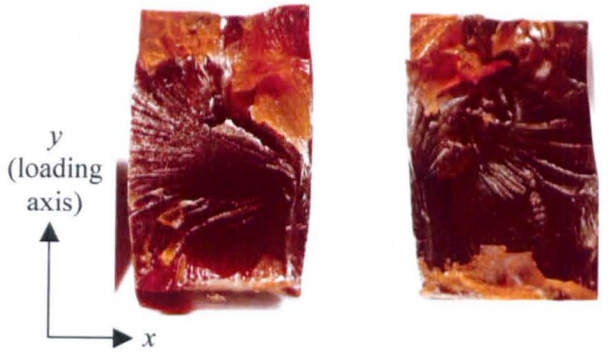

Figure 4.21: Examples of axially loaded cubic type specimens failed via barrelling and longitudinal cracking followed by end crushing at higher loading.

Table 4.5: Effect of specimen shape on compressive properties of pure Cycom 977-20 polymer.

Compressive property	**Specimen type**	
	Cylindrical	**Cubic**
Compressive modulus, E (GPa)	4.01 ± 0.05	4.00 ± 0.02
Compressive stress at yield, σ_y (MPa)	158.0 ± 0.90	151.45 ± 0.36
Compressive strain at yield point, ε_y (%)	10.96 ± 0.18	9.87 ± 0.37
Compressive strength, σ_u (MPa)	205.81 ± 1.84	151.45 ± 0.36
Compressive strain at break, ε_f (%)	37.16 ± 0.27	20.61 ± 0.88

4.3.4 Tensile properties

The stress-strain response of pure Cycom 977-20 polymer dogbone shape specimens loaded in tension is shown in Figure 4.22. The graph exhibits an initially straight portion with an average elastic modulus of 3.51 ± 0.03 GPa measured at 0.1-0.25% applied strain and followed by a continuously curved portion with a tangential modulus at failure of approximately 40% less than that of the linear part. The average failure strength was 62.60 ± 2.41 MPa and the mean failure strain was 2.27 ± 0.15%.

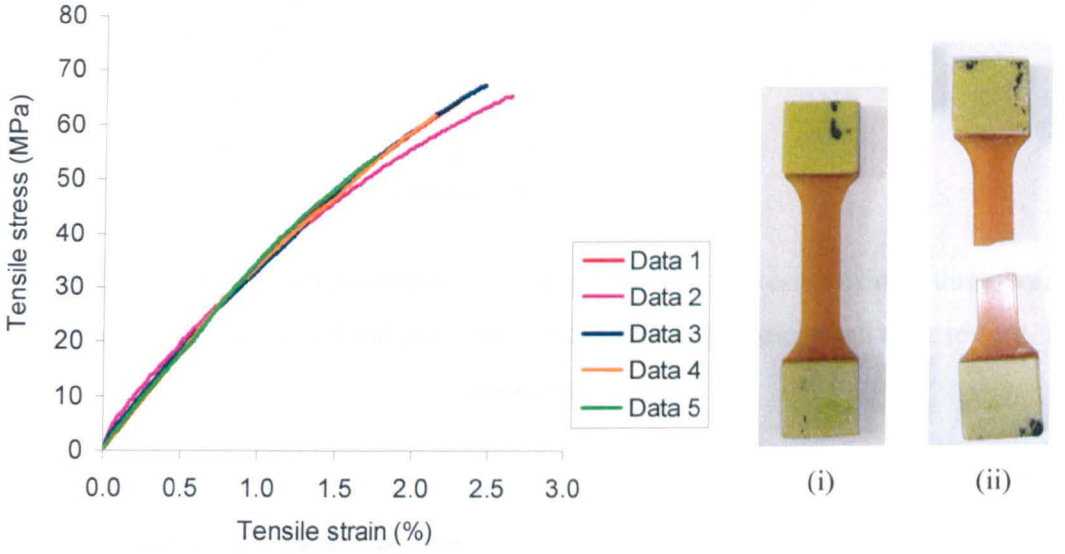

Figure 4.22: Stress-strain curves of five dogbone shape specimens loaded in tension. (i) and (ii) show typical specimens before and after testing, respectively.

4.3.5 Flexural properties

Figure 4.23 shows the flexural stress-strain curves of pure Cycom 977-20 polymer. This Figure shows that the stress initially increases proportionally to the strain until it reaches the proportional limit at about 2.5% flexural strain (see point A). Beyond this limit, the strain begins to increase more rapidly for each increment in stress until it breaks at point B. Five specimens were tested and the average flexural modulus, flexural strength and failure strain of the resin were 3.61 ± 0.03 GPa, 135.78 ± 8.81 MPa and 5.05 ± 0.60%, respectively.

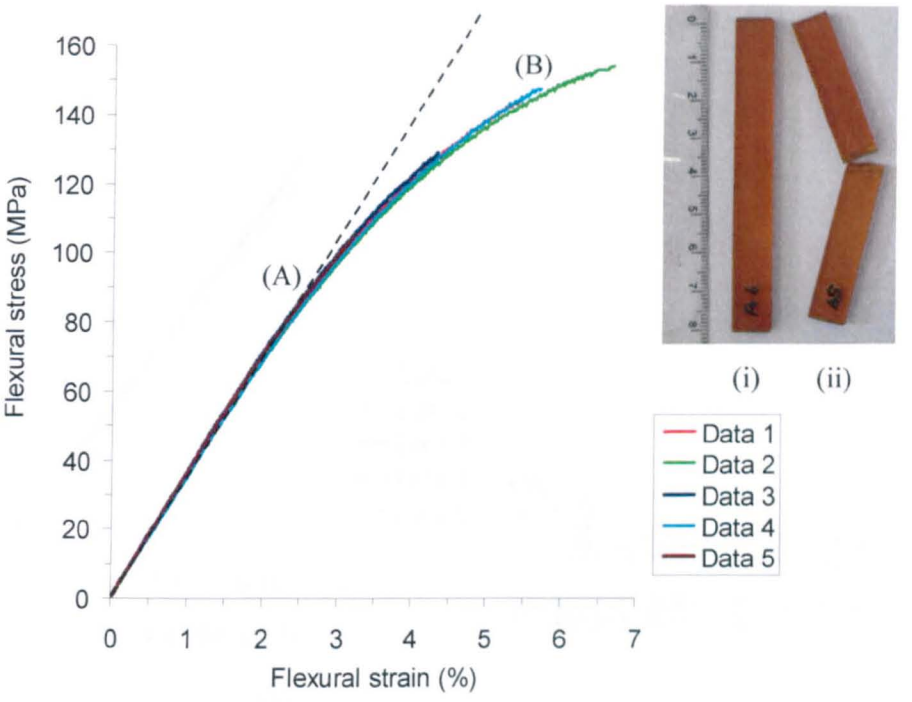

Figure 4.23: Flexural stress-strain response of five samples tested using a three-point bending test fixture. (i) and (ii) show typical specimens before and after testing, respectively.

4.3.6 Fracture toughness properties

The fracture toughness test was conducted on the single-edge-notch bending specimen (SENB). The load was applied at 1 mm/min crosshead speed, due to a small crack propagation area, and the corresponding typical force-crack opening displacement curves were illustrated in Figure 4.24a. This figure shows that the graph begins with a straight line, where the force is proportional to the displacement, until it reaches the ultimate force, where cracks start to growth and catastrophic failure occurs. The material fails before any yielding or plastic deformation takes place therefore it fails in a brittle manner. The average of load at crack growth initiation was 49.61 ± 1.59 N. The mean critical stress intensity factor K_{IC} and mean critical energy release rate G_{IC} were 1.14 ± 0.04 MPa.$\sqrt{\text{m}}$ and 373.72 ± 14.67 J/m^2, respectively. Figure 4.24b shows the example of SENB specimen before and after testing.

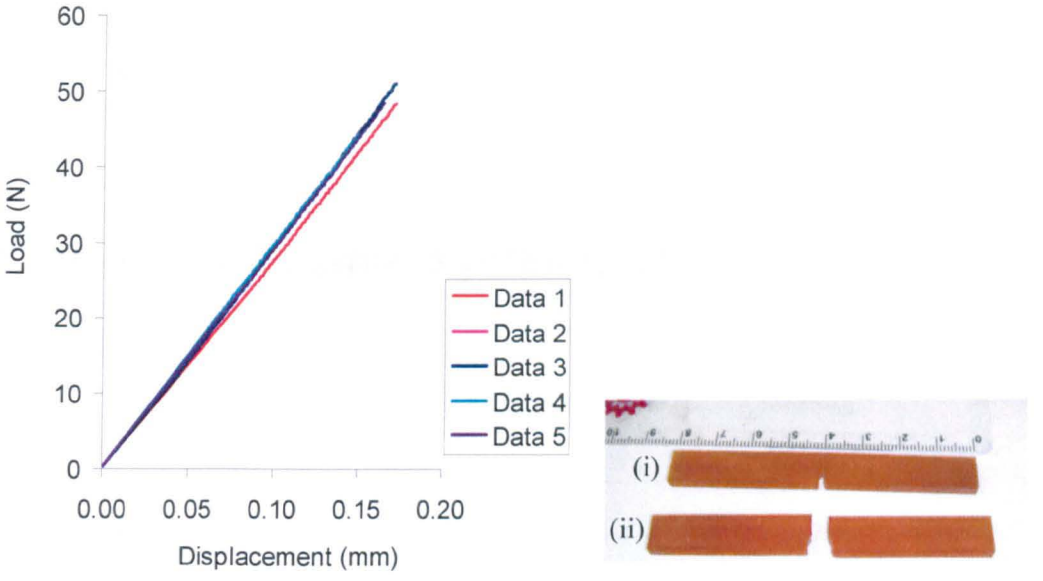

Figure 4.24: (a) Typical load – displacement curves of SENB specimens loaded at 1 mm/min strain rate for the measurement of fracture toughness of pure Cycom 977-20 polymer and (b) examples of SENB specimens (i) before and (ii) after testing.

4.4 Concluding remarks

The pure resins of Epikote 828 and Cycom 977-20 were characterised based on their physical, thermal and mechanical properties. Based on the results, the Cycom 977-20 epoxy system exhibited a better performance compared to the Epikote 828. The results of materials properties such as constituent content, CTE, Tg, elastic modulus, yield stress and strain, ultimate stress and strain, fracture toughness were described in detail. These data are used as reference for the following chapter to study the effect of nanoparticles on the physical, thermal and mechanical properties of these resin systems.

Chapter 5

Nanomodified-resins: Synthesis, characterisation and analysis

5.1 Summary

The objectives of this chapter are (1) to characterise nanomodified epoxy polymers based on their mechanical, physical and thermal properties and (2) to select the best performance of the nanomodified resins for the fabrication of the nanomodified-CFRP composites. Mechanical performance of the nanomodified polymer systems was evaluated using compression, tensile, flexural and fracture toughness tests while the thermal properties were determined using TGA, TMA and DSC. The quality of the nanocomposites, such as the degree of dispersion or exfoliation of the nanoparticles in the matrix, was evaluated using TEM. The effects of nanosilica, CNT and nanoclay on the properties of Epikote 828 were studied. In addition, the effect of nanoclay on the properties of commercial aerospace grade epoxy (Cycom 977-20) was also evaluated. All results are presented in the following sections and Appendix A.

5.2 Nanosilica-filled Epikote 828 epoxy polymer

5.2.1 Morphology

Homogeneous dispersion of nanofillers in a polymer is one of the major challenges in fabricating nanocomposites. Agglomeration of nanoparticles (usually in micrometer size clumps) often gives adverse effects on the thermal and mechanical properties of the epoxy. Hence, this does not represent the properties of a desired nanocomposite.

In this study, a uniform distribution of nanosilica in Epikote 828 was achieved. This is supported by the TEM micrographs presented in Figure 5.1. There was no

agglomeration of the SiO_2 nanoparticles even at high volume fraction (see Figure 5.1c). The spherical shape silica nanoparticles have a mean particle size of 20 nm and maximum diameter of 40 nm as observed at high magnification (see Figure 5.1b(iii)). Since the TEM slice is approximately 85 nm thick these TEM images do not reflect the actual volume fraction of nanosilica in the matrix. The volume fraction of the nanosilica was therefore measured using thermo-gravimetry analysis (TGA) that is discussed in the following section.

5.2.2 Thermogravimetry analysis and constituent volume fraction

The volume fraction of nanosilica in the epoxy was determined using TGA. Besides, TGA was also used to study the effect of nanosilica on thermal degradation behaviour of Epikote 828. Figure 5.2a illustrates percentage of weight loss and rate of weight loss as a function of sample temperature. All samples started to decompose at about 250°C. The decomposition mechanisms involved during combustion of pure Epikote 828 has been explained in the previous chapter (see Section 4.2.1). As shown in Figure 5.2a, nanocomposites exhibited similar thermal decomposition mechanisms to that of the pure epoxy. However in the last stage (Stage D), the material remaining behind after exposing the nanocomposites to air was the inert silica nanofiller. Table 5.1 summarises the average constituent weight fraction and maximum degradation temperature of the pure and nanomodified epoxy with their carbon residues. At least three specimens were tested for each system.

Table 5.1 shows that, for the 1st heating program, the pure and nanomodified resins undergo maximum thermal degradation at about 440°C and the percentage of total weight loss decreasing with increasing in the nanosilica content. After holding at 550°C for 1 hr, the nitrogen gas flowing over the sample was automatically switched to oxygen and hence, the carbon residues which were left from the combustion of the epoxy resins were burnt off with a total mass loss of about 17-20 wt%. Table 5.1 shows that the maximum degradation temperature of carbon residues (identified by the second peak of the rate of weight loss versus sample temperature curve as shown in Figure 5.2a) was increased with increasing in nanosilica content. For instance, the addition of 13 wt% nanosilica into the epoxy matrix increased the maximum degradation temperature of carbon residues by 70°C compared to the neat resin. This suggests that the nanofiller-matrix interfacial bonding is very strong and therefore a higher

temperature is needed to remove the epoxy which is stuck on the particle surface. Finally, the material remaining behind after exposing the sample to oxygen was the silica nanofiller, which the Table 5.1 shows 5.36 ± 0.03 wt%, 12.96 ± 0.08 wt% and 25.23 ± 0.33 wt% nanosilica content for the three nanomodified systems investigated in the present study.

In addition, the specimens were heated in two other conditions to study their thermal degradation behaviour and to confirm the amount of epoxy resin and silica nanofiller obtained using heating program 1 (see table 5.1). In order to confirm the weight fraction of epoxy resin, the specimens were heated from 25°C to 800°C in nitrogen. TGA profiles, as shown in Figure 5.2b, show that the residual weight at temperature 600-700°C was almost constant. The average amount of epoxy resin obtained from Heating program 2 as shown in Table 5.1 was close to that obtained using heating program 1. Figure 5.2c shows that the maximum degradation temperature of the epoxy resins and their residues occurred at lower temperature by exposing to air compared to burnt in the first condition. The amount of ash left after combustion using heating program 3 confirmed the amount of nanosilica in the epoxy which were obtained using the first heating program as shown in Table 5.1.

Table 5.2 summarises density and volume fraction of nanosilica in Epikote 828. A density of 1.22 g/cm^3 was measured for the unmodified Epikote 828. The measured density was found to increase with the nanosilica content (see Table 5.1). The increase in density is expected because the density of silica, ρ_{si} = 1.8 g/cm^3, is greater than that of the epoxy matrix. The inclusion of 25 wt% nanosilica increased the density of the epoxy for about 11%. The measured density was compared to the theoretical prediction based on the rule of mixtures. All measured densities were closed to the theoretical values. However, at high nanosilica content the measured density was slightly higher compared to the predicted value. This is due to the fact that some particle agglomeration or clusters of nanosilica rich region may occur at high filler content. These density data were used for the calculation of nanosilica volume fraction in the epoxy resin. Table 5.2 shows that for the three nanomodified systems investigated in the present study the average volume fraction of nanosilica in the epoxy resin was 3.7 vol%, 9.3 vol% and 19.1 vol%.

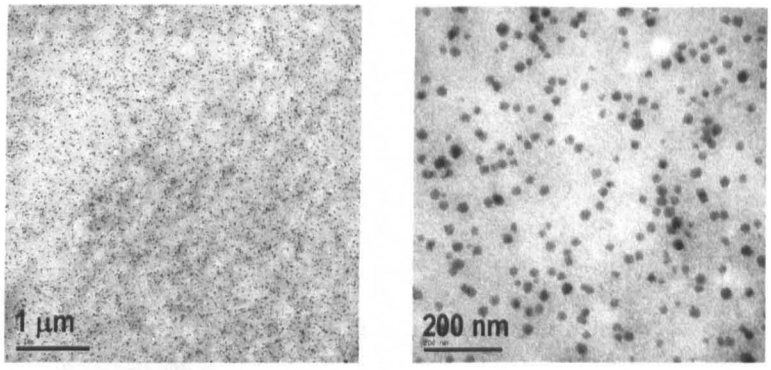

(i) 22500x (ii) 115000x

(a) 5 wt% nanosilica

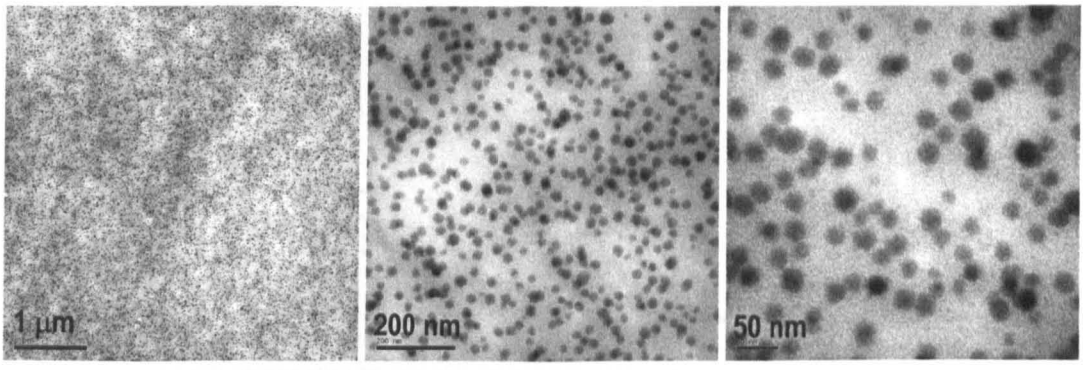

(i) 22500x (ii) 115000x (iii) 225000x

(b) 13 wt% nanosilica

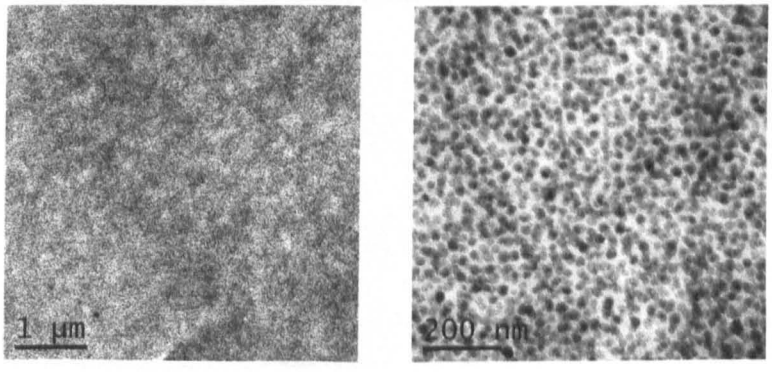

(i) 22500x (ii) 115000x

(c) 25 wt% nanosilica

Figure 5.1: TEM micrographs showing a homogeneous dispersion of (a) 5 wt%, (b) 13 wt% and (c) 25 wt% silica nanospheres in Epikote 828 observed under three different magnifications. The spherical silica nanoparticles have mean diameter of 20 nm and maximum diameter of 40 nm.

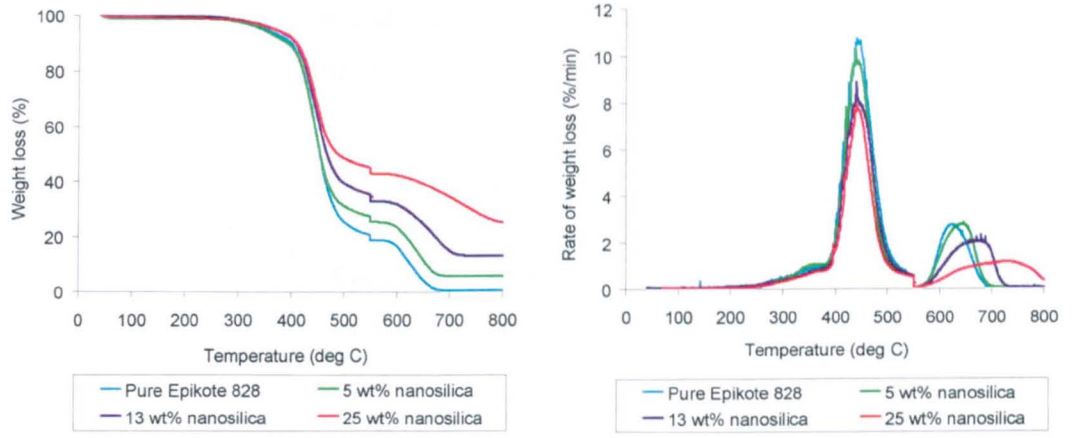

(a) burnt in N_2 from 40 °C to 550°C, kept at 550°C for 1 hr, then heated to 800°C in air

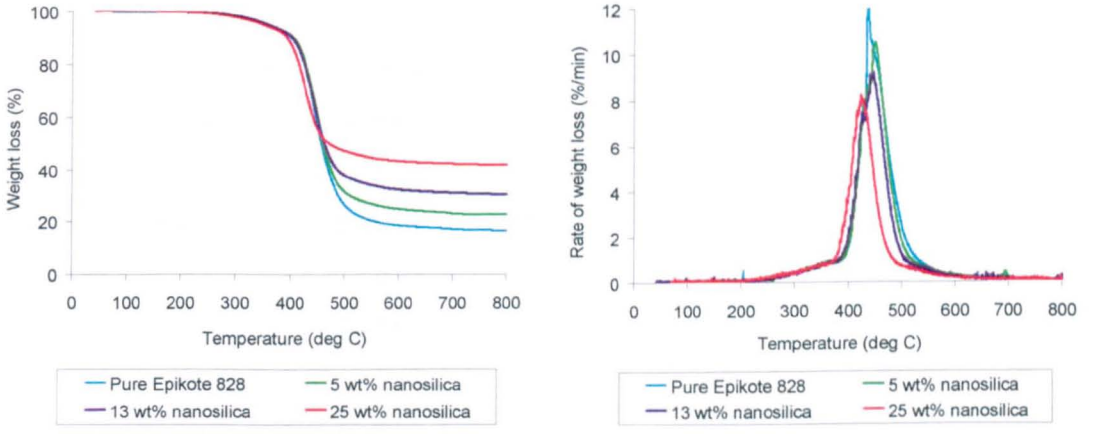

(b) burnt in N_2 from 25°C to 800°C

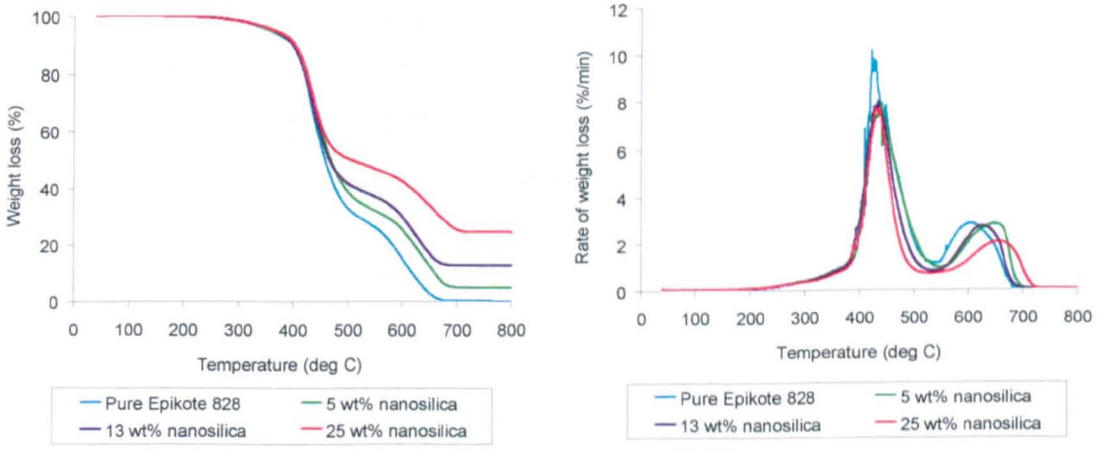

(c) burnt in air from 25°C to 800°C

Figure 5.2: Typical TGA results of nanosilica-filled Epikote 828 system, which were heated in three different heating conditions.

Table 5.1: Weight fraction and maximum degradation temperature of nanosilica-filled Epikote 828 resin based on TGA results.

Heating program	Epoxy system	Weight fraction (wt%)			maximum degradation temperature (°C)	
		Epoxy resin	carbon residue	Silica nanofiller	Epoxy resin	carbon residue
*Heating program 1	Pure	81.33 ± 0.17	18.29 ± 0.15	-	438.61 ± 2.20	609.67 ± 4.02
	5 wt% nanosilica	74.44 ± 0.25	19.80 ± 0.32	5.36 ± 0.03	441.85 ± 3.60	650.79 ± 4.20
	13 wt% nanosilica	65.51 ± 0.74	20.70 ± 0.65	12.96 ± 0.08	442.33 ± 2.08	680.03 ± 5.46
	25 wt% nanosilica	56.68 ± 0.15	17.25 ± 0.37	25.23 ± 0.33	444.39 ± 2.84	740.73 ± 7.54
**Heating program 2	Pure	81.60 ± 0.25	18.32 ± 0.23	-	430.17 ± 3.90	-
	5 wt% nanosilica	74.34 ± 0.18	-	-	451.72 ± 2.82	-
	13 wt% nanosilica	66.97 ± 0.32	-	-	446.67 ± 1.93	-
	25 wt% nanosilica	56.03 ± 0.16	-	-	428.22 ± 2.09	-
***Heating program 3	Pure	73.02 ± 0.59	26.83 ± 0.64	-	424.34 ± 1.81	605.69 ± 2.09
	5 wt% nanosilica	68.00 ± 0.30	26.18 ± 0.23	5.04 ± 0.12	435.14 ± 2.59	647.70 ± 1.41
	13 wt% nanosilica	63.03 ± 0.44	23.26 ± 0.37	13.02 ± 0.10	430.48 ± 0.72	631.99 ± 1.64
	25 wt% nanosilica	53.91 ± 0.20	20.77 ± 0.58	24.85 ± 0.22	431.38 ± 1.06	654.59 ± 1.19

*Heating program 1: Heating from 25°C to 550°C in N_2 and then kept at 550 °C for 1 hr, followed by heating to 800°C in air,

**Heating program 2: Heating from 25°C to 800°C in N_2

***Heating program 3: Heating from 25°C to 800°C in O_2

Table 5.2: Average density and volume fraction of nanosilica in Epikote 828.

Properties	Pure resin	Nanomodified system (NMS)		
		5 wt% si	13 wt% si	25 wt% si
Density (measured by density balance), ρ_{nc} (g/cm^3)	1.22	1.25	1.29	1.36
Theoretical density (calculated using the rule of mixtures) $\rho_{nc}(g/cm^3) = \rho_{ep}V_{ep} + \rho_{si}V_{si}$	1.22	1.24	1.27	1.33
Weight fraction of nanosilica (wt%) (from Table 5.1), $W_{si}(\%)$	-	5.36	12.96	25.23
Volume fraction of nanosilica (vol%) $V_{si}(\%) = W_{si} \times \frac{\rho_{nc}}{\rho_{si}}$, (where ρ_{si} = 1.8 g/cm^3)	-	3.72	9.29	19.06

5.2.3 Dimensional stability and glass transition temperature

The effect of nanosilica on thermal properties, such as CTE and Tg, of Epikote 828 was studies using TMA and DSC. The mean CTE below Tg was measured from the initial linear slope of the thermal strain-temperature plot (at temperature between 70 to 110°C) while the CTE above Tg was measured from the second linear slope of the curve between 150-180°C. Figure 5.3 shows the effects of 5, 13 and 25 wt% nanosilica on the thermal strain-temperature response of Epikote 828. In general, the addition of nanosilica reduced the slope of the thermal strain-temperature curve of the Epikote 828. This means that the presence of nanosilica restrains the expansion of the Epikote 828 and therefore contributes to a lower CTE value. In this study, Pyris series Diamond TMA software was used to determine the Tg and mean CTE below and above Tg. At least three specimens were tested for each system and the results were summarised in Table 5.3.

Table 5.3 shows that the mean CTE below and above Tg were reduced with increasing in nanosilica content. For instance, the incorporation of 25 wt% nanosilica reduced the CTE below Tg for about 18% and CTE above Tg for about 9% than the pure epoxy. This is because nanosilica has a higher modulus and a lower CTE than that of the pure Epikote 828. As the temperature of the material increases the matrix tries to

expand in its usual way. However, the nanofillers resist this dimensional change resulting in reduction in dimensional expansion of the polymer. This contributes to the lower CTE values for nanosilica-filled epoxy system.

Table 5.3 also shows the effect of nanosilica content on the Tg of the Epikote 828. It was found that the nanocomposite has a lower Tg than the pure epoxy. The Tg value decreased steadily with the increasing of nanosilica content was identified by both TMA and DSC instruments. For instance, the addition of 25 wt% nanosilica reduced the Tg by about 10% which were measured by TMA while DSC recorded reduction of 7%. The different in Tg values recorded by TMA and DSC was due to the different in measuring concept. DSC marked Tg by the change in energy absorbed by the epoxy while TMA marked Tg by the shift in thermal expansion of the material. In addition, a different heating rate was employed (in accordance to British Standards) for these two instruments. The reduction of Tg value with increasing nanosilica content was certified using these two instruments. This is possibly because of a decrease in crosslink density of the epoxy resin.

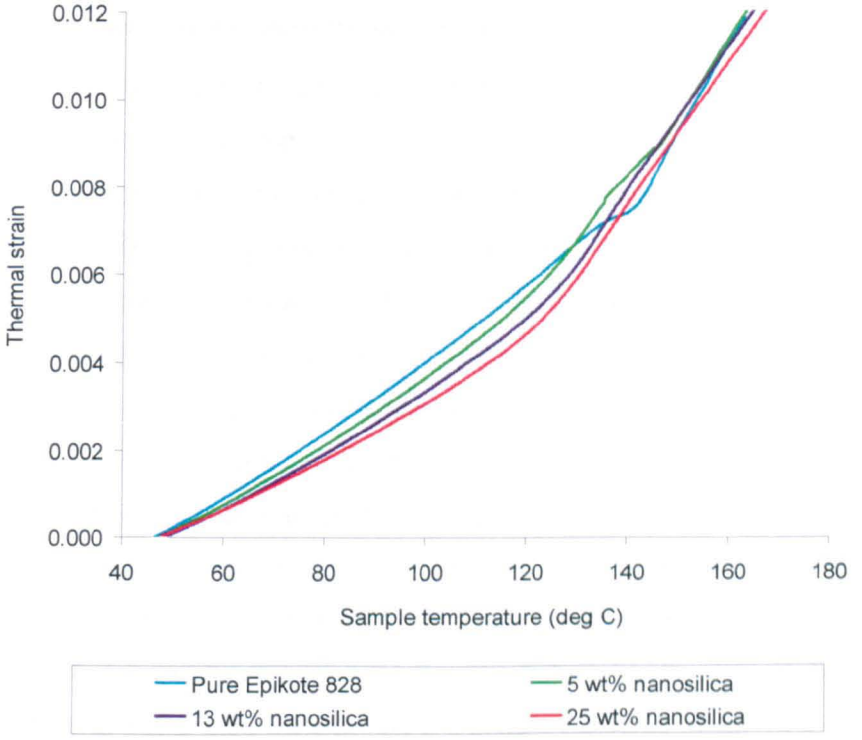

Figure 5.3: Thermal strain versus sample temperature of nanosilica filled Epikote828 epoxy nanocomposite. The mean CTE below and above Tg were calculated based on the first linear slope and second linear slope of the curve, respectively.

Table 5.3: Effect of nanosilica on CTE and Tg of Epikote 828.

Thermal properties	Pure resin	Nanomodified system (NMS)		
		5 wt% si	13 wt% si	25 wt% si
Mean CTE below Tg (με/°C)	79.78 ± 0.47	76.08 ± 0.38	68.23 ± 0.79	65.68 ± 1.64
Mean CTE above Tg (με/°C)	187.76 ± 3.59	182.07 ± 1.61	173.15 ± 1.85	170.56 ± 1.14
Tg measured by TMA (°C)	139.52 ± 1.02	134.36 ± 0.67	128.64 ± 0.52	124.68 ± 0.20
Tg measured by DSC (°C)	141.91 ± 0.77	136.48 ± 0.60	133.97 ± 1.05	131.60 ± 0.22

5.2.4 Compressive properties

5.2.4.1 True compressive stress-strain behaviour

The effect of nanosilica on the true compressive stress-strain response of the epoxy polymer is illustrated in Figure 5.4. It can be seen that the presence of nanosilica enhanced the compressive stress-strain behaviour of the epoxy polymer. In conventional systems, the addition of rigid microfillers or agglomerated nanofillers into epoxy resins commonly increases the stiffness but leads to a detrimental effect on the strain to failure [4,43,44,59,107,117]. Moreover, the strength of the composite is also reduced as the amount of fillers is increase. This is due to the high local stress concentration, which leads to premature failure. Additionally, reduction in strength and failure strain demonstrated that the load transfer between matrix and particles is insufficient and the interface is weak. In contrast, for the current system, Figure 5.4 shows that the incorporation of nanosilica increased the compressive modulus and strength of the polymer without any significant reduction in failure strain even at high nanosilica content. A rigid silica nanoparticle has a Young's modulus of 70 GPa [73] while the neat Epikote 828 has an E=3 GPa. The presence of nanosilica improved ductility and promoted higher plastic hardening behaviour after yielding of the epoxy without reducing its strain to failure. This suggests that the rigid nanoparticles introduce additional mechanisms of energy absorption during compression. This gives a higher

resistance to deformation, which results in higher compressive stress and plastic hardening. In addition, the homogeneous dispersion of these high stiffness nanofillers in the matrix enhanced the fracture toughness of the system (larger area under stress-strain curve, see Figure 5.4).

5.2.4.2 Compressive properties

The compressive properties of nanosilica-filled Epikote 828 are summarised in Table 5.4. It was found that the addition of nanosilica improved the compressive properties of the epoxy. For instance, the addition of 13 wt% nanosilica into the epoxy matrix enhances the compressive modulus by 19% and compressive strength by 58% with no significant changes in yield stress and failure strain. The highest content of nanosilica in the epoxy (25 wt%) gave a tremendous increase in compressive modulus and strength of more than 30% and 70%, respectively, compared to the neat polymer. This suggests that the nanofiller-matrix interaction is very favourable and therefore stresses are efficiently transferred via the interface, which leads to higher strength compared to the pristine polymer.

5.2.4.3 Effect of specimen shape

Figure 5.5 shows typical true stress-strain curves of prismatic specimens which were loaded in compression. The strain to failure and compressive strength of the pristine polymer were relatively lower than those of the nanomodified polymer. The resistance to plastic deformation of the nanomodified resin is higher compared to the pure resin system due to the presence of rigid nanoparticles. Table 5.4 also shows the comparison between the compressive properties of cylindrical and cubic specimens. It was found that both have a similar Young's modulus, however, the measured compressive strength and failure strain of the cube type specimens were significantly lower than those of the cylindrical specimens. This is due to the fact that the cubic specimens undergo a non-uniform deformation during compression (as explained in Section 4.2.3) therefore the actual compressive stress induced especially in the plastic region cannot be accurately determined.

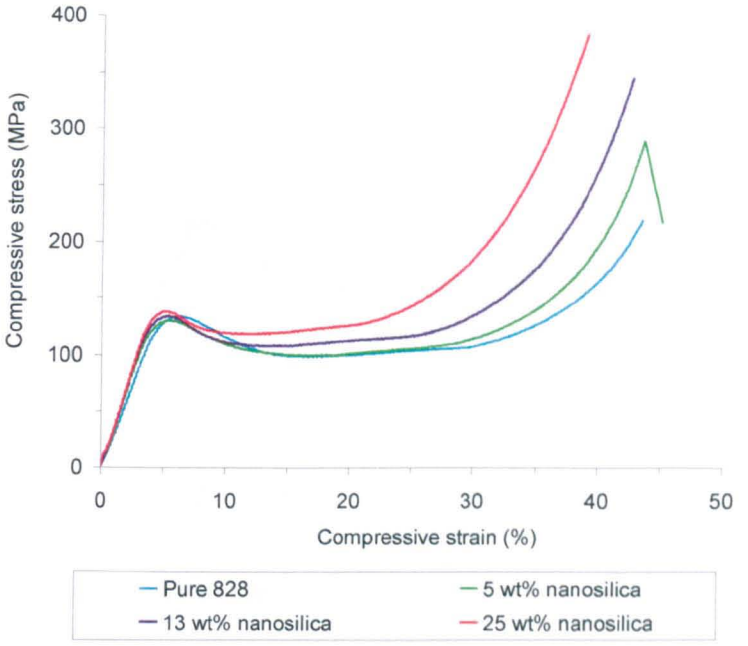

Figure 5.4: Typical true stress-strain curves of cylindrical specimens loaded in static uniaxial compression showing the effect of nanosilica on the compressive stress-strain behaviour of Epikote 828.

Table 5.4: Effect of specimen shape and geometry on the compressive properties of nanosilica-filled epoxy nanocomposites.

Compressive property	**Pure Epikote 828**		**Nanomodified system**					
			5 wt% si		**13 wt% si**		**25 wt% si**	
	Cyl.	**Cubic**	**Cyl.**	**Cubic**	**Cyl.**	**Cubic**	**Cyl.**	**Cubic**
Elastic modulus, E (GPa)	3.02 ± 0.06	3.12 ± 0.02	3.34 ± 0.08	3.39 ± 0.02	3.58 ± 0.02	3.60 ± 0.01	4.05 ± 0.07	4.04 ± 0.07
Yield stress σ_y (MPa)	132.99 ± 0.20	126.59 ± 0.39	130.35 ± 0.31	130.93 ± 0.65	133.08 ± 0.39	131.80 ± 0.97	138.88 ± 0.84	130.75 ± 1.13
Strain at yield point, ε_y (%)	6.50 ± 0.05	5.53 ± 0.03	5.70 ± 0.10	5.37 ± 0.04	5.46 ± 0.05	4.91 ± 0.11	5.12 ± 0.07	4.49 ± 0.06
Compressive strength, σ_u (MPa)	211.47 ± 3.17	126.59 ± 0.39	274.60 ± 2.66	130.93 ± 0.65	335.03 ±13.35	131.80 ± 0.97	372.00 ± 7.64	158.69 ± 9.68
Strain at break, ε_f (%)	42.66 ± 0.65	16.49 ± 1.56	39.74 ± 2.55	23.67 ± 2.40	42.17 ± 0.48	28.54 ± 1.57	38.89 ± 0.19	27.96 ± 1.34

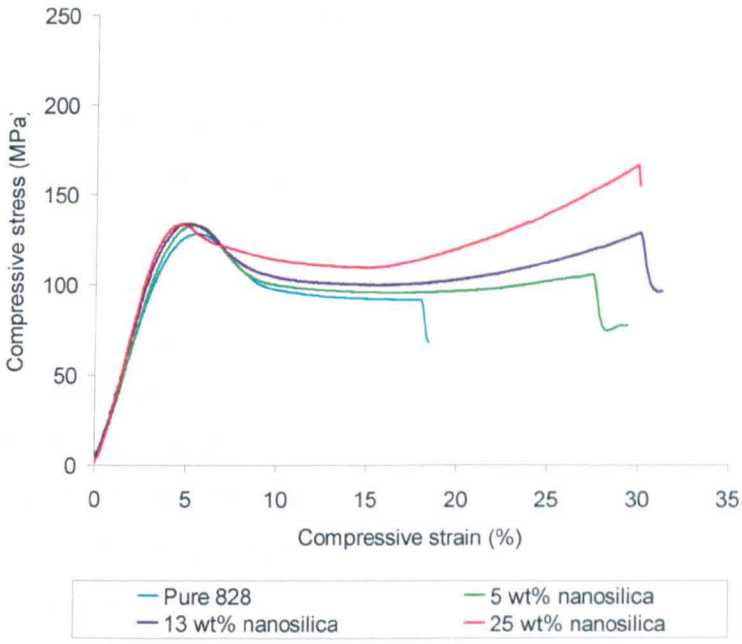

Figure 5.5: Typical true stress-strain curves of prismatic (cubic) specimens loaded in static uniaxial compression showing the effect of nanosilica on the compressive stress-strain behaviour of Epikote 828.

5.2.4.4 Prediction of compressive modulus

The elastic response of most polymer matrices is usually similar in tension and compression, and therefore the compressive elastic modulus of the studied systems was estimated using various models suggested and reviewed in [41,42,169-172]. Table 5.5 summarises several theoretical models that are commonly used to predict the modulus of elasticity of particle-modified polymers. These are rule of mixtures, Halpin-Tsai [171] and Lewis-Nielsen [41,42,172] models. Figure 5.6 shows the theoretical predictions of compressive modulus compared to the measured values. It was found that most of the prediction curves were in a good agreement with the measured data, where the compressive modulus increases with the nanosilica content. The upper bound rule of mixtures equation gives poor prediction when compared to the present experimental data. The Halpin-Tsai model [171] includes the shape factor of the filler particle; it should be noted that this equation is based on the early micromechanics work by Hill [170] and experimental measurements and observations (semi-empirical). It appears to give reasonable stiffness prediction for certain material systems. For the case of spherical particles used in the present work, the length of the particle w equals the thickness of the particle t and therefore the shape factor $\zeta=2w/t=2$. For a low volume

fraction of the nanofiller, the Halpin-Tsai prediction gives a very good agreement with the experimental data. However, when the silica nanoparticle content is more than 5 vol% the prediction curve lies above the measured values, see Figure 5.6.

The Lewis-Nielsen model takes into account the degree of dispersion of particles in the matrix, V_{max} and the particle-matrix adhesion, k_E. Figure 5.1 shows no agglomeration of the nanosilica particles, therefore for random close packing and non-agglomerated spheres, V_{max}=0.632 was used in the calculation. Additionally, Figure 5.4 shows that the compressive strength of the nanomodified system was higher than that of the pure polymer. This suggests a very strong nanofiller-matrix interfacial adhesion, which helps the load to be effectively transferred via the interface. Therefore, a perfect adhesion of k_E=2.167 was assumed in the non-slip Lewis-Nielsen model. This model gives the best agreement to the measured values when compared with the other models. However, at a very high nanofiller content (more than 19 vol%) the measured compressive modulus is lower than the predicted value. This is a common observation, since the model assumes that there is perfect bonding between the particles and the matrix, which may not be the case at very high filler content. This is due to the fact that some particle agglomeration may occur at high filler content in addition to particle slippage and imperfect adhesion.

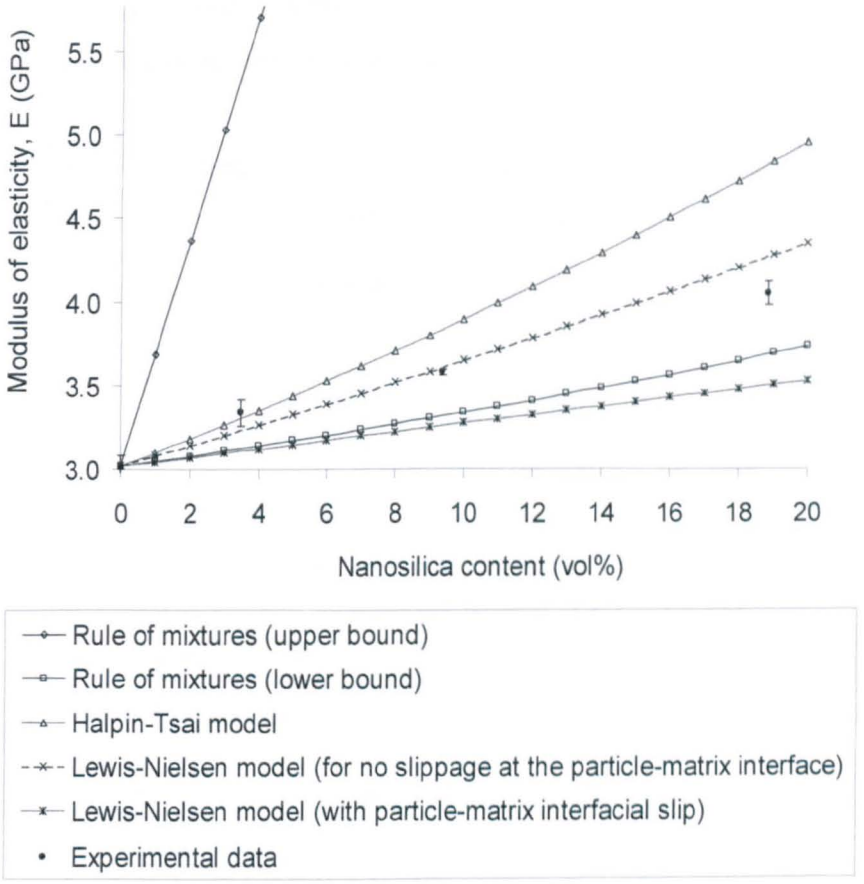

Figure 5.6: Theoretical prediction of the compressive modulus of nanosilica-modified Epikote 828 in comparison with the measured data. All curves were calculated based on models and input data summarised in Table 5.5.

Table 5.5: Prediction of compressive modulus of nanosilica-filled Epikote 828 nanocomposites using several types of theoretical models.

Theoretical models	Ref.	Equation and input data
Rule of mixtures	[169]	Upper bound, $E_{nc} = E_{si}V_{si} + E_{ep}V_{ep}$ Lower bound, $E_{nc} = \frac{E_{si}E_{ep}}{E_{si}V_{ep} + E_{ep}V_{si}}$ where E_{nc} = predicted nanocomposites modulus E_{ep} = modulus of the epoxy = 3.02 GPa E_{si} = modulus of the nanosilica = 70 GPa V_{ep} = volume fraction of the epoxy V_{si} = volume fraction of the nanosilica
Halpin-Tsai model	[171]	$E_{nc} = \frac{1+\zeta\eta V_{si}}{1-\eta V_{si}} E_{ep}$ where ζ =shape factor = 2 for spherical particles $\eta = \frac{\left(\frac{E_{si}}{E_{ep}} - 1\right)}{\left(\frac{E_{si}}{E_{ep}} + \zeta\right)} = 0.88$
Lewis-Nielsen model	[41,42, 172]	$E_{nc} = \frac{1+(k_E-1)\beta V_{si}}{1-\beta\mu V_{si}} E_{ep}$ where k_E = 2.167 if there is no slippage at the particle-matrix interface [73] k_E = 0.867 if there is interfacial slip occurred [73] $\beta = \frac{\left(\frac{E_{si}}{E_{ep}} - 1\right)}{\left(\frac{E_{si}}{E_{ep}} + (k_E - 1)\right)}$ $\mu = 1 + \frac{(1-V_{si})}{V_{max}}[(V_{max}V_{si}) + (1-V_{max})(1-V_{si})]$ V_{max} = 0.632 for random close packing, non-agglomerated spheres [42]

5.2.5 Tensile properties

The effect of nanosilica on the tensile stress-strain response of the epoxy polymer is illustrated in Figure 5.7. It can be seen that the presence of nanosilica enhanced the tensile stress-strain behaviour of the epoxy polymer. Nanocomposites exhibited higher tensile modulus (as measured at the initial slope of the graph) and strength without reducing its failure strain even at high nanosilica content. The increase in modulus is expected because the modulus of silica is about 70 GPa [73]. In addition, the homogeneous dispersion of these high stiffness nanofillers in the matrix enhanced the fracture toughness of the system as indicated by the larger area under stress-strain curve of the nanocomposite system, see Figure 5.7. As the tensile load increases, the matrix tries to elongate in its usual way. However, the nanofillers resist deformation. This results in smaller deformation compared to the neat polymer. Therefore, nanocomposites sustain more loads compared to the pure systems and contribute to a higher tensile modulus and strength.

Table 5.6 summarises the tensile properties of nanomodified system compared to the pure resin. It was found that the addition of nanosilica improved the tensile properties of the epoxy. For instance, the addition of 13 wt% nanosilica into the epoxy matrix enhances the tensile modulus by 21%, tensile strength by 20% and failure strain by 10%. The highest content of nanosilica in the epoxy (25 wt%) give a remarkable increase in tensile modulus and strength of about 38% and 24%, respectively, compared to the neat polymer without sacrificing the strain to failure. This suggests that the nanofiller-matrix interaction is very strong therefore the nanocomposites exhibited higher strength compared to the pristine polymer.

5.2.6 Flexural properties

Figure 5.8 shows the typical flexural stress-strain curves recorded at 2 mm/min of strain rate for neat and nanosilica-filled systems. It was found that the slope of the stress-strain curves increases with increasing in nanosilica content. This indicates that nanosilica enhances the flexural modulus of the epoxy. As the flexural load increases, the nanomodified system exhibited less deflection compared to that of the unmodified system. The nanomodified system sustains more loads at the same flexural strain to the neat epoxy. The degree of plastic deformation increases especially with 5 wt% nanosilica as shown in Figure 5.8. This shows that the presence of rigid nanosilica

particles does not restrict the mobility of the molecular chain to pass each other and results in higher failure stress and strain. Therefore the nanocomposites give benefits to elastic modulus and strength without sacrificing the strain to failure of the epoxy.

The flexural tests were conducted on at least five specimens for each system. Table 5.6 shows the summary of the flexural properties. The addition of nanosilica enhances flexural modulus and strength of the epoxy without any significant reduction in its failure strain. For example, the addition of 5 wt% nanosilica in the epoxy matrix enhances the elastic modulus by 13%, flexural strength by 26% and failure strain by 15%. The elastic modulus improves significantly with 25 wt% nanosilica, by about 36%, without any further enhancement in the ultimate stress and strain to break. Nanosilica rich region or particle agglomeration may occur at higher nanosilica content hence contribute to a premature failure of the specimens. Therefore, this limits the flexural strength and failure strain enhancement.

5.2.7 Fracture toughness properties

Table 5.6 shows also the effect of nanosilica on fracture toughness of Epikote 828. At least five specimens were tested for each system and the results of typical load-crack opening displacement curves obtained from the compact tension tests with 5 – 25 wt% nanosilica were given in Appendix A. It was found that, the load at crack growth initiation F_Q for nanomodified system was higher than that of the neat epoxy. Hence, the nanocomposites enhanced significantly the fracture toughness of the epoxy, see Table 5.6. For instance, the addition of 25 wt% nanosilica increased maximum load to about 82% compared with the pure Epikote 828. This gives enhancement in critical stress intensity factor and critical energy release rate of about 84% and 163%, respectively. The fracture energy increases steadily with the nanosilica content. This indicates a very good interfacial adhesion between matrix and nanofiller.

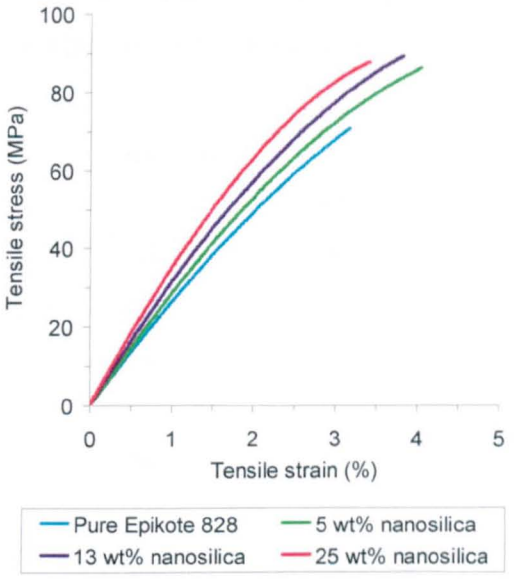

Figure 5.7: Typical tensile stress-strain curves of nanosilica-modified Epikote 828 compared to the neat epoxy.

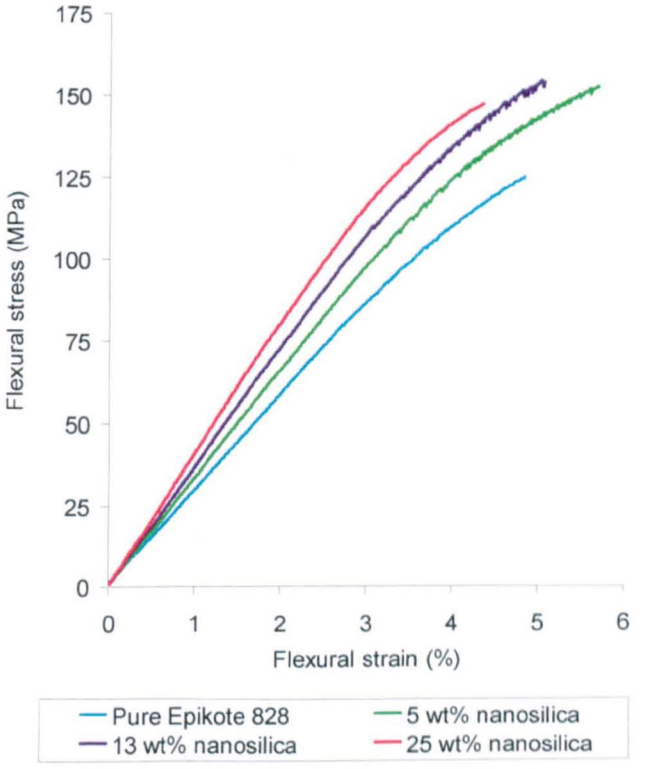

Figure 5.8: Typical flexural stress-strain curves of nanosilica-modified Epikote 828 compared to the neat epoxy.

Table 5.6: Tensile, flexural and fracture toughness properties of the unmodified and nanomodified Epikote 828 resin with various concentrations of silica nanoparticles.

Material properties	**Pure resin**	**Nanomodified system (NMS)**		
		5 wt% si	**13 wt% si**	**25 wt% si**
Tensile modulus, E_t (GPa)	2.75 ± 0.02	3.08 ± 0.04	3.33 ± 0.04	3.80 ± 0.04
Tensile strength, $\sigma_{u,t}$ (MPa)	70.84 ± 1.08	79.42 ± 4.00	85.25 ± 2.47	88.11 ± 1.41
Tensile strain at break, $\varepsilon_{f,t}$ (%)	3.28 ± 0.09	3.47 ± 0.30	3.62 ± 0.23	3.52 ± 0.22
Flexural modulus, E_b (GPa)	2.88 ± 0.03	3.25 ± 0.02	3.56 ± 0.02	3.93 ± 0.03
Flexural strength, $\sigma_{u,b}$ (MPa)	117.73 ± 8.70	148.82 ± 5.29	145.17 ± 6.63	139.30 ± 8.55
Flexural strain at break, $\varepsilon_{f,b}$ (%)	4.84 ± 0.61	5.58 ± 0.40	4.89 ± 0.36	4.30 ± 0.47
Maximum load, F_Q (N)	217.35 ± 7.43	279.30 ± 8.17	344.04 ± 8.58	395.21 ± 4.90
Critical stress intensity factor, K_{IC} (MPa.$\sqrt{\text{m}}$)	0.67 ± 0.02	0.87 ± 0.03	1.07 ± 0.03	1.23 ± 0.02
Critical energy release rate, G_{IC} (J/m^2)	152.73 ± 10.84	239.87 ± 13.16	329.91 ± 17.42	400.84 ± 14.53

5.3 CNT-filled Epikote 828 epoxy polymer

5.3.1 Morphology

A good dispersion of 0.5 and 1 wt% multiwalled CNT in the Epikote 828 is illustrated in Figures 5.9 and 5.10, respectively. At high magnification, the TEM images show the presence of clusters of entangled CNT in the matrix. The multiwalled CNT has an average diameter of 10 nm as shown in high magnification TEM images.

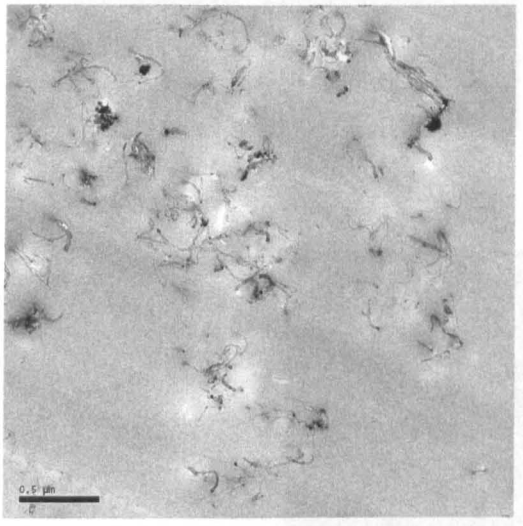

(a) 34000x

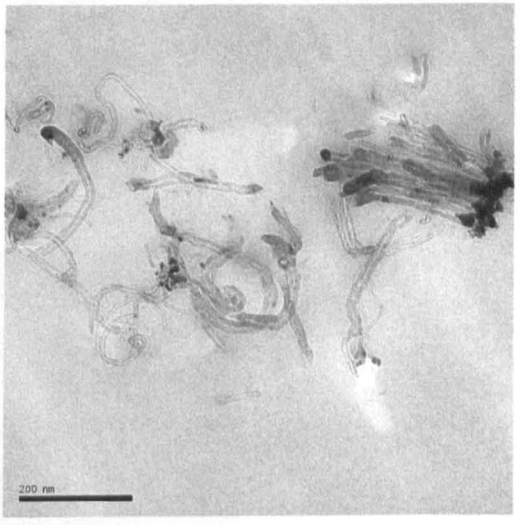

(b) 115000x

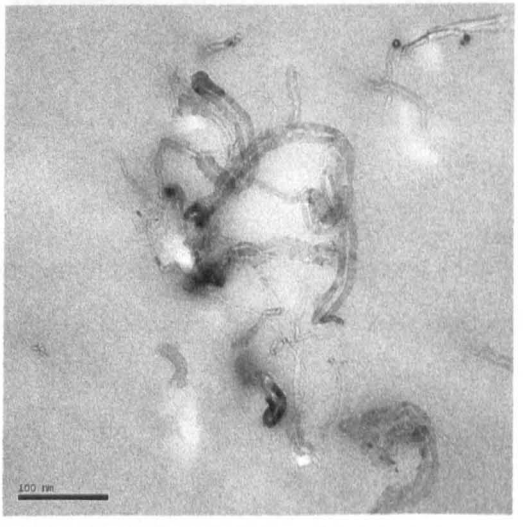

(c) 170000x

Figure 5.9: TEM micrographs showing a homogeneous dispersion of 0.5 wt% CNT in Epikote 828 observed under three different magnifications.

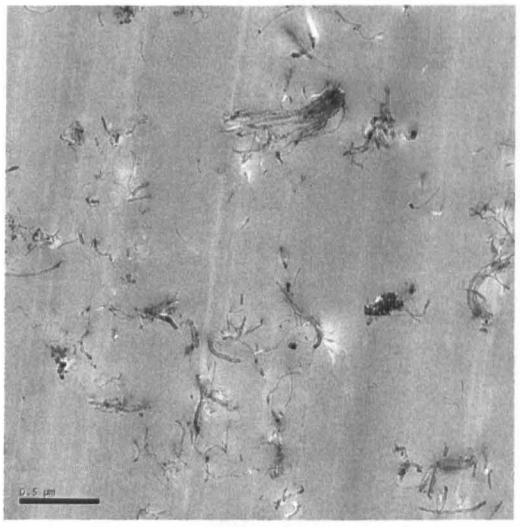

(a) 34000x

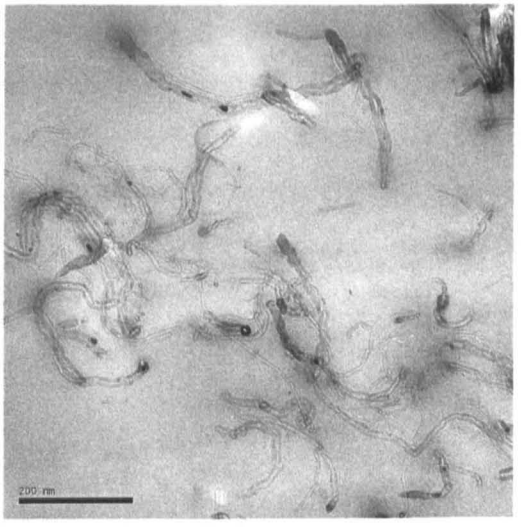

(b) 115000x

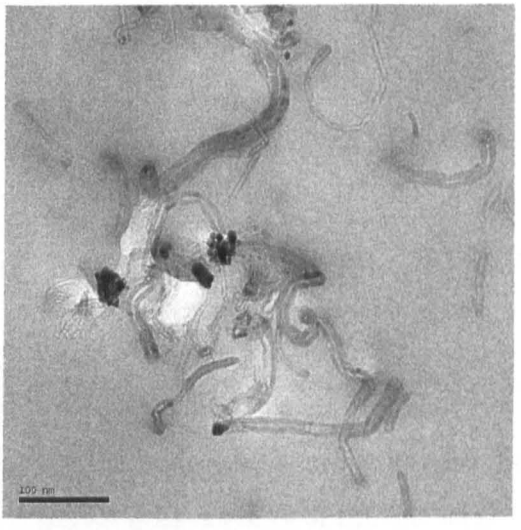

(c) 170000x

Figure 5.10: TEM micrographs showing a good dispersion of 1 wt% CNT in Epikote 828 observed under three different magnifications.

5.3.2 Dimensional stability and glass transition temperature

Figure 5.11 illustrates the effects of 0.5 and 1 wt% CNT on the dimensional stability of Epikote 828. At least three samples were tested for each system. Table 5.7 summarises the mean CTE and Tg for nanomodified system compared to the neat epoxy. It was found that the mean CTE of the Epikote 828 epoxy resin was slightly decreased by incorporation of CNT. By adding 1 wt% CNT, the mean CTE below and above Tg were reduced for about 3-4%. There was also no significant effect on the Tg by adding CNT to Epikote 828, see Table 5.7. This was recorded by both TMA and DSC instruments.

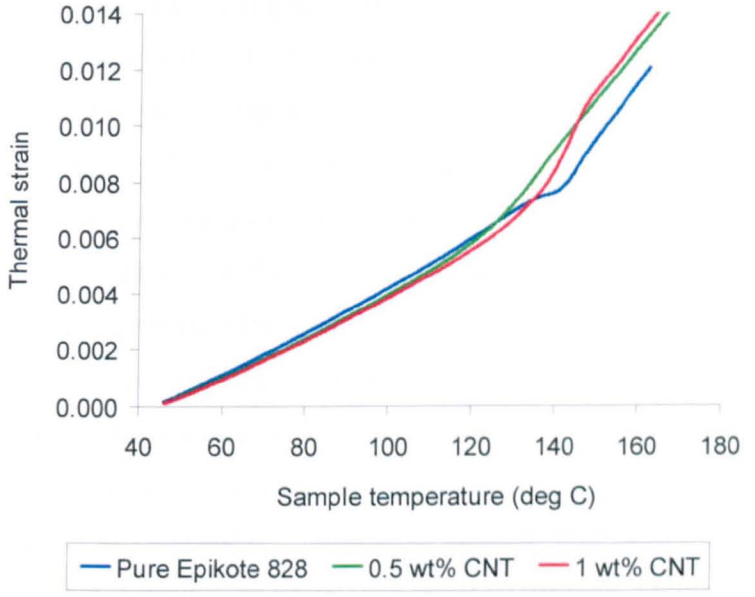

Figure 5.11: Typical thermal strain-temperature curves showing the effect of CNT on dimensional stability of Epikote 828.

Table 5.7: Effect of CNT on CTE and Tg of Epikote 828.

Thermal properties	Pure resin	Nanomodified system (NMS)	
		0.5 wt% CNT	1 wt% CNT
Mean CTE below Tg (με/°C)	79.78 ± 0.47	77.30 ± 0.17	76.23 ± 0.29
Mean CTE above Tg (με/°C)	187.76 ± 3.59	183.70 ± 0.97	182.26 ± 0.25
Tg measured by TMA (°C)	139.52 ± 1.02	137.69 ± 0.12	136.71 ± 0.42
Tg measured by DSC (°C)	141.91 ± 0.77	139.53 ± 0.19	138.87 ± 0.09

5.3.3 Compressive properties

The effect of multiwalled CNT on the true compressive stress-strain response of the epoxy polymer was illustrated in Figure 5.12. It can be seen that the presence of multiwalled CNT enhanced the compressive stress-strain behaviour of the epoxy polymer. The presence of CNT gives a higher resistance against deformation, which results in higher compressive strength and plastic hardening. In addition, nanocomposites exhibited a larger area under stress-strain graph compared to the pure system. This implies that nanocomposites has better fracture toughness properties. The compressive properties of CNT-filled Epikote 828 are summarised in Table 5.8. It was found that the addition of CNT improved the compressive modulus and strength without any significant reduction in failure strain of the epoxy. For instance, the addition of 1 wt% CNT into the epoxy matrix enhances the compressive modulus by 19% and compressive strength by 9%. However the yield strength of the epoxy reduces with an increase in CNT content. The addition of 1 wt% CNT slightly reduces the yield strength by about 2%. This implies that the interfacial bonding between CNT and epoxy matrix is not strong enough to resist plastic deformation of the material. Therefore the plastic deformation of the nanocomposites took place earlier than that of the pure resin.

Table 5.8 shows also the comparison between the compressive properties of cylindrical and cubic specimens. It was found that both have a similar Young's modulus, however, the measured compressive strength and failure strain of the cube type specimens were significantly lower than those of the cylindrical specimens. This is due to the fact that the cubic specimens undergone non-uniform deformation during compression and premature failure was triggered by the sharp corners. Therefore, the actual compressive stress induced especially in the plastic region cannot be accurately determined. Figure 5.13 shows typical true stress-strain curves of prismatic specimens that were loaded in compression. The elastic modulus, strain to failure, compressive strength and fracture toughness (area under graph) of the nanocomposites were relatively higher than those of the pure polymer.

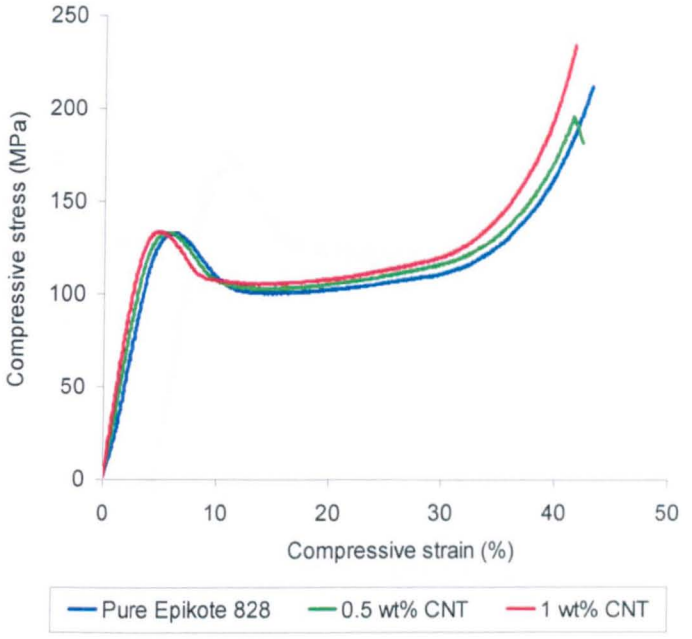

Figure 5.12: Typical true stress-strain curves of cylindrical specimens loaded in static uniaxial compression showing the effect of multiwalled CNT on the compressive stress-strain behaviour of Epikote 828.

Table 5.8: Compressive properties of multiwalled CNT-modified Epikote 828 compared to the pure system. Compression tests were conducted on two different specimens; (i) cylindrical and (ii) cubic.

Compressive property	**Pure Epikote 828**		**Nanomodified system**			
			0.5 wt% CNT		**1 wt% CNT**	
	Cyl.	**Cubic**	**Cyl.**	**Cubic**	**Cyl.**	**Cubic**
Elastic modulus, E (GPa)	3.02 ± 0.06	3.12 ± 0.02	3.39 ± 0.01	3.37 ± 0.02	3.60 ± 0.03	3.59 ± 0.03
Yield stress, σ_y (MPa)	132.99 ± 0.20	126.59 ± 0.39	132.10 ± 0.27	131.49 ± 0.53	130.93 ± 0.63	130.90 ± 0.87
Strain at yield point, ε_y (%)	6.50 ± 0.05	5.53 ± 0.03	5.85 ± 0.06	5.20 ± 0.06	5.33 ± 0.11	5.00 ± 0.07
Compressive strength, σ_u (MPa)	211.47 ± 3.17	126.59 ± 0.39	188.32 ± 7.82	131.49 ± 0.53	231.51 ± 2.66	130.90 ± 0.87
Strain at break, ε_f (%)	42.66 ± 0.65	16.49 ± 1.56	41.22 ± 0.61	28.13 ± 1.63	42.62 ± 0.36	28.79 ± 1.58

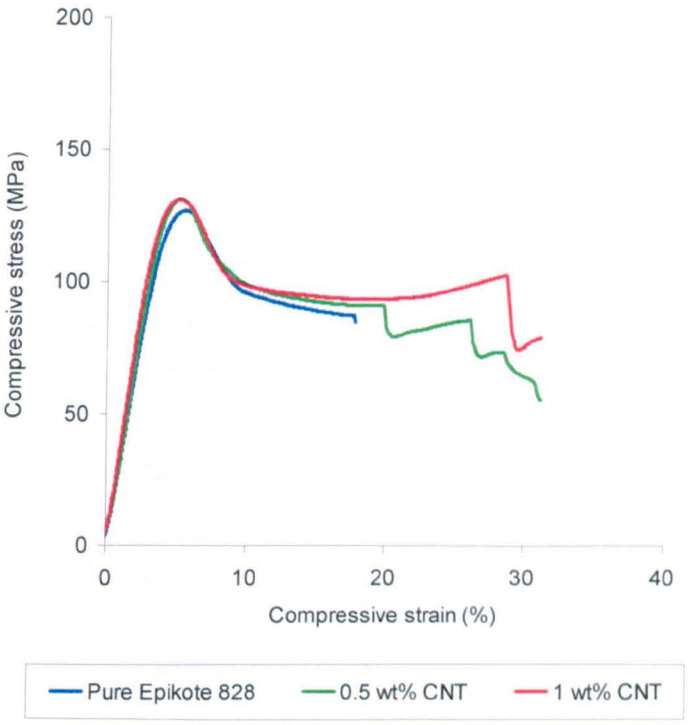

Figure 5.13: Typical true stress-strain curves of prismatic (cubic) specimens loaded in static uniaxial compression showing the effect of multiwalled CNT on the compressive stress-strain behaviour of Epikote 828.

5.3.4 Tensile properties

The effect of multiwalled CNT on the tensile stress-strain response of the epoxy polymer was illustrated in Figure 5.14. It was found that the slope of the stress-strain curves increases with increases in CNT content. This indicates that the CNT enhances the tensile modulus of the epoxy. Table 5.9 summarises the tensile properties of nanomodified system compared to the neat resin. The addition of 0.5 and 1 wt% CNT enhanced the tensile modulus by 16% and 23%, respectively. However, it slightly improved the tensile strength and slightly reduced the failure strain. TEM images (as shown in Figures 5.9 and 5.10) show the evidence of some entanglements of the tubes at some locations of CNT rich regions presence in the nanocomposites. This may contribute to high localised stresses in the material during tension and cause a premature failure at high stress. In addition, a reduction in compressive yield strength obtained in the previous section showed the evidence of weak CNT-epoxy interfacial adhesion. This limits the stress transfer capability via the interface during tensile loading hence

moderately enhancing the flexural strength and gives detrimental effect on the failure strain.

5.3.5 Flexural properties

The effect of multiwalled CNT on the flexural modulus, strength and failure strain was shown in Table 5.9. Figure 5.15 shows the typical flexural stress-strain curves recorded at 2 mm/min of strain rate for neat and CNT-filled systems. Flexural modulus is the ratio of stress to strain within the elastic limit and this property was used to indicate the bending stiffness of the material while flexural strength shows the ability of the material to resist deformation under load. Figure 5.15 shows that the addition of multiwalled CNT enhances both the flexural modulus and strength of the epoxy without sacrificing its failure strain. The presence of high modulus and strength of CNT does not restrict the mobility of the molecular chain and promotes plastic deformation of the epoxy. This results in higher failure stress and strain. Table 5.9 shows that the elastic modulus, flexural strength and failure strain increases with CNT content. For instance, the addition of 1 wt% CNT into the epoxy matrix enhances the elastic modulus by 22%, flexural strength by 25% and failure strain by 17%. Nanocomposites show a better performance in bending and compression compared to that in tension. This is due to the fact that the tensile properties are primarily determined by flaws and submicroscopic cracks. In flexural tests part of the specimen is under tension and part under compression. Therefore the flexural strength tends to be greater than tensile strength and lower than the compressive strength. CNT-filled composites failed at low failure strain in tension compared to that of in compression. Therefore in bending, the failure of the specimens may initiate in tension region due to maximum stretching.

5.3.6 Fracture toughness properties

Table 5.6 shows also the effect of CNT on fracture toughness of Epikote 828. At least five specimens were tested for each system and the results of typical load-crack opening displacement curves obtained from the compact tension tests with 0.5 and 1 wt% CNT were given in Appendix A. It was found that, the fracture toughness increased with increasing CNT content. The load at crack growth initiation F_Q for nanomodified system was higher than that of the neat epoxy. For instance, the addition of 0.5 and 1

wt% CNT increased maximum load for about 31% and 53%, respectively, compared to that of the pure Epikote 828. This gives enhancement in the critical stress intensity factor for about 33% and 54%, respectively and, also, enhancement in fracture energy for about 62% and 100%, respectively. This suggests that, high modulus and strength of CNT introduce additional mechanisms of energy absorption during fracture. This gives higher resistance to plastic deformation and crack propagation, hence, improves its toughness.

Table 5.9: Tensile, flexural and fracture toughness properties of the unmodified and nanomodified Epikote 828 resin with 0.5 and 1 wt% of multiwalled CNT.

Material properties	**Pure resin**	**Nanomodified system (NMS)**	
		0.5 wt% CNT	**1 wt% CNT**
Tensile modulus, E_t (GPa)	2.75 ± 0.02	3.20 ± 0.02	3.39 ± 0.01
Tensile strength, $\sigma_{u,t}$ (MPa)	70.84 ± 1.08	75.09 ± 0.87	74.76 ± 1.73
Tensile strain at break, $\varepsilon_{f,t}$ (%)	3.28 ± 0.09	3.11 ± 0.07	3.06 ± 0.12
Flexural modulus, E_b (GPa)	2.88 ± 0.03	3.31 ± 0.04	3.51 ± 0.07
Flexural strength, $\sigma_{u,b}$ (MPa)	117.73 ± 8.70	140.02 ± 6.88	147.38 ± 3.70
Flexural strain at break, $\varepsilon_{f,b}$ (%)	4.84 ± 0.61	5.38 ± 0.57	5.68 ± 0.57
Maximum load, F_Q (N)	217.35 ± 7.43	285.60 ± 4.75	331.60 ± 4.26
Critical stress intensity factor, K_{IC} (MPa.$\sqrt{\text{m}}$)	0.67 ± 0.02	0.89 ± 0.02	1.03 ± 0.01
Critical energy release rate, G_{IC} (J/m^2)	152.73 ± 10.84	246.82 ± 7.33	305.05 ± 9.20

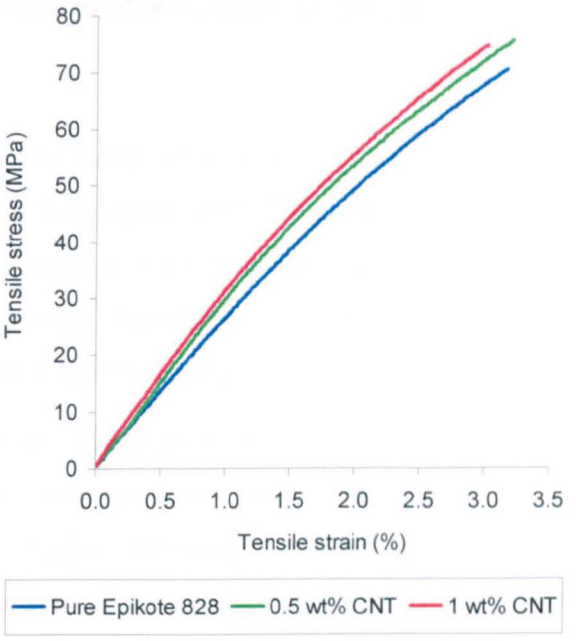

Figure 5.14: Typical tensile stress-strain curves of multiwalled CNT-modified Epikote 828 compared to the neat epoxy.

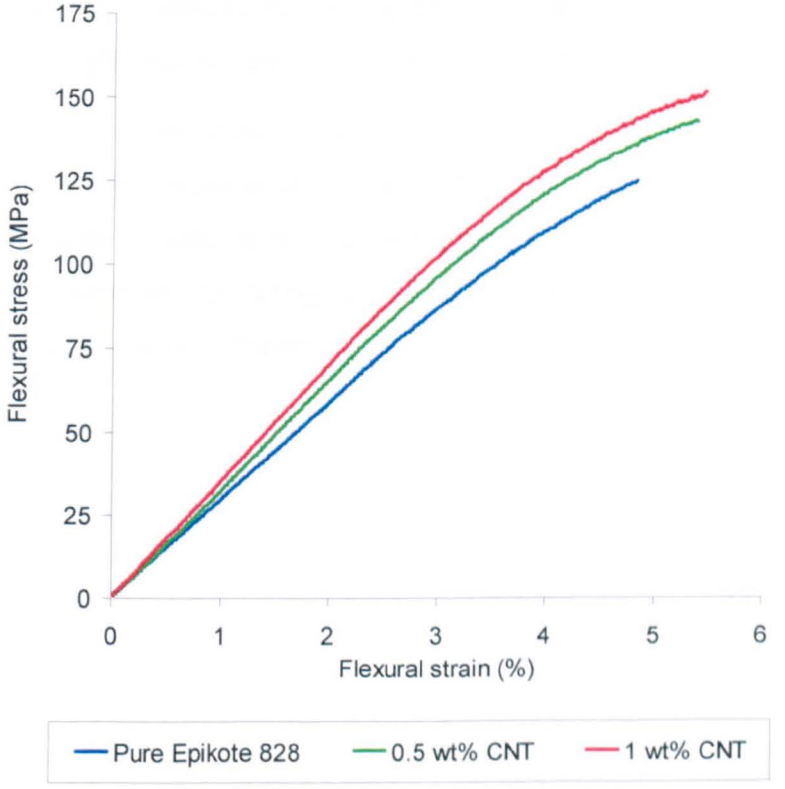

Figure 5.15: Typical flexural stress-strain curves of multiwalled CNT-modified Epikote 828 compared to the neat epoxy.

5.4 Nanoclay-filled Epikote 828 epoxy polymer

5.4.1 Morphology

The I.28 montmorillonite (MMT) clay has dry particle size of 8–10 μm. It was a great challenge to transform the micron-sized clay particles into exfoliated state, which has a huge amount of nanoplatelets in the epoxy matrix, using a mechanical stirring technique. The gap between two adjacent silicate platelets in I.28 nanoclay is about 2.4 nm. One clay sheet has 1 nm thickness.

Figure 5.16 shows the dispersion of 1, 3 and 5 wt% I.28 MMT nanoclay in Epikote 828. At low magnification, TEM images show clusters of nanofiller-rich regions and resin-rich region. All TEM images at high magnification (170,000x) show that the gap between two adjacent platelets is more than 2.4 nm but less that 8 nm. These indicate that the nanocomposite has an intercalated structure. The d-spacing was seen to reduce with increasing clay content. The d-spacing of 5 wt% nanoclay in epoxy is about 3-4 nm (see Figure 5.17). Since a very small area of the specimen was sampled in each TEM image, at least 3 samples were examined for each epoxy system and at least 5 images were captured for each sample and the measurement of d-spacing was taken from multiple images captured from various locations of the specimen.

The viscosity of the resin increases with increasing in the nanoclay content and the processing time was limited to 90 minutes after adding hardener into the epoxy. Clay content of more that 3 wt% led to processing problems, especially the degassing process of the resin mixture prior to curing became impossible. This results in entrapped air in the cured epoxy as shown in Figure 5.16c.

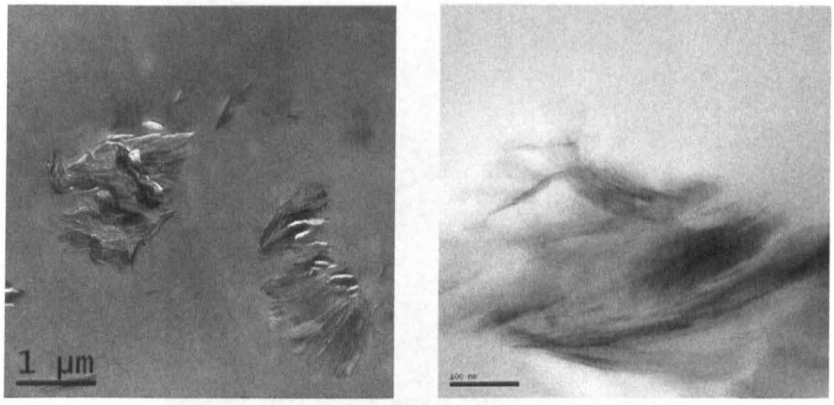

(i) (ii)

(a) 1 wt% nanoclay

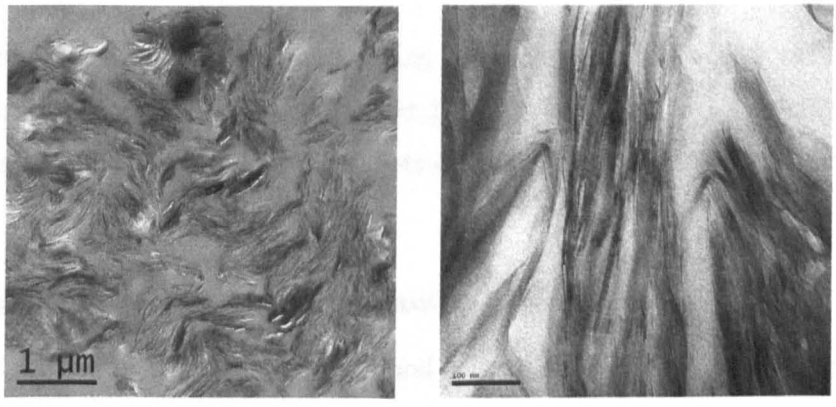

(i) (ii)

(b) 3 wt% nanoclay

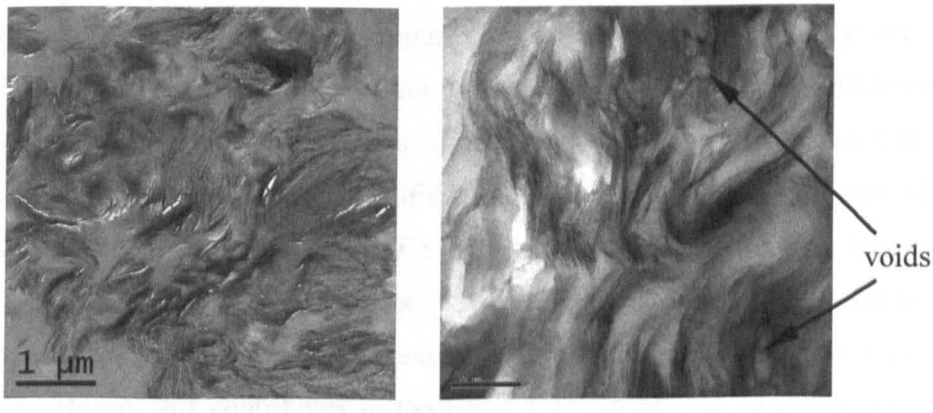

(i) (ii)

(c) 5 wt% nanoclay

Figure 5.16: TEM micrographs showing an intercalated structure of (a) 1 wt%, (b) 3 wt% and (c) 5 wt% clay nanoplatelets in Epikote 828, prepared using the mechanical stirring technique and observed under two different magnifications, (i) 22500x and (ii) 170000x.

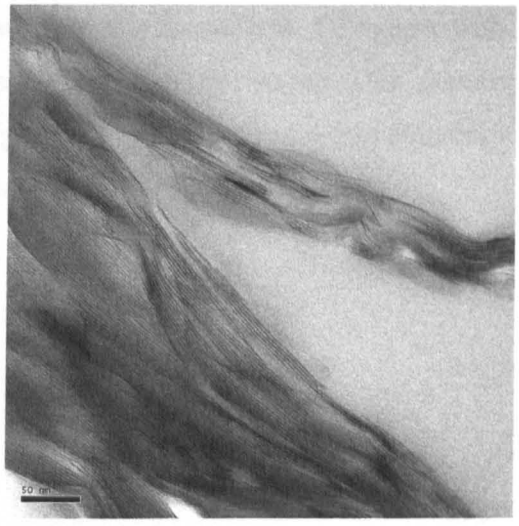

Figure 5.17: TEM micrographs showing intercalated structures of 5 wt% clay nanoplatelets in Epikote 828 observed under 225000x magnification. One clay sheet has 1nm thickness. The d-spacing in between silicate layers is about 3-4 nm.

5.4.2 Dimensional stability and glass transition temperature

Figure 5.18 illustrates the effects of 1, 3 and 5 wt% I.28 nanoclay on the dimensional stability of Epikote 828. The inclusion of nanoparticles significantly reduced the slope of thermal strain-temperature curve of the epoxy. This implies a better dimensional stability of the nanocomposites at elevated temperatures. At least three samples were tested for each system. Table 5.10 summarises the mean CTE and Tg for the nanomodified system compared to the neat epoxy. It was found that the inclusion of nanoclay enhanced the thermal properties of Epikote 828. Table 5.10 shows that the mean CTE below and above Tg were significantly reduced with increasing in nanosilica content. For instance, the incorporation of 5 wt% nanoclay reduced the CTE below Tg by about 11% and CTE above Tg by about 14% than the pure epoxy. This is due to the particle rigidity which obstructs the expansion of polymer chains at elevated temperatures. Hence, this contributes to the lower CTE values for nanoclay-modified Epikote 828 system.

Table 5.10 also shows the effect of nanoclay on the Tg of the Epikote 828. It was found that the nanocomposite has a higher Tg compared to the pure epoxy. The Tg values increased steadily with the increasing of nanoclay content. This was identified by both TMA and DSC instruments. For instance, the addition of 5 wt% nanoclay increased Tg by about 12% which was measured by TMA, while 13% increase was

recorded by DSC. Therefore the increase in Tg values with increasing in nanoclay content was certified using these two instruments. This increase is possibly due to large surface areas (750 m^2/g) provided by the nanoclay obstructing the segmental motion of cross-links of the polymer at elevated temperature.

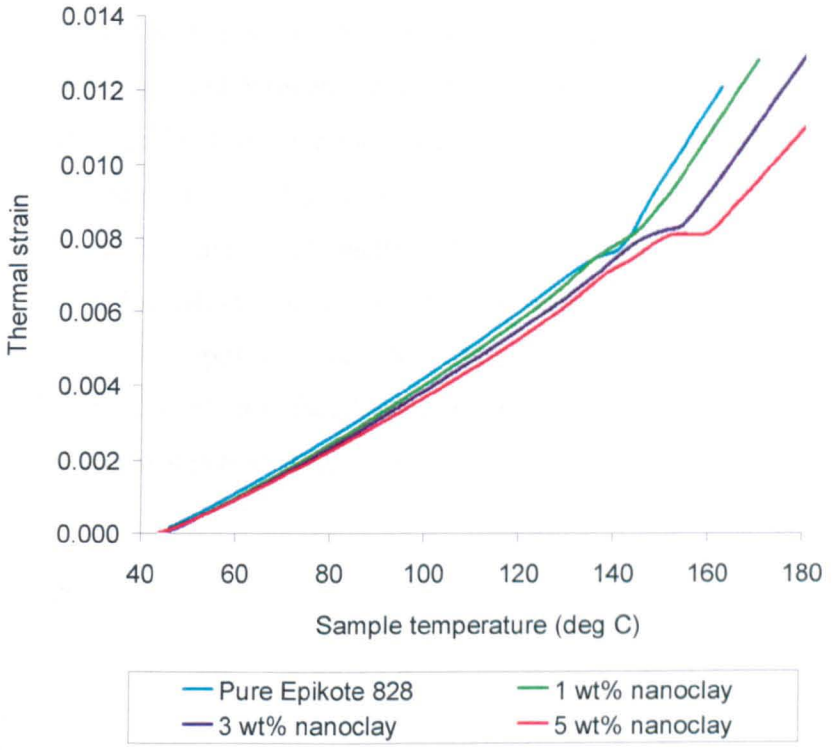

Figure 5.18: Typical thermal strain-temperature curves showing the effect of I.28 nanoclay on dimensional stability of Epikote 828.

Table 5.10: Effect of nanoclay on CTE and Tg of Epikote 828.

Thermal properties	**Pure resin**	**Nanomodified system (NMS)**		
		1 wt% clay	**3 wt% clay**	**5 wt% clay**
Mean CTE below Tg (με/°C)	79.78 ± 0.47	77.27 ± 0.43	74.88 ± 0.24	71.29 ± 0.56
Mean CTE above Tg (με/°C)	187.76 ± 3.59	184.59 ± 6.54	173.59 ± 4.32	160.79 ± 8.89
Tg measured by TMA (°C)	139.52 ± 1.02	140.65 ± 0.95	149.86 ± 1.74	155.80 ± 1.11
Tg measured by DSC (°C)	141.91 ± 0.77	146.89 ± 0.98	155.87 ± 0.44	161.09 ± 0.20

5.4.3 Compressive properties

Typical true stress-strain curves of cylindrical and cubic specimens loaded in static uniaxial compression were illustrated in Figures 5.19 and 5.20. Both figures show the effect of I.28 nanoclay on the compressive stress-strain behaviour of Epikote 828. It was found that the nanoclay enhanced the compressive modulus of the epoxy as indicated by a steeper slope in elastic region of the stress-strain curve. However a detrimental effect on the compressive yield strength and failure strain was observed. Reduction in compressive strength for 1 and 3 wt% nanoclay was also recorded. This shows that the intercalated structure of nanoclay create high localised stresses in the matrix during compression. A weak nanoparticle-matrix interface restricts the ability of transferring load and plastic deformation. This causes the nanocomposites to fail prematurely. Table 5.11 shows that nanocomposites have lower yield strength compared to the pure system. This is evidence of weak interfacial adhesion between the particles and the matrix which leads to inter-platelets sliding and reduction in plastic yielding stress and strain.

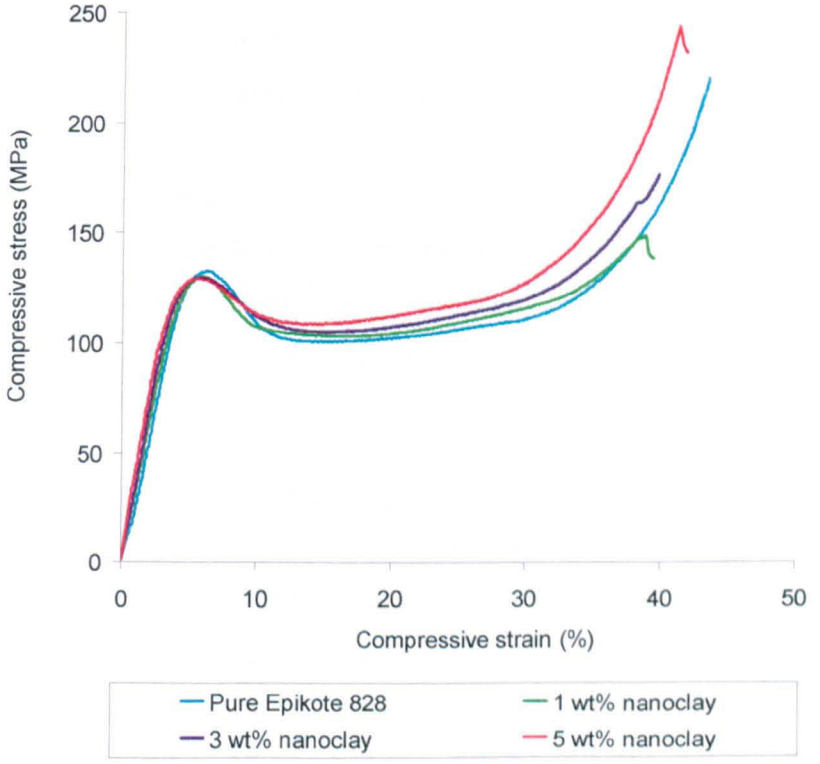

Figure 5.19: Typical true stress-strain curves of cylindrical specimens loaded in static uniaxial compression showing the effect of I.28 nanoclay on the compressive stress-strain behaviour of Epikote 828.

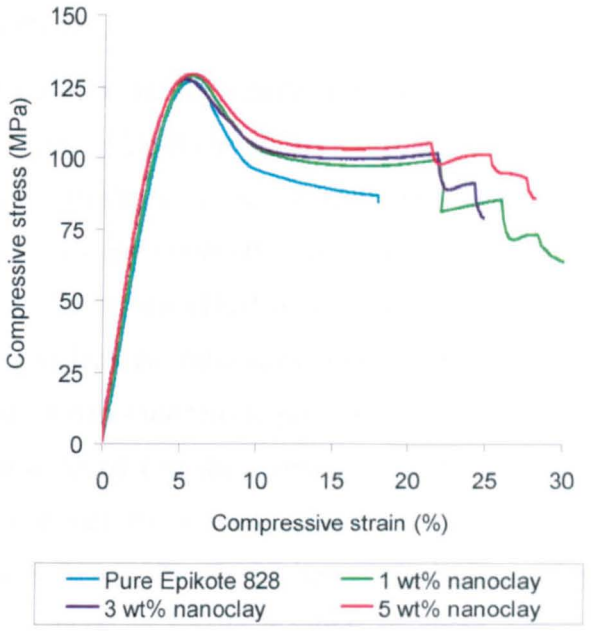

Figure 5.20: Typical true stress-strain curves of prismatic (cubic) specimens loaded in static uniaxial compression showing the effect of nanosilica on the compressive stress-strain behaviour of Epikote 828.

Table 5.11: Effect of specimen shape and geometry on the compressive properties of nanoclay-filled epoxy nanocomposites.

Compressive property	**Pure Epikote 828**		**Nanomodified system**					
			1 wt% nanoclay		**3 wt% nanoclay**		**5 wt% nanoclay**	
	Cyl.	**Cubic**	**Cyl.**	**Cubic**	**Cyl.**	**Cubic**	**Cyl.**	**Cubic**
Elastic modulus, E (GPa)	3.02 ± 0.06	3.12 ± 0.02	3.28 ± 0.01	3.27 ± 0.01	3.44 ± 0.04	3.45 ± 0.01	3.60 ± 0.03	3.58 ± 0.01
Yield stress σ_y (MPa)	132.99 ± 0.20	126.59 ± 0.39	129.95 ± 0.54	127.94 ± 0.18	129.63 ± 0.21	127.78 ± 0.27	128.90 ± 0.11	128.08 ± 0.30
Strain at yield point, ε_y (%)	6.50 ± 0.05	5.53 ± 0.03	5.65 ± 0.09	5.83 ± 0.04	5.77 ± 0.07	5.73 ± 0.06	5.53 ± 0.07	5.62 ± 0.10
Compressive strength, σ_u (MPa)	211.47 ± 3.17	126.59 ± 0.39	153.76 ±13.43	127.94 ± 0.18	179.32 ± 3.60	127.78 ± 0.27	231.26 ±10.82	128.08 ± 0.30
Strain at break, ε_f (%)	42.66 ± 0.65	16.49 ± 1.56	36.74 ± 2.12	23.82 ± 1.37	40.02 ± 0.23	23.92 ± 1.19	41.28 ± 0.27	21.23 ± 1.39

5.4.4 Tensile properties

The effect of I.28 nanoclay on the tensile stress-strain response of the epoxy polymer was illustrated in Figure 5.21. It can be seen that the presence of nanosilica increased the slope of the stress-strain curve. Nanocomposites exhibited higher tensile modulus, however a reduction in tensile strength and failure strain was recorded. Moreover, the fracture toughness of the nanomodified system was also lower than that of the pure resin as indicated by the smaller area under stress-strain curve, see Figure 5.21.

Table 5.12 summarises the tensile properties of nanomodified system compared to the pure resin. It was found that the compressive modulus increases with increases in nanoclay content. The increase in modulus is expected because the elastic modulus of nanoclay is about 170 GPa [117]. The highest content of nanoclay in the epoxy (5 wt%) give a remarkable increase in tensile modulus of about 22%. In contrast, the tensile strength and failure strain were reduced with increasing in nanoclay content. For example, the addition of 5 wt% nanoclay reduced the tensile strength and failure strain for about 22% and 40%, respectively. The presence of particle agglomeration or clusters of intercalated rich regions, voids in the specimen and weak interfacial adhesion between nanoclay and the matrix are some factors which possibly degrade the tensile properties of the epoxy.

5.4.5 Flexural properties

Figure 5.22 shows the typical flexural stress-strain curves of neat and nanomodified polymers. In general, it has a similar effect as loading in tension. It was found that the slope of the stress-strain curves increases with increasing in nanoclay content. This indicates that nanoclay enhances the flexural modulus of the epoxy. The nanocomposites fail in a brittle manner without any plastic deformation. Table 5.12 summarises the flexural properties of neat and nanomodified systems. The addition of nanoclay enhanced flexural modulus however, reduced the flexural strength and failure strain of the epoxy. For example, the addition of 5 wt% nanoclay enhanced the elastic modulus by 22% and reduced the flexural strength by 29% and failure strain by 50%. The reduction in flexural strength and failure strain may be due to similar reasons discussed earlier.

5.4.6 Fracture toughness properties

Table 5.12 shows also the effect of nanoclay on fracture toughness of Epikote 828. At least five specimens were tested for each system and the results of typical load-crack opening displacement curves obtained from the compact tension tests with 1 – 5 wt% nanoclay were given in Appendix A. It was found that, the load at crack growth initiation F_Q for nanomodified system was slightly higher than that of the neat epoxy. Hence, the nanocomposites slightly enhanced the fracture toughness of the epoxy, see Table 5.12. For instance, the addition of 3 wt% nanoclay increased maximum load by about 28% compared to that of the pure Epikote 828. This gives enhancement in critical stress intensity factor and critical energy release rate by about 30% and 60%, respectively. There is no further improvement in fracture toughness by adding more than 3 wt% nanoclay. This is due to a weaker interfacial adhesion between matrix and nanofiller with increasing in nanoclay content.

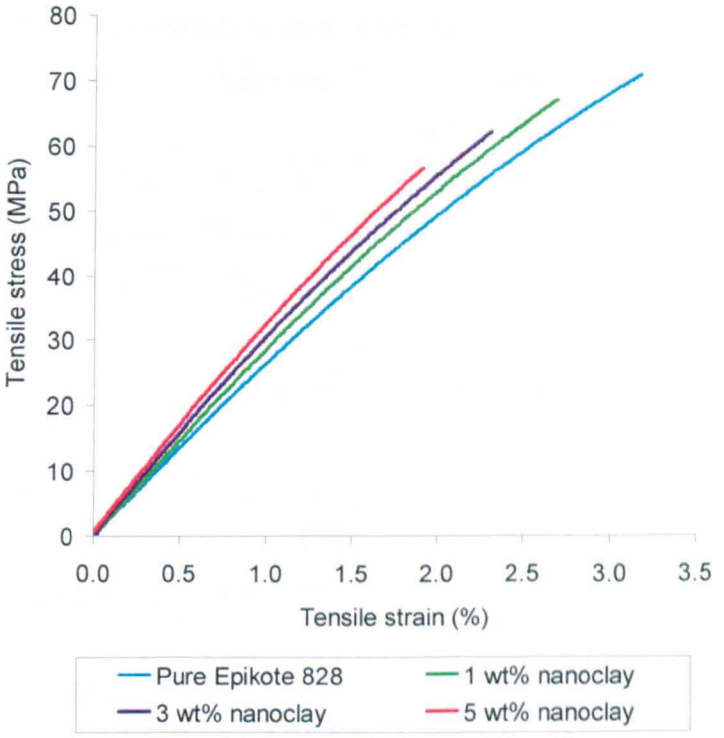

Figure 5.21: Typical Tensile stress-strain curves of I.28 nanoclay-filled Epikote 828 compared to the neat epoxy.

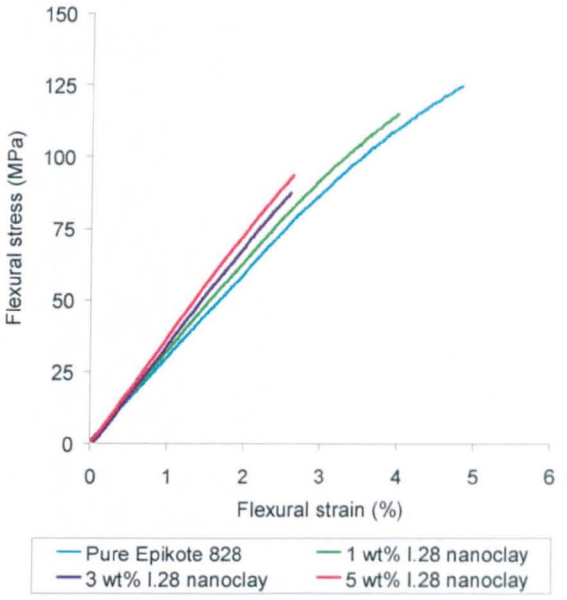

Figure 5.22: Typical flexural stress-strain curves of I.28 nanoclay-filled Epikote 828 compared to the neat epoxy.

Table 5.12: Tensile, flexural and fracture toughness properties of the unmodified and nanomodified Epikote 828 resin with various concentration of I.28 nanoclay.

Material properties	**Pure resin**	**Nanomodified system (NMS)**		
		1 wt% clay	**3 wt% clay**	**5 wt% clay**
Tensile modulus, E_t (GPa)	2.75 ± 0.02	3.03 ± 0.01	3.16 ± 0.01	3.34 ± 0.01
Tensile strength, $\sigma_{u,t}$ (MPa)	70.84 ± 1.08	66.77 ± 3.51	57.88 ± 4.68	55.09 ± 4.00
Tensile strain at break, $\varepsilon_{f,t}$ (%)	3.28 ± 0.09	2.71 ± 0.17	2.16 ± 0.19	1.97 ± 0.17
Flexural modulus, E_b (GPa)	2.88 ± 0.03	3.22 ± 0.03	3.38 ± 0.07	3.50 ± 0.03
Flexural strength, $\sigma_{u,b}$ (MPa)	117.73 ± 8.70	113.93 ± 11.19	84.55 ± 1.99	83.41 ± 4.49
Flexural strain at break, $\varepsilon_{f,b}$ (%)	4.84 ± 0.61	4.13 ± 0.55	2.49 ± 0.04	2.43 ± 0.15
Maximum load, F_Q (N)	217.35 ± 7.43	229.20 ± 5.04	278.90 ± 9.46	249.20 ± 11.25
Critical stress intensity factor, K_{IC} (MPa. $\sqrt{m}$)	0.67 ± 0.02	0.71 ± 0.02	0.87 ± 0.03	0.77 ± 0.03
Critical energy release rate, G_{IC} (J/m^2)	152.73 ± 10.84	179.87 ± 7.18	244.63 ± 15.42	177.05 ± 15.80

5.5 Nanoclay-filled Cycom 977-20 epoxy polymer

5.5.1 Morphology

The degree of dispersion and exfoliation of the clay nanoplatelets in the epoxy matrix was investigated using the TEM. Low magnification TEM micrographs (at 22,500x) show a good dispersion of nanoclay in the resin with three different clay contents prepared using two different methods as shown in Figure 5.23 (nanocomposites prepared using the 3-roll mill) and Figure 5.24 (nanocomposites prepared using the mechanical stirring). All TEM images at high magnification (170,000x) show that the gap between two adjacent platelets is more than 2.37 nm (see Figures 1 and 2). This indicates that the nanocomposites prepared using both methods produced either intercalated or exfoliated structures. This is very good since closely spaced platelets limit the ability of the polymer chains to intercalate the gallery (d-spacing) and this reduces the load transfer capability between nanoclay and polymer.

It was observed that, the 3-roll mill processing technique was more effective than the mechanical stirring method in separating nanomers I.30 nanoclay (which has a mean dry particle size of 8-10 μm) in the polymer. High magnification TEM images (at 170,000x) shows that the distance between clay platelets is more than 8 nm, see Figure 5.23. These indicate that 3-roll mill technique successfully produced an exfoliated type nanocomposite. At low clay content (≤ 3 wt%) a fully exfoliated structure with randomly dispersed nanoplatelets were observed with an occasional presence of ordered exfoliated structure. However, at clay content more than 3 wt%, the TEM images show an ordered exfoliated structure with d-spacing of 10-17 nm (see Figure 5.25a). Since a very small area of the specimen was sampled in each TEM image, all measurements of d-spacing were taken from multiple images captured from various locations of the specimen (at least 3 samples and 5 images for each sample). At high clay content (≥ 5 wt%), even though the morphology of nanoclay is predominantly exfoliated with ordered structure, low magnification TEM image shows evident of resin-rich region and nanofillers-rich region (see Figure 5.23c(i)), therefore there may be some intercalated nanoclay structures presence at very high nanofillers-rich regions.

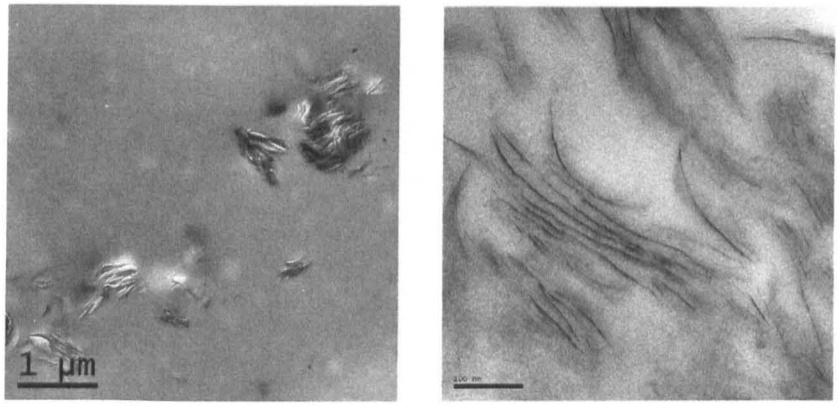

(i) (ii)

(a) 1 wt% nanoclay

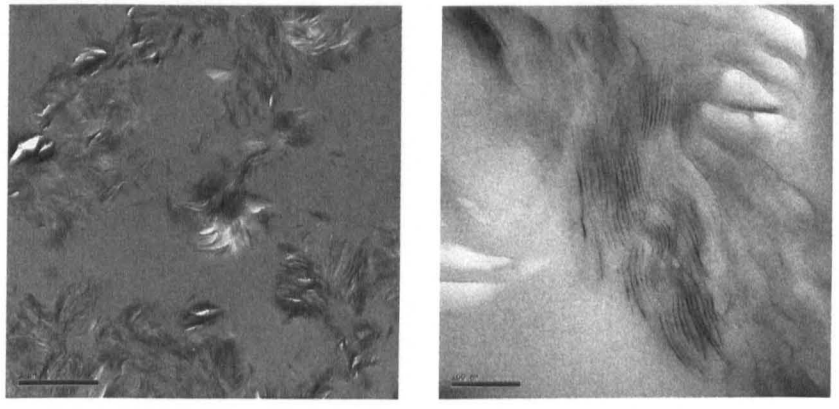

(i) (ii)

(b) 3 wt% nanoclay

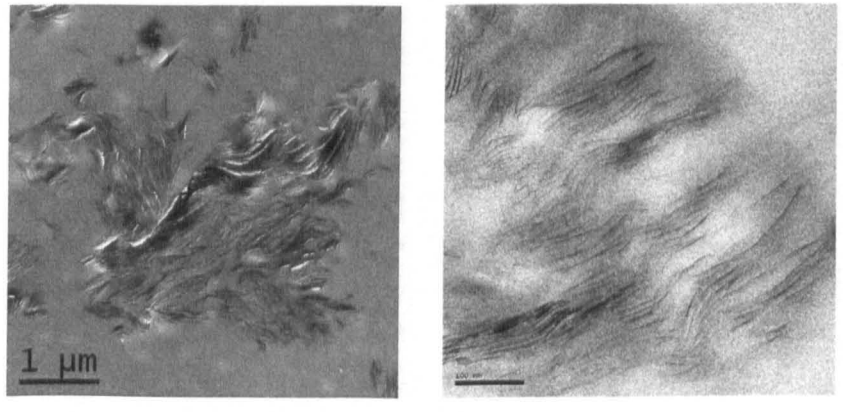

(i) (ii)

(c) 5 wt% nanoclay

Figure 5.23: TEM micrographs showing (a) a random exfoliated structure of 1 wt%, (b) an ordered exfoliated structure of 3 wt% and (c) an ordered exfoliated structure of 5 wt% clay nanoplatelets in Cycom 977-20, prepared using the 3-roll mill method and observed under two different magnifications, (i) 22500x and (ii) 170000x.

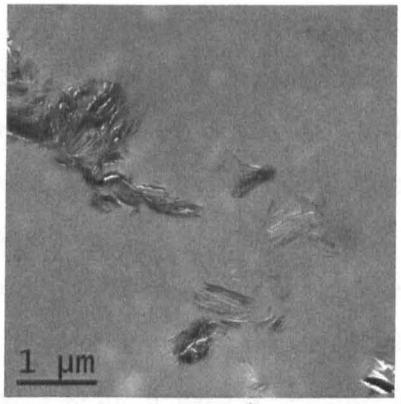

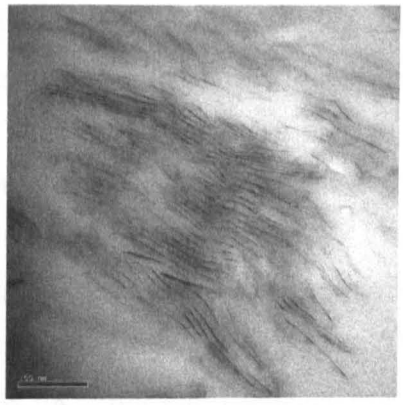

(i) (ii)

(a) 1 wt% nanoclay

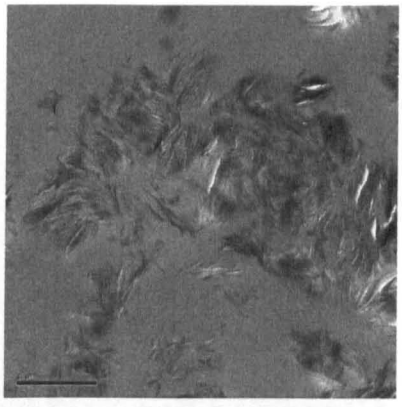

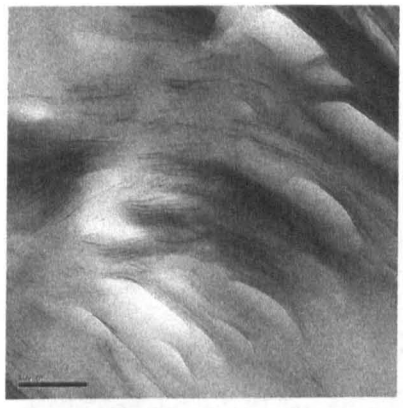

(i) (ii)

(b) 3 wt% nanoclay

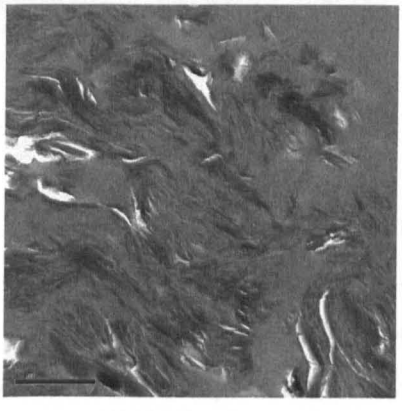

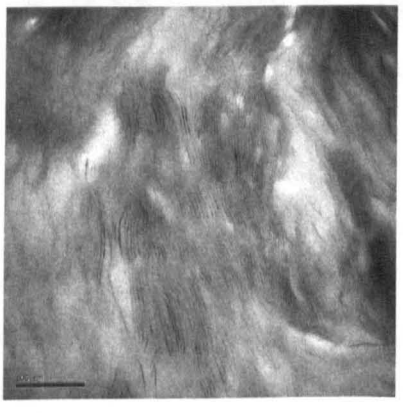

(i) (ii)

(c) 5 wt% nanoclay

Figure 5.24: TEM micrographs showing (a) an ordered exfoliated structure of 1 wt%, (b) an intercalated structure of 3 wt% and (c) an intercalated structure of 5 wt% clay nanoplatelets in Cycom 977-20, prepared using the mechanical stirring technique and observed under two different magnifications, (i) 22500x and (ii) 170000x.

For the nanocomposites prepared using the mechanical stirring method, the morphology of nanoclay is predominantly intercalated with some exfoliated regions (see Figure 5.24). At low clay content, 1 wt%, TEM image shows an ordered exfoliated structure with occasionally presence of randomly oriented clay nanoplatelets (see Figure 5.24a). The d-spacing was seen to reduce with increasing clay content. At more than 3 wt% nanoclay, TEM images show an intercalated structure of nanocomposites. The d-spacing of 5 wt% nanoclay in epoxy is about 5-6 nm (see Figure 5.25b). This is very low compared to the d-spacing obtained using the 3-roll mill technique at similar clay content (see Figure 5.25a).

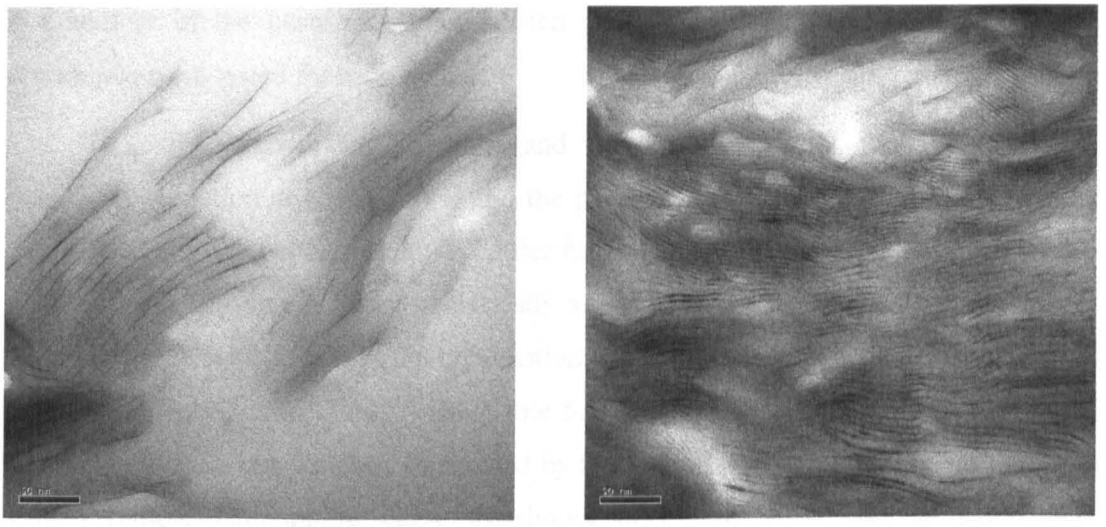

(a) 3-roll mill
(d-spacing 10-17 nm)

(b) Mechanical stirring
(d-spacing 5-6 nm)

Figure 5.25: TEM micrographs showing (a) an ordered exfoliated and (b) intercalated structures of 5 wt% clay nanoplatelets in Cycom 977-20 prepared using the 3-roll mill and mechanical stirring methods, respectively, and observed under 225000x magnification. One clay sheet has 1nm thickness and about 100-200 nm length.

5.5.2 Thermogravimetry analysis and constituent volume fraction

The effect of I.30 nanoclay on themal degradation behaviour and density of Cycom 977-20 was studied. The volume fraction of nanoclay in epoxy matrix was calculated based on the TGA results. Figure 5.26 illustrates (i) percentage of weight loss and (ii) rate of weight loss as a function of sample temperature. All samples started to decompose at about 340°C. The decomposition mechanisms involved during combustion of pure Cycom 977-20 were explained in the previous chapter (see Section 4.3.1). As shown in Figure 5.26, nanocomposites exhibited a similar thermal decomposition mechanism to that of the pure epoxy. However at the last stage (Stage D), the material remaining behind after exposing the nanocomposites to air was the white powder clay. Table 5.13 summarises the average constituent weight fraction and maximum degradation temperature of the pure and nanomodified epoxy with their carbon residues. Three specimens were tested for each system.

Table 5.13 shows that the pure and nanomodified resins undergo maximum thermal degradation at about 430°C and the percentage of total weight loss decreasing with increasing the nanoclay content. After holding at 550°C for 1 hr, the nitrogen gas flowing over the sample was automatically switched to oxygen and hence, the carbon residues which were left from the combustion of the epoxy resins were burnt off with a total mass loss of about 27-30 wt%. Table 5.13 shows that the maximum degradation temperature of carbon residues (identified by the second peak of the rate of weight loss versus sample temperature curve as shown in Figure 5.26) was increased with increasing nanoclay content. For instance, the addition of 5 wt% nanoclay increased the maximum degradation temperature of resin residues by 64°C compared to the neat polymer. This suggests that the nanofiller-matrix interfacial bonding is very strong and therefore higher temperatures are needed to remove the epoxy which is stuck on the particle surface. Finally, the material remaining behind after exposing the sample to oxygen was the nanoclay. Table 5.13 shows that for the three nanomodified systems investigated in the present study, the average nanoclay weight fraction was 1.1, 2.7 and 4.8 wt%.

Table 5.13 summarises also the density and volume fraction of nanoclay in the epoxy matrix. A density of 1.297 g/cm^3 was measured for the unmodified resin. The measured density was found to increase with the nanoclay content. The increase in density is expected because the density of silica, ρ_{si} = 1.71 g/cm^3, is greater than that of

the epoxy matrix. For instance, the inclusion of 5 wt% nanoclay increased the density of the epoxy by about 1.5%. The measured density was compared to the theoretical prediction based on the rule of mixtures. It was found that the measured density was in a very good agreement to the theoretical values. However, at high nanoclay content the measured density was slightly lower compared to the predicted value. The viscosity of the resin increased with increasing nanoclay content. Therefore the degassing process became crucial and a small amount of air entrapped after curing slightly reduced the density of the high clay content nanocomposite. These density data were used for the calculation of nanoclay volume fraction in the epoxy resin. Table 5.13 shows that for the three nanomodified systems investigated in the present study the average volume fraction of nanoclay in the epoxy resin was 0.8, 2.1 and 3.7 vol%.

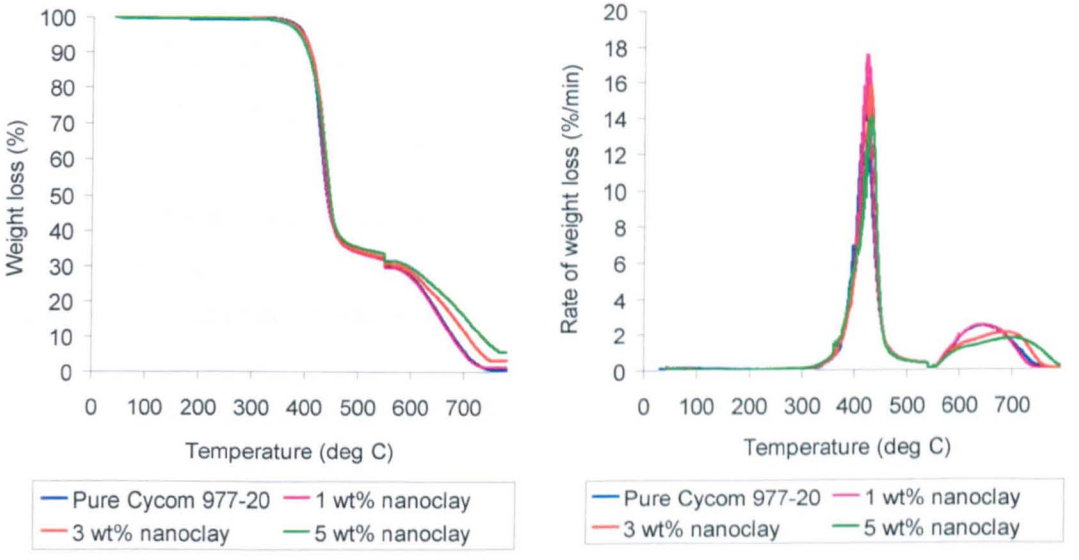

Figure 5.26: Typical TGA results showing the effect of I.30 nanoclay on thermal degradation behaviour of Cycom 977-20.

Table 5.13: Physical and thermal properties of nanoclay-modified Cycom 977-20 compared to the pure resin.

Physical and thermal properties	**Pure resin**	**Nanomodified system (NMS)**		
		1 wt% clay	**3 wt% clay**	**5 wt% clay**
Weight fraction of epoxy resin (%)	70.18 ± 1.11	69.82 ± 1.59	68.45 ± 0.72	67.02 ± 1.06
Maximum degradation temperature of epoxy resin (°C)	427.17 ± 3.71	429.77 ± 3.53	435.88 ± 2.90	439.24 ± 2.50
Weight fraction of carbon residue (%)	29.67 ± 0.59	28.88 ± 1.14	28.05 ±0.64	27.28 ± 1.19
Maximum degradation temperature of carbon residue (°C)	645.80 ± 1.40	646.13 ± 3.51	696.75 ± 6.34	710.64 ± 9.02
Weight fraction of nanoclay (wt%) (measured by TGA), W_{clay} (%)	-	1.10± 0.09	2.73 ± 0.21	4.81 ± 0.15
Density (measured by density balance), ρ_{nc} (g/cm^3)	1.297 ± 0.001	1.300 ± 0.002	1.305 ± 0.001	1.312 ± 0.001
Theoretical density (calculated using the rule of mixtures) $\rho_{nc}(g/cm^3) = \rho_{ep}V_{ep} + \rho_{si}V_{clay}$	1.297	1.302	1.308	1.316
Volume fraction of nanoclay (vol%) $V_{clay}(\%) = W_{clay} \times \frac{\rho_{nc}}{\rho_{clay}}$	-	0.8	2.1	3.7

5.5.3 Dimensional stability and glass transition temperature

Figures 5.27 and 5.28 illustrate the effects of 1, 3 and 5 wt% I.30 nanoclay on the dimensional stability of Cycom 977-20. Figure 5.27 shows that the incorporation of nanoclay into the epoxy reduces the slope of the thermal strain-temperature curve. This means that the presence of nanoclay reduces the CTE of the epoxy. This can clearly be seen in the differential CTE curve as shown in Figure 5.28. Nanocomposites exhibited lower CTE (for both below and above Tg) compared to the pure resin. Figure 5.28

shows that the nanofilled system has similar thermal behaviour to that of the pure resin. The CTE value increases linearly with the sample temperature, until it reaches glass transition temperature where the rate of expansion changes and cause significant disruptions to the CTE. After this region, the CTE value is more than twice as high compared to the CTE value below the Tg region. The lower CTE of the nanomodified system is always related to the lower CTE and high modulus of elasticity of the nanoclay. As the material is heated, the nanoclay restrains the dimensional expansion and reduces the CTE value.

At least three samples were tested for each system. Table 5.14 shows that the mean CTE below and above Tg were reduced with increases in nanoclay content. For instance, the incorporation of 5 wt% nanoclay reduced the CTE below Tg for about 11% and CTE above Tg for about 10% than the pure epoxy. In addition, Table 5.14 shows the effect of nanoclay on the Tg of Cycom 977-20. It was found that the nanocomposite has a lower Tg compared to the pure epoxy. The Tg values decreased steadily with the increasing of nanoclay content. This was identified by both TMA and DSC instruments. For instance, the addition of 5 wt% nanoclay decreased Tg for about 3% which were recorded by both TMA and DSC.

Clay particles have high specific surface area (about 750 m^2/g [117]) therefore this provides a huge amount of interfacial area if the nanoclay is fully exfoliated in the resin. In order for the nanoclay to be compatible with the epoxy and to promote clay-epoxy bonding, the surfaces of the nanoclay were treated with surfactant (for instance Octadecylamine is used to modify I.30 nanoclay). Good adhesion is achieved by proper interaction of the treated surface of the particles and the polymer chains. This drastically alters the cross-link density of the resin. In addition, the interphase, in between the silicate layers and the epoxy matrix, was formed due to the surfactant. The properties of this interphase region are different from the matrix. At high temperature, this region may be weaker than the epoxy matrix and contributes to a lower Tg of the nanocomposites compared to the pure polymer.

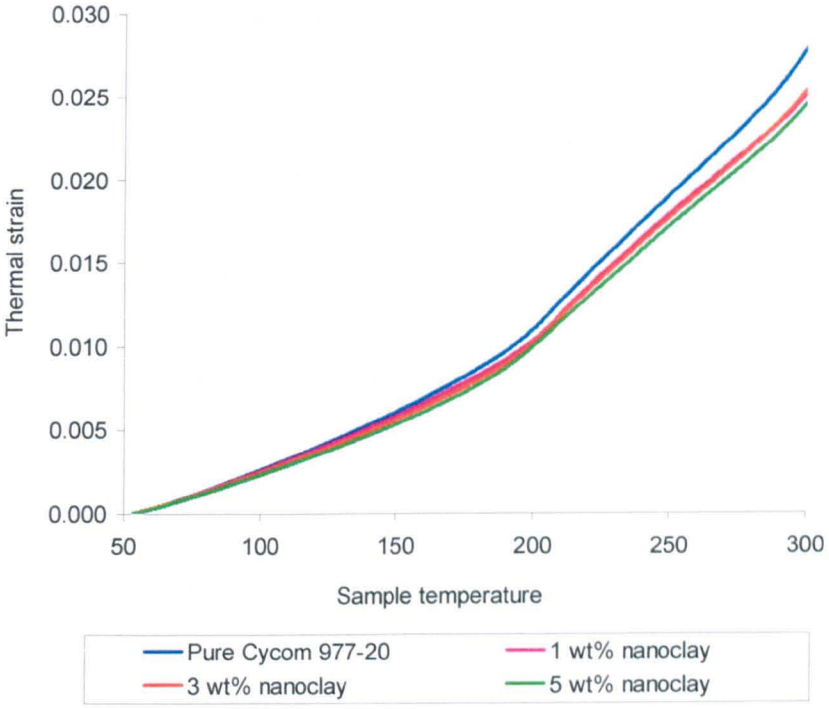

Figure 5.27: Typical thermal strain-temperature curves showing the effect of I.30 nanoclay on dimensional stability of Cycom 977-20.

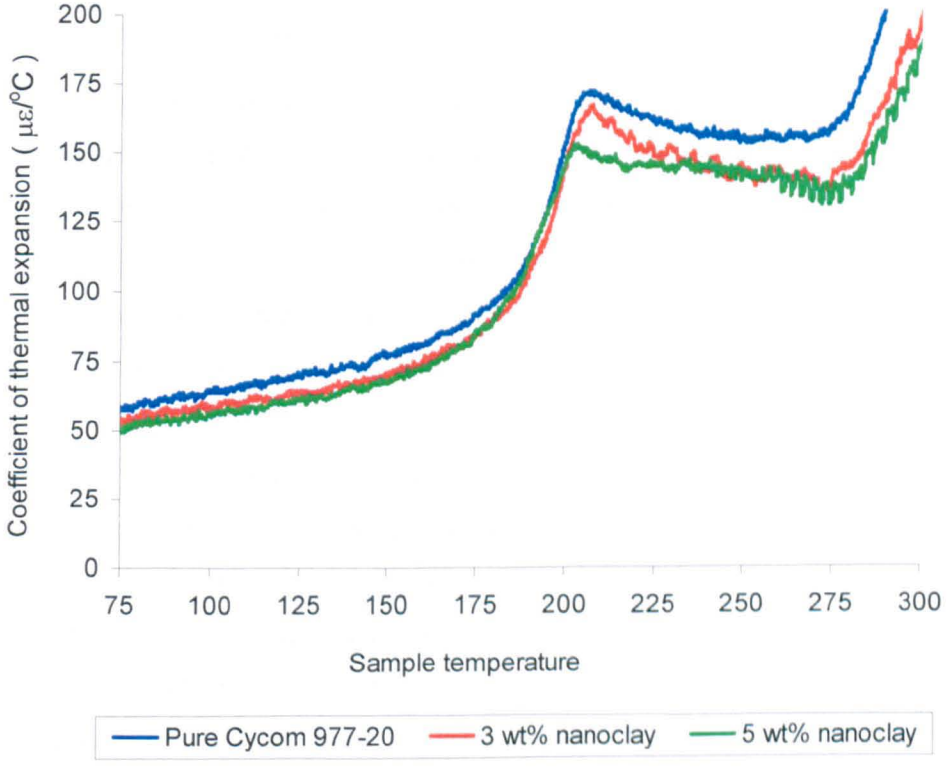

Figure 5.28: Typical CTE-temperature curves showing the effect of 3 and 5 wt% nanoclay on CTE of Cycom 977-20.

Table 5.14: A summary of CTE and Tg of nanoclay-modified Cycom 977-20 compared to the pure system.

Thermal properties	Pure resin	Nanomodified system (NMS)		
		1 wt% clay	3 wt% clay	5 wt% clay
Mean CTE below Tg (με/°C)	64.62 ± 0.24	62.54 ± 1.00	59.39 ± 0.83	57.25 ± 0.67
Mean CTE above Tg (με/°C)	156.21 ± 1.18	148.26 ± 4.12	144.86 ± 1.28	140.76 ± 0.74
Tg measured by TMA (°C)	199.77 ± 1.80	198.20 ± 0.65	196.74 ± 1.10	194.41 ± 0.60
Tg measured by DSC (°C)	210.33 ± 0.85	208.42 ± 0.39	206.09 ± 0.56	203.45 ± 0.45

5.5.4 Compressive properties

5.5.4.1 The effect of nanoclay on stress-strain behaviour and compressive properties

The effect of nanoclay on the true compressive stress-strain response of the epoxy polymer prepared using the 3-roll mill method was illustrated in Figure 5.29. It can be seen that the presence of nanoclay enhanced the compressive stress-strain behaviour of the epoxy polymer. The slope of the elastic region shows that the incorporation of nanoclay increases the compressive modulus. The ultimate stress was also increased with increasing nanoclay content. In addition, the presence of rigid nanoclay particles (Young modulus = 170GPa) improves ductility and promoted higher plastic hardening behaviour after yielding of the epoxy without reducing its strain to failure. This suggests that the rigid nanoparticles introduce additional mechanisms of energy absorption during compression. This gives a higher resistance to deformation which results in higher compressive stress and plastic hardening. The homogeneous dispersion of these high stiffness nanofillers in the matrix enhanced the fracture toughness of the system (larger area under stress-strain curve, see Figure 5.29).

The compressive properties of nanomodified epoxy systems, which were prepared using the 3-roll mill technique, are summarised in Table 5.15. Generally, it was found that the addition of nanoclay improved the compressive properties of the epoxy.

Incorporation of fully exfoliated and randomly dispersed 1 wt% nanoclay enhanced the compressive modulus and strength by 11%, yield stress by 4% and failure strain by 12%. This suggests that the nanofiller-matrix interaction is very favourable and therefore stresses are efficiently transferred via the interface, which leads to higher strength compared to the pristine polymer. As the clay content increases, the elastic modulus, strength and failure strain also increases. It is very interesting to note that the nanocomposites exhibit an improvement in elastic modulus without sacrificing their strength and strain to failure.

The enhancement of these properties is directly attributed to the reinforcement provided by the dispersed clay nanoplatelets. At high nanoclay content (≥ 3 wt%), the presence of rich regions of ordered exfoliated structure and possibly some intercalated structures limits the reinforcement capability. For instance, the addition of 5 wt% nanoclay enhanced the compressive modulus by 19%, compressive strength by 17% and failure strain by 29% with slightly increased in stress at yield of 6%. It can be seen that, even though, the compressive modulus show substantial improvement with increasing in the clay content, the yield strength was moderately improved. The yield strength of the polymer is one of the most important characteristics to determine quality of interfacial adhesion between the particles and the polymer. In theory, a strong particle/matrix interfacial bonding restricts the mobility of polymer chains hence increases the yield strength of the polymer under loading. Therefore, the reinforcement benefit is substantially greater for the fully exfoliated nanocomposite (of 1 wt% clay) compared to the ordered exfoliated and intercalated nanocomposite (>1 wt% clay).

5.5.4.2 The effect of processing methods

The effect of processing methods (3-roll mill and mechanical stirring) on the true compressive stress-strain response and compressive properties of the epoxy was also studied. Figure 5.30 shows the stress-strain response of nanocomposites prepared using mechanical stirring method compared to the unmodified system. It can be seen that the presence of nanoclay improves ductility and promotes higher plastic hardening behaviour of the epoxy polymer. However the performance of the nanocomposites significantly depends on the morphology of the nanoclay in the epoxy. It shows a similar reinforcement effect as nanocomposites prepared using the 3-roll mill method (see Figure 5.29).

The compressive properties were summarised in Table 5.15. The measured modulus was found to increase with an increasing proportion of nanoclay. Incorporation of 1 wt% nanoclay (with ordered exfoliated structure) enhanced the compressive modulus by 11%, compressive strength by 6%, failure strain by 14% and a small improvement in yield stress. As the clay content increases, it was observed that there was no further improvement in compressive properties. This is due to the intercalated structure of the nanoclay which limits the stress transfer capability between the nanofillers and matrix when loaded in compression.

The yield stress of nanocomposites prepared using the mechanical stirrer was lower than those prepared using the 3-roll mill suggesting a weaker interface between the nanofiller-matrix which perhaps contribute to interplatelets sliding under compression. Lower strength and strain to failure recorded possibly because of the presence of intercalated rich regions, Figure 5.24c(i) introducing high local stress concentrations and, hence, led to premature failure. In general, the compressive properties were improved with increasing in the degree of clay nanolayer separation. Therefore, 3-roll mill was more effective than direct mixing to produce high performance nanocomposite systems.

5.5.4.3 The effect of specimen shape

The compression tests were also conducted on prismatic specimens (of nanocomposites prepared using mechanical stirring method) to study the effect of specimen shape and geometry on the compressive properties. Figure 5.31 shows typical true compressive stress-strain curves of nanocomposites compared to the unmodified system and table 5.15 shows the summary of compressive properties. It was found that the compressive modulus was increased significantly with increasing clay content. This is similar to those tested using cylindrical specimens. However, there was no significant improvement in compressive strength and yield stress by adding nanoclay into the epoxy and even worse, it gave a detrimental effect on failure strain. The prismatic specimens failed prematurely due to buckling, which was triggered by longitudinal cracking formed at the specimen's edges (sharp corners) near the loaded ends.

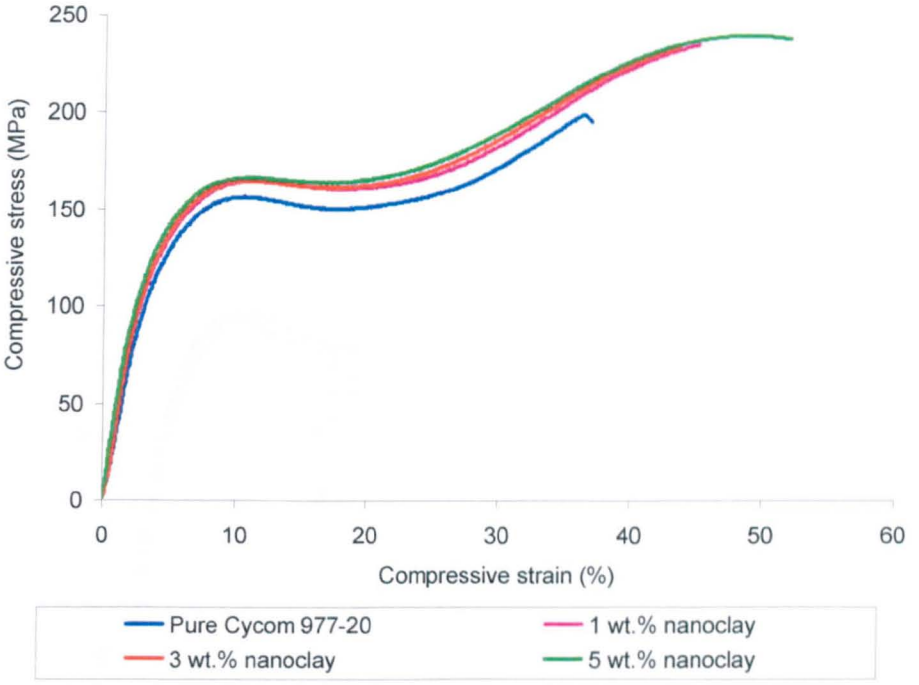

Figure 5.29: Typical true stress-strain curves of cylindrical specimens of clay-epoxy nanocomposites (prepared using the 3-roll mill technique) loaded in static uniaxial compression.

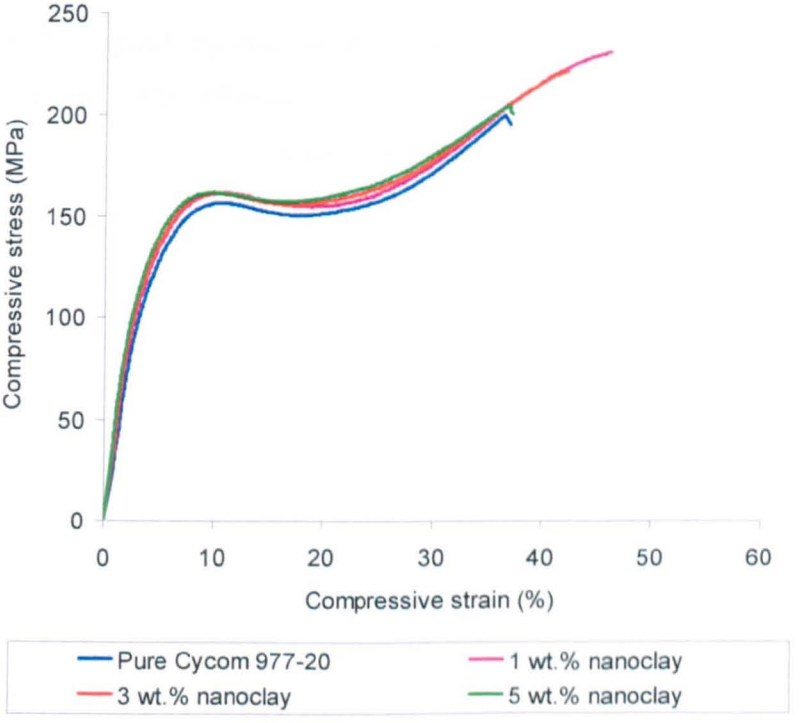

Figure 5.30: Typical true stress-strain curves of cylindrical specimens of clay-epoxy nanocomposites (prepared using the mechanical stirring method) loaded in static uniaxial compression.

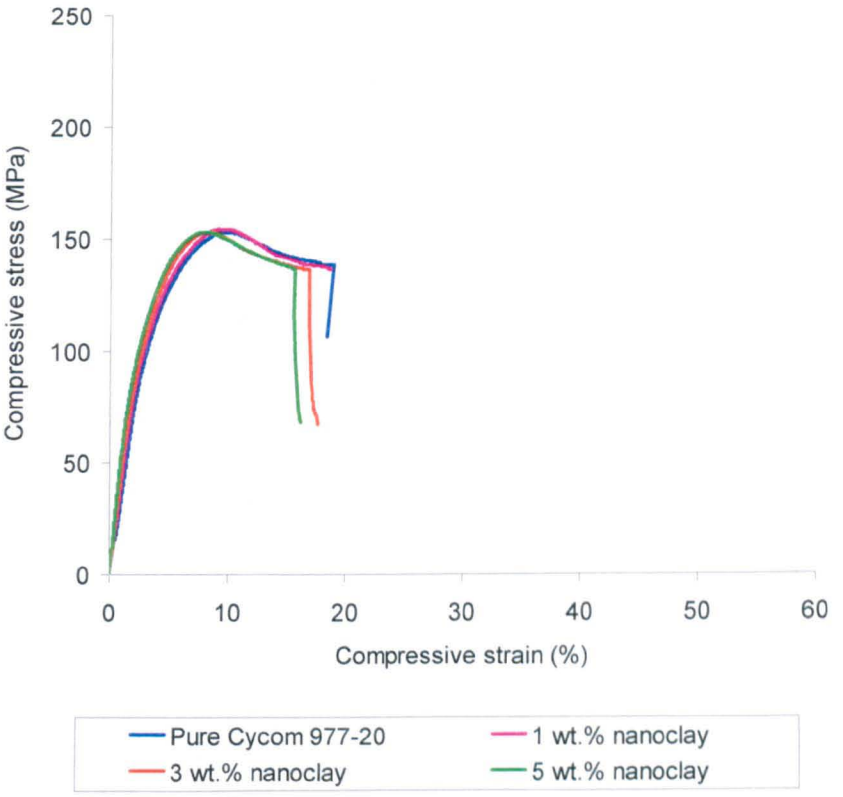

Figure 5.31: Typical true stress-strain curves of cubic specimens of clay-epoxy nanocomposites (prepared using the mechanical stirring method) loaded in static uniaxial compression.

Table 5.15: Summary of compressive properties of nanoclay-modified Cycom 977-20 epoxy nanocomposites compared to the neat system. This table shows the effect of clay contents, processing methods and specimen shape and geometry on the compressive properties of epoxy polymer.

Compressive properties	**Nanomodified system**										
	Three-roll mill (Cylindrical specimen)				**Mechanical stirrer (Cylindrical specimen)**			**Mechanical stirrer (Cubic specimen)**			
	0 wt% (pure)	**1 wt%**	**3 wt%**	**5 wt%**	**1 wt%**	**3 wt%**	**5 wt%**	**0 wt% (pure)**	**1 wt%**	**3 wt%**	**5 wt%**
Compressive modulus, E (GPa)	4.01 ± 0.05	4.43 ± 0.08	4.63 ± 0.06	4.75 ± 0.03	4.41 ± 0.02	4.62 ± 0.02	4.70 ± 0.01	4.00 ± 0.02	4.39 ± 0.04	4.65 ± 0.02	4.81 ± 0.02
Compressive stress at yield, σ_y (MPa)	158.00 ± 0.90	164.60 ± 0.62	162.90 ± 0.53	167.20 ± 0.28	161.30 ± 0.44	160.50 ± 0.53	161.60 ± 0.42	151.45 ± 0.36	151.94 ± 0.72	151.92 ± 0.48	152.51 ± 0.85
Compressive strain at yield point, ε_y (%)	10.96 ± 0.18	11.11 ± 0.06	10.36 ± 0.09	10.52 ± 0.14	10.33 ± 0.13	10.25 ± 0.13	10.11 ± 0.11	9.87 ± 0.37	9.87 ± 0.30	8.86 ± 0.37	8.43 ± 0.23
Compressive strength, σ_u (MPa)	205.81 ± 1.84	228.19 ± 7.74	228.00± 2.31	239.79 ± 1.39	218.65 ± 10.39	214.76 ± 9.90	207.22± 11.95	151.45 ± 0.36	151.94 ± 0.72	151.92 ± 0.48	152.51 ± 0.85
Compressive strain at break, ε_f (%)	37.16 ± 0.27	41.49 ± 1.80	43.04 ± 0.90	47.78 ± 1.50	42.34 ± 2.52	41.72 ± 2.73	39.17 ± 3.77	20.61 ± 0.88	20.18 ± 0.82	19.69 ± 1.63	19.43 ± 1.25

5.5.4.4 Prediction of compressive modulus

The compressive modulus for unmodified Cycom 977-20 polymer was 4.01 GPa, as shown in Table 5.15. The measured modulus was found to increase with the nanoclay content. A maximum modulus of 4.75 GPa was measured for the epoxy polymer with 5 wt% of nanoclay. The increase in modulus was expected because of the stiffer nanoclay (E = 172 GPa [121,173-175]), provided that there is a strong adhesion between the nanofillers and the resin.

The measured elastic modulus can be compared to theoretical predictions. In tension, there are several models that are commonly used to estimate the modulus of elasticity of particle-modified polymers [41,42,169-172,176-178]. The most widely used are the rule of mixtures [169], Halpin-Tsai [171,176], Lewis-Nielsen [41,42,172] and Mori-Tanaka [174-175,177-178]. Since the elastic response of most polymer matrices is similar in tension and compression, in the present work the compressive modulus is estimated using the rules of mixtures and Halpin Tsai models. Table 5.16 summarises relationships and the input data used to predict the elastic modulus of clay/epoxy nanocomposite. The upper bound rule of mixtures assumes that the material is a continuous fibre composite where the fibres are unidirectionally-aligned parallel to the direction of loading while the lower bound assumes the fibres unidirectionally aligned transverse to the direction of loading. The upper bound rule of mixtures always over predicts the elastic modulus of the nanocomposites since the particles cannot be treated like a continuous fibre. This can clearly be seen from Figure 32 where the upper bound rule of mixtures equation gives poor prediction when compared to the present experimental data.

The Halpin-Tsai model [171,176] includes the shape factor of the filler particle. This is a well known composite theory for predicting the stiffness of unidirectional fibre composite as a function of aspect ratio. The longitudinal and transverse elastic modulus are expressed in the general form:

$$E_c = \frac{1+\zeta\eta V_f}{1-\zeta V_f} E_m \tag{5.1}$$

where E_c and E_m represent the Young's modulus of the composite and matrix, respectively, ζ is a shape parameter dependent on the filler geometry and loading direction, V_f is the volume fraction of the fibre and η is given by

$$\eta = \frac{\frac{E_f}{E_m} - 1}{\frac{E_f}{E_m} + \zeta} \tag{5.2}$$

where E_f is the Young's modulus of the fibre. Halpin and Tsai noted that the value of ζ must lie between zero and infinity. If ζ=0 then Equation 5.1 reduces to the upper bound rule of mixtures while if ζ=∞ then it reduces to the lower bound rule of mixtures. In this study the clay nanoplatelets are treated as rectangular shape particles with thickness t=1 nm and width w=100 nm. The shape factors of ζ=2w/t and ζ=2 are used to calculate the elastic modulus of a polymer with particles aligned with the loading direction (called longitudinal elastic modulus E_L) and with particles perpendicular to the loading direction (called transverse elastic modulus E_T), respectively. However, Van Es [173] reported that the value of ζ=2w/t is too high for most particle modified polymers and recommended using ζ=2w/3t for the prediction of longitudinal elastic modulus. For polymers with randomly distributed particles, Van Es [173] proposed that the elastic modulus:

$$E_c = 0.49E_L + 0.51E_T \tag{5.3}$$

where the longitudinal and transverse moduli are calculated using the Halpin-Tsai model with ζ=2w/3t and ζ=2, respectively. This is known as Halpin-Tsai random model. Halpin-Tsai-Longitudinal (ζ=2w/t and ζ=2w/3t), Halpin-Tsai-Transverse (ζ=2) and Halpin-Tsai-Random models were used to estimate the compressive modulus of clay/epoxy system in this study. However, as shown in Figure 5.32, none of these models can successfully predict the measured increase in stiffness. This is because no ideal conditions are achieved for full exfoliation, dispersion and orientation of the clay platelets in the matrix. TEM micrographs show a mixture of randomly dispersed nanoplatelets and ordered exfoliated clusters (see Figure 5.23). Therefore, the shape

factor should include the effect of particle volume fraction and the degree of exfoliation or intercalation.

The effective thickness of clay nanoplatelets was estimated based on the TEM micrograph; for 1 wt% nanoclay/epoxy system (see Figure 5.23a), the stacked nanoplatelets (in ordered exfoliated nanocomposite) has an effective thickness of 10 nm (t_{eff} = 10 nanoplatelets x 1nm). Thus for 3 and 5 wt% nanoclay/epoxy have 30 and 50 effective thickness, respectively. The estimation of effective thickness t_{eff} was used to develop the shape factor ζ as a function of the clay volume fraction V_{cl} as follows:

$$\left(\zeta = \frac{2w}{t_{eff}}\right) \tag{5.4}$$

where the effective thickness is a function of particle volume fraction ($t_{eff} = 1200V_{cl}$), see Figure 5.33. This ζ value is incorporated into the Halpin-Tsai model to predict the compressive elastic modulus of the current clay/epoxy system. Figure 5.33 illustrates that for a very low nanoclay volume content, it is assumed that the nanocomposite has a randomly exfoliated structure and therefore, the effective thickness of clay nanoplatelets t_{eff}= 1 nm (actual thickness of one nanoclay sheet). For a high nanoclay content (usually max. of 7-10 vol.%) the effective thickness equals its width t_{eff} = 100 nm, which represents the tactoid type nanoclay.

Figure 5.32 shows that the current modified-Halpin-Tsai model gives a good agreement to the measured values. This analysis captured the effect of nanoclay volume fraction on the shape factor ζ where the stacked nanoplatelets reduce its value. This relationship was developed based on the number of clay nanoplatelets showed on the TEM micrographs and results in a reasonable correlation with experimental measurements.

Table 5.16: Prediction of compressive modulus of nanoclay-modified Cycom 977-20 epoxy nanocomposites using several types of theoretical models.

Theoretical models	**Ref.**	**Eqn. and input data**
Rule of mixtures	[169]	Upper bound, $E_{nc} = E_{cl}V_{cl} + E_{ep}V_{ep}$ Lower bound, $E_{nc} = \frac{E_{cl}E_{ep}}{E_{cl}V_{ep} + E_{ep}V_{cl}}$ where, E_{nc} = predicted nanocomposites modulus, E_{ep} = modulus of the epoxy = 4.01 GPa, E_{cl} = modulus of the nanoclay = 172 GPa, V_{ep} = volume fraction of the epoxy, V_{cl} = volume fraction of the nanoclay
Halpin-Tsai	[171,176]	$E_{nc} = \frac{1+\zeta\eta V_{cl}}{1-\eta V_{cl}} E_{ep}$; where, a) For longitudinal elastic modulus ζ =shape factor = $\frac{2w}{t} = 200$ (for rectangular shape clay nanoplatelet of width=100nm and thickness=1nm) $\eta = \left(\frac{E_{cl}}{E_{ep}} - 1\right) \Big/ \left(\frac{E_{cl}}{E_{ep}} + \zeta\right) = 0.17$ b) For transverse elastic modulus $\zeta = 2$ and $\eta = 0.93$ c) Van Es [173] proposed $\zeta = \frac{2w}{3t} = 66.67$ and $\eta = 0.38$ for longitudinal elastic modulus.
Halpin-Tsai-Random	[173]	$E_{nc} = 0.49E_L + 0.51E_T$; where, For longitudinal elastic modulus E_L, $\zeta = \frac{2w}{3t} = 66.67$ and $\eta = 0.38$ and for transverse elastic modulus E_T, $\zeta = 2$ and $\eta = 0.93$
Modified-Halpin-Tsai (present model)	-	$E_{nc} = \frac{1+\zeta\eta V_{cl}}{1-\eta V_{cl}} E_{ep}$; where, $\zeta = \frac{2w}{t_{eff}}$ shape factor as a function of V_{cl} $t_{eff} = 1200V_{cl}$ (for $0 < V_{cl} \le 0.1$) = effective thickness of the stacked nanoclay platelets. $\eta = \left(\frac{E_{cl}}{E_{ep}} - 1\right) \Big/ \left(\frac{E_{cl}}{E_{ep}} + \zeta\right)$

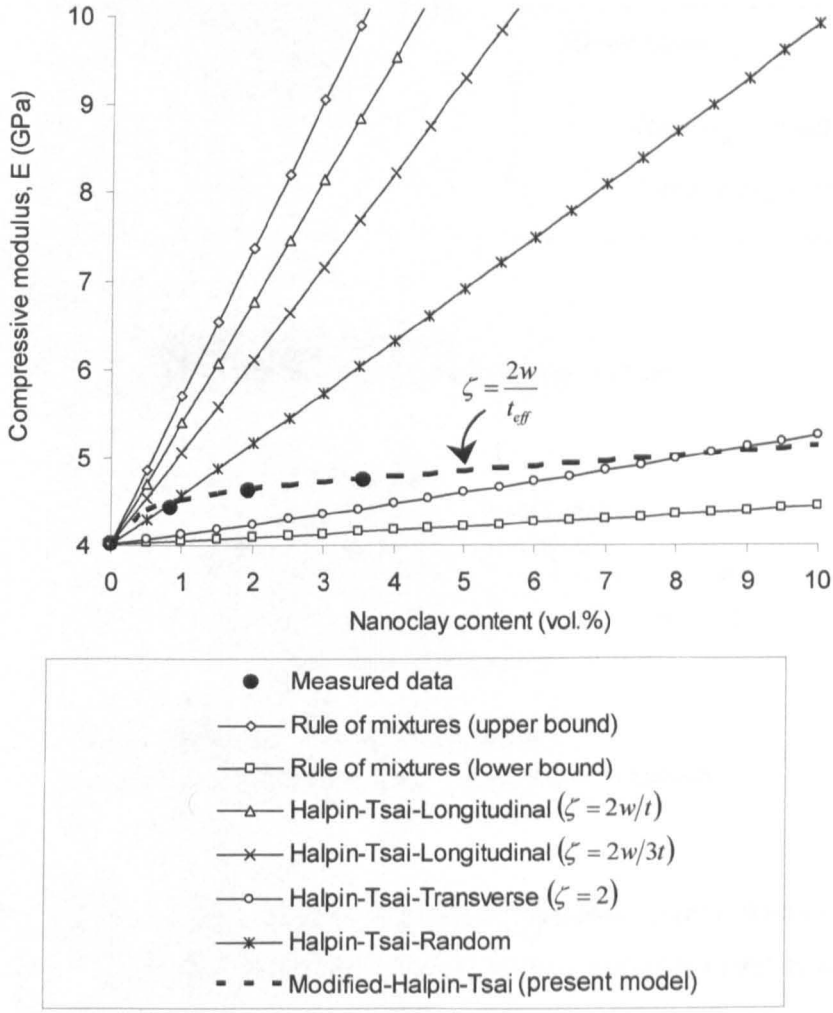

Figure 5.32: Theoretical prediction of the compressive modulus of nanoclay-modified Cycom 977-20 nanocomposite in comparison with the experimental values. All curves were calculated based on models and input data summarised in Table 5.16.

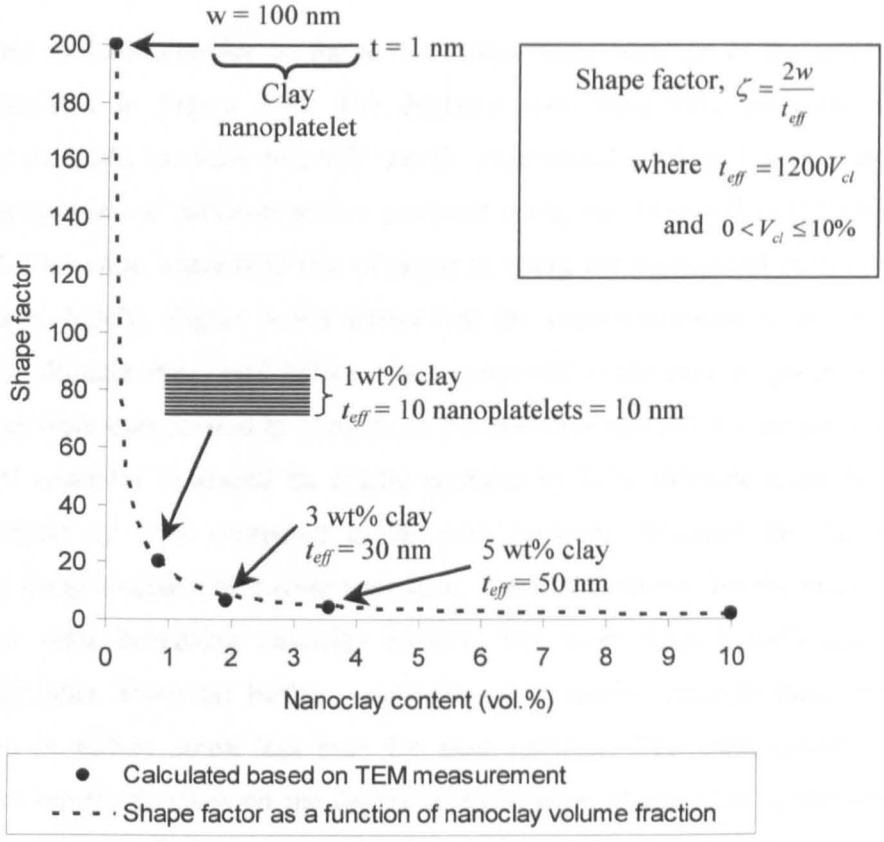

Figure 5.33: Shape factor ζ as a function of the nanoclay volume fraction V_{cl} (which corresponds to the effective thickness t_{eff} of the stacked nanoclay platelets in the epoxy). The stacked nanoplatelets in ordered exfoliated type nanocomposites reduce the shape factor. (1 wt% = 0.84 vol.%, 3 wt% = 1.93 vol.% and 5 wt% = 3.56 vol.%)

5.5.5 Tensile properties

The effect of I.30 nanoclay on the tensile stress-strain response of the epoxy polymer was illustrated in Figure 5.34. The dogbone specimens were prepared using two different methods, (a) three-roll mill and (b) mechanical stirring. It was found that the tensile properties of nanocomposites prepared using the three-roll mill technique (see Figure 5.34a) were better than that of prepared using the mechanical stirring technique (see Figure 5.34b). Figure 5.34a shows that the nanocomposites have better tensile modulus, ultimate stress and failure strain compared to the pure polymer. The overall properties were summarised in Table 5.17. For the three roll mill technique, the addition of 5 wt% nanoclay enhanced the elastic modulus by 21%, ultimate stress by 25% and failure strain by 23% compared to the pure polymer. Whereas for the specimens prepared using mechanical stirring technique, Table 5.17 shows that the elastic modulus improved with increasing nanoclay content. For more than 1 wt% nanoclay, the nanocomposites show no further improvement in tensile strength and, even worst, reduction in failure strain less than the pure polymer. The enhancement in tensile properties mostly depends on the degree of exfoliation of nanoclay in the resin. Three roll mill technique produced fully exfoliated nanocomposites therefore the interfacial adhesion between nanoclay-epoxy is very strong. As a result, the nanocomposites prepared using this technique exhibited better overall tensile properties.

5.5.6 Flexural properties

Figure 5.35 shows the effect of nanoclay on flexural stress-strain curves compared to the neat system. The tests were conducted on two different specimens; (a) prepared using the three-roll mill and (b) prepared using the mechanical stirring. It was found that the slope of the stress-strain curves increases with increasing nanoclay content as shown in Figure 5.35. This indicates that nanoclay enhanced the flexural modulus of the epoxy. The degree of reinforcement depends on the degree of dispersion of the nanoclay in the epoxy. Table 5.17 shows that the nanocomposites prepared using the three roll mill technique enhanced the flexural strength, however this coincided with a slight reduction in failure strain. While the nanocomposites prepared using the mechanical stirring technique reduced both the flexural strength and failure strain with increasing in nanoclay content. This may be due to the presence of particle agglomeration or clusters of intercalated rich regions, voids in the specimen and weak interfacial adhesion

between nanoclay and the matrix that contribute to a lower flexural properties compared to the neat epoxy.

5.5.7 Fracture toughness properties

Graphs in Figure 5.36 show the effect of nanoclay on the load-crack opening displacement curves for two different specimens that were prepared using (a) three-roll mill and (b) mechanical stirring techniques. Table 5.17 summarises the fracture toughness properties of neat and nanomodified systems. It was found that, the load at crack growth initiation F_Q for nanocomposites prepared using the three roll mill technique was higher than that of the neat epoxy. Hence, the nanocomposites significantly enhanced the fracture toughness of the epoxy, see Table 5.17. For both techniques, the addition of 1 wt% nanoclay gave the highest fracture toughness properties. There was no further improvement in fracture toughness by adding clay more that 1 wt%. This indicates that fully exfoliated nanoclay in the epoxy provide good interfacial adhesion between matrix and nanofiller therefore enhanced the fracture toughness properties.

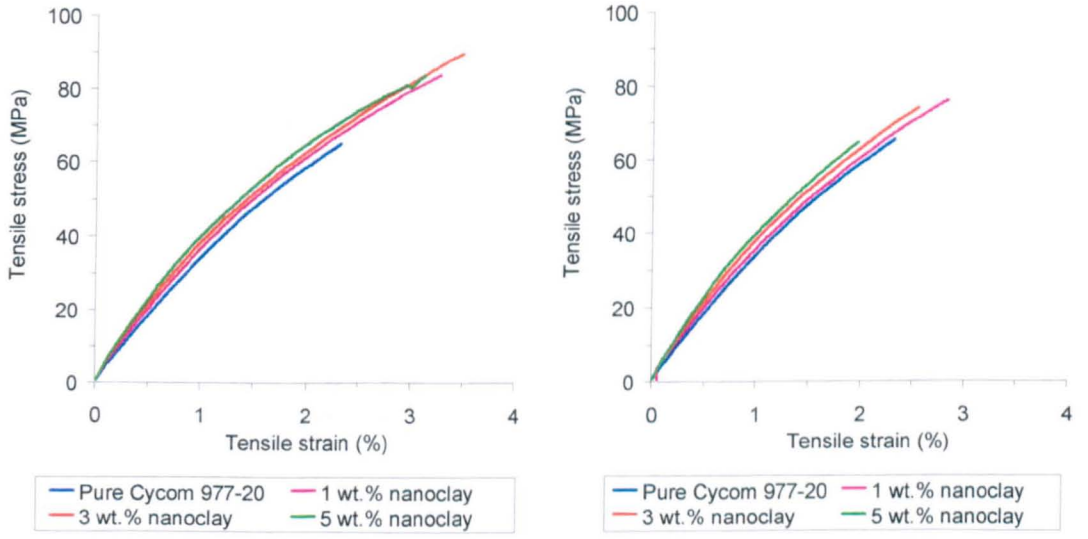

Figure 5.34: Typical tensile stress-strain curves of I.30 nanoclay-modified Cycom 977-20, prepared using two different methods (a) three-roll mill and (b) mechanical stirring, compared to the neat epoxy.

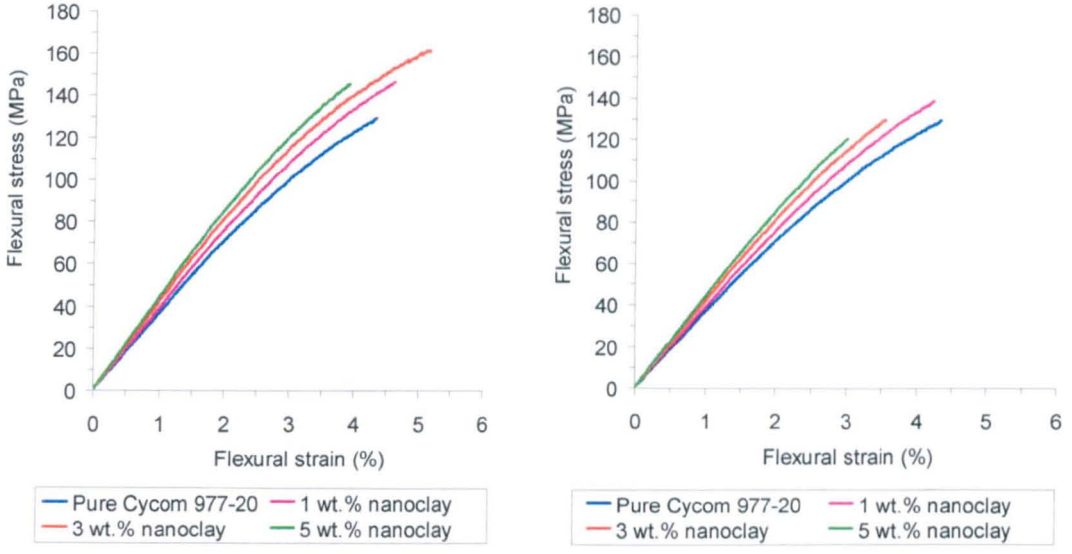

Figure 5.35: Typical flexural stress-strain curves of I.30 nanoclay-modified Cycom 977-20, prepared using two different methods (a) three-roll mill and (b) mechanical stirring, compared to the neat epoxy.

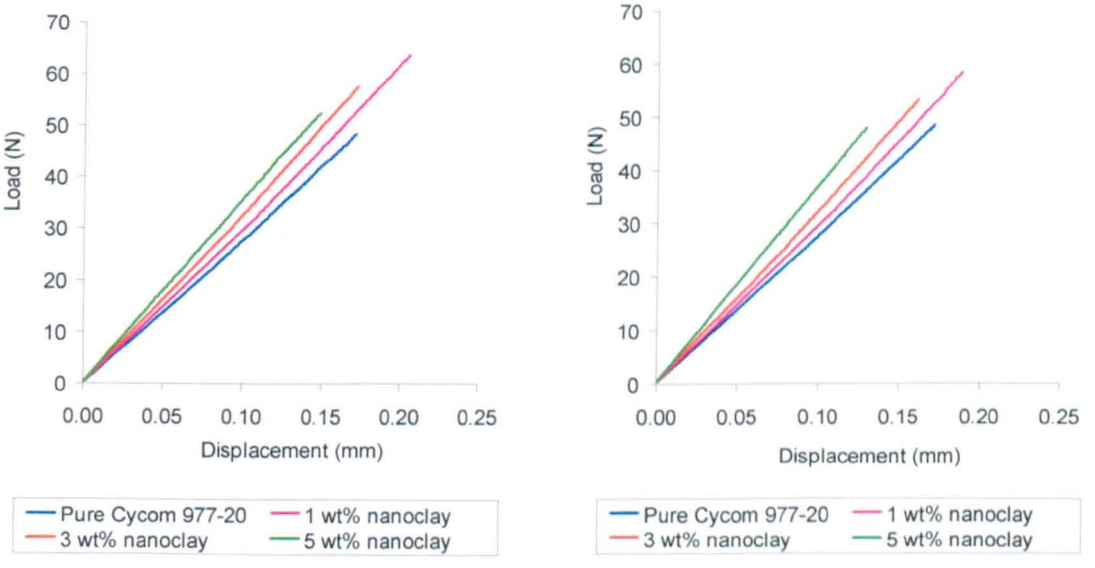

Figure 5.36: Typical load-displacement curves of I.30 nanoclay-modified Cycom 977-20, prepared using two different methods (a) three-roll mill and (b) mechanical stirring, compared to the neat epoxy.

Table 5.17: Tensile, flexural and fracture toughness properties of the unmodified and nanomodified Cycom 977-20 resin with various concentrations of I.30 clay nanoparticles.

Material properties	Unmodified system	Nanomodified system					
		Three-roll mill			Mechanical stirrer		
		1 wt% clay	3 wt% clay	5 wt% clay	1 wt% clay	3 wt% clay	5 wt% clay
Tensile modulus, E_t (GPa)	3.51 ± 0.03	3.84 ± 0.03	4.07 ± 0.02	4.24 ± 0.04	3.86 ± 0.08	4.03 ± 0.09	4.20 ± 0.06
Tensile strength, $\sigma_{u,t}$ (MPa)	62.60 ± 2.41	73.92 ± 4.96	75.77 ± 7.73	78.19 ± 4.49	71.01 ± 3.90	66.02 ± 6.75	64.28 ± 4.51
Tensile strain at break, $\varepsilon_{f,t}$ (%)	2.27 ± 0.15	2.86 ± 0.29	2.81 ± 0.41	2.79 ± 0.24	2.85 ± 0.27	2.48 ± 0.27	2.16 ± 0.18
Flexural modulus, E_b (GPa)	3.61 ± 0.03	3.92 ± 0.03	4.16 ± 0.04	4.33 ± 0.06	3.91 ± 0.07	4.15 ± 0.03	4.31 ± 0.04
Flexural strength, $\sigma_{u,b}$ (MPa)	136.79 ± 9.38	143.31 ± 8.52	149.40 ± 15.55	141.48 ± 10.17	134.70 ± 10.62	128.33 ± 6.10	118.26 ± 5.60
Flexural strain at break, $\varepsilon_{f,b}$ (%)	5.27 ± 0.76	4.47 ± 0.41	4.85 ± 0.81	3.92 ± 0.39	4.01 ± 0.35	3.46 ± 0.19	3.00 ± 0.21
Maximum load, F_Q (N)	49.61 ± 1.60	59.85 ± 0.98	55.79 ± 0.57	53.42 ± 0.58	56.07 ± 1.15	51.68 ± 1.28	47.10 ± 1.51
Critical stress intensity factor, K_{IC} (MPa. $\sqrt{m}$)	1.14 ± 0.04	1.37 ± 0.02	1.28 ± 0.01	1.23 ± 0.01	1.29 ± 0.03	1.19 ± 0.03	1.08 ± 0.04
Critical energy release rate, G_{IC} (J/m^2)	373.72 ± 14.67	535.94 ± 16.36	446.67 ± 4.58	377.72 ± 11.69	476.15 ± 20.70	390.50 ± 20.41	289.27 ± 16.10

5.6 Concluding remarks

Polymer nanocomposites were manufactured using three types of modifiers, including silica nanospheres, carbon nanotubes and clay nanoplatelets. The performance of the nanocomposites was evaluated based on the degree of dispersion in the epoxy, thermal, mechanical and fracture properties. All TMA results showed that nanocomposites have a better dimensional stability (due to reduced in CTE) when compared to the pure polymers. Thermogravimetry analysis on silica/828 and clay/977 systems showed that nanocomposites have better thermal stability (due to increased in thermal degradation temperature) compared to the pure systems.

The compressive, tensile and flexural moduli of the epoxies were improved with increases in multiwalled CNT and MMT nanoclay content. However, the degree of enhancement in ultimate strengths and failure strains was limited by the presence of entangled CNT or clusters of intercalated structure nanoclay in the epoxies. In addition, the degassing process of the mixtures became very challenging at high CNT and clay content, hence air was entrapped in the cured resins. These reduced the strength, failure strain and fracture toughness properties of the nanocomposites.

In contrast, the addition of nanosilica offered a very significant increase in the compressive, tensile and flexural moduli and strengths without any significant reduction in failure strains of the epoxy. Moreover, the fracture toughness of the epoxy was enhanced tremendously. For example, a 160% increase in fracture energy by adding 25 wt% nanosilica. In addition, homogeneous dispersion and relatively low viscosity during processing even at high silica content (25 wt%) rendered this nanomodified-epoxy to be the most suitable candidate for impregnation process with carbon fibre. Therefore, the effect of nanosilica on the carbon fibre reinforced polymer composite is discussed in Chapter 6. The results are also compared with the HTS40/977-2 CFRP composites that are currently used for commercial aircraft structures. A full discussion on the influence of nanofillers on the properties of epoxy polymers and how they contribute to the enhanced mechanical properties of CFRP laminates is presented in Chapter 7.

Chapter 6

Compressive strength of nanomodified-CFRP composite laminates

6.1 Summary

The effect of nanosilica on the compressive properties of unidirectional (UD) HTS40/828 laminates was studied. At first, the quality of the UD laminates was evaluated using an image analysis technique and the volume fraction of nanosilica was determined using TGA. Scanning electron microscopy (SEM) and optical microscopy were used to study the failure mechanisms involved during compression. In addition, the effect of nanosilica on in-plane shear properties of the HTS40/828 $[\pm 45]_{2s}$ laminate was also investigated. The compressive strength of the UD laminate was estimated using several models based on fibre microbuckling and kinking failure modes. The results are compared to HTS40/977-20 thermoplastic-toughened CFRP composite system, which is currently used in aerospace structural applications. All results are presented in the following sections and Appendix B.

6.2 Nanosilica-filled HTS40/828 CFRP composite

6.2.1 Physical and thermal properties

Figure 6.1 shows a typical SEM micrograph of cross-section of UD CFRP composite, which was made of HTS40 carbon fibre and Epikote 828 resin. The carbon fibre has been treated with polyurethane to promote interfacial bonding to the matrix. The strength of the UD composite laminate in compression mainly depends on the quality of the fabricated specimens and the properties of the matrix, fibres and fibre/matrix interfacial adhesion. Imperfections in the laminate, such as non-uniform fibre

distributions (presence of fibre- and matrix-rich regions), misalignments of fibres (or fibre waviness) and microvoids in the matrix, could not be completely eliminated during the manufacturing process. These defects could act as sites of local stress concentration, which can initiate failure. In this study, the quality of the fabricated specimens was evaluated using image analysis and TGA techniques.

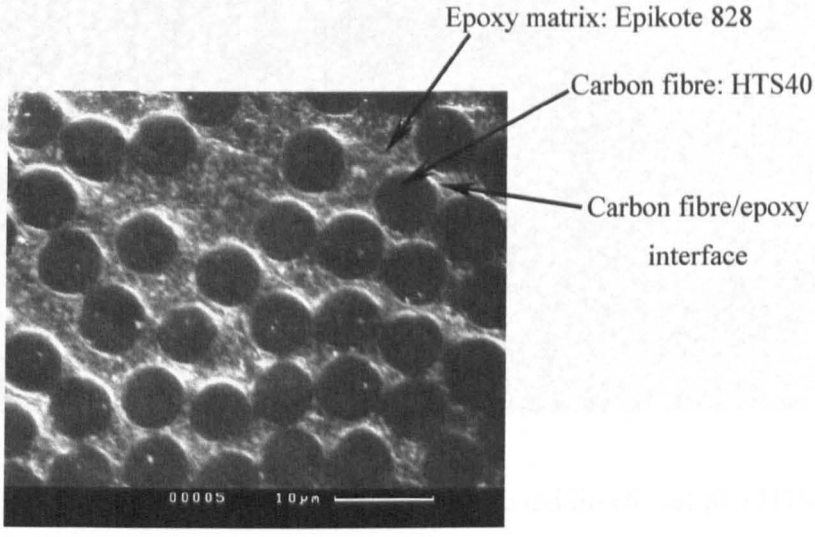

Figure 6.1: A typical SEM micrograph showing the cross section of UD HTS40/828 laminate.

6.2.1.1 Fibre distribution

Figure 6.2 shows the optical micrograph of a polished transverse section of HTS40/828 UD laminate. This low magnification (20x) image shows that the fibres have a uniform circular cross-section. The average diameter of the fibre was measured using images at higher magnification (100x). Figure 6.3 shows the diameter distribution as measured with KSRUN ZEISS image analyser. These high tensile strength (HTS40) carbon fibres have a narrow diameter distribution with mean diameter of 6.97 μm and standard deviation of 0.18 μm. Figure 6.2 shows that the fibres are non-uniformly distributed, with regions of high and low packing fraction while this is undesirable it is typically observed in FRP composite systems.

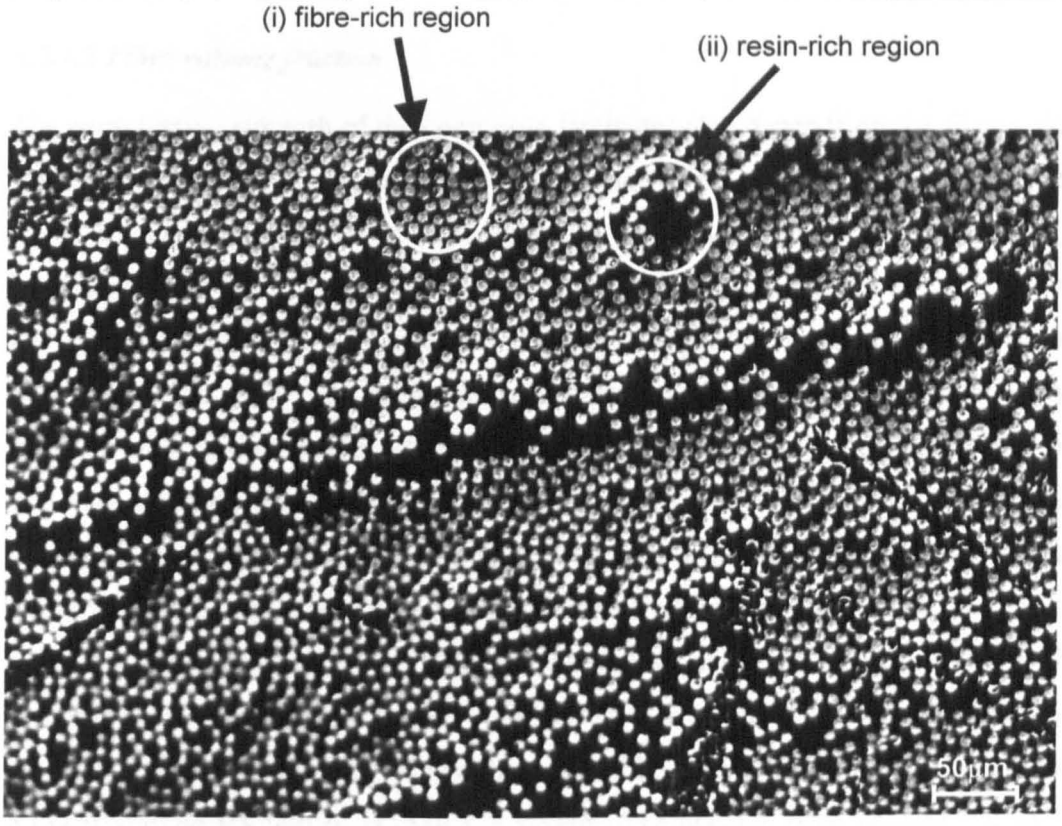

Figure 6.2: Fibre distribution across thickness of the unidirectional $[0]_8$ HTS40/828 laminate.

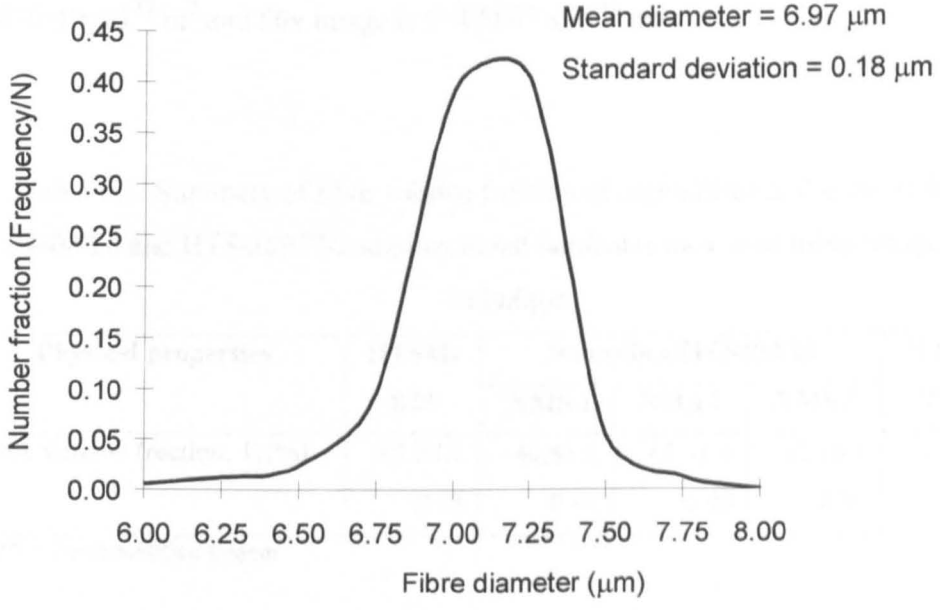

Figure 6.3: Diameter distribution of HTS40 carbon fibre; sample size (N) of 498 was used.

6.2.1.2 Fibre volume fraction

The compressive strength of the composite laminates also depends on the fibre volume fraction, V_f. This is because the fibre supports most of the applied load. After the fibres break, the load is supported by the matrix. The volume fraction of carbon fibre in the laminate mostly depends on the type of fabrication method. For instance, the 8 layers of UD HTS40/977-2 CFRP fabricated using hot press technique produced a laminate with average V_f = 58 vol.% [7]. While, in current work, a similar 8 layers prepreg prepared using an autoclave method produced a laminate with average V_f = 62 vol.%. The pure and nanomodified HTS40/828 systems, which were manufactured using a technique described in Section 3.4.1 (using the dry filament winding, resin impregnation and vacuum bagging), have an average fibre volume fraction of 41-43 vol.%, as shown in Table 6.1. The V_f of the UD laminate was determined using the image analysis method as outlined in Section 3.5.4.2. Figure 6.4 shows that the cross-section fibre density in the HTS40/977-2 composite is higher than that of the HTS40/828 system. This indicates a lower volume fraction of HTS40/828 system. The average fibre volume fraction, as given in Table 6.1, was calculated based on at least 25 optical micrographs for each system using the KSRUN version 3.0 ZEISS software. The greyscale image was converted into binary image, as shown in Figure 6.4. The V_f was calculated by dividing the total field area to the total frame area. The total frame area for 100x image is 12870.05×10^{-12} m^2 and 50x image is 51479.97×10^{-12} m^2.

Table 6.1: Summary of fibre volume fraction of unmodified and nanomodified-HTS40/828 and HTS40/977-2 unidirectional laminates measured using image analysis technique.

Physical properties	HTS40/ 828	Nanosilica/HTS40/828			HTS40/ 977-2
		*NMS 1	NMS 2	NMS 3	
Fibre volume fraction, V_f(%)	42.27 ± 0.98	40.66 ± 0.92	43.31 ± 0.90	42.16 ± 0.95	62.43 ± 1.29

*NMS = Nanomodified system

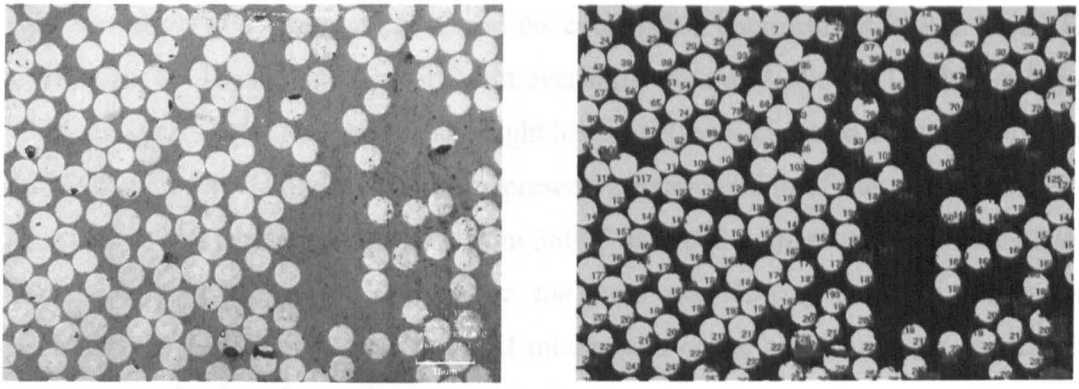

(i) (ii)

(a) HTS40/828

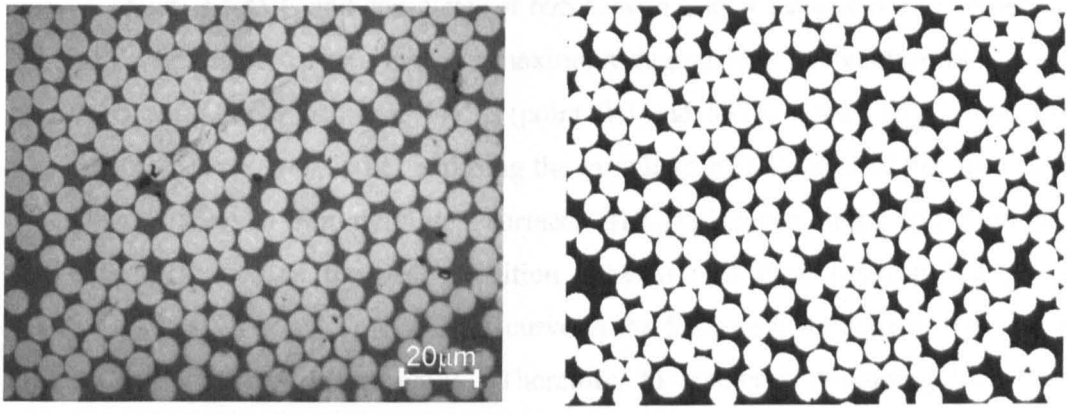

(i) (ii)

(b) HTS40/977-2

Figure 6.4: Optical micrographs of cross sections of (a) HTS40/828 and (b) HTS40/977-2 unidirectional laminates showing greyscale images (i) that were converted into binary images (ii) for the measurement of fibre volume fraction using the KSRUN ZEISS software.

6.2.1.3 Thermogravimetry analysis and nanosilica volume fraction

The amount of nanosilica content in the composite laminate was determined using the TGA technique as described in section 3.5.3. In addition TGA was also used to study the thermal stability of pure and nanomodified HTS40/828 CFRP composite systems. Figure 6.5a illustrates the thermal degradation behaviour of pure HTS40/828 laminate, which was burned in N_2 gas from 40°C to 550°C at 10°C/min then kept at 550°C for 1 hr and followed by heating in air to 1000°C at 10°C/min. This figure shows that the

laminate starts to degrade at 250°C and the combustion completes at 961°C. This TGA profile can be divided into five different events (marked as A, B, C, D and E on Figure 6.5a). Stage A shows that the initial weight loss of 0.1 wt% occurred due to vaporization of moisture in the laminate. Stage B represents decomposition of the resin in nitrogen. The weight loss gradually increases from 380°C to 550°C with a total mass loss of 38.6 wt%. After holding at 550°C for 1 hr, the purge gas flowing over the sample was automatically switched to air. The SEM micrograph of the sample residue, which was collected at 550°C, shows that the resin remains deposited on the carbon fibres, see Figure 6.6b. Therefore, the sample was heated to 1000°C in air to remove the resin residue and then burn off the carbon fibres. Figure 6.5a shows that the resin residue starts to burn at 575°C and completes at 695°C with a total mass loss of 10.6 wt%, see Stage C. Figure 6.5b shows that the maximum degradation temperature of the epoxy resin and its residues occur at 441°C (point (i)) and 637°C (point (ii)), respectively. Figure 6.6c illustrates that after exposing the sample to 650°C, most of the resin residue was already removed from the fibre's surfaces. The TGA curve for the CFRP composite was also compared to the decomposition behaviour of pure Epikote 828 polymer (obtained from Section 4.2). The TGA curve of the Epikote 828 confirms that the resin was completely burnt off at 680°C. Therefore, the material remaining behind after 695°C is the carbon fibres. Stage D shows that the carbon fibre starts to burn at 700 °C and completes at 962°C with a total mass loss of 49.7 wt%. The maximum degradation temperature of the carbon fibre as identified by the peak of the rate of weight loss versus sample temperature curve (see Figure 6.5(iii) is 910°C. This is confirmed by the TGA curve of the neat HTS40 carbon fibre, which was burnt under similar conditions. The TGA curve of neat HTS40 carbon fibre shows that it starts to burn at 650°C and completes at 872°C (see Figure 6.5a) with a maximum combustion rate occurs at 852°C (see Figure 6.5b). A slightly higher degradation temperature of carbon fibres in CFRP composite was recorded compared to that of the pure carbon fibres because of the presence of resin residue, which was deposited on the fibre surface. Finally, stage E shows that there is no material remaining behind after exposing the sample to more that 962°C. This suggests no contamination of the pure HTS40/828 laminate.

The fibre and resin volume fractions in HTS40/828 laminate were calculated in accordance to ASTM standard D3171-99 (as discussed in Chapter 3 Section 3.5.4). Three samples were tested. The TGA results showed that the average weight fraction of the carbon fibre and resin was 51.11 wt% and 48.22 wt%, respectively. The average

density of HTS40/828 CFRP composite, which was determined using a density balance, was 1.45 g/cm^3. The density of HTS40 carbon fibre, as provided by the manufacturer, was 1.77 g/cm^3 and the density of Epikote 828 polymer was 1.22 g/cm^3 (determined using the density balance). The fibre and resin volume fractions in the CFRP composite were 41.87 vol.% and 57.31 vol.%, respectively. The fibre volume fraction measured using the TGA technique was very close to the value obtained using the image analysis technique as given in Table 6.1. The average of void volume fraction in the laminate was 0.8%. This shows a good quality CFRP composite. A good composite usually has less than 1 vol.% voids, whereas a poorly manufactured composite can has up to 5 vol.% voids [165].

The effect of nanosilica on the thermal degradation behaviour of HTS40/828 laminate was studied. As shown in Figure 6.7, nanomodified CFRP systems exhibited similar thermal decomposition mechanisms to that of the unmodified HTS40/828 system. However, in the final stage (Stage E), the material remaining behind after exposing the nanomodified laminates to air was the inert silica nanofiller. At least three samples were tested for each system. Table 6.2 summarises the average weight fraction of nanosilica in the laminate.

Figure 6.7 shows that all nanomodified laminate samples start to burn at slightly higher temperature than that of the pure system. These show that nanomodified system has a better thermal stability. The nanomodified epoxy starts to burn at 330°C and finished at 550°C. After isothermal temperature of 550°C, the carbon fibres were covered with the nanosilica and carbon residues, which were left from the nanomodified-epoxy. These residues underwent thermal degradation at a higher temperature compared to the carbon residues left from pure Epikote 828, as explained in Section 5.2.2 (see Figure 5.2a). Therefore, the weight fraction of carbon fibre in nanomodified CFRP composite system could not be determined through TGA curves due to a high thermal stability of the nanomodified-matrix. The resin residues and carbon fibre were completely burnt off at 990°C. After this temperature, the material left was silica nanofiller.

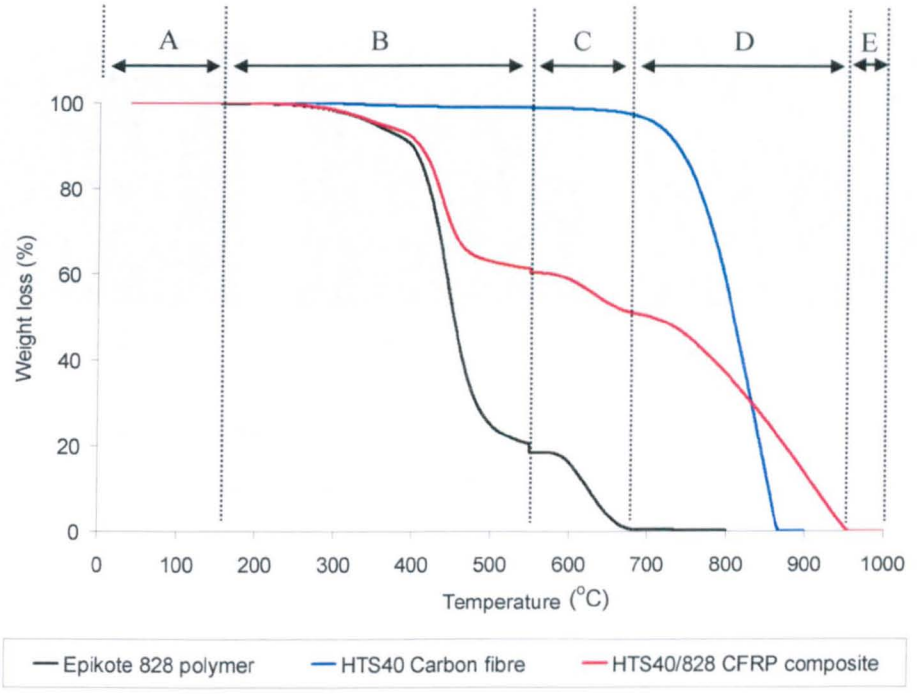

(a)

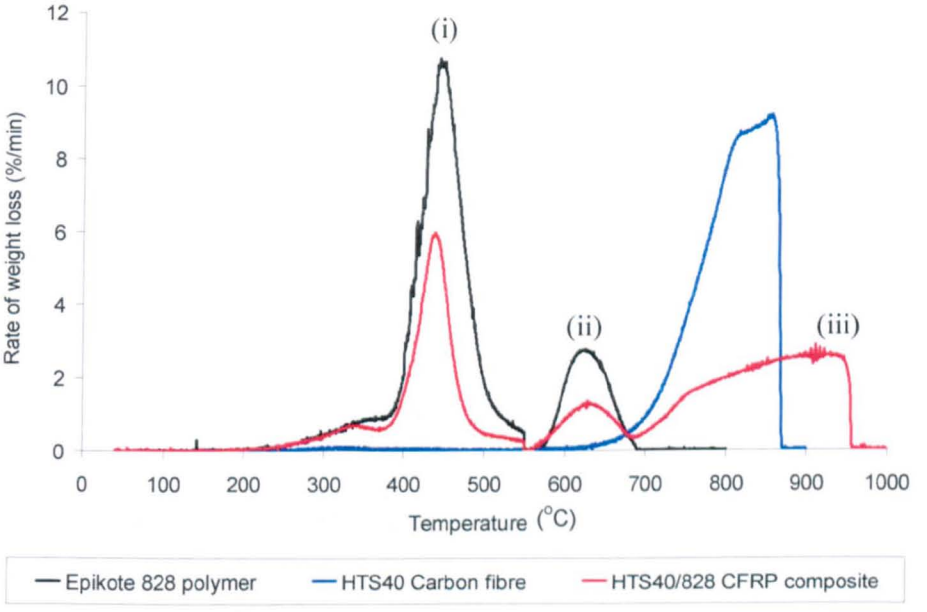

(b)

Figure 6.5: Typical TGA results showing (a) percentage of weight loss and (b) rate of weight loss versus temperature of Epikote 828 resin, HTS40 carbon fibre and HTS40/828 CFRP composites, which were burnt in N_2 from 40°C to 550°C and then kept at 550°C for 1 hr, followed by heating to 1000°C in air.

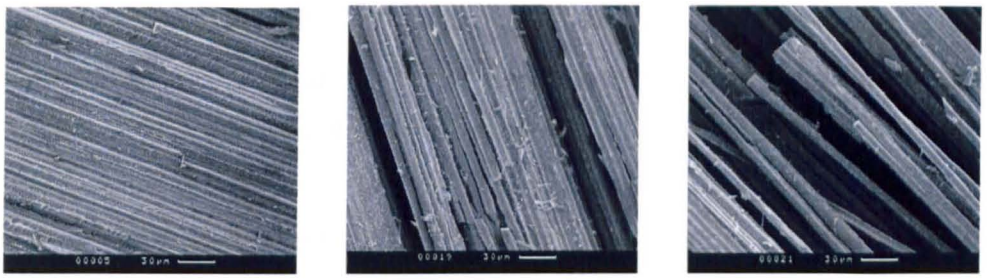

(a) 25 °C (b) 550 °C (c) 650 °C

Figure 6.6: Typical SEM micrographs showing the UD HTS40/828 TGA specimen before heating (a) and after heating at 550°C (b) and 650°C (c).

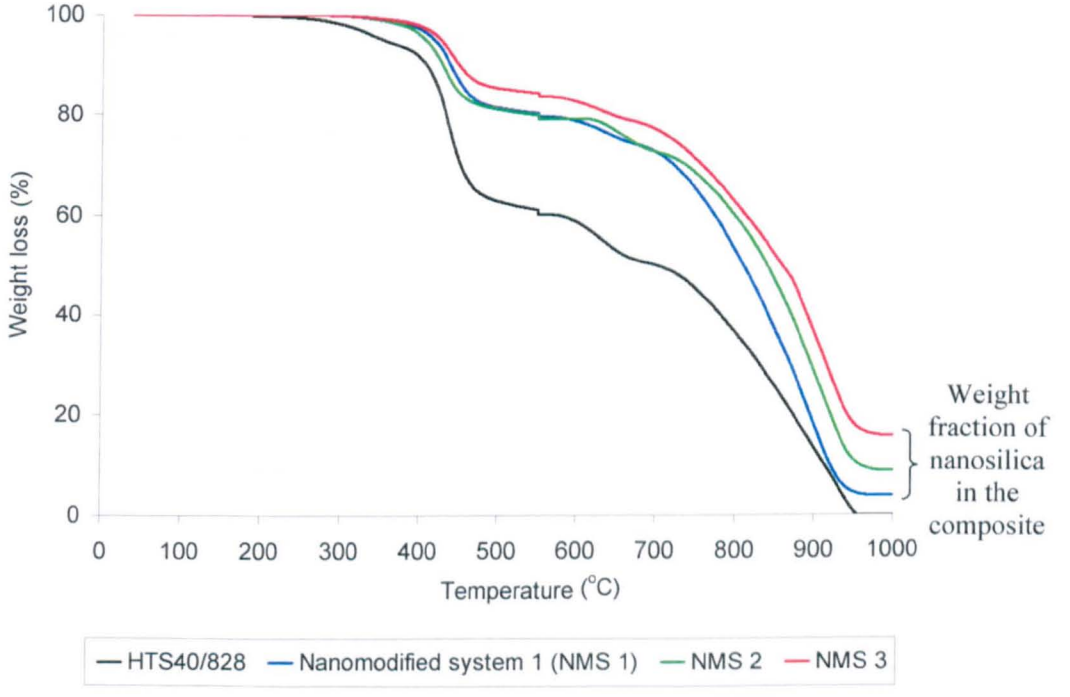

Figure 6.7: Typical TGA results showing thermal degradation behaviour of unmodified and nanosilica-modified HTS40/828 CFRP composite. The material remaining behind after exposing the nanomodified-HTS40/828 samples to air is the inert silica nanofiller.

Table 6.2 shows that the average weight fraction of nanosilica in three different nanomodified systems was 3.83, 8.96 and 15.49 wt%. The measured density of the nanomodified CFRP composite systems using the density balance was also summarised in Table 6.2. The measured density of nanomodified system was found to increase with an increase in the nanosilica content. The increase in density is expected because the density of silica, ρ_{si} = 1.8 g/cm^3, is greater than that of the pure HTS40/828 system (ρ_c = 1.45 g/cm^3). The volume fraction of nanosilica in the laminate for the three different nanomodified CFRP composite systems was about 3, 7 and 13 vol.%, which were calculated using equation given in Section 3.5.4.

Table 6.2: Summary of density of pure and nanomodified HTS40/828 CFRP composite measured using a density balance and nanosilica content in the laminate measured by TGA.

Physical properties	**HTS40/828**	**Nanosilica/HTS40/828**		
		***NMS 1**	**NMS 2**	**NMS 3**
Weight fraction of nanosilica, W_{si}(%)	-	3.83 ± 0.32	8.96 ± 0.52	15.49 ± 0.63
Density, ρ_c (g/cm^3)	1.450 ± 0.006	1.473 ± 0.007	1.494 ± 0.003	1.534 ± 0.001
Volume fraction of nanosilica $V_{si}(\%) = W_{si} \times \frac{\rho_c}{\rho_{si}}$ (vol%)	-	3.12	7.43	13.13

*NMS = Nanomodified system

6.2.1.4 Fibre misalignment

Fibre misalignment or fibre waviness is one of the manufacturing defects, which occurs during the fibre winding process or the curing process. The compressive strength of the composites is mostly influenced by the initial fibre misalignment in the composite. For instance, the compressive failure strength of HTS40/977-2 system, which has initial fibre misalignment of 5° is 61% lower than that of laminate with 1° initial fibre misalignment [7]. Therefore, the strength of the composite reduces with increasing fibre misalignment angle in the composite.

The distribution of fibre misalignment angle for UD unmodified and nanomodified HTS40/828 laminates was measured using Yugartis method, as described in Chapter 3 Section 3.5.7. Figure 6.8 shows a typical optical micrograph of UD HTS40/828 laminate compared to that of UD HTS40/977-2 laminate (prepared using autoclave), which were sectioned at an angle of approximately θ_{cut}=5° to the 0°-fibre axis. Non-uniform distribution of the fibre's elliptical cross section of HTS40/828 laminate indicated a large distribution of fibre misalignment in the composite. The major axial length of the cut fibre's elliptical surface as shown in Figure 6.9 was measured using the KSRUN ZEISS software. About 2000 or more ellipse lengths were measured for each system. The angle of cut for each fibre θ_i was calculated and sorted into the class interval width at the angle of 0.5° as shown in Figure 6.10. The actual plane cut angle for each system was determined based on the mean of fibre waviness distribution and summarised in Table 6.3. Finally, the transformation between θ_i and ϕ_i was made. The results of fibre misalignment angle distribution for unmodified and nanomodified-HTS40/828 systems were illustrated in Figure 6.11 and summarised in Table 6.3. It was found that the maximum fibre misalignment angle for unmodified and nanomodified HTS40/828 system was 4-5°. However, it is interesting to note that the presence of nanosilica results in a narrow fibre angle distribution of the UD HTS40/828 laminate, where a smaller standard deviation of fibre distribution was recorded for nanomodified systems compared to the unmodified system. Figure 6.11 shows that for the unmodified system about 90% of the fibre volume was within ±2° to the 0°-fibre direction while the addition of 7 and 13 vol.% of nanosilica reduced the fibre misalignment to ±1.5°. This indicates that the nanomodified resin contributes to a better fibre alignment in the laminate. This probably due to the fact that a lower CTE of nanomodified resin reduces the thermal mismatch between fibre and the matrix during curing hence reduces the fibre waviness. The UD HTS40/977-2 laminate, which was prepared using the autoclave, had a very narrow fibre distribution where 95% fibre volume was within ±1° to the 0°-fibre direction, as shown in Figure 6.12. This type of laminate was manufactured using prepreg material and had a V_f = 62%, therefore densely packed fibres provide a better fibre alignment when compared to the HTS40/828 system. In addition the Cycom 977-2 has lower CTE compared to that of Epikote 828, therefore this perhaps contributes to lower fibre waviness of the HTS40/977-2 laminate.

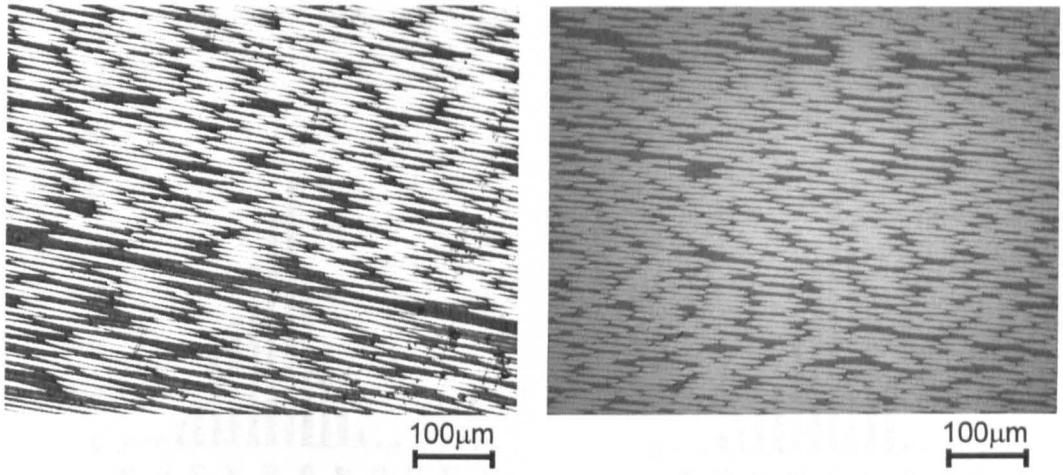

(a) HTS40/828 (b) HTS40/977-2

Figure 6.8: Optical micrographs of (a) HTS40/828 and (b) HTS40/977-2 unidirectional laminates sectioned at an angle of approximately 5° to the fibre for the measurement of fibre misalignment.

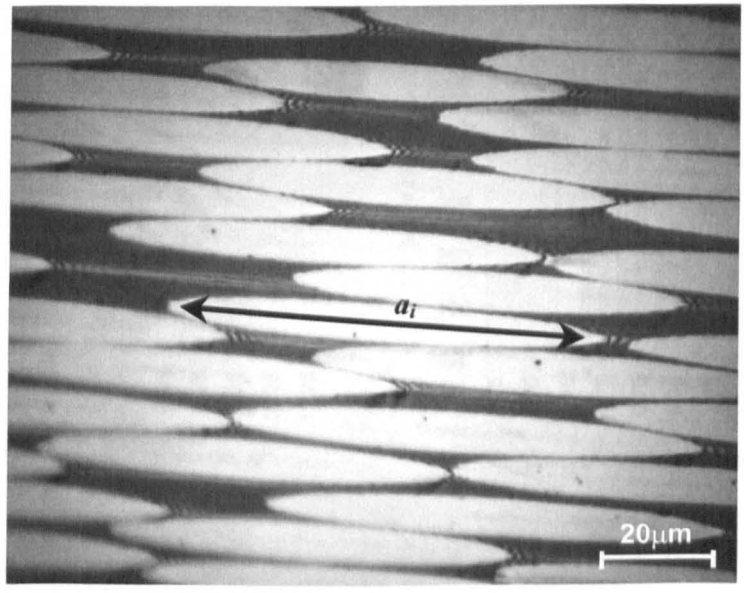

Figure 6.9: Measurement of major axial length of the cut fibre's elliptical surface a_i using the KSRUN ZEISS software.

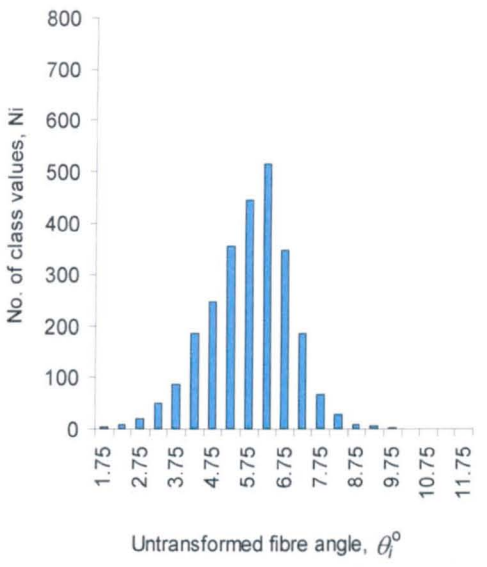

(a) HTS40/828

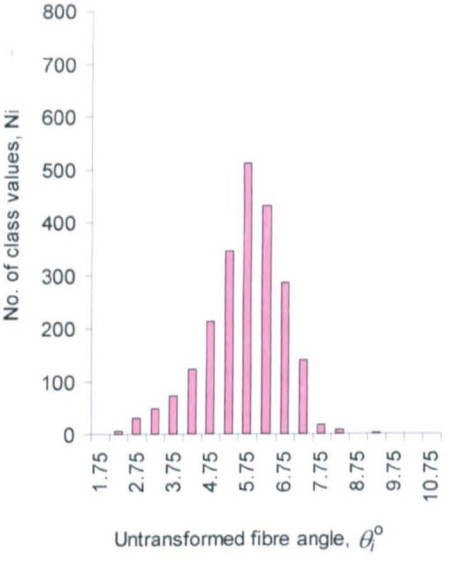

(b) 3vol%si/HTS40/828

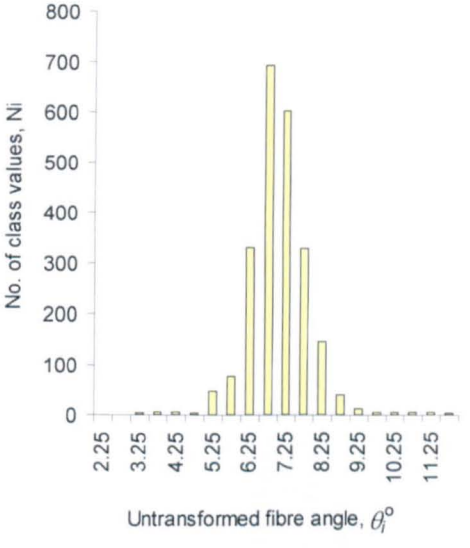

(c) 7vol%si/HTS40/828

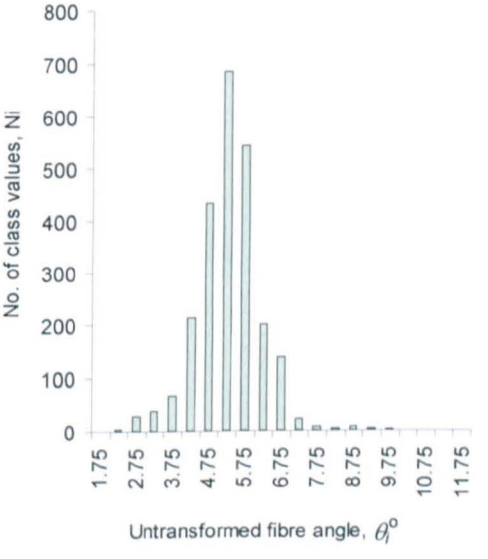

(d) 13vol%si/HTS40/828

Figure 6.10: Untransformed fibre angle distribution of pure and nanomodified HTS40/828 composite laminate as determined using Yugartis method. Sample size (N) of at least 2000 was used.

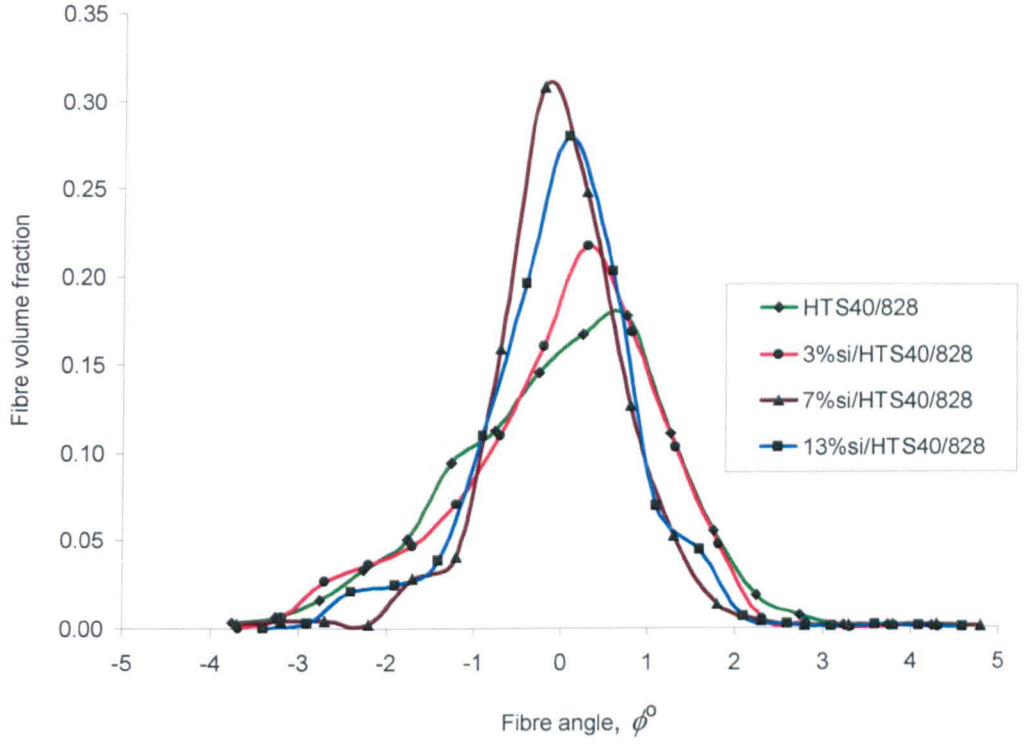

Figure 6.11: Fibre angle distributions of the unmodified and nanomodified-HTS40/828 CFRP composites; showing the effect of nanosilica on fibre misalignment angle distribution in the laminate.

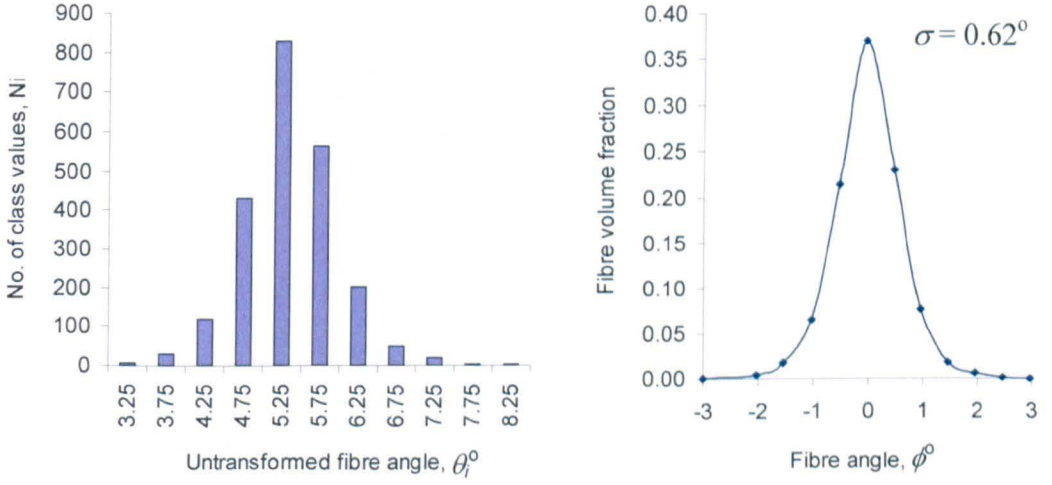

Figure 6.12: (a) Untransformed and (b) transformed fibre angle distribution of UD HTS40/977-2 laminate with the distribution of standard deviation, σ.

Table 6.3: Summary of fibre misalignment angle of pure and nanomodified HTS40/828 CFRP composite compared to HTS40/977-2 system.

Physical properties	HTS40/ 828	Nanosilica/HTS40/828			HTS40/ 977-2
		3 vol.%	7 vol.%	13 vol.%	
Actual plane-cut angle, ϕ_{pc}°	5.50	5.44	6.95	5.15	5.28
Overall fibre misalignment distribution	-3.75° to 4.25°	-3.19° to 3.81°	-3.70° to 4.80°	-2.90° to 4.60°	-2.03° to 2.97°
Standard deviation	1.19°	1.11°	0.84°	0.89°	0.62°
Fibre misalignment angle	91% within ±2.0°	92% within ±2.0°	93% within ±1.5°	90% within ±1.5°	95% within ±1.0°

6.2.2 Compressive properties

6.2.2.1 Compressive stress-strain behaviour

The compressive stress-strain response of a typical UD HTS40/828 specimen is shown in Figure 6.13. The longitudinal strain on front and back faces (strain gauges 1 and 2) of the specimen was initially the same, however as the compressive load was increased, the strains diverge indicating some bending of the specimen. This is probably due to a slight lack of flatness of the specimen or slight misalignment of the test piece in the test rig. The graph was linear up to a strain of 0.7% with an elastic modulus of 86 GPa measured at 0.25% applied strain and followed by a continuously curved portion with a tangential modulus at failure of approximately 15% less than that of the linear part. This non-linearity seems to be caused by the non-linear behaviour or instability of the fibre since the matrix was observed to remain elastic at this compressive strain value (as observed in Section 5.2.4, Figure 5.4). Catastrophic failure occurred at the average failure stress of 826 MPa and strain at failure of 1.02%.

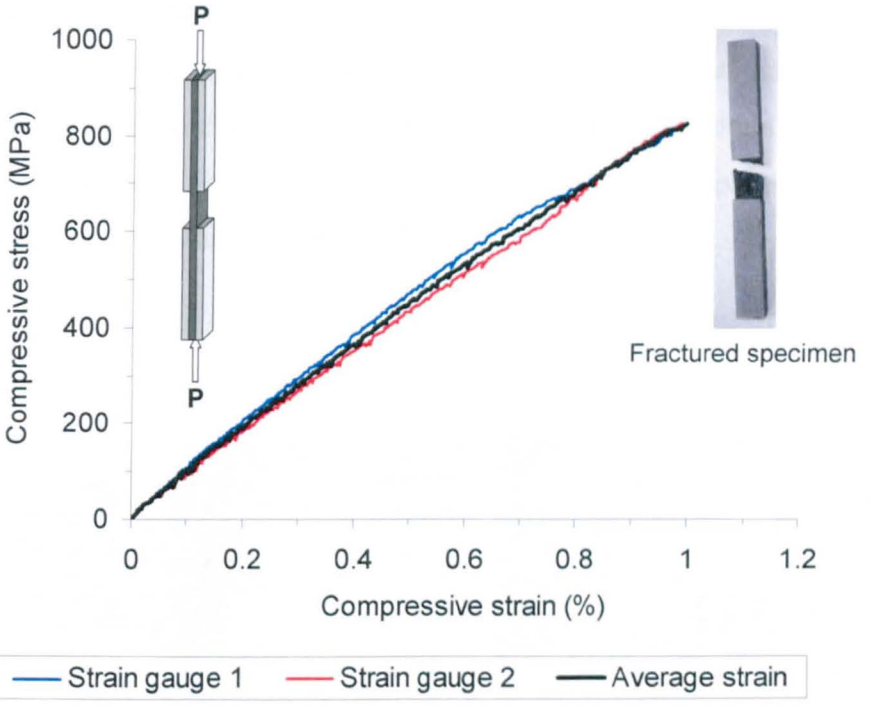

Figure 6.13: A typical compressive stress-strain response of a UD HTS40/828 CFRP composite laminate and fractured specimen.

6.2.2.2 Characteristics of fractured surface

At least five specimens were tested for each system. All specimens failed suddenly and catastrophically near the junction of the end tab and gauge section, as shown in Figure 6.13, accompanied by the spontaneous release of sound. Fracture occurred within the specimen gauge length, implying that the test was successful. This is an acceptable failure mode according to the ASTM D3410 [164], which was identified as transverse shear near top grip/tab failure (code TAT).

Figure 6.14a shows an overall failure mode of a typical UD specimen after loading in compression. The test piece was partitioned into two pieces with fracture surfaces inclined at typical angles β between 10-30°, as shown in Figure 6.14c. The failure was caused by the instability of the fibres, which induced fibre microbuckling and subsequent fibre kinking mechanisms. The fracture surface also exhibited some longitudinal splitting and interlaminar cracking, as shown in Figure 6.14b. However, this was attributed to post-failure damage rather than being a cause of failure. The failure may initiate from the specimen free edge or pre-existing material imperfections such as voids, fibre misalignment and resin rich regions. Figure 6.15 illustrates in-plane

fibre microbuckling failure mode, which initiates from (a) the specimen's free edge and (b) the resin rich region. It shows that the fibres break at two points and create a kink band inclined at an angle β to the transverse direction. The fibres within the band rotate by the angle ϕ from the initial fibre direction and the kinked fibres propagate across the width. Finally, this mechanism causes final collapse of the specimen.

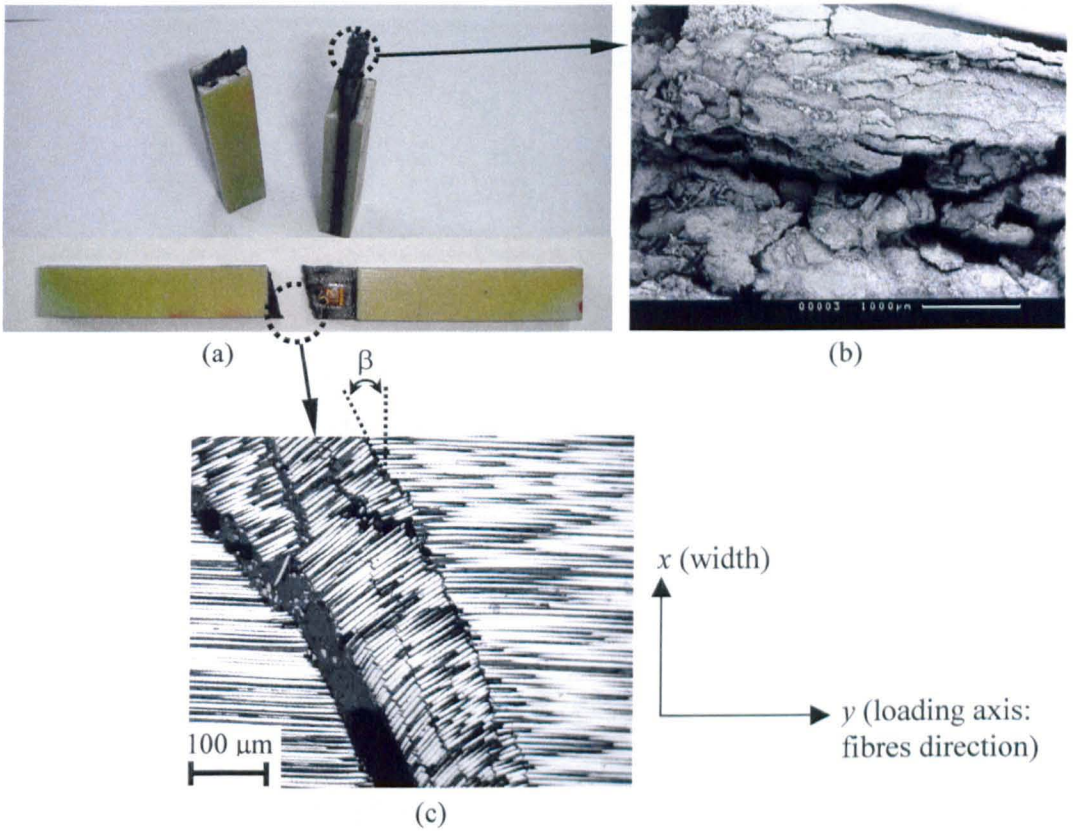

Figure 6.14: Overall failure modes of UD HTS40/828 laminate after compression (a) as observed under SEM (b) and optical microscopy (c).

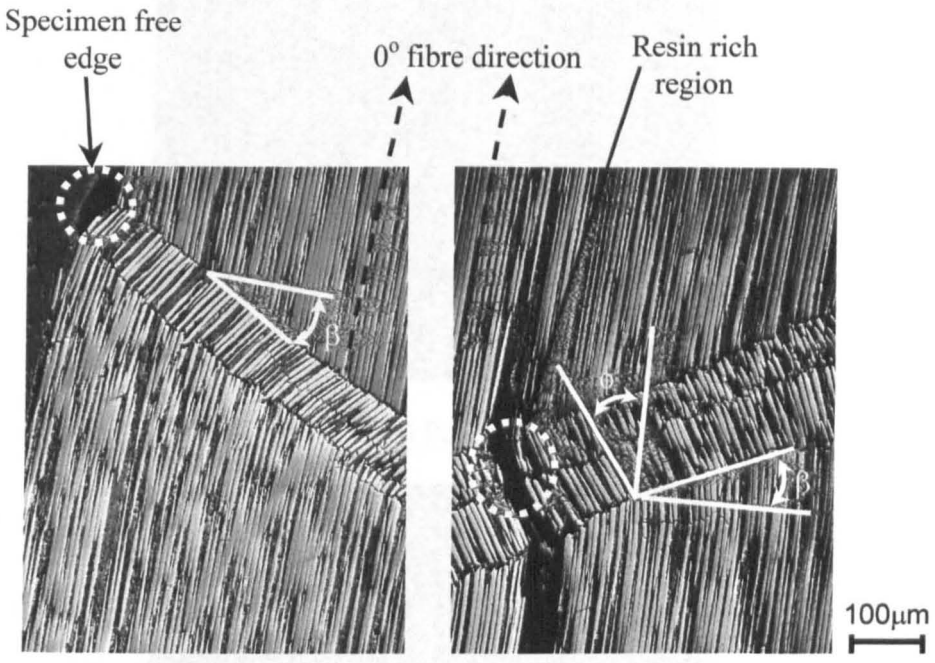

Figure 6.15: Optical micrographs showing in-plane fibre microbuckling in a HTS40/828 unidirectional laminate. The failure initiates from the specimen's free edge or from the resin rich region. It grows at an angle β=20-30° across the specimen width.

Post failure examination on the fracture surface of unmodified and nanomodified HTS40/828 system using a scanning electron microscope revealed that the specimens failed via fibre microbuckling, as shown in Figures 6.16-6.18. Figure 6.16 shows that the fibres fail in rows and plastic deformation of the matrix occurs due to bending of the fibres. Figure 6.17 shows a hackle or serration markings on the matrix between adjacent fibres, which indicates the formation of resin shear yielding due to local shear loading. This figure shows that the fibre/matrix interfacial bonding is strong since no evidence of extensive matrix cracking was observed between adjacent fibres. Closer inspection on the fracture surface reveals that the individual fibre failed in bending as shown in Figure 6.18. The fracture surface of the fibre can be divided into two distinct regions; (i) smooth surface indicates tensile region and (b) rough, irregular and serrated surface indicate compressive region.

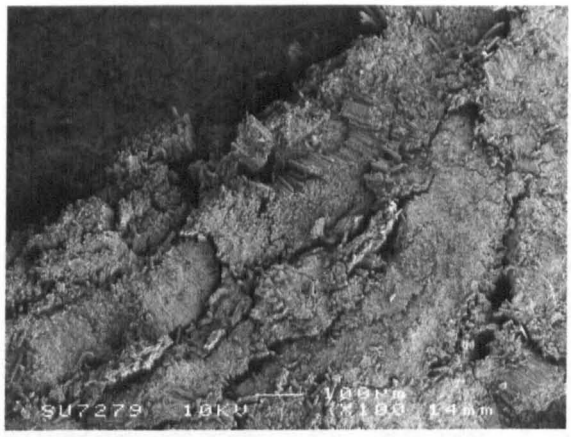

(a) Pure

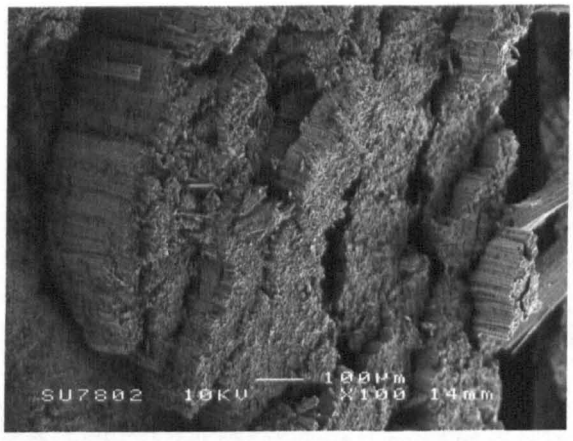

(b) 3 vol% nanosilica

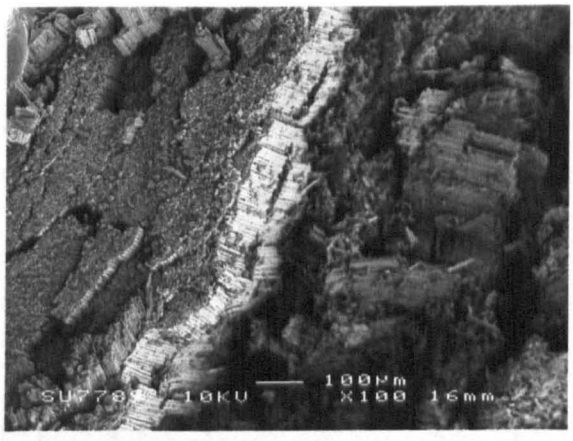

(c) 13 vol% nanosilica

Figure 6.16: Fracture surface of pure and nanomodified HTS40/828 UD laminate after compression. SEM micrographs show fibres fail in rows due to micro-bending (microbuckling). The specimens fail in compression catastrophically therefore some areas on the fibre surface were crushed due to overload compressive force on the surface of broken fibres.

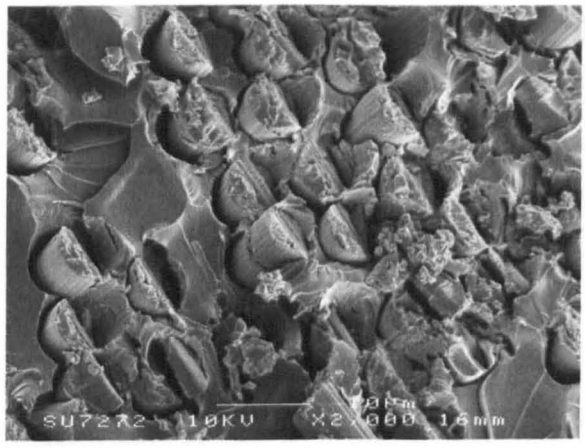

(a) Pure

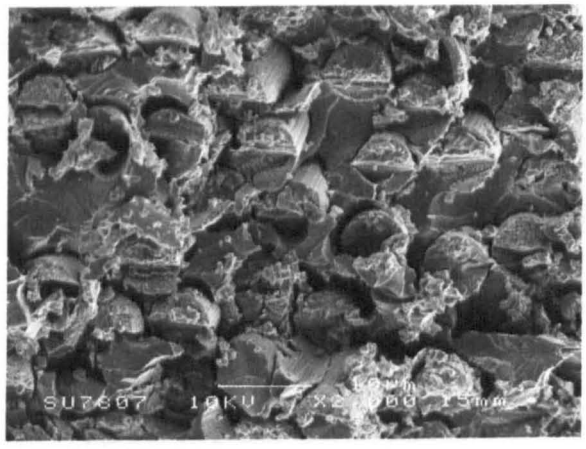

(b) 3 vol% nanosilica

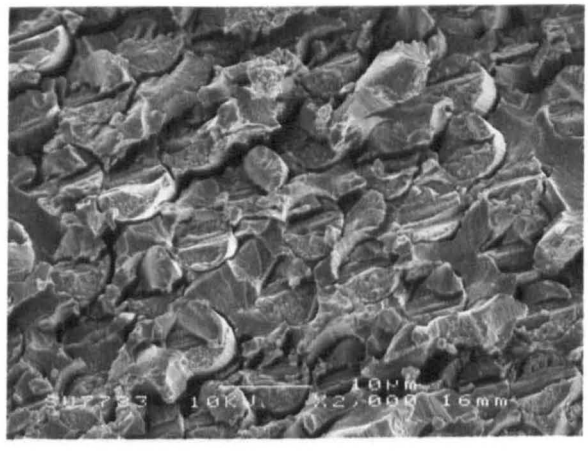

(c) 13 vol% nanosilica

Figure 6.17: SEM micrographs show that individual fibres failed due to microbuckling and plastic deformation of the matrix. Matrix cracking or fibre/matrix interface debonding occurred due to high compressive and shear (at the interface) stresses.

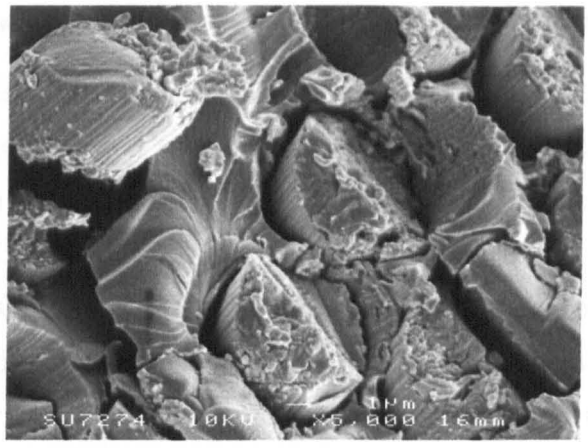

(a) Pure

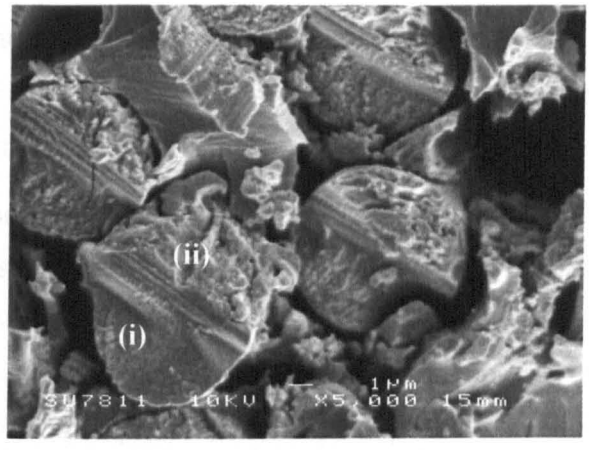

(b) 3 vol% nanosilica

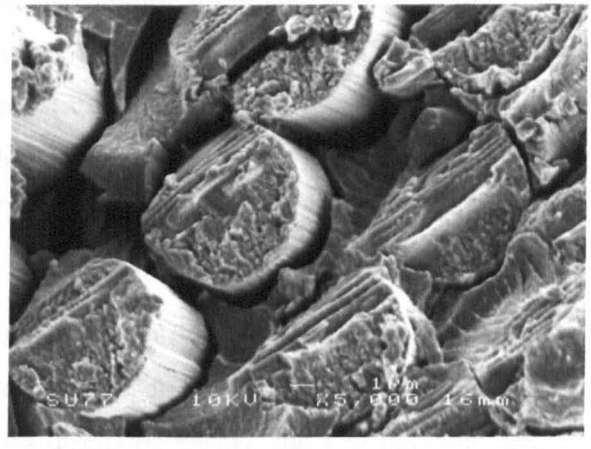

(c) 13 vol% nanosilica

Figure 6.18: SEM micrographs illustrate tensile (i) and compressive (ii) surfaces on individual fibre failed due to microbuckling at high magnification, as marked in (b). The compressive surface (ii) appears to be more serrated, irregular and rougher while the tensile surface (i) is relatively smoother.

6.2.2.3 Effect of nanosilica on compressive properties of HTS40/828 CFRP composite

Table 6.4 summarises the compressive properties of unmodified and nanomodified HTS40/828 systems compared to the commercial system HTS40/977-2. It shows the effect of nanosilica on compressive modulus, strength and failure strain of the UD laminate. It was found that the addition of nanosilica improved the compressive properties considerably. For instance, the addition of 7 vol.% nanosilica into the CFRP composite enhanced the compressive modulus by 40%, compressive strength by 54% and failure strain by 23%. The highest content of nanosilica in the CFRP composite (13 vol.%) gave a tremendous increase in compressive modulus of about 54% compared to the neat polymer with less than 3% reduction in failure strain. This suggests that the nanofiller-matrix interaction is very good and therefore stresses are more efficiently transferred via the interface, which leads to higher compressive properties when compared to the unmodified CFRP system.

In conventional systems, the addition of rigid micron-sized fillers or ply interleaf between fibres plies or agglomerated nanofillers into epoxy resins commonly increase the stiffness but have a detrimental effect on the failure strain [4,42,56,59]. Moreover, the strength of the composite is also reduced as the amount of these fillers increases. Premature failure of the composite laminate mainly occurs due to the high local stress concentrations caused by agglomeration or non-uniform dispersion of the fillers. Also, reduction in strength and failure strain can be due to improper load transfer between matrix and fillers (caused by a poorly optimised interface). In contrast, in the present study, Figure 6.19 and Table 6.4 show that the incorporation of nanosilica enhances the compressive modulus and strength of the laminate without reducing its failure strain even at high nanosilica content. The Poisson's ratio of nanomodified-CFRP composite is less than the pure system. This indicates a stiffer system.

A rigid silica nanoparticle has a Young's modulus of 70 GPa [73]. Once it is dispersed in Epikote 828, the elastic modulus of the matrix increases with increasing nanosilica content. As discussed earlier, the UD laminate fails due to fibre instability under compression. Therefore, the nanomodified resin (which has a higher stiffness than the pure resin) provides a better support to the fibre and enhances the stiffness and strength of the composite. This means that nanosilica gives a better resistance against microbending to the fibre and plastic deformation to the matrix. Therefore it introduces additional mechanisms of energy absorption during compression. SEM observation on

fracture surface of nanomodified CFRP composite, as shown in Figures 6.17 and 6.18 b-c, show no evidence of particle agglomeration even at high silica content. Homogeneous distribution of silica nanoparticles promotes more textured fracture surfaces in the matrix due to plastic shear yielding deformation, as clearly can be seen in Figure 6.18c, compared to a more brittle fracture surface (smooth surface) of pure resin as shown in Figure 6.18a. This is evidence of tougher matrix.

These results give a promising future for the development of better CFRP systems using nano-modifiers. For example, the addition of 13 vol% of nanosilica into HTS40/828 CFRP composite offered a better compressive modulus (E=132 GPa) compared to that of a commercial aerospace grade HTS40/977-2 system prepared using hot press (E=112 GPa) [7] and prepared using autoclave (E=130 GPa), see Table 6.4. At high nanosilica content (13vol.%si) the composite failed prematurely. This perhaps due to the presence of nanosilica rich regions, which contribute to higher stress concentrations in the laminate or other imperfections such as nanovoids and fibre misalignment. However, the 7%si/HTS40/828, which has E=120 GPa and fails at 1268 MPa compressive strength, is also comparable to the HTS40/977-2 system. The performance of these two different systems is comparable since the fibre volume fraction of the 7%si/HTS40/828 system is 43 vol.% when compared to the HTS40/977-2 system having V_f = 58 vol.% [7] (prepared using hot press) and V_f = 62 vol.% (prepared using autoclave). Higher fibre volume fraction contributes to higher compressive properties of the composite laminate. Therefore it can be concluded that the nanomodified CFRP system developed using appropriately treated nanosilica and low cost epoxy (Epikote 828) provides comparable if not better performance when compared to the commercial system HTS40/977-2 currently being used for the construction of aircraft structures such as the Boeing 787. This is a very promising new result but, of course, hygrothermal and fatigue properties of the nanomodified system need also to be considered before it can be selected for the fabrication of primary aerostructures.

Table 6.4: Compressive properties of nanosilica-modified HTS40/828 laminate compared to pure system and commercial system HTS40/977-2.

Compressive properties	HTS40/ 828	Nanosilica/HTS40/828			HTS40/ 977-2
		3 vol.%	7 vol.%	13 vol.%	
Compressive modulus, E (GPa)	85.74 ± 2.27	107.75 ± 1.63	120.42 ± 1.90	132.38 ± 4.40	129.66 ± 1.48
Compressive strength, σ_u (MPa)	825.93 ± 12.60	1150.60 ± 31.78	1268.01 ± 45.78	1172.20 ± 46.17	1505.48 ± 29.67
Compressive strain at break, ε_f (%)	1.06 ± 0.02	1.24 ± 0.07	1.30 ± 0.08	1.03 ± 0.05	1.32 ± 0.08
Principal Poisson's ratio, ν_{12}	0.330 ± 0.006	0.300 ± 0.005	0.290 ± 0.003	0.260 ± 0.006	0.300 ± 0.005

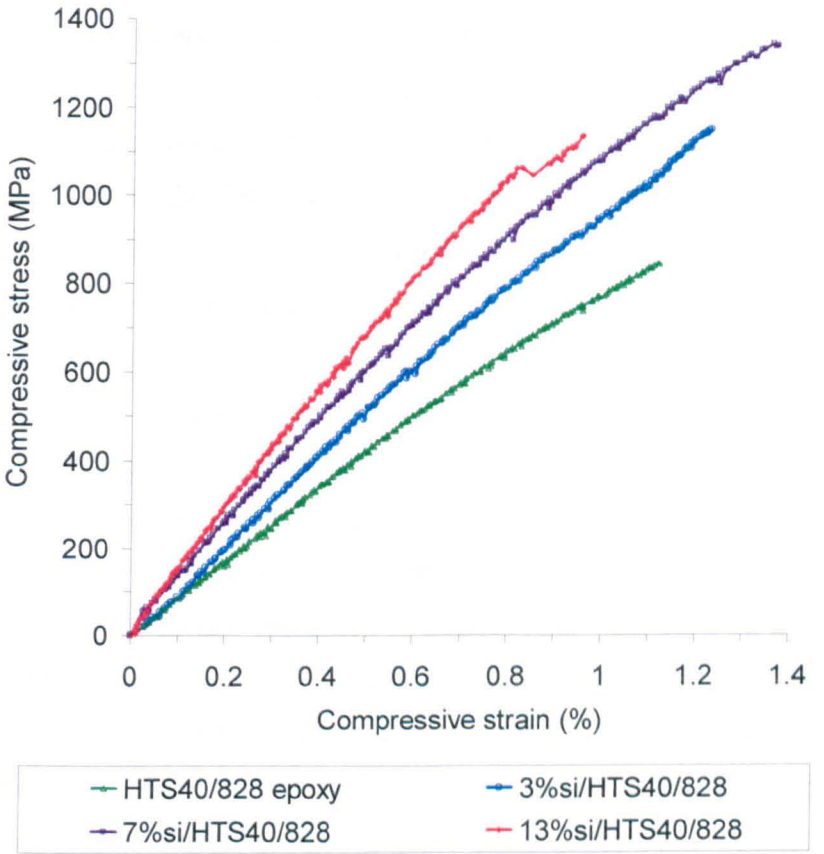

Figure 6.19: Typical compressive stress-strain curves of unmodified and nanomodified UD HTS40/828 CFRP composites specimens loaded in static uniaxial compression.

6.2.3 In-plane shear properties

Figure 6.20a shows a typical normal stress-strain response obtained from the tensile test of the $[\pm 45]_{2s}$ HTS40/828 composite laminate and a typical failed specimen. The corresponding in-plane shear stress-strain curve, as shown in Figure 6.21, was plotted based on this graph (Figure 6.20a) to determine the shear modulus, shear yield stress and strain, shear strength and failure strain. Figure 6.21 shows that the material undergoes elastoplastic behaviour before rupture. The stress initially increases proportional to the strain, obeying Hooke's law, until it reaches an elastic limit (point A). In this elastic region, the elastic shear modulus was calculated at 0.1-0.5% shear strain. Beyond the proportional limit, the strain begins to increase more rapidly for each increment in stress until it reaches maximum load at point C. The materials failed at 45° to the loading axis as shown in Figure 6.20b. This indicates a pure shear failure mode.

In the previous section, observation of fractured specimens of UD laminates after loaded in compression showed that the specimens failed due to fibre microbuckling and kinking. Budiansky [45] suggested that composites failed when the shear yield strength is reached causing fibre kinking. While, Berbinau et al [46] proposed that the composites failed when the initially misaligned fibre reached its maximum amplitude due to bending. This fibre microbuckling mechanism is mainly influenced by the initial misalignment angle of the fibre and the in-plane shear modulus of the composite. In the current work, Berbinau's concept was extended to incorporate the non-linear in-plane shear modulus (as a function of the shear strain) based on the elastoplastic shear stress-strain response into the fibre microbuckling model. These show that the in-plane shear modulus and yield stress play an important role in determining the strength of the composite system loaded in compression.

There is no standard method to determine the shear yield stress (τ_y) and strain (γ_y). Mackinley [47] and Lee [165] used a graphical method to determine the yield point. This method involves several steps; (i) two tangent lines were draw on the shear stress-strain curve at the origin and at 6% shear strain, (ii) a vertical line was plotted through the point of intersection of the tangents and (iii) the yield stress was taken based on the point at which the vertical line intersected with the τ-γ curve. The yield stress obtained using this method is similar to the value of 0.5% offset shear stress. This can be determined by translating the shear modulus of elasticity line along the strain axis from the origin by 0.5% strain. This offset line is extended until it intersects the τ-γ curve where this intersection point is the shear yield point. This 0.5% offset technique is more

reliable since the $[\pm 45]_{2s}$ laminate with reduced gauge length of 50 mm failed at less thatn 6% shear strain, as shown in Figure 6.20a. Moreover, a standard technique needs to be consistently employed in order to study the effect of nanosilica on the shear yield stress of the HTS40/828 CFRP composite. Therefore, this 0.5% offset technique was implemented in this study to determine the yield point, as shown in Figure 6.21 point B.

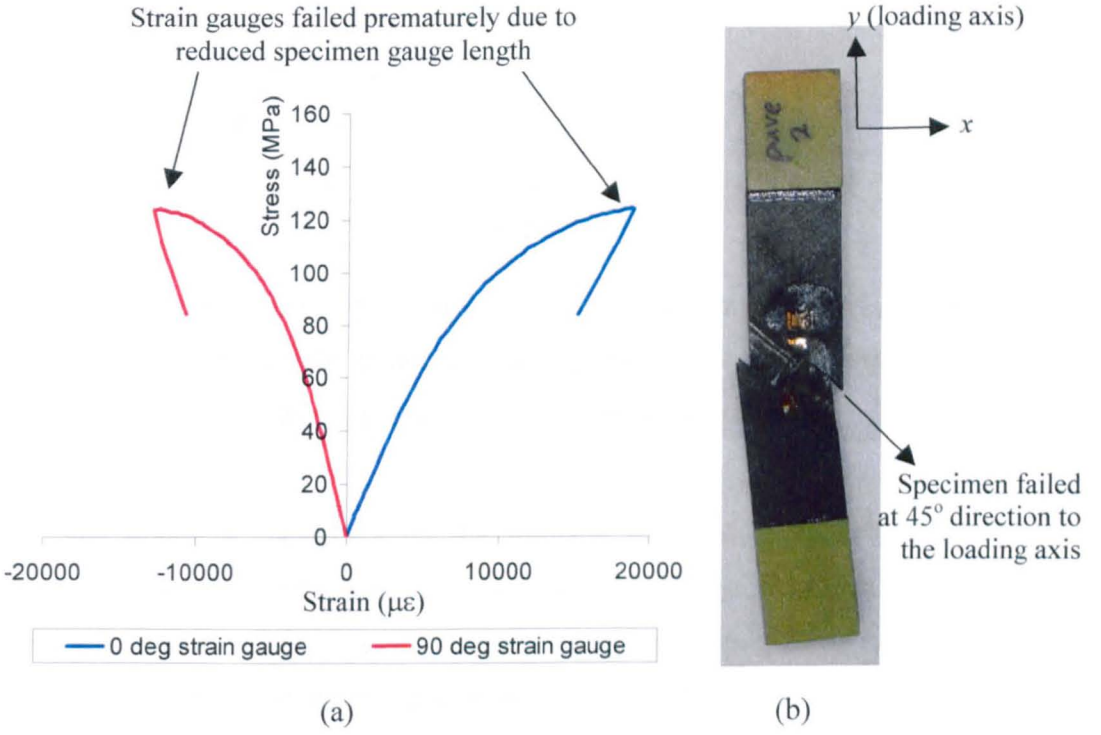

Figure 6.20: (a) A typical normal stress-strain response of a $[\pm 45]_{2s}$ HTS40/828 laminate loaded in tension and (b) an example of failed specimen . The normal and transverse strains were measured by 120Ω strain gauges.

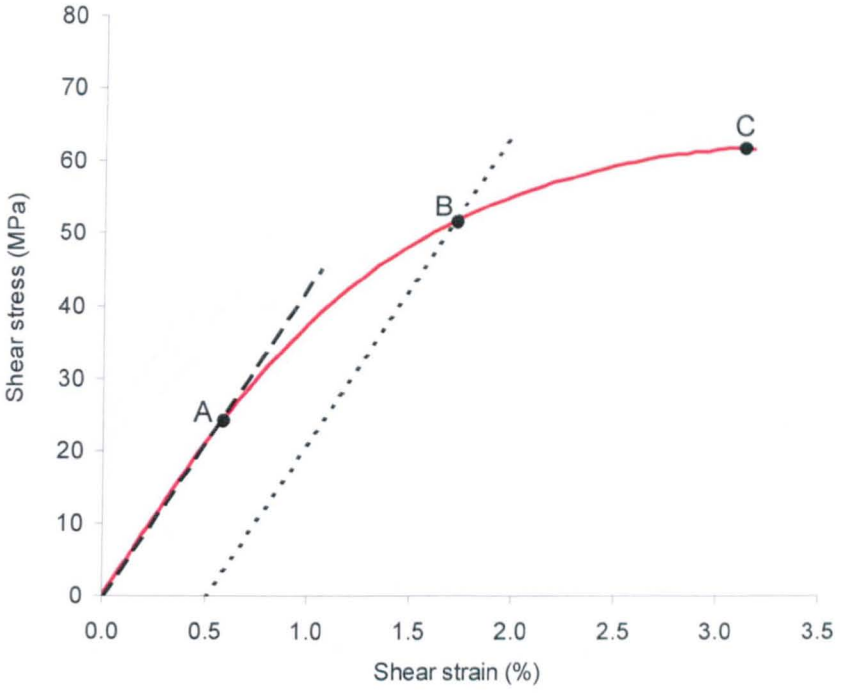

Figure 6.21: A typical in-plane shear stress-strain response of $[\pm 45]_{2s}$ HTS40/828 laminate showing the elastic limit, point A, yield point at 0.5% offset (offset shear stress), point B, and shear strength, point C.

The effect of nanosilica on the in-plane shear stress-strain response of the HTS40/828 system is illustrated in Figure 6.22. It can be seen that the presence of nanosilica enhanced the in-plane shear properties of the CFRP composite. The nanomodified CFRP exhibited higher elastic shear modulus (as measured at the initial slope of the graph) and shear strength compared to the unmodified system. The increase in shear modulus is expected because the elastic moduli of Epikote 828 in compression, tension and bending were increased with increasing nanosilica content. Therefore a stiffer matrix enhances the stiffness of the HTS40/828 system.

Table 6.5 summarises the in-plane shear properties of nanomodified CFRP compared to the unmodified system. The in-plane shear modulus, strength and yield stress were increased with increasing nanosilica content. The table shows that the HTS40/828 system has average in-plane shear modulus, strength and yield stress of 4.27 GPa, 61 MPa and 52 MPa, respectively. By adding 13 vol% nanosilica into the HTS40/828 laminate enhanced the in-plane shear modulus by 49%, strength by 45% and yield stress by 40%. The improvement in the shear properties suggests that the high stiffness matrix introduce higher resistance to shear deformation and failure.

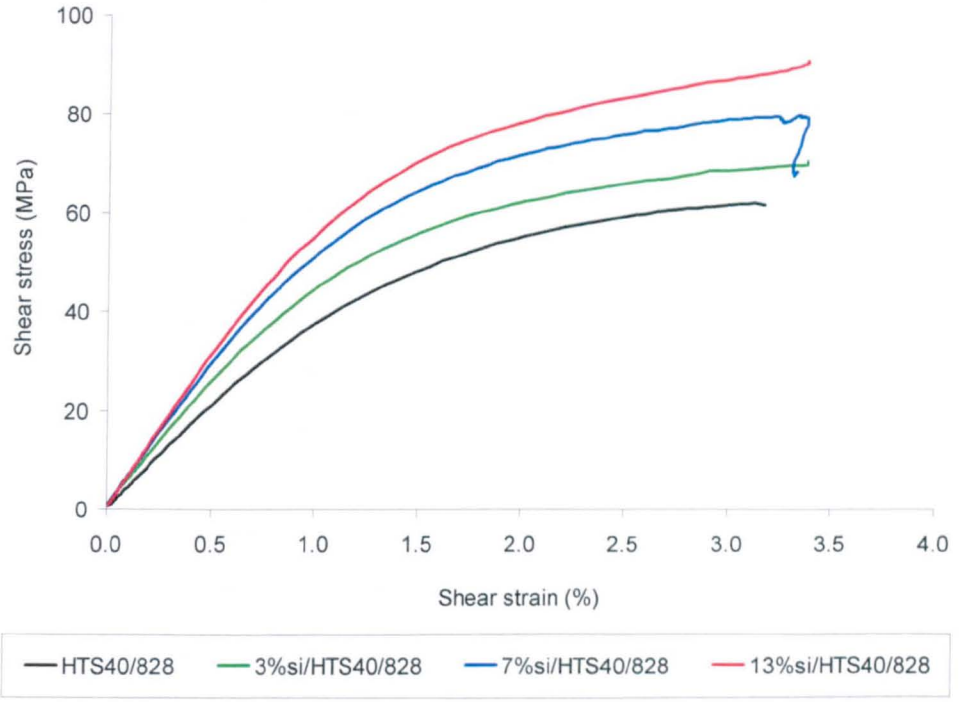

Figure 6.22: The effect of nanosilica on in-plane shear stress-strain response of HTS40/828 CFRP composite.

Table 6.5: In-plane shear properties of nanosilica-modified HTS40/828 laminate compared to pure system and commercial system HTS40/977-2.

In-plane shear properties	**HTS40/ 828**	**Nanosilica/HTS40/828**			**HTS40/977-2**	
		3 vol%	**7 vol%**	**13 vol%**	**50 mm GL**	**100 mm GL**
Elastic in-plane Shear Modulus, G_{12}^{e} (GPa)	4.27 ± 0.07	5.33 ± 0.09	5.72 ± 0.22	6.37 ± 0.13	5.39 ± 0.04	5.45 ± 0.10
In-plane shear strength, τ_{ult} (MPa)	61.00 ± 1.24	72.23 ± 1.47	77.93 ± 1.12	88.69 ± 1.52	82.88 ± 0.99	112.80 ± 1.05
Maximum shear strain, γ_{ult} (%)	2.96 ± 0.17	3.25 ± 0.05	3.23 ± 0.11	3.30 ± 0.08	3.38 ± 0.00	16.81 ± 0.31
In-plane shear yield strength, τ_y (MPa)	51.48 ± 0.41	58.67 ± 0.62	64.51 ± 0.56	72.25 ± 0.78	64.25 ± 0.78	62.09 ± 0.77
In-plane shear strain at yield, γ_y (%)	1.71 ± 0.01	1.61 ± 0.03	1.64 ± 0.04	1.64 ± 0.02	1.70 ± 0.01	1.73 ± 0.03

In table 6.5, the results of unmodified and nanomodified HTS40/828 were also compared to the commercial HTS40/977-2 system. The $[\pm 45]_{2s}$ HTS40/977-2 laminate was fabricated using prepreg materials and cured using the autoclave. This industry standard fabrication technique produced a very high quality composite with fibre volume fraction of 62 vol%. While in the current work, HTS40/828 and its nanomodified system were produced using the dry filament winding and wet resin impregnation technique. This lab scale technique produced a 42 vol % CFRP composite. The viscosity of the resin increases with increasing nanosilica content. Therefore the wet resin impregnation technique fully degassed the resin before curing process. This minimises the void content in the cured specimen even at high filler content. This contributes to the enhancement in the shear properties of the HTS40/828 by adding nanosilica. However, this lab-scale fabrication technique limits the in-plane shear specimen geometry to 50 mm gauge length. This limitation causes a premature failure in the composite laminate when it was loaded in tension. This was proven by conducting the in-plane shear tests on HTS40/977-2 system with a gauge length of 50 mm and 100 mm (according to ASTM D3518). Figure 6.23 shows typical shear stress-strain results of HTS40/977-2 system with these two different gauge lengths. The 100 mm specimen exhibits higher shear strength and strain compared to the 50 mm specimen. Table 6.5 shows that the 100 mm specimens failed at an average of 16.8% failure strain and 112.8 MPa shear strength, while only 3.38% failure strain and 82.9 MPa shear strength were recorded for the 50 mm specimen.

It is interesting to note that the nanomodified HTS40/828 with 13 vol.% nanosilica exhibited a higher overall shear properties compared to that of the HTS40/977-2 system (with 50 mm gauge length) as illustrated in Figure 6.23 and shown in Table 6.5. The shear modulus, strength and yield stress were higher than that of the HTS40/977-2 system by 18%, 7% and 13%, respectively. These are very promising results since the fabricated nanomodified CFRP system has a low fibre volume fraction. The shear properties of composites are mostly determined by the properties of the matrix and the quality of the fabricated specimen.

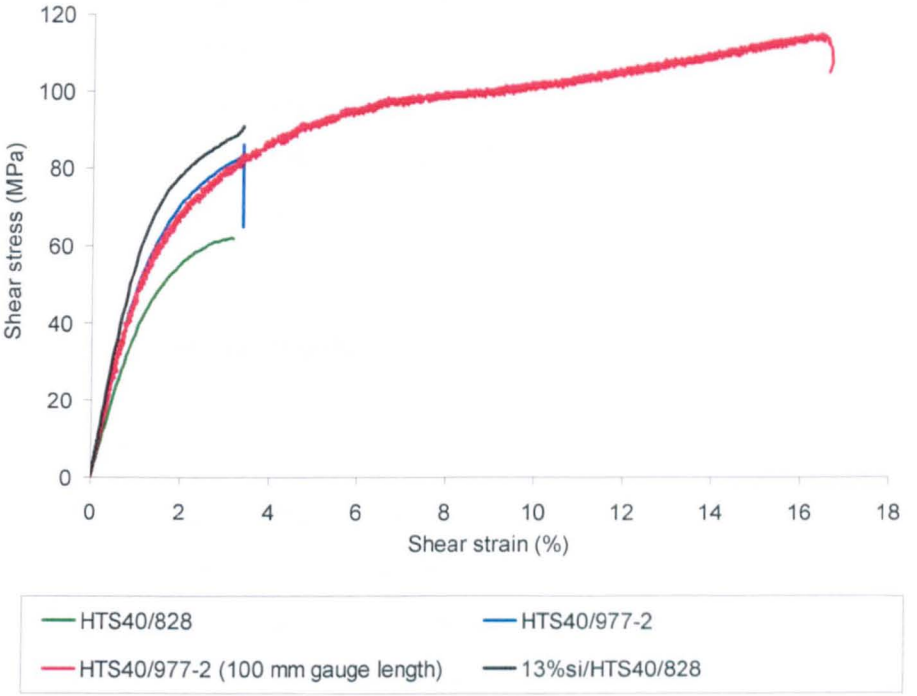

Figure 6.23: Comparison of in-plane shear stress-strain response of HTS40/828 system with the HTS40/977-2 CFRP system.

6.3 Prediction of compressive strength of UD laminates

The experimentally observed fracture mechanisms of UD unmodified and nanomodified HTS40/828 CFRP composite laminate, which was loaded in compression, involved both fibre microbuckling and plastic fibre kinking. These mechanisms were governed by initial waviness of the fibres in the matrix and the shear response of the matrix material. It is assumed that the failure is triggered by the local instability of misaligned fibres embedded in the matrix. The misaligned fibres break at two points upon reached maximum micro-bending deformation. This leads to the formation of two planes of fracture. The kinked fibres disrupt the stability of the adjacent ones, and hence the neighbouring fibres also fail in buckling. The process continues across the specimen's width until the whole laminate breaks, at a certain kink band inclination angle, into two pieces. These scenarios were proposed based on extensive experimental observations as discussed in Section 6.2.2. Therefore, in this section, the compressive strength of UD HTS40/828 laminate and its nanomodified system are predicted using fibre microbuckling and fibre kinking models. The results are compared to the measured

values. In addition, the performance of this new developed system is also evaluated by comparing to the compressive strength of the commercial UD HTS40/977-2 laminate.

The fibre microbuckling models, which were developed by Rosen [48] and Berbinau et al. [46] and the fibre kinking models, which were developed by Argon [49] and Budiansky [45], are implemented and discussed in detail in the following sections.

6.3.1 Fibre microbuckling models

6.3.1.1 Rosen's model

One of the earliest experimental works conducted by Rosen [48] investigated the compressive failure of UD glass-epoxy composite plates. The compressive failure was assumed to be triggered by the local instability of fibres embedded in the matrix. The failure of these plates was due to fibres microbuckling, analogous to the buckling of columns supported by an elastic matrix. In the 2-dimension model, the UD fibre composite was treated as parallel fibre layers. The fibre layers were initially perfectly straight aligned and evenly spaced. Both the matrix and the fibre materials were assumed to be linear elastic. When the compressive load was applied, the fibres buckled into either one of two possible microbuckling modes: the extension mode or the shear mode as shown in Figure 6.24a-b.

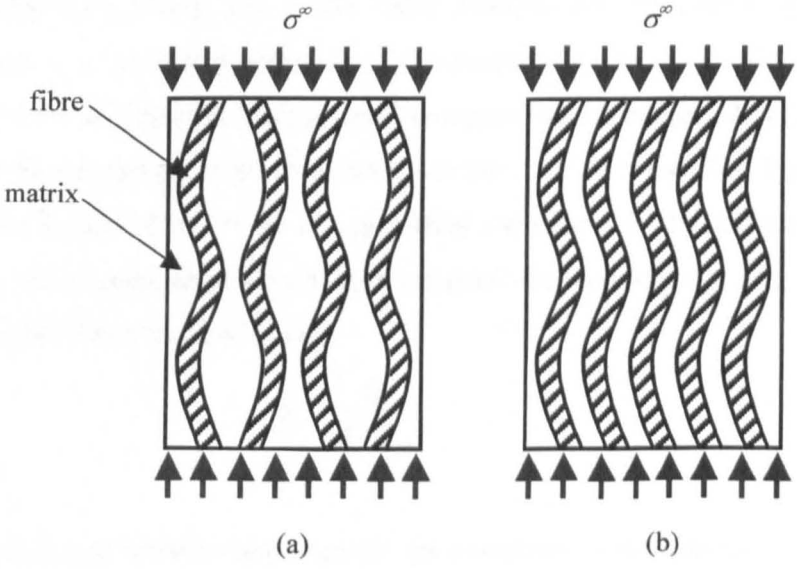

Figure 6.24: Failure modes of UD composite subjected to longitudinal compressive load: (a) fibre microbuckling in extensional mode and (b) fibre microbuckling in shear mode.

The adjacent fibres in a composite may buckle independently of each other or cooperatively with each other. In the first case, the matrix deforms in extension mode causing the fibres to buckle out of phase relative to each other as shown in Figure 6.24a. This buckling mode is possible if the fibre-to-fibre distance is quite large or when the fibre volume fraction of the composite is very small (V_f<0.4) [48]. In the second case, the matrix deforms in shear mode causing transverse deformation in adjacent fibres, which are in phase with each other as shown in Figure 6.24b. This type of buckling mode is the most common failure mode observed in CFRP composites, which has fibre volume fraction more than 40%. Rosen [48] derived analytical equations for the prediction of compressive strength using an energy method for both extension and shear modes. For the extension mode, the compressive strength can be calculated using the following equation:

$$\sigma_c = 2V_f\sqrt{\frac{V_f E_m E_f}{3(1-V_f)}} \tag{6.1}$$

and for the shear mode, the compressive strength is

$$\sigma_c = \frac{G_m}{1-V_f} + \frac{\pi^2 V_f d_f}{12\lambda} \tag{6.2}$$

where V_f is the fibre volume fraction, E_m and E_f are the Young's modulus for the matrix and the fibre respectively, G_m is the shear modulus for the matrix, d_f is the fibre diameter and λ is the half-wavelength of the buckling mode shape. The magnitude of the second term in Equation (6.2) is small compared to the magnitude of the first term since the half-wavelength is much greater than the fibre diameter (see Figure 6.15, the length of the broken fibres = 60-100 μm while the diameter of the fibre = 6.97 μm). Neglecting the second term Rosen [48] obtained the approximate and often quoted equation for the shear mode as below:

$$\sigma_c = \frac{G_m}{1-V_f} \tag{6.3}$$

According to Rosen's bifurcation analysis, the compressive strength of a UD composite was approximately equal to the elastic shear modulus, G_{12} of the composite. Therefore Equation (6.3) becomes:

$$\sigma_c = \frac{G_m}{1 - V_f} \approx G_{12} \tag{6.4}$$

In the current work, the fibre volume fraction obtained for unmodified and nanomodified systems was 41-43 vol.%. If the composite fails in extension mode, the predicted compressive strength, using Equation (6.1) and data in Table 6.6, deviated from the measured values, see Table 6.7. This confirms that the HTS40/828 system fails in shear mode. However, the compressive strength as predicted using Equation (6.4) showed four to five times greater than experimental values as shown in Table 6.7. Similar results were reported elsewhere [3,46,50-52] for various types of CFRP composite systems. Even though Rosen's predictions overestimated the UD compressive strength and are not acceptable for the case of modern CFRP composite systems, the model highlights the properties of the polymer matrix and their vital role in determining the compressive strength of the composites.

Table 6.6: Input data for the prediction of compressive strength using Rosen model.

Input data	**Sym-bol**	**HTS40/ 828**	**Nanosilica/HTS40/828**			**HTS40/ 977-2**
			3 vol%	**7 vol%**	**13 vol%**	
Fibre volume fraction (%)	V_f	42	41	43	42	62
Elastic modulus of the fibre (GPa)	E_f	239	239	239	239	239
Elastic modulus of the matrix (GPa)	E_m	2.75	3.08	3.33	3.80	3.52

Table 6.7: Predicted compressive strength using Rosen's model compared to the experimental values.

Compressive strength	**Eqn**	**HTS40/ 828**	**Nanosilica/HTS40/828**			**HTS40/ 977-2**
			3 vol%	**7 vol%**	**13 vol%**	
Extensional mode microbuckling (MPa)	(6.1)	10580	10710	12200	12400	26500
Shear mode microbuckling (MPa)	(6.4)	4270	5330	5720	6370	5450
*Measured compressive strength (MPa)	-	826	1151	1268	1172	1505

*Experimental data from Section 6.2.2

6.3.1.2 Berbinau's model

Based on the concept proposed by Rosen [48], Berbinau et al. [46] suggested that in addition to the shear modulus, the unidirectional compressive strength also depends on the quality of the laminate and the properties of the fibre. Several important factors that contribute to the strength of the laminate were considered in Berbinau's model. These include the configuration of fibre waviness (initial fibre misalignment and wavelength), in-plane shear properties (shear yield stress and strain, shear strength and modulus), fibre properties (diameter and elastic modulus) and fibre volume fraction.

Berbinau et al. [46] developed a general fibre microbuckling equation of 0^{o} fibre under compressive load by assuming that the fibre (possessing an initial fibre misalignment) acted as an Euler slender column supported by a non-linear foundation (resin). Based on the fact that carbon fibres in the 0^{o} UD laminates are not perfectly aligned with the loading direction, (in current work, up to 5^{o} fibre misalignment, see Figure 6.11), Berbinau et al [46] modelled the initial fibre waviness by a sine function $v_0(x)$ as shown in Figure 6.25a.

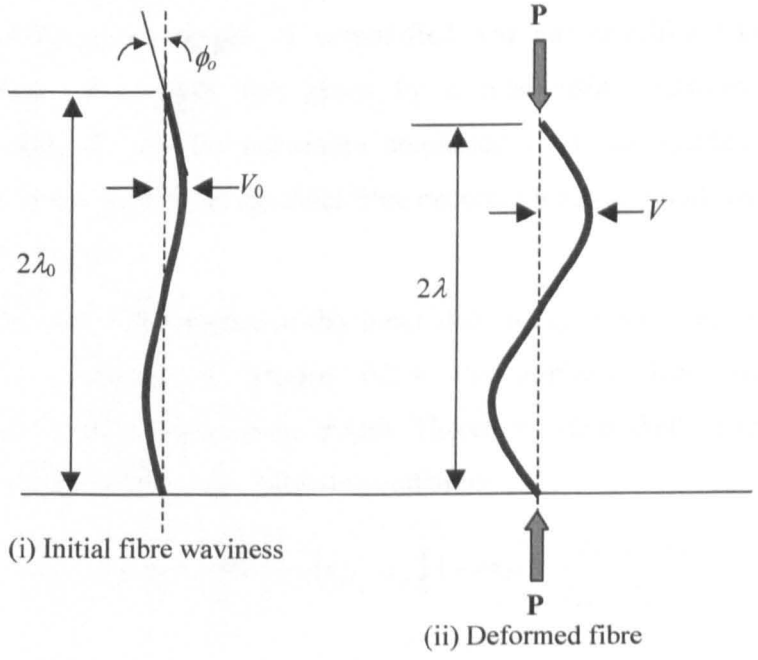

Figure 6.25: A schematic diagram of fibre microbuckling mode [46].

The following 4^{th} order differential equation was derived by Berbinau et al. [46] based on a free body diagram of an infinitesimal element of a deformed fibre proposed

by Hahn and Williams [53], refer to Appendix C for details. The following equation when solved gives the 0° fibre stress as a function of amplitude v:

$$E_f I_f \frac{d^4(v-v_0)}{dx^4} + \frac{A_f \sigma_0}{V_f}\frac{d^2 v}{dx^2} - A_f G_{12}^{ep}(\gamma)\frac{d^2(v-v_0)}{dx^2} = 0 \tag{6.5}$$

where E_f and I_f are the elasticity modulus and the second moment of area of the fibre, respectively. A_f is the fibre cross-section area, V_f is the fibre volume fraction and $G_{12}^{ep}(\gamma)$ is the experimental nonlinear shear modulus as a function of shear strain. The expression of $G_{12}^{ep}(\gamma)$ is given by:

$$G_{12}^{ep}(\gamma) = G_{12}^{e}\exp\left(-\frac{G_{12}^{e}\gamma}{\tau_y}\right) + G_{12}^{p}\exp\left(-\frac{G_{12}^{p}\gamma}{\tau_{ult}-\tau_y}\right) \tag{6.6}$$

where G_{12}^{e} is the elastic shear modulus (tangent at 0.1-0.5% shear strain) and G_{12}^{p} is the plastic shear modulus (calculate tangent at yield point). τ_y and τ_{ult} are the yield and ultimate shear stresses, respectively.

In this study, Equation (6.5) was solved numerically using Fortran programming. This programme was compiled and executed via a commercial Fortran compiler to predict the compressive strength of unmodified and nanomodified-UD HTS40/828 CFRP composite. The result was given by a relationship between the applied compressive stress σ^{∞} and the maximum amplitude V of the buckled fibre during uniaxial compression. Failure of the axial fibre occurred when its amplitude V started to increase asymptotically.

Tables 6.6 and 6.8 summarise the input data which were used in the Fortran programme. As discussed in Section 6.2.3, the in-plane shear samples failed prematurely due to the reduced gauge length. Therefore, the overall shear-stress strain response were predicted using the following equation:

$$\tau(\gamma) = \tau_y\left(1-\exp\left(-\frac{G_{12}^{e}\gamma}{\tau_y}\right)\right) + \left(\tau_{ult}-\tau_y\right)\left(1-\exp\left(-\frac{G_{12}^{p}\gamma}{\tau_{ult}-\tau_y}\right)\right) \tag{6.7}$$

This equation is developed based on Berbinau-Soutis earlier work [46] and derived from the experimental shear stress-strain curve. Figure 6.26 presents the overall in-plane shear stress-strain response of unmodified and nanomodified HTS40/828 CFRP composite systems predicted using Equation (6.7) that shows a very good

agreement when compared to the experimental curves. The predicted in-plane shear properties based on all experimental results (where at least five specimens were tested for each system) are summarised in Table 6.8. In addition, the fibre diameter d_f = 6.97 μm, initial half fibre wavelength λ_o =10 d_f, laminate width w = 10 mm, laminate thickness t_o = 2 mm and number of plies n = 8 were also used as the input data.

Table 6.8: Input data for the prediction of compressive strength using Rosen model.

Input data	Sym -bol	HTS40/ 828	Nanosilica/HTS40/828			HTS40/ 977-2
			3 vol%	7 vol%	13 vol%	
Initial misalignment angle	ϕ_o	1-2°	1-2°	1-2°	1-2°	1°
In-plane shear yield strength (MPa)	τ_y	51.48	58.67	64.51	72.25	64.25
In-plane shear strain at yield (%)	γ_y	1.71	1.61	1.64	1.64	1.70
In-plane shear strength (MPa)	τ_{ult}	70.2	77.4	87.6	97.8	112.80
Maximum shear strain (%)	γ_{ult}	7.00	7.00	7.00	7.00	16.81
Elastic in-plane Shear Modulus (GPa)	G_{12}^e	4.27	5.33	5.72	6.37	5.45
Plastic in-plane Shear Modulus, (GPa)	G_{12}^p	1.23	1.34	1.52	1.65	0.89

Figure 6.27a presents the maximum amplitude V of the 0° buckled fibre versus the applied stress σ^∞ curves for the UD HTS40/828 CFRP composite laminate which were predicted using three different initial fibre misalignment angles; ϕ_o=1°, 1.5° and 2°. All curves show that V increases slowly with increasing applied stress σ^∞ and then grows exponentially until it reaches the maximum microbuckling stress σ_{mb} where the curve increases asymptotically. Fibre breakage is assumed to occur when the fibre amplitude increases without any significant changes in applied stress. The predicted microbuckling stress σ_{mb} of the HTS40/828 UD composite laminate at ϕ_o=1° is 610 MPa, which is 26% lower than the experimentally measured compressive strength. The microbuckling stress is reduced to 417 MPa at an assumed value ϕ_o=2°. From the fibre waviness distribution as shown in Figure 6.11, most of the fibres lie in between 1 to 2° from the 0° fibre axis.

If the mean fibre waviness of ϕ_o=2° is applied, the compressive strength predicted using Berbinau's model is about 50% less than the measured value.

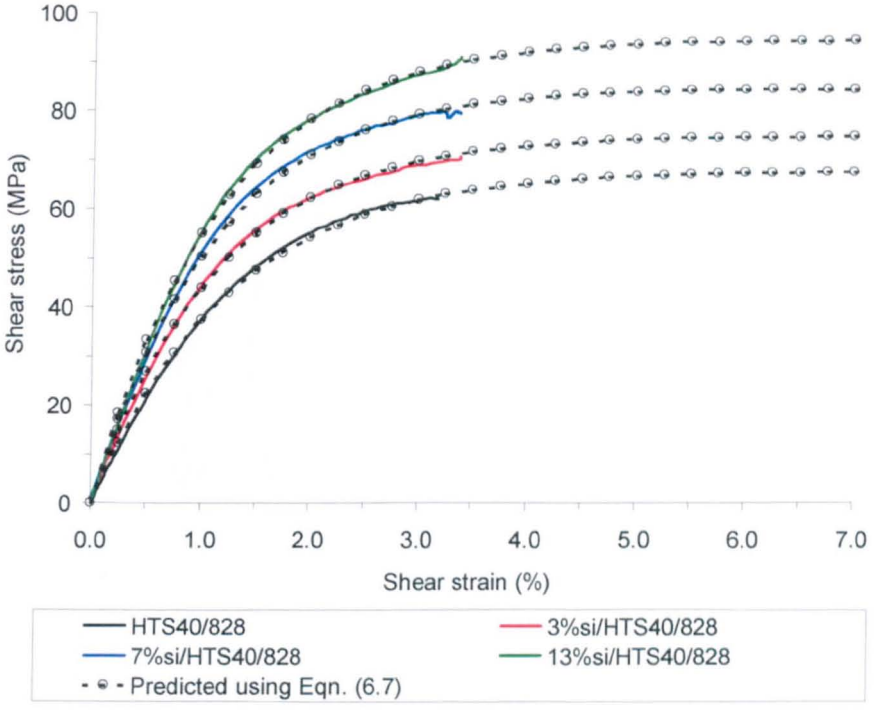

Figure 6.26: Typical predicted in-plane shear stress-strain curves of HTS40/828 CFRP composite system compared to the experimental results. The predicted curves were plotted based on analytical Equation (6.7).

Figure 6.27 shows that the microbuckling stress increases with increasing nanosilica content at a similar value of ϕ_o. For instance, the addition of 3, 7 and 13 vol.% nanosilica in HTS40/828 increased the microbuckling stress by 35%, 74% and 110%, respectively, at ϕ_o=1°. All predicted values of compressive stress using Berbinau's model, as shown in Figure 6.27, exhibit lower than the experimental values except 13%si/HTS40/828 laminate which is predicted at ϕ_o=1°. As explained in Section 6.2.2, the 13%si/HTS40/828 laminate failed prematurely during the compression test at 1172 MPa. As shown in Figure 6.27d, the predicted compressive strength is 1283 MPa at ϕ_o=1°. Figure 6.28 shows that the compressive strength of the UD HTS40/977-2 composite laminate at ϕ_o=1° is 1232 MPa, which is 22% lower than the experimentally measured compressive strength. This figure also shows the fibre microbuckling stress of the 7%si/HTS40/828 is 16% lower than that of the HTS40/977-2 system. These two

systems are comparable since the V_f = 43 vol.% was used to predict the compressive strength of 7%si/HTS40/828 compared to V_f = 62 vol.% for the HTS40/977-2 system.

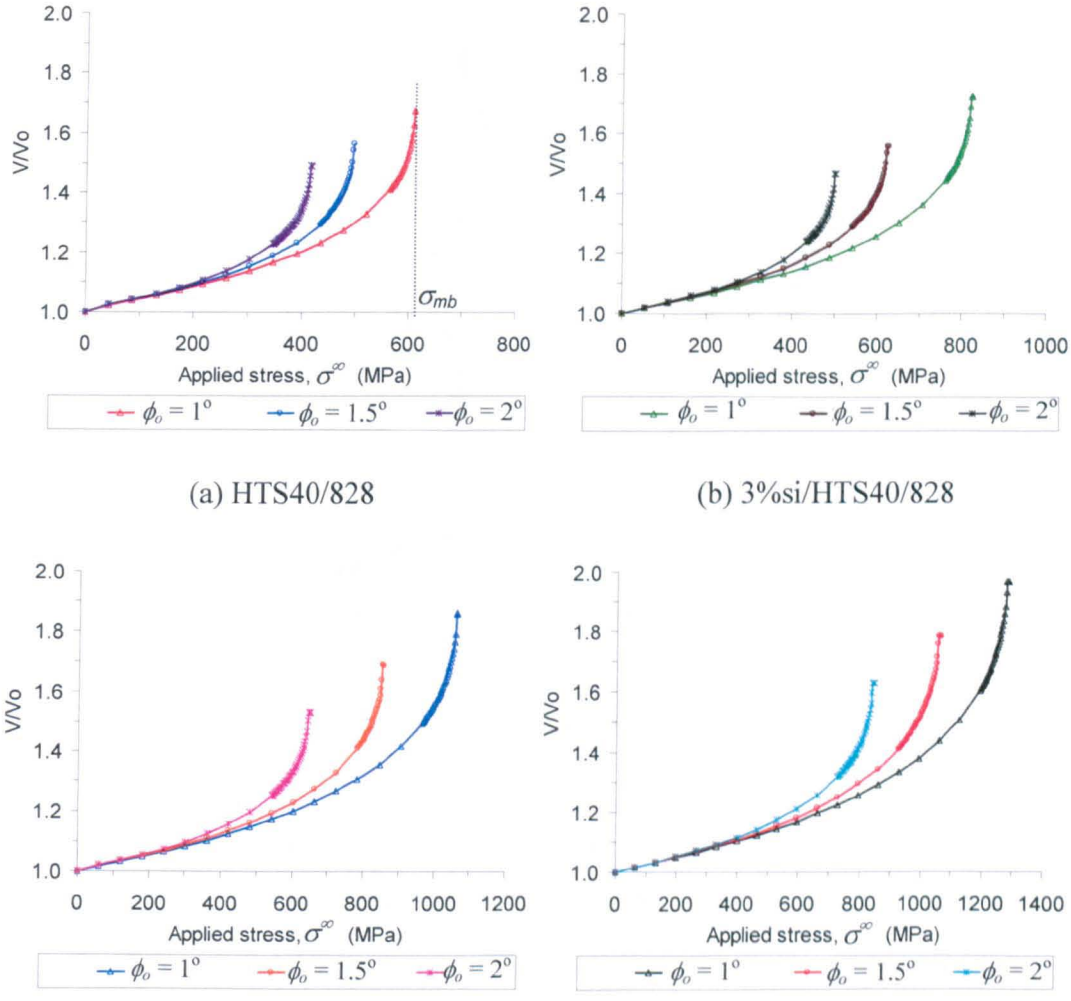

(a) HTS40/828

(b) 3%si/HTS40/828

(c) 7%si/HTS40/828

(d) 13%si/HTS40/828

Figure 6.27: Fibre amplitude V normalised by initial fibre imperfection V_o versus applied compressive stress σ^{∞} curves for unmodified (a) and nanomodified (b-d) UD HTS40/828 CFRP composite. The unidirectional compressive strength is predicted for three different initial fibre misalignment angle; ϕ_0 = 1°, 1.5° and 2°.

The results showed that Berbinau's model underestimates the actual compressive strength. This is because it assumes that the catastrophic failure of the composites occurs when the fibre microbuckling initiates, where this is not necessarily the final

failure stress of the whole laminate. Experimental observation showed that the UD laminate collapsed due to fibre instability or microbuckling and fibre kinking. The composite failure by kinking mechanism is discussed in the following section.

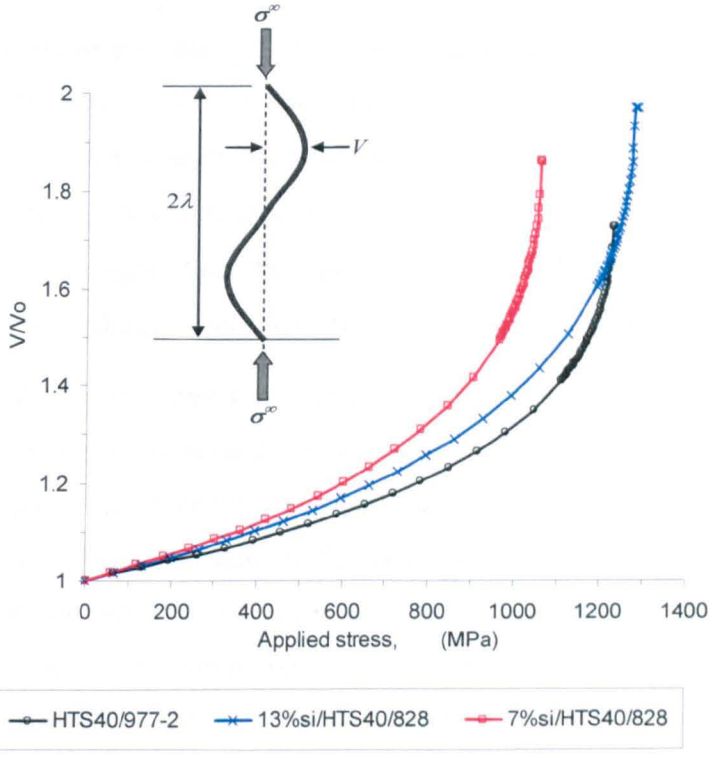

Figure 6.28: Predition of microbuckling stress of HTS40/977-2 UD laminate compared to HTS40/828 laminate, which was modified with 7 vol% and 13 vol.% nanosilica.

6.3.2 Fibre kinking models

6.3.2.1 Argon's model

Argon [49] proposed that the compressive failure is initiated by plastic shear deformation of the matrix associated with the rotation of initial misaligned fibres within a certain band before final failure occurs. This model considered both plastic shear deformation and initial fibre misalignment. A simple model developed by Argon [49] was based on the assumption that once the shear stress in the region of fibre misalignment reaches the composite shear yield strength, the composite failure would take place. This model is called fibre kink band model and the compressive strength is expressed as:

$$\sigma_c = \frac{\tau_y}{\phi_o} \tag{6.8}$$

where τ_y is the shear yield stress of the composite and ϕ_0 is the initial fibre misalignment angle.

The UD compressive strength for unmodified and nanomodified HTS40/828 UD CFRP composite system was predicted using Argon's model based on input data summarised in Table 6.8. Table 6.9 shows the predicted compressive strength using two different initial misalignment angles: ϕ_0 = 1° and 2°. It was found that the predicted values were 4-5 times higher than the experimental values if ϕ_0 = 1°, while by assuming average ϕ_0 = 2° the predicted values were twice as high as the measured values.

In general, Argon's model over predicted the longitudinal compressive strength for UD CFRP composite systems as shown in Table 6.9. From the analysis, Argon's model shows that shear strength and fibre misalignment are important parameters affecting the compressive strength of the composite. The initial maximum angular misalignment or waviness of the fibres ϕ_0 causes shear stresses to develop at the fibre-matrix interface as the compressive load is applied as illustrated in Figure 6.29a. However, Equation (6.8) predicts a kink orientation angle β = 0 which is not in agreement with the experimental observation β = 20°-30° (see Section 6.2.2 Figure 6.15).

Table 6.9: Predicted compressive strength using Argon's model compared to the experimental values.

Compressive strength	**HTS40/ 828**	**Nanosilica/HTS40/828**			**HTS40/ 977-2**
		3 vol%	**7 vol%**	**13 vol%**	
Predicted compressive strength, with ϕ_0 = 1°, (MPa)	2949	3361	3696	4139	3681
Predicted compressive strength, with ϕ_0 = 2°, (MPa)	1475	1681	1848	2070	1840
*Measured compressive strength (MPa)	826	1151	1268	1172	1505

*Experimental data from Section 6.2.2

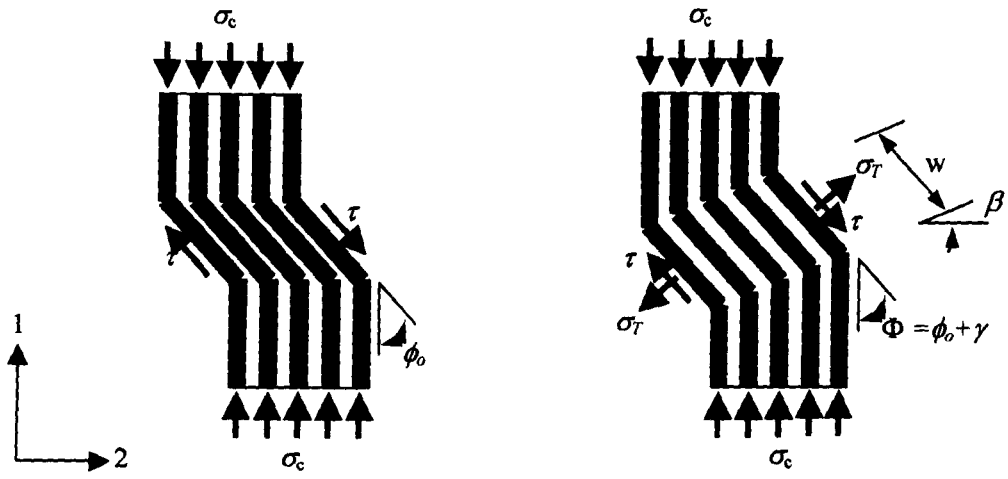

(a) Argon's model (b) Budiansky's model

Figure 6.29: Fibre kinking models (a) Argon's model with schematic geometry of the initial maximum angular misalignment of the fibres ϕ_o and (b) Budiansky's model with schematic geometry of a kink band width w oriented at an angle Φ to the 1-direction (fibre direction).

6.3.2.2 Budiansky's model

Experimental observations, based on optical microscopy and SEM micrographs (in Section 6.2.2) revealed that the laminate failed via fibre microbuckling, which is associated with yielding of the matrix to form fibre kinking. Budiansky [45] extended Argon's model by considering elastic-perfectly plastic matrix material behaviour in the kink band model. The theory for failure of composites in a kink mode proposed by Budiansky [45], as illustrated in Figure 6.29b, involves two stages as follows:

(i) Elastic deformation

When the compressive load (parallel to the fibres) is applied to the UD fibre polymer matrix with wavy fibres, shear stresses are developed due to the angle between the misaligned fibres and the loading axis (ϕ_o). Hence the resulting shear strains increase the misalignment angle of the fibres ($\phi_o+\gamma$). For a small applied stress, equilibrium is obtained and the materials deformed elastically.

(ii) Plastic deformation

As the stress is increased, the fibres, which are supported by the matrix, become unstable. Yielding of the matrix and fibres contribute to large plastic deformations. This leads to fibres breaking in a cooperative manner between adjacent fibres forming two planes of fracture. A narrow band inclined at an angle β to the horizontal axis is formed called fibre kink band. As a consequence, the fibre kinking phenomena causes catastrophic compression rupture of the UD laminate when the ultimate stress is reached.

Based on this theory, Budiansky [45] suggested that the compressive strength of the composites (derived in [54-55]) is expressed as:

$$\sigma_c = \frac{\tau_y \sqrt{1 + \left(\frac{\sigma_{Ty}}{\tau_y}\right)^2 \tan^2 \beta}}{\phi_o + \gamma_y} \tag{6.9}$$

where τ_y is the in-plane shear yield strength, σ_{Ty} is the transverse yield strength, γ_y is the shear yield strain, ϕ_0 is the initial fibre misalignment angle and β is the kink band inclination angle of the composite. For a very small β, equation (6.9) becomes:

$$\sigma_c = \frac{\tau_y}{\phi_o + \gamma_y} \tag{6.10}$$

Figure 6.30 shows the theoretical compressive stress σ_c versus fibre rotation response Φ (refer to Figure 6.29b) graph for UD HTS40/828 CFRP composite system. This graph was developed based on Equation (6.10) by assuming the initial fibre misalignment angle $\phi_0 = 2°$. The curve describes the post buckling behaviour of the composite material which consists of: (a) initiation of HTS40 fibre microbuckle, (b) the fibres break, (c) the matrix or interface between the matrix and the fibres fails and finally (d) the overall composite collapses. The predicted compressive strength of the HTS40/828 laminate by Budiansky's model is 990 MPa (see point (b), Figure 6.30). The system is assumed to fail when the elastic shear yield point is reached and plastic deformation has taken place causing catastrophic failure at point (b).

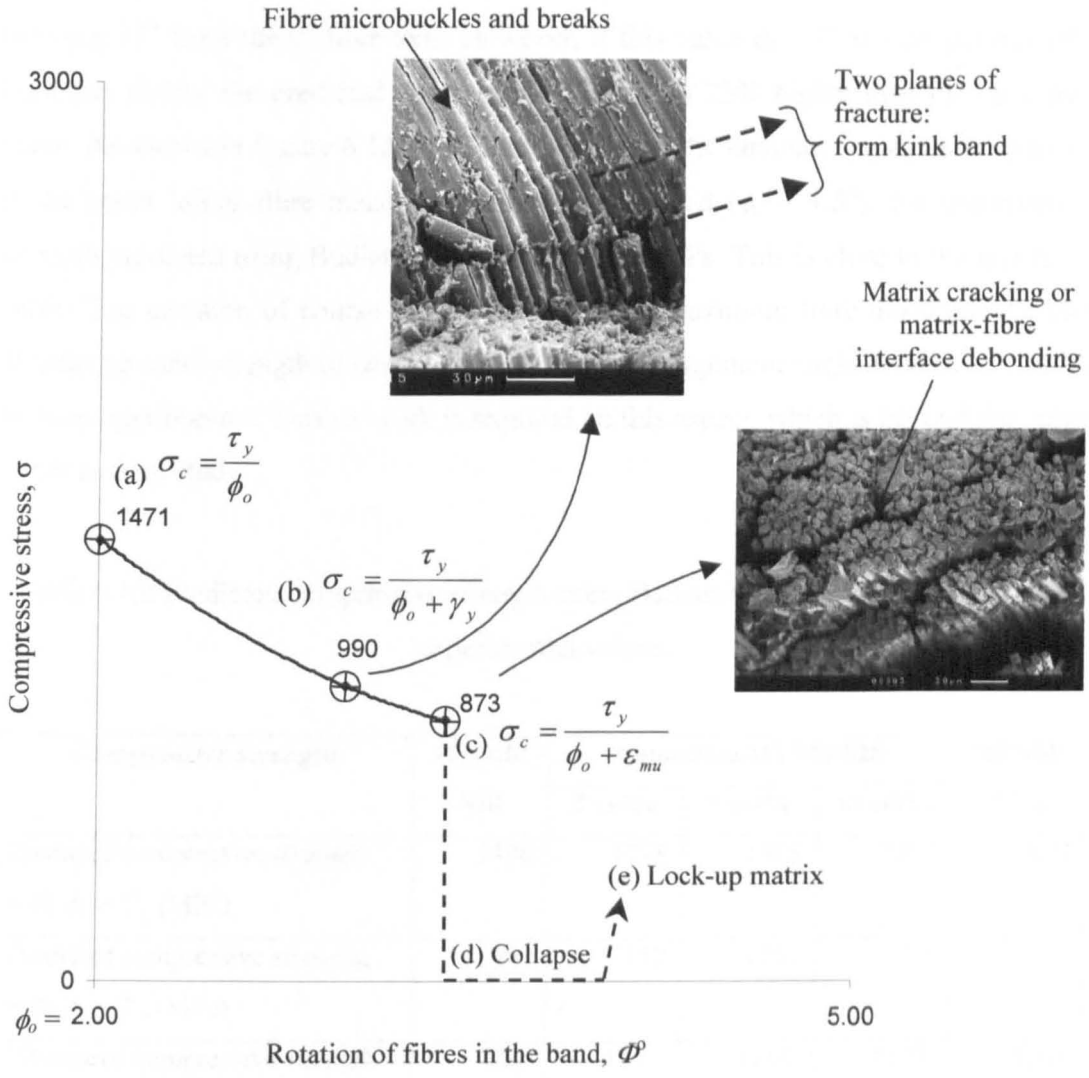

Figure 6.30: Theoretical stress-strain response of HTS40/828 UD composite laminate after the initiation of fibre microbuckling.

Table 6.10 summarises the predicted UD compressive strength values for unmodified and nanomodified HTS40/828 UD system using Budiansky's model (Equation 6.10) based on input data summarised in Table 6.8. The compressive strength was predicted using two different initial misalignment angles: ϕ_o = 1° and 2°. It was found that the predicted value for the unmodified HTS40/828 system, using ϕ_o = 2°, was 20% higher than the experimental value. For the nanomodified system with 3 and 7 vol.% nanosilica, the predicted compressive strength values, using ϕ_o = 2°, showed a very good agreement with the measured data. The experimental result of fibre waviness

distribution of the HTS40/977-2 system (see Figure 6.12) showed that 95% fibres lie in between ±1° from the 0° fibre axis. However, if this value ϕ_0 = 1° is incorporated into Equation (6.10), the predicted compressive strength is 23% higher than the measured value. As shown in Figure 6.12, the fibre waviness in the laminate varies until up to 3°. If the mean initial fibre misalignment angle is applied (ϕ_0 = 1.5°), the compressive strength predicted using Budiansky's model is 1494 MPa. This is close to the measured value. The question of course then becomes: is the maximum fibre misalignment that dictates ultimate strength or some statistical fibre misalignment angle distribution would be more appropriate? Further work is required on this aspect, which is beyond the scope of the present study.

Table 6.10: Predicted compressive strength using Budiansky's model compared to the experimental values.

Compressive strength	**HTS40/ 828**	**Nanosilica/HTS40/828**			**HTS40/ 977-2**
		3 vol%	**7 vol%**	**13 vol%**	
Predicted compressive strength, with ϕ_0 = 1°, (MPa)	1490	1748	1905	2097	1849
Predicted compressive strength, with ϕ_0 = 2°, (MPa)	990	1150	1257	1392	1231
*Measured compressive strength (MPa)	826	1151	1268	1172	1505

*Experimental data from Section 6.2.2

6.4 Concluding remarks

A new CFRP composite system was developed based on nanosilica modified epoxy resin. The results showed that the presence of nanosilica in the UD laminate improved the compressive modulus and strength without sacrificing the failure strain, provided that the volume fraction of the nanosilica is less than 13 vol.% and carefully dispersed nanosilica in the resin as discussed in Chapter 5. In addition the in-plane shear properties were also increased by incorporation of silica nanoparticles. SEM and optical microscopy revealed that the fibre microbuckling mechanism triggered the failure of the UD laminate during compression. The Budiansky model gave a good estimate of the

compressive strength. The addition of nanosilica enhanced the shear properties and hence the compressive properties of the HTS40/828 laminate. It is interesting to note that the compressive strength of the 13%si/HTS40/828 laminate was 1392 MPa as predicted using the Budiansky's model. This shows that the compressive properties of 7 and 13 vol% nanosilica-filled CFRP composite systems (V_f = 42%) were comparable to that of the commercial system HTS40/977-2 (V_f = 62%). The performance of this new system (especially 13 vol.% silica-filled HTS40/828) would perhaps out-perform the commercial system HTS40/977-2 if a better fabrication method is employed. As a conclusion, these results are very promising in an effort to develop a more damage tolerant and damage resistance CFRP system using appropriate nano-modifiers; see Chapter 7 for further discussion.

Chapter 7

Overall discussion

7.1 Summary

This chapter discusses the influence of nanofillers on the properties of epoxy polymers and how it contributes to the degree of reinforcement in a CFRP composite. The effects of (i) nanosilica, multiwalled CNT and I.28 nanoclay on the physical, thermal and mechanical properties of Epikote 828 and (ii) I.30 nanoclay on the overall properties of Cycom-977-20 are discussed based on the results reported in Chapter 5. Based on all results obtained in Chapter 5, nanosilica-modified Epikote 828 was found to improve the elastic moduli, strengths and fracture toughness properties of the Epikote 828 without any significant reduction in thermal properties and failure strains. Therefore the study was extended to the investigation of the properties of a nanomodified CFRP composite. The effects of nanosilica on the mechanical properties of HTS40/828 carbon fibre-epoxy system are discussed based on the results reported in Chapter 6. SEM was used to identify the failure modes and toughening mechanisms involved during mechanical tests. Therefore this chapter is divided into two sections; (i) the effect of nanofillers on the properties of epoxy polymers and (ii) the effect of nanosilica on the properties of HTS40/828 CFRP laminates.

7.2 Effect of nanoparticles on the properties of epoxy polymers

7.2.1 Degree of nanofiller distribution

The degree of dispersion of the nanofiller in the matrix indicates the quality of the fabricated nanocomposites. Nanosilica, multiwalled CNT and I.28 nanoclay were dispersed in the Epikote 828 using a mechanical stirrer at 400 rpm. The mixing time of

the nanomodified epoxy with the hardener and accelerator was limited to 20 min. Degassing of the mixtures in vacuum at 80°C was limited to a maximum of 90 min, by which the time the viscosity started to increase. Unlike Cycom 977-20, Epikote 828 cures at a lower temperature (120°C) and has less processing time.

The TEM results (as reported in Sections 5.2.1, 5.3.1 and 5.4.1) on the morphology of nanomodified systems showed that the nanosilica/epoxy system has the best degree of dispersion. The nanosilica, which was supplied by the Nanoresins AG (Germany), has been surface-treated with organosilane and pre-dispersed in the epoxy. This nanomodifed epoxy was successfully cured with anhydride type curing agent (NMA). A very good system was created, based on these materials (Nanosilica, Epikote 828 and NMA) where a homogeneously dispersed and non-agglomerated nanosilica in the epoxy, even at high weight fraction of 25 wt%, was revealed by the TEM micrographs.

Pre-dispersed surface-treated multiwalled CNTs in epoxy resin, which was supplied by Nanocyl (Belgium), was also used in this study. The TEM micrographs showed a good dispersion of CNT with occasional presence of entangled nanotubes. Even though the processing of 1 wt% CNT in the epoxy resin was difficult due to high viscosity, no evidence of entrapped air was present in the matrix as observed using the TEM. This shows complete degassing.

I.28 montmorillonite (MMT) nanoclay, which was supplied by Nanocor Inc (USA), has been surface treated with trimethyl stearyl ammonium to be compatible with DGEBA epoxy and anhydride type hardener. The dry MMT clay, that initially has 8-10 μm particle size, was successfully dispersed in the epoxy with intercalated structure. The nanocomposites have a d-spacing (the distance between silicate platelets) of more than 4 nm as revealed by the TEM. However the presence of voids at high nanoclay content (more than 3 wt%) showed a low quality nanocomposite. The viscosity of the clay/epoxy mixtures increased exponentially with the clay content. Limitation on mixing and degassing time was a major factor which contributes to clusters of intercalated nanoclay structures and nanovoids. These factors contribute to a low quality nanocomposite and of course, this will influence the overall mechanical properties of the material system.

High performance epoxy resin, such as Cycom 977-20, was cured at high temperature and can be processed for a longer time compared to the low molecular

weight epoxy, such as Epikote 828. In this study, a series of epoxy/clay nanocomposite was fabricated using three roll mill and conventional mechanical stirring techniques. An octadecylamine-treated MMT nanoclay namely nanomer I.30 (supplied by Nanocor Inc.) was specifically designed to be dispersed in amine-cured epoxy resins. Therefore it was mixed with Cycom 977-20 at three different weight fractions; 1, 3 and 5 wt%.

TEM micrographs (as reported in Section 5.5.1) showed that the 8-10 μm MMT clay particle was successfully dispersed in Cycom 977-20, using both methods, with d-spacing of more than 6 nm. It was found that the three roll mill produced a better quality of nanocomposites where a combination of ordered and disordered (random) exfoliated clay nanoplatelets in the epoxy matrix was revealed by the TEM micrographs. However, the conventional technique (mechanical stirring) produced intercalated structure nanocomposites. This suggests that the 3-roll mill successfully exfoliate the stacked layers of silicate clay in the epoxy matrix in two steps: (i) the external shear forces generated between the adjacent rollers dispersed the particles into smaller tactoids, followed by (ii) the combined shear and diffusion processes helped the separation and penetration of polymer between clay platelets to form the exfoliated structure.

In addition, the nanocomposites, which were prepared using the 3-roll mill in the present study, were better than those prepared using the other methods reported in [118-121,124] on similar type and amount of nanoclay. The TEM micrographs also showed no evidence of voids in the nanocomposites. Unlike clay/828 system, the Clay/977-20 resin can be degassed to a maximum time of 3 hours. Therefore cured epoxy was fully degassed. This contributes to a good quality of nanocomposites.

7.2.2 Thermal degradation temperature

The effect of nanoparticles on the thermal degradation temperature of the epoxy was studied using two systems; (i) nanosilica-filled Epikote 828 and (ii) I.30 nanoclay-filled Cycom 977-20 that demonstrated the best mechanical properties, see Sections 5.2 and 5.5. Figure 7.1 summarises the maximum degradation temperature of resin residue of nanocomposites compared to the neat polymers. The results of both systems showed that the nanocomposites have a better thermal stability due to a higher thermal degradation temperature compared to that of the unreinforced polymers. The maximum increase in the temperature of about 22% was recorded for the addition of 25 wt%

nanosilica into the Epikote 828. This suggests that the interfacial adhesion between particle and matrix is very good therefore higher temperatures are needed to remove the epoxy which is stuck on the particles' surface.

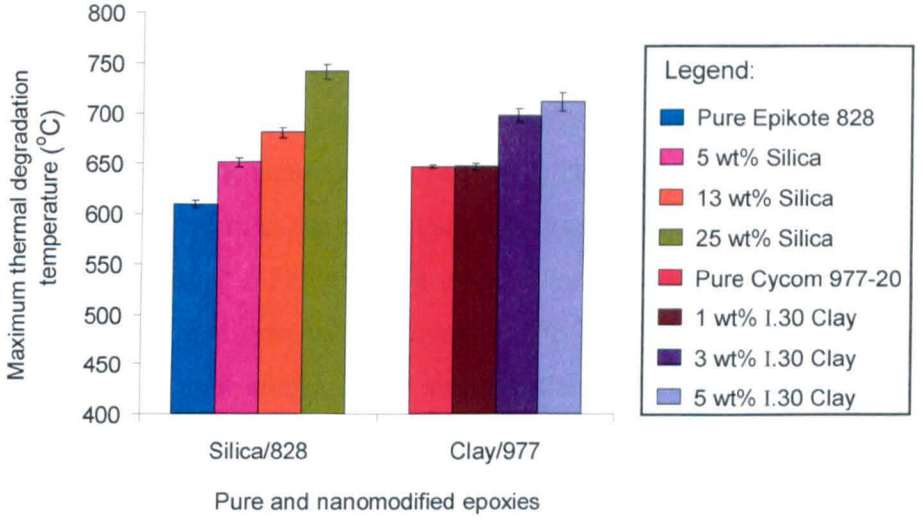

Figure 7.1: Comparison of maximum thermal degradation temperatures of two different types of nanocomposites with the unmodified Epikote 828 and Cycom 977-20 epoxies.

7.2.3 Coefficient of thermal expansion

Coefficient of thermal expansion (CTE) is one of the most important considerations for the fabrication of polymer composite structures. For CFRP composite systems, the epoxy has much larger CTE than the carbon fibres. Therefore, during heating or cooling, the epoxy expands or contracts more than the fibres. This mismatch in the CTE induces thermal residual stress in the composite materials [179]. The polymer near to the surface of the fibres may be subjected to strong internal tensile forces. This could lead to internal micro-cracks and reduce the strength of the composites. Micro-cracking phenomena could obviously be observed when the material was exposed to cryogenic cycling [131].

The CTE plays an important role especially during cooling down (after curing temperature) in the fabrication of CFRP composites. If the adhesion of the polymer to the long fibre is good, the fibre can be buckled into a wavy shape. This fibre undulation mechanism was properly studied by Jochum *et al.* [180] using a single T300 carbon fibre in an LY556 epoxy. The CTE of the carbon fibre is –0.74 $\mu\varepsilon/^{\circ}C$ while the matrix

has CTE=150 με/°C, therefore during cooling the matrix shrinks 200 times more than the carbon fibre. This contributes to fibre waviness. Fibre waviness is one of the most important factors which contributes to a low compressive strength of CFRP composite. Therefore, in theory, introducing a lower CTE of the matrix will reduce CTE mismatch to the fibre and therefore produce a better quality of CFRP.

The inclusion of rigid nanofillers, which have low CTE values compared to the epoxy such as nanosilica, nanoclay and MWCNT, is expected to reduce the CTE of the polymer. This was proven in the current study by experimental observations. Figure 7.2 shows the comparison of CTE below Tg values of nanomodifed epoxies with their pure resins. All nanomodified systems have a lower CTE compared to that of the unmodified resin. This was a very promising result since, in theory, this will minimise the thermal mismatch between carbon fibre and epoxy, thus reducing fibre waviness due to lower thermal shrinkage of the epoxy during curing of CFRP composites. Therefore, better quality composites are achieved compared to conventional systems. Figure 7.2 shows that the nanosilica-filled Epikote 828 system has the biggest effect on reducing CTE. For example the addition of 25 wt% nanosilica reduced CTE by about 18%. This was followed by nanoclay-filled Cycom 977-20 system, where inclusion of 5 wt% nanoclay reduced CTE by about 12%.

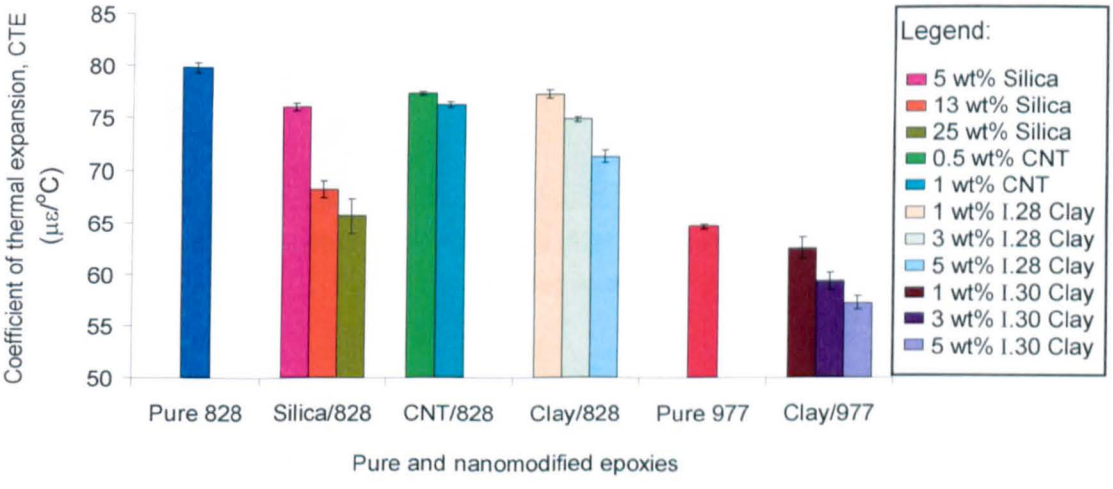

Figure 7.2: Comparison of CTE values of four different types of nanocomposites with the unmodified Epikote 828 and Cycom 977-20 epoxies.

7.2.4 Glass transition temperature

The glass transition of a polymer composite is a temperature-induced change in the matrix material from the glassy to the rubbery state during heating or from a rubber to a glass during cooling. The glass transition is determined or marked by (1) a change in the coefficient of thermal expansion or thermal strain of the material which is measured by TMA or (2) a change in the heat capacity of the material which is measured by DSC or (3) a change in matrix stiffness which is measured by DMA. In this study, TMA and DSC were used to study the effect of nanoparticles on Tg. All nanocomposites showed a slight reduction in Tg compared to the pure systems except I.28 nanoclay-filled Epikote 828 as shown in Figure 7.3. This effect was recorded by both, TMA and DSC. I.28 nanoclay enhanced the Tg of Epikote 828 for a maximum of 12% with the addition of 5 wt%. Nanoclay has the best effect on Tg for low molecular weight epoxy, such as Epikote 828, by restricting the segmental motion of cross-links at matrix-nanoplatelet interfaces [181].

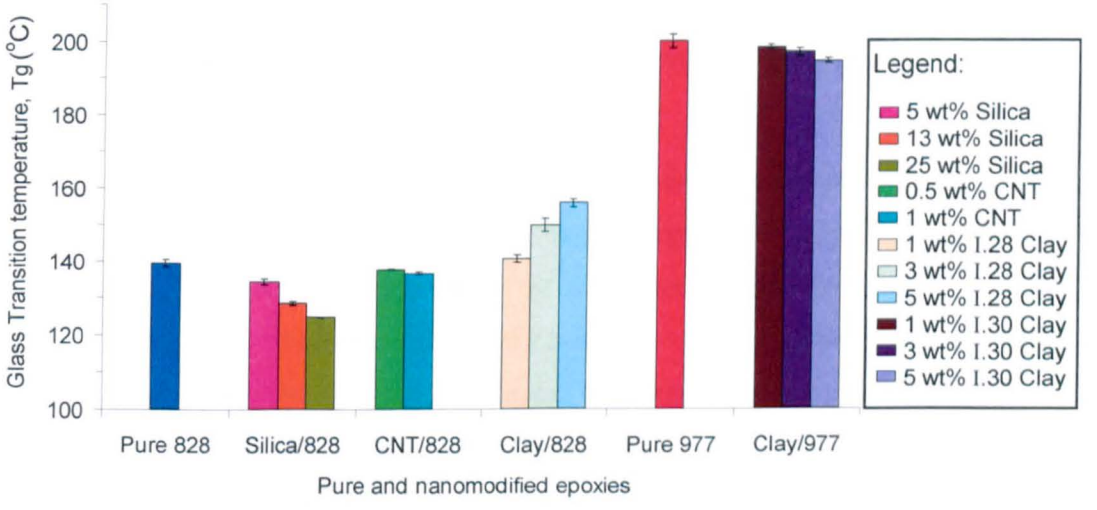

Figure 7.3: Comparison of Tg values of four different types of nanocomposites with the unmodified Epikote 828 and Cycom 977-20 epoxies.

7.2.5 Stress-strain behaviour

Figure 7.4 shows the example of stress-strain behaviour of pure and nanomodified Epikote 828 systems. Stress-strain curves are very dependent on the type of loading. In

tension and bending, epoxy polymer fails in a brittle manner, while in compression it behaves like a ductile material with a yield point and has higher failure strain. In tension and bending, cured Epikote 828 failed at a very low failure strains, of about 3.3% and 4.8% respectively, while in compression it exhibited a large plastic deformation, up to 43% failure strain. These three curves show that the materials properties, such as elastic modulus, ultimate strength and failure strain, have absolutely different values. Even the first parts of the curves, determined by the Young's modulus are different. The elastic modulus determined using the true compressive stress-strain curve is slightly higher than those determined in tension and bending. The tensile properties are largely determined by specimen imperfections such as flaws and submicroscopic cracks therefore the material is no longer continuum. However, the compressive stresses tend to close the cracks rather than open them. This behaviour was also observed by Nielsen and Landel [42]. The effects of defects are therefore minimised in compression tests. This means that the compression test characterises the actual properties of the pure polymer, provided that the effects of friction are eliminated by proper lubrication and proper selection of a specimen dimensions and geometry. In bending, part of the specimen is under tension and part under compression. The failure of the specimen is expected to be initiated in the tension part rather than the compression part due to a lower tensile failure strain.

In the present work, the objective of conducting the mechanical tests was to investigate the stiffening, strengthening and toughening effects caused by nanomodifiers in the epoxy. The stress-strain response of the nanomodified systems under several types of loading (compression, tension and bending) was compared to the unmodified systems. Figure 7.4 shows that the mechanical performance of the epoxy can easily and effectively be studied through a compression test. For example, the addition of 26 wt% nanosilica into the Epikote 828, as shown in Figure 7.4b, enhanced the (i) elastic modulus (indicated by the initial slope), (ii) ultimate stress (indicated by the highest stress value), (iii) yield stress (indicated by the peak stress at the transition from elastic to plastic behaviour) and (iv) fracture toughness (indicated by the area under graph) without any significant changes in strain at failure of the epoxy. Compared to the results in tension and bending, the elastic modulus, ultimate stress and failure strain depends on the quality of the specimens and test procedures where specimen misalignment and imperfections (such as agglomerated nanoparticles or inhomogeneous nanoparticle

distribution and low particle-matrix adhesion, voids and microcracks) causes premature failure in the systems.

The true compressive stress-strain response of almost all nanomodified epoxy systems (results presented in Chapter 5 and Appendix A) showed that the presence of nanomodifiers, especially nanosilica and I.30 nanoclay, stiffened and strengthened the matrix, improved ductility and promoted higher plastic hardening behaviour after yielding. Of course the degree of reinforcement depends on the quality of the fabricated nanocomposites such as the degree of dispersion and microstructure of the nanoparticles in the epoxy, particle-matrix adhesion and voids. The effect of nanoparticles on mechanical properties, which were obtained from the stress-strain curves, is discussed in detail in the following sections.

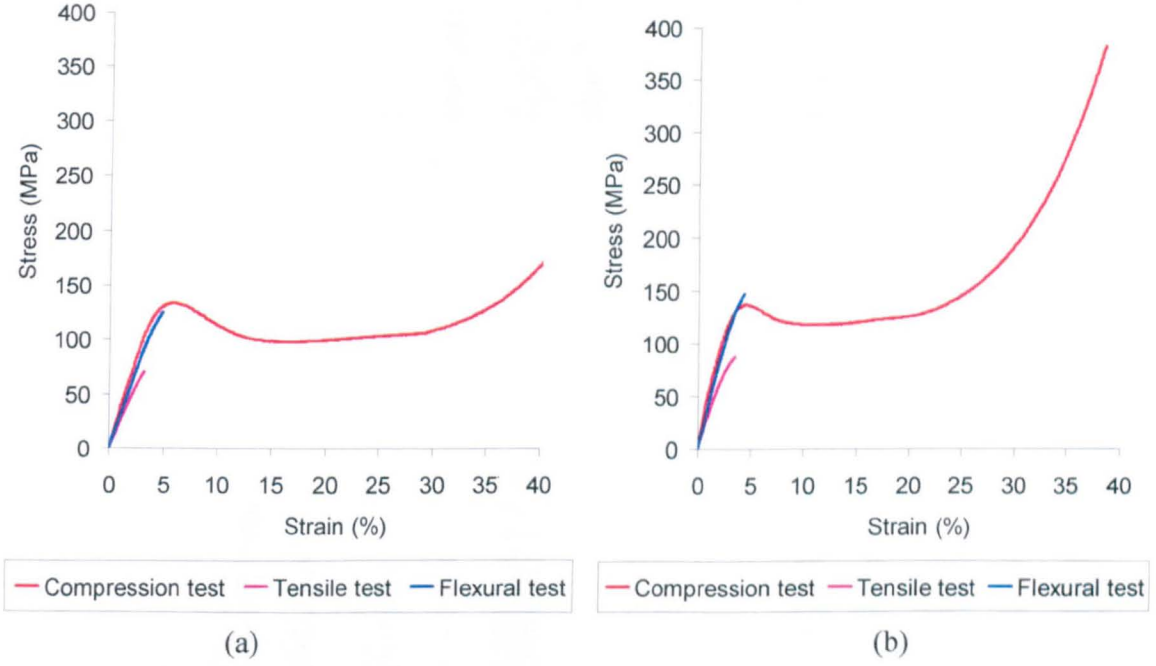

Figure 7.4: Stress-strain behaviour of (a) pure Epikote 828 and (b) 25 wt% silica in Epikote 828 polymers loaded in compression, tension and bending.

7.2.6 Elastic modulus

Elastic moduli measure the resistance to deformation of materials when external forces are applied, where stiffer materials show higher value of Young's modulus. Numerous methods have been used to measure the elastic modulus. The most common tests are

tensile, compression and flexural. In this study, these tests were conducted to study the effect of nanofillers on the elastic moduli of epoxy. Elastic modulus was determined by taking the initial slope of the stress-strain curve in the elastic region. The results were summarised in Figure 7.5. This figure shows that the nanocomposites offer higher stiffness subjected to all types of loading. The elastic moduli were found to increase with increasing nanofiller content.

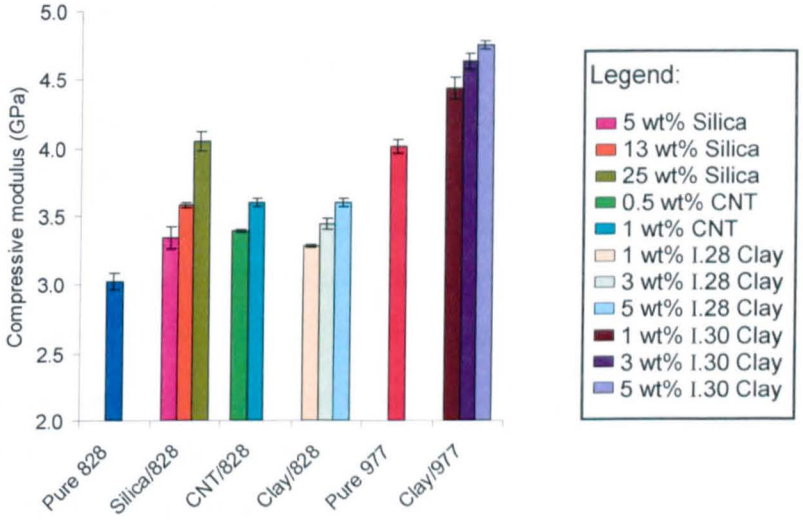

(a)

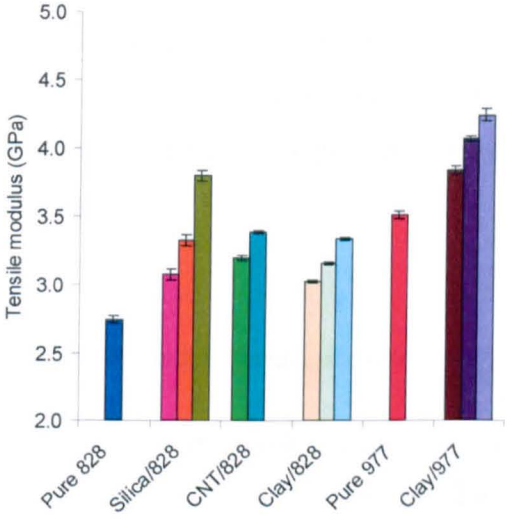

(b)

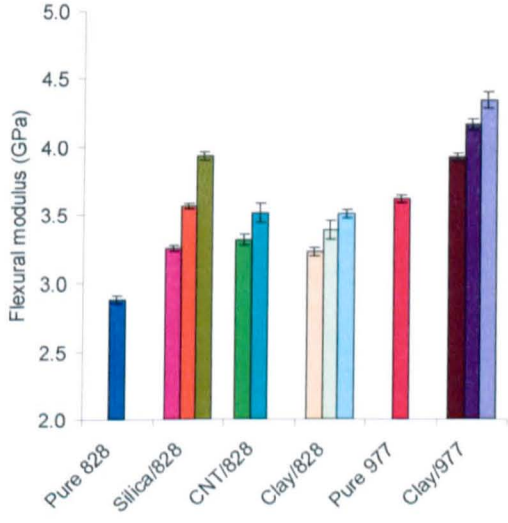

(c)

Figure 7.5: Comparison of (a) compressive, (b) tensile and (c) flexural moduli of four different types of nanocomposites with the unmodified Epikote 828 and Cycom 977-20.

The degree of reinforcement was mainly determined by the stiffness and volume content of the nanofillers. A rigid nanosilica has Young's modulus of 70 GPa [73]. Therefore, the highest content of nanosilica in Epikote 828 (25 wt%) gave a maximum reinforcement to the epoxy where it enhanced the compressive modulus by 34%, the tensile modulus by 38% and flexural modulus by 37%. It is interesting to note that by adding only 1 wt% of CNT, improves compressive, tensile and flexural moduli by 19%, 23% and 21%, respectively. This is due to the Young's modulus of multiwalled CNT of 1000 GPa [86]. Therefore, the effect of CNT is highly significant even at a low volume content. However, in this study the maximum CNT content was limited to 1 wt% because the viscosity of the resin was too high for further addition of the CNT and this led to degassing problems. The addition of MMT nanoclay, which has E=170 GPa [121], into epoxy was also found to enhance the elastic moduli for both systems; clay/828 and clay/977. The inclusion on 5 wt% nanoclay into the epoxy, enhanced the compressive, tensile and flexural moduli by 19-21% for both systems.

Additionally, the compressive modulus of silica/828 and clay/977 systems was also estimated using several types models (as presented in Sections 5.2.4.4 and 5.5.4.4). For silica/828 system, the predicted modulus of elasticity using the Lewis-Nielsen model showed a very good agreement when compared to measured values. While, for the clay/977 system the modified Halpin-Tsai model was proposed to predict the compressive modulus. This model captured the effect of nanoclay volume fraction on the shape factor ζ, where the stacked nanoplatelets reduced the shape factor. This relationship successfully predicted the elastic modulus of the nanocomposite at various clay contents.

7.2.7 Yield and Ultimate stresses

The influence of nanofillers on yield strength of epoxy polymers was studied on four different systems loaded in compression as shown in Figure 7.6. This figure shows that Cycom 977-20 system has higher yield strength when compared to a lower molecular weight epoxy, Epikote 828. This could be due to the presence of aromatic groups in a densely crosslinked molecular network of Cycom 977-20. The presence of high content of nanosilica (25 wt%) slightly increased the yield strength of Epikote 828 while there was no improvement recorded for the CNT/828 system. For the clay/828 system, the yield strength reduced with rising filler content. But for the clay/977 system,

nanocomposites (which were prepared using the three roll mill method) have a better yield strength compared to the pure polymer. The maximum of 6% increased was recorded, by adding 5 wt% I.30 into Cycom 977-20. However, clay/977 nanocomposites prepared using a mechanical stirring method recorded less than 3% improvement in yield strength, see Section 5.5.4 Table 5.15.

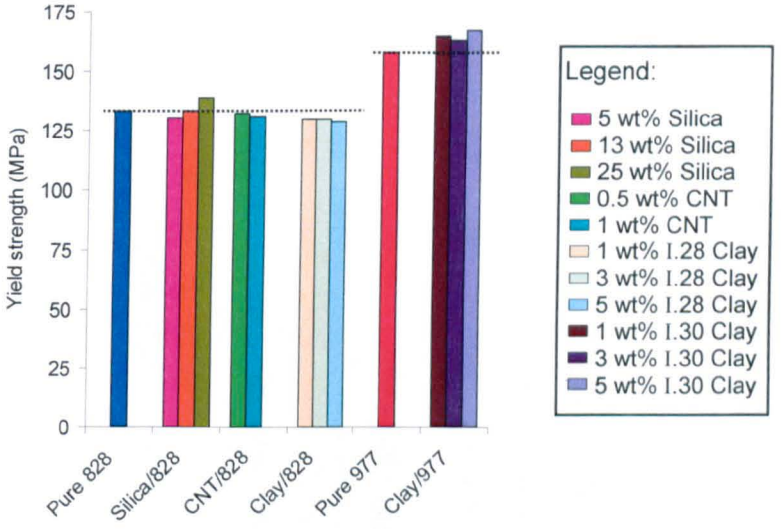

Figure 7.6: Comparison of compressive yield stress of four different types of nanocomposites with the unmodified Epikote 828 and Cycom 977-20 epoxies.

For nanocomposite systems, the degree of reinforcement in the yield and ultimate stresses are usually related to the quality of the nanofiller-matrix interface. This is true because nanofillers produce an enormous amount of surface area once dispersed in the matrix. For example, silica nanospheres provide 50-380 m^2/g, carbon nanotubes provide 250-300 m^2/g and clay nanoplatelets provide 750 m^2/g specific surface areas [56,61,117]. Therefore, the particle/matrix adhesion strength and the interfacial stiffness play an important role to transfer stresses and elastic deformation from the matrix to the nanofillers [72-74]. If the nanofillers-matrix interaction is poor, the fillers are unable to carry any part of the external load therefore the strength of the nanocomposite cannot be higher than that of the neat polymer. Moreover, if the bonding between nanofillers and the matrix is strong enough, the yield strength of the nanocomposite can be higher than that of the pure polymer. Of course, a high interfacial stiffness corresponds to a high nanocomposite modulus. The effect of nanofillers on the compressive, tensile and flexural strengths of epoxy polymers was illustrated in Figure 7.7. Silica/828 system has

very good compressive and tensile strengths compared to the pure polymer and the other systems. This suggests that the quality of the nanosilica-epoxy interface is very good therefore the stresses are efficiently transferred via the interface. In contrast, the CNT/828 system shows a slight improvement in tensile and compressive strengths, for about 6-10% increase compared to the pure Epikote 828. Even though CNT's have a tensile strength of 11-200 GPa [61] compared to that of 60-80 MPa only for neat epoxies, it does not contribute to the maximum enhancement to the properties of the nanocomposites. This indicates that the stress is not effectively transfer to the CNT through the interface.

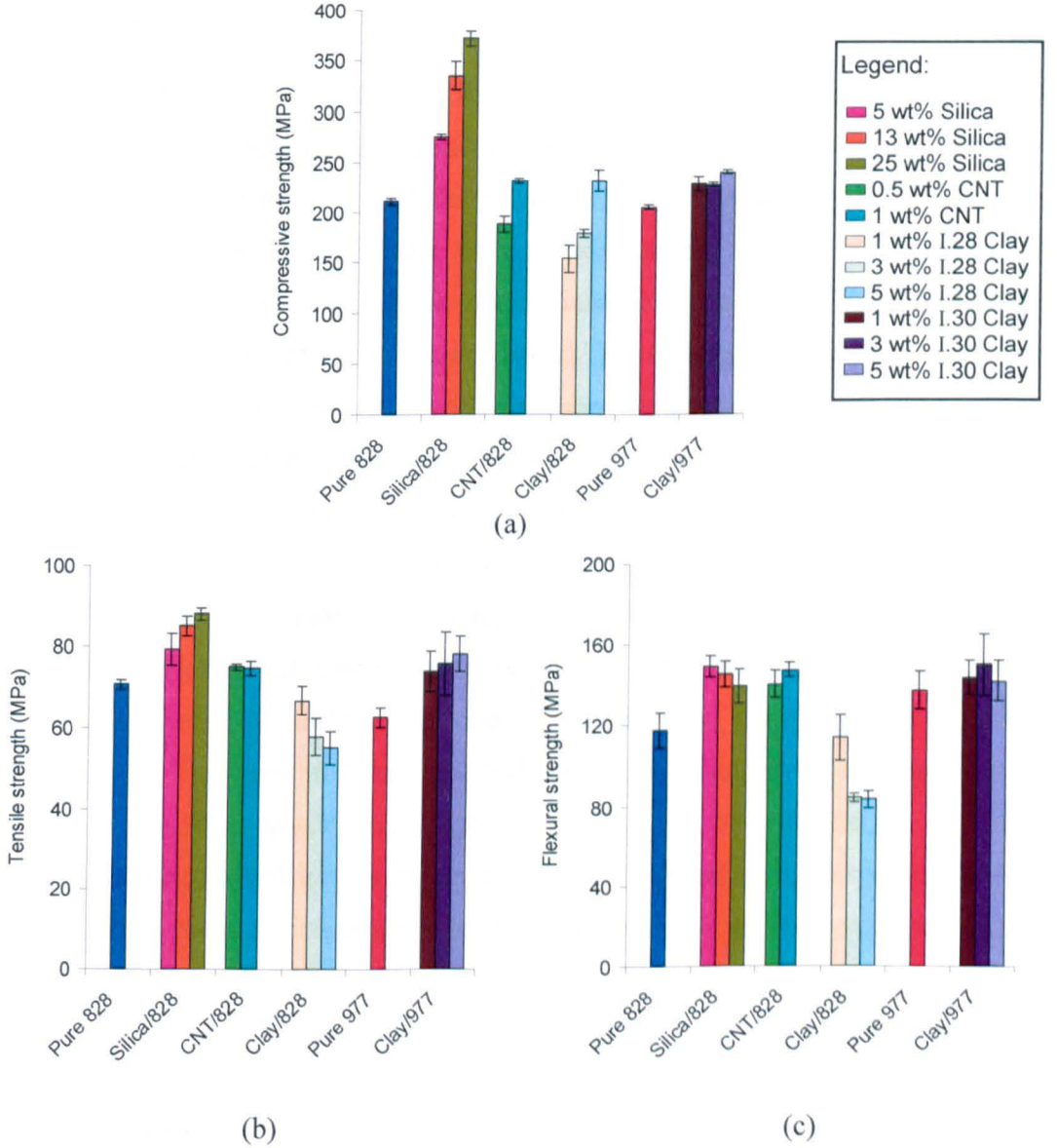

Figure 7.7: Comparison of (a) compressive, (b) tensile and (c) flexural strengths of four different types of nanocomposites with the unmodified epoxy systems.

For the clay/epoxy system, the reinforcement benefits were determined by the degree of exfoliation of the clay nanoplatelets in the matrix. In the case when fully exfoliation clay-platelets in the matrix was not achieved, where clusters of intercalated structures remain in the matrix, a local concentration stress built up with the applied load and then easily induced the initiation of the final failure. This obviously can be seen in clay/828 system where at higher filler contents, more intercalates clumps and voids are likely to be found. A low quality of fabricated clay/828 nanocomposites contributes to lower compressive, tensile and flexural strengths compared to that of the pure polymer. As expected, the reinforcement benefit is substantially greater for the exfoliated nanocomposites where the presence of I.30 nanoclay improved the overall strengths of Cycom 977-20.

As mentioned above, the reinforcement effect of the clay/epoxy system is dependent on the extend of silica nanolayer separation where closely spaced platelets (low d-spacing) limit the ability of the polymer chains to intercalate the gallery. This reduces the load transfer capability of the epoxy to the fillers and increases the possibility of interplatelets sliding due to weak interfacial adhesion. These contribute to low strength properties of the nanocomposites. This effect can obviously be seen by comparing the strength results of clay/977 nanocomposites that were prepared using the three roll mill and mechanical stirring techniques. The three roll mill produced an exfoliated structure while the mechanical stirring produced predominantly intercalated structure nanocomposite. Using the mechanical stirring technique, the nanocomposite slightly improved the compressive strength by 1-6% and tensile strength by 3-13% while reduced the flexural strength to a maximum of 14% compared to the pure Cycom 977-20, see Section 5.5 Tables 5.15 and 5.17. However, clay/977 nanocomposites prepared using the three roll mill method significantly improved the compressive strength by 10-17%, tensile strength by 18-24 % and flexural strength by 3-9% compared to the pure polymer as shown in Figure 7.7. Therefore the dispersion state of the nanofillers plays an important role in determining the overall properties of the nanocomposites.

7.2.8 Failure strain

For nanocomposite systems, most deformation comes from the polymer. This is due to the fact that, rigid nanofiller has a very high stiffness compared to that of the resin, such

as the Young's modulus of nanosilica is 70 GPa, CNT is 1000 GPa and nanoclay is 170 GPa compared to only 3 GPa elastic modulus of pure epoxy. Therefore, when the nanocomposite is loaded in compression, tension or bending, the nanofiller restrains the deformation of the polymer provided that the interfacial stiffness between the filler and the matrix is strong. This resistance against deformation mechanisms contribute to the higher modulus of the nanocomposites in the elastic region. However, the degree of deformation in the plastic region depends on the interfacial stiffness. Figure 7.8 shows the effect of nanofillers on the failure strains of epoxy polymers that were loaded in compression, tension and bending. It is surprising to observe that there is no significant reduction in failure strain in the nanocomposites, except the clay/828 system, which fails prematurely due to several imperfections or defects of the fabricated specimens as discussed earlier. This shows that there is a strong interfacial stiffness between the filler and the matrix which contributes to the extent of matrix deformation.

It is interesting to note that the silica/828 system offers a simultaneous improvement in the compressive, tensile and flexural moduli and strengths without sacrificing the failure strains, as shown in Figures 7.5, 7.7 and 7.8. This suggests that the nanoparticles are able to introduce additional mechanisms of energy absorption without heavily blocking the matrix deformation. In addition, this is in contrast to conventional composites systems, where the addition of rigid micron-sized fillers enhanced the stiffness, however reduced the strain to failure with rising filler content. The addition of elastic micron-sized fillers (such as rubber and elastomers) increased the strain to failure on the one hand, but on the other hand, gives detrimental effect on elastic modulus and strength [4,25,26,33,36,37,43,44,56,59,117].

CNT/828 nanocomposite was also expected to enhance both the overall stiffness and strength, due to the excellent properties of the CNT. However, it was found that the nanocomposite when subjected to compression and tension, did not maximise the capability of the CNT. The presence of CNT moderately improved the tensile and compressive properties with no noticeable increased in the failure strains. However, the CNT contributes to a good resistance to deflection when the nanocomposite was loaded in bending, where it enhanced the flexural modulus, strength and failure strain simultaneously, as shown in Figures 7.5, 7.7 and 7.8.

In contrast to clay/828 system, a highly exfoliated I.30 clay nanoplatelets enhanced the overall properties of Cycom 977-20. The clay/977 nanocomposite has a

higher compressive, tensile and flexural moduli and strengths compared to the pure polymer. The improvement in strain to failures of the nanocomposites loaded in compression and tension was also recorded, see Figure 7.8. However, the presence of clusters of ordered exfoliated clay nanoplatelets in the nanocomposite may reduce the matrix deformation when it was loaded in bending, hence reduced the flexural strain at fracture.

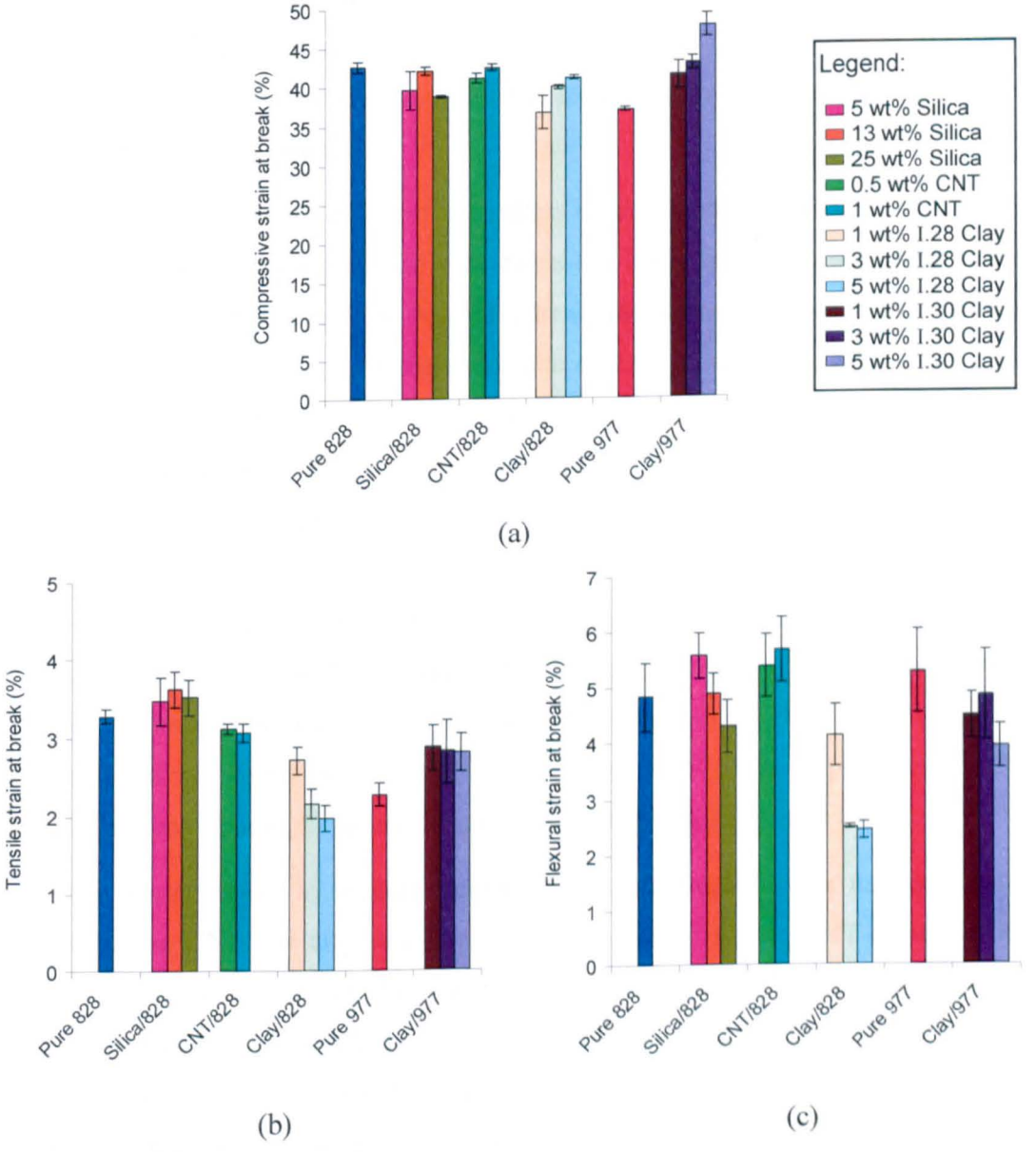

Figure 7.8: Comparison of (a) compressive, (b) tensile and (c) flexural strains at break of four different types of nanocomposites with the unmodified polymers.

7.2.9 Fracture toughness and toughening mechanisms

Fracture toughness is one of the most important characteristics that needs to be considered in the fabrication of polymer composites. It measures the ability of the material to resist the extension of a pre-existing crack by a specified type of stress, which can be defined in terms of two factors; (i) a critical stress intensity factor K_{IC} or (ii) a critical strain energy release rate G_{IC} [160]. From the load at which the crack starts to rapidly propagate (F_Q), the fracture surface energy can be calculated for a specimen of specified geometry (refer to Section 3.6.4) using equations given in British standard 13586 [160]. Higher values of K_{IC} and G_{IC} represent higher fracture toughness properties of the composite system where the material shows higher resistance against crack initiation and propagation.

Figure 7.9 shows the effect of nanofillers on the fracture toughness properties of epoxy polymers. All nanocomposite systems show a better fracture toughness compared to the pure polymers. Silica/828 showed a tremendous improvement in K_{IC} and G_{IC} compared to the neat epoxy. As the nanosilica content is increased, both the K_{IC} and G_{IC} increase. The addition of 25 wt% nanosilica offered a maximum improvement to the K_{IC} for about 84% and G_{IC} for about 163%. It is interesting to note that the nanosilica improves fracture toughness, elastic moduli and strengths simultaneously and with no detrimental effect on failure strain and thermal properties of the Epikote 828. This is totally different to the conventional composite systems, such as rubber-, glass beads-, elastomer-, thermoplastic-, alumina- microparticle-filled epoxy, where attempts to improve toughness usually accompanied by reduction in thermal and stiffness properties and vice-versa [4,25,26,33,36,37,43,44,56,59,117]. The improvement in K_{IC} and G_{IC} indicates that higher energy is needed to initiate and propagate crack.

The improvement in fracture toughness was also recorded for nanocomposites prepared using CNT and clay nanofillers. The addition of 1 wt% CNT improved K_{IC} and G_{IC} of Epikote 828 by 54% and 100%, respectively. While, the degree of enhancement in fracture toughness for clay/828 system is dependent on the quality of the fabricated samples. At high clay content, the presence of nanoclay rich regions and voids limits the toughening capability of the nancomposites due to a lower epoxy-clay adhesion. The incorporation of I.30 nanoclay improved the fracture toughness of Cycom 977-20. A fully exfoliated nanocomposite of 1 wt% nanoclay offered 20 % increased in K_{IC} and 43% increased in G_{IC} values compared to that of the neat epoxy. However,

further addition of the nanofillers decreased slightly the fracture toughness but remains above that of the neat matrix. This is due to the presence of ordered exfoliated structure of nanoclay in the epoxy at high filler content.

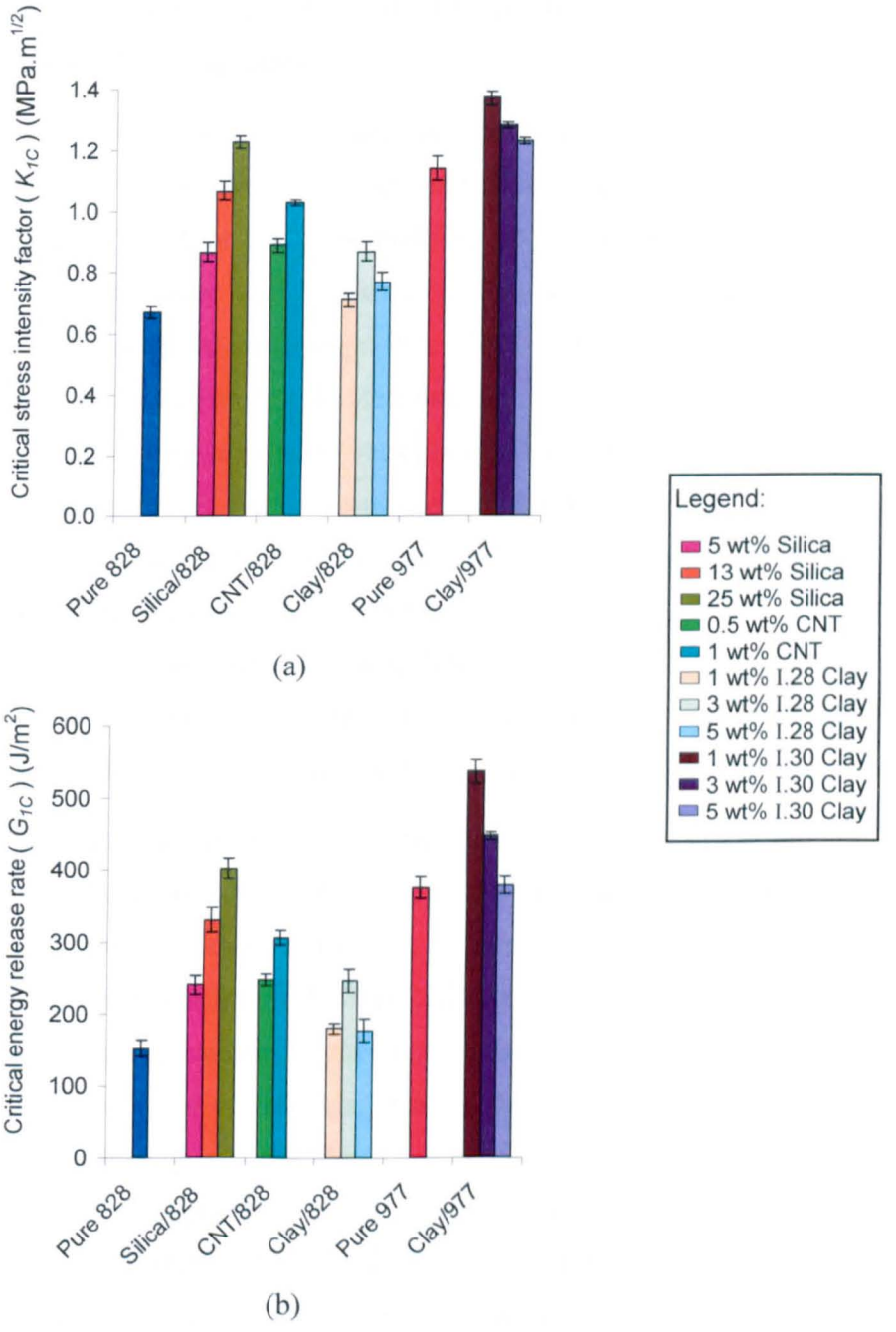

Figure 7.9: Comparison of fracture toughness properties; (a) critical stress intensity factor and (b) critical energy release rate, of four different types of nanocomposites with the unmodified polymers.

In addition, the increased of the area under the stress-strain curves of the nanomodified polymer loaded in compression, tension and bending, as discussed previously in Section 7.2.5, also indicated improvement in fracture toughness when compared to the neat polymer. In order to explain the increase in energy absorption of nanocomposites, visual examinations of the fracture surfaces of neat and nano-filled polymers using SEM were conducted.

Figure 7.10a shows the prismatic specimens after compression where the failure of the specimens was via barrelling and longitudinal cracking. SEM examination of the fracture surfaces of neat and nanomodified epoxy polymers can provide detailed information on the cause and location of failure and, hence, explain the increase in fracture toughness of the nanocomposites. The fracture surface of neat and modified epoxy samples can be roughly divided into two regions: crack initiation zone (high stress concentration region where crack initiates) and crack propagation zone (crack growth region where the cracks propagate) as shown in Figure 7.10b. The effect of nanofillers on the morphology of fracture surface of the epoxy at these two different zones was studied. Figures 7.11-7.14 show the SEM images of broken cubic specimens of nanosilica-, CNT- and nanoclay-filled Epikote 828 systems after compression, while Figures 7.15-7.16 show SEM images of broken nanoclay-modified Cycom 977-20 samples after compression, tension, bending and fracture toughness tests.

There are various toughening mechanisms, such as crack pinning, particle bridging, void nucleation, crack tip blunting or crack tip deformation, localised inelastic matrix deformation, crack path deflection, particle yielding induced shear banding, step formations and microcracking [26,43,44,27,28,38], that have been used to explain the energy-dissipative mechanisms of the conventional rigid particle filled epoxy systems loaded in various types of loadings. Among these, crack pinning, crack deflection, filler/matrix debonding, crack bridging, shear yielding and shear banding have been proposed as applicable for nanofiller-modified epoxy systems [56,60,70,73,75,77,118,121,182,183]. In the current work, some of these mechanisms such as large scale plastic deformation (shear yielding, shear banding and step formation) of the matrix and crack deflection can clearly be observed on the fracture surface of nanocomposites as shown in Figures 7.11-7.16.

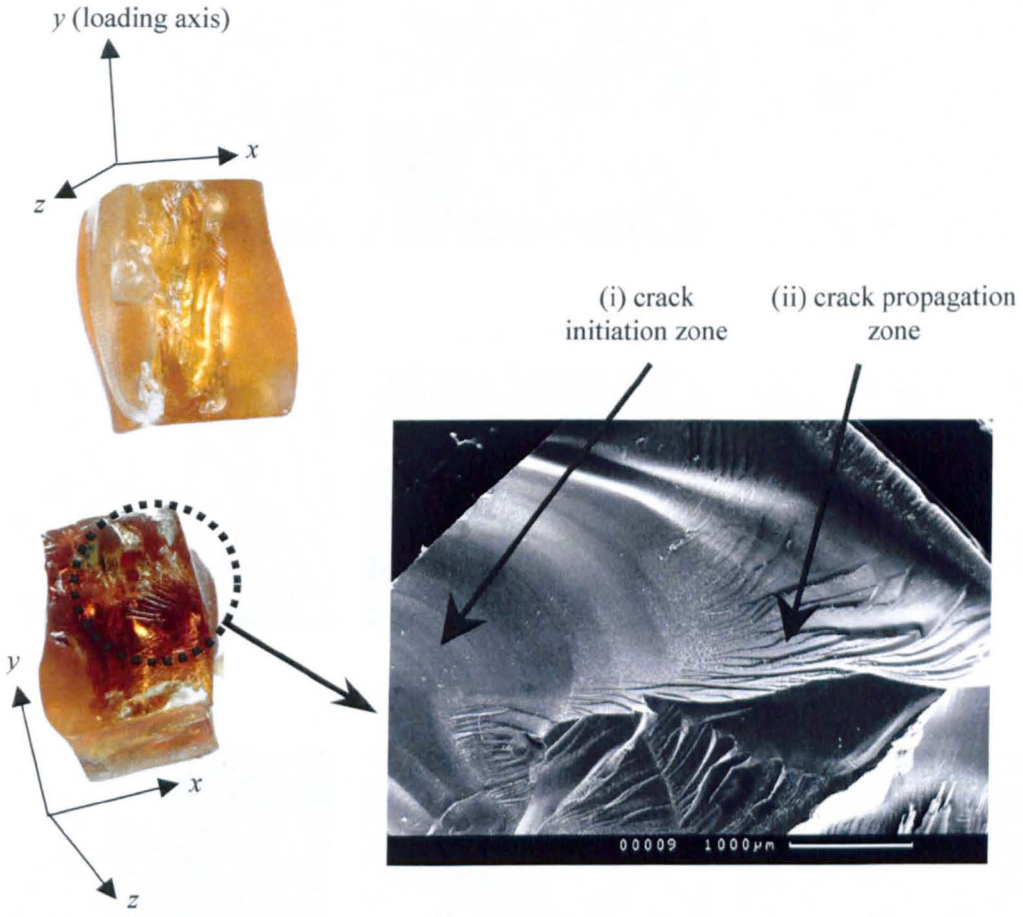

Figure 7.10: (a) Axially loaded cube type specimens fail via barrelling and longitudinal cracking followed by buckling at higher loading and (b) SEM micrograph of the fracture surface showing crack initiation and crack propagation zones.

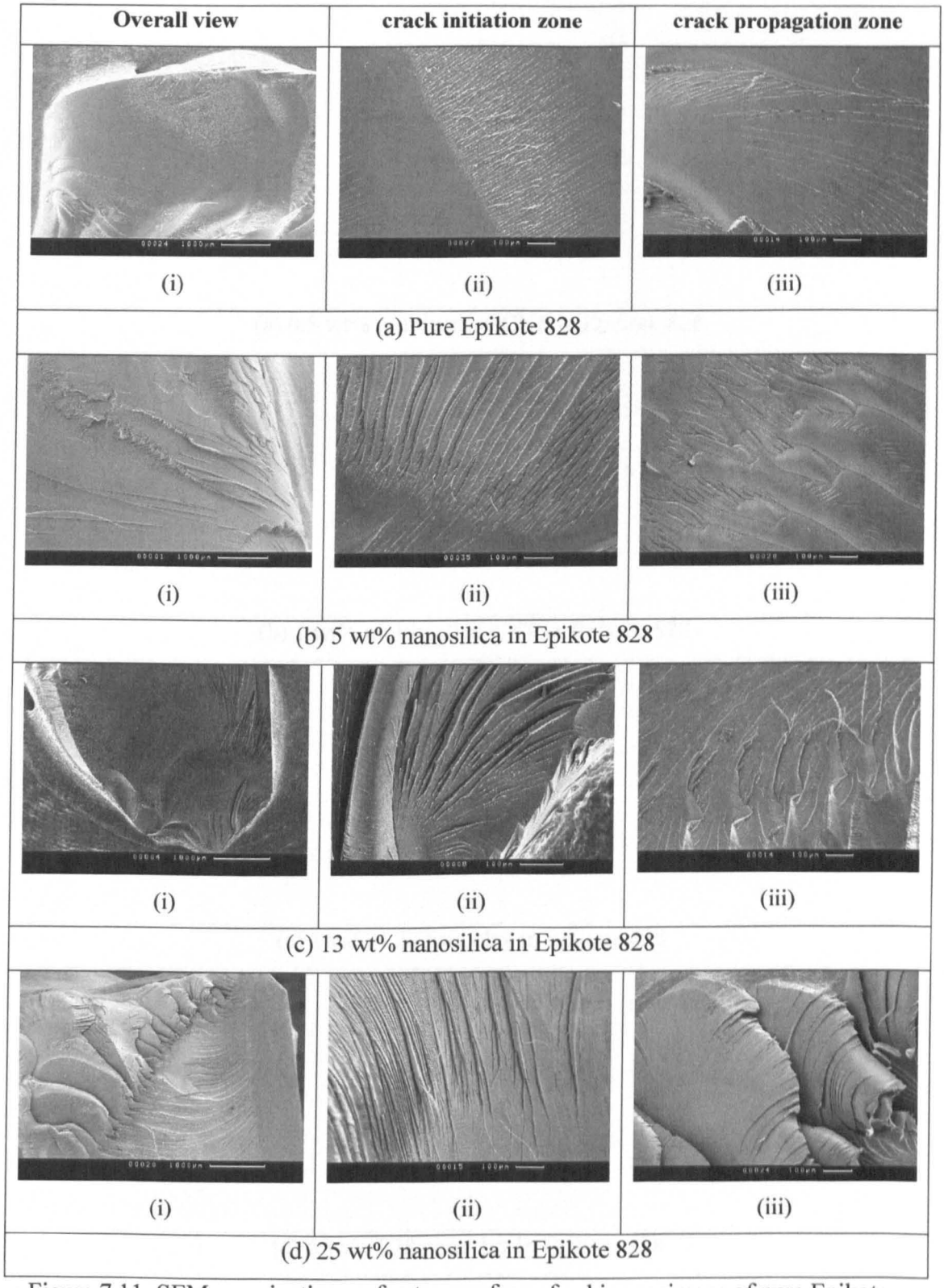

Figure 7.11: SEM examination on fracture surface of cubic specimens of pure Epikote 828 and nanosilica-filled Epikote 828 after compression. Pure Epikote 828 (a) shows smooth fracture surface while nanocomposites (b, c and d) show crack deflection mechanism and large scale resin shear deformation that leads to the formation of shear bands. More textured surface is observed as the nanoparticle content is increased (d).

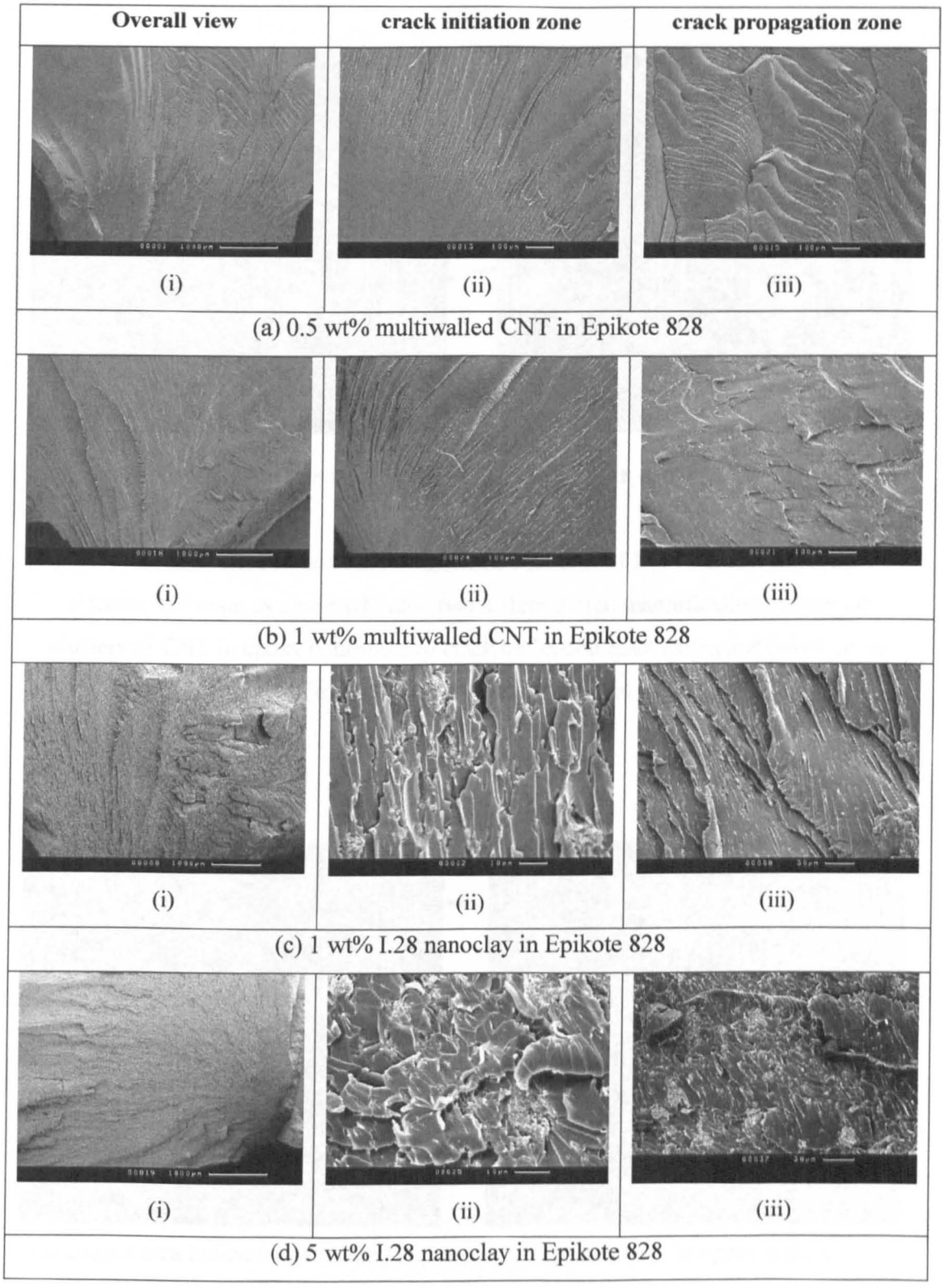

Figure 7.12: SEM examination on fracture surface of cubic specimens of CNT/828 and clay/828 nanocomposite systems after compression.

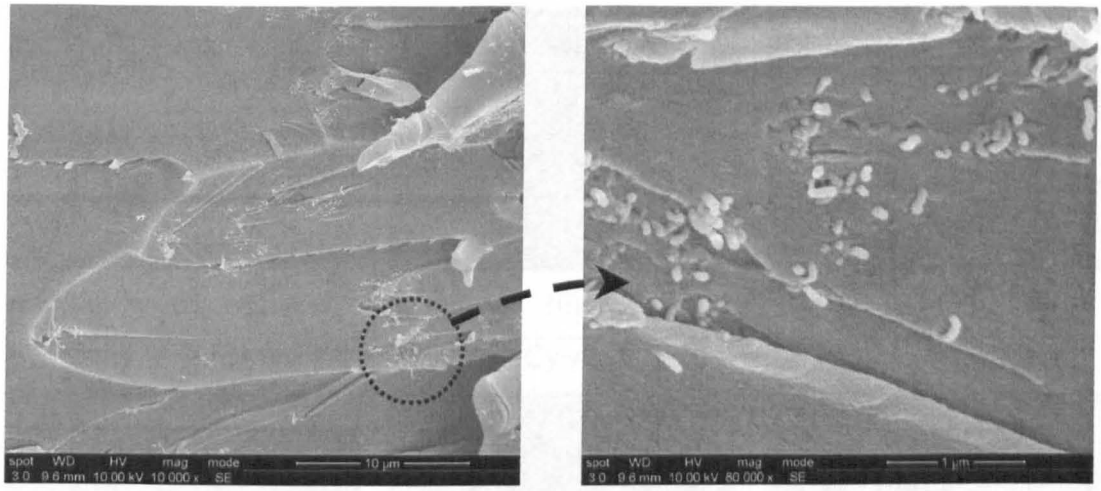

(a) circled area indicate cluster of CNT (b) CNT in epoxy at 80000x

Figure 7.13: SEM micrographs showing fracture surface of 1 wt% multiwalled CNT in Epikote 828 resin as observed under two different high magnifications where (a) clusters of CNT in epoxy contribute to crack deflection mechanism and (b) close-up view of a cluster of multiwalled CNT in epoxy.

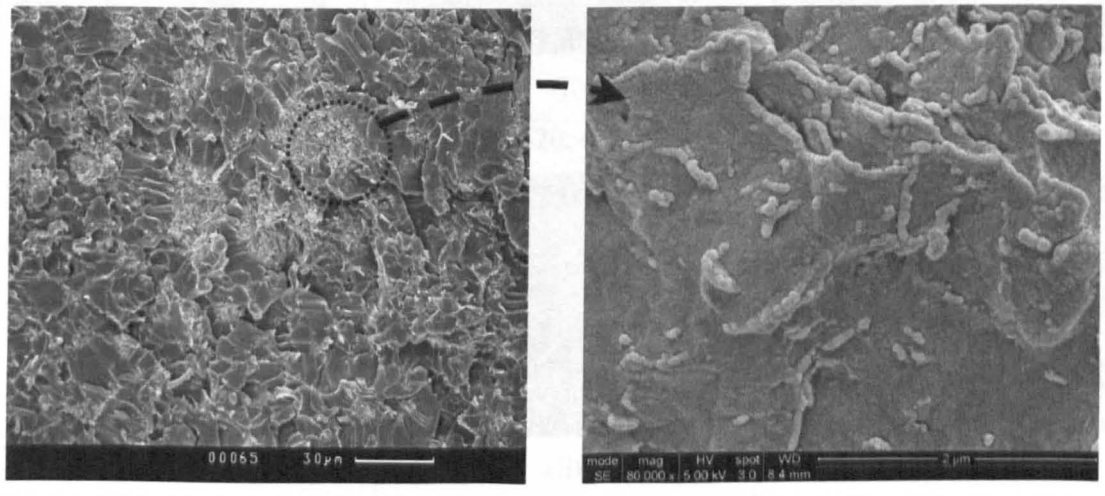

(a) circled area indicate intercalated region (b) nanoclay in epoxy matrix

Figure 7.14: SEM micrographs showing fracture surface of 5 wt% clay/epoxy nanocomposite prepared using mechanical stirring technique observed under two different magnifications where (a) clusters of nanoclay in epoxy (max. size 15-25 μm) and (b) intercalated structure clay/epoxy nanocomposite.

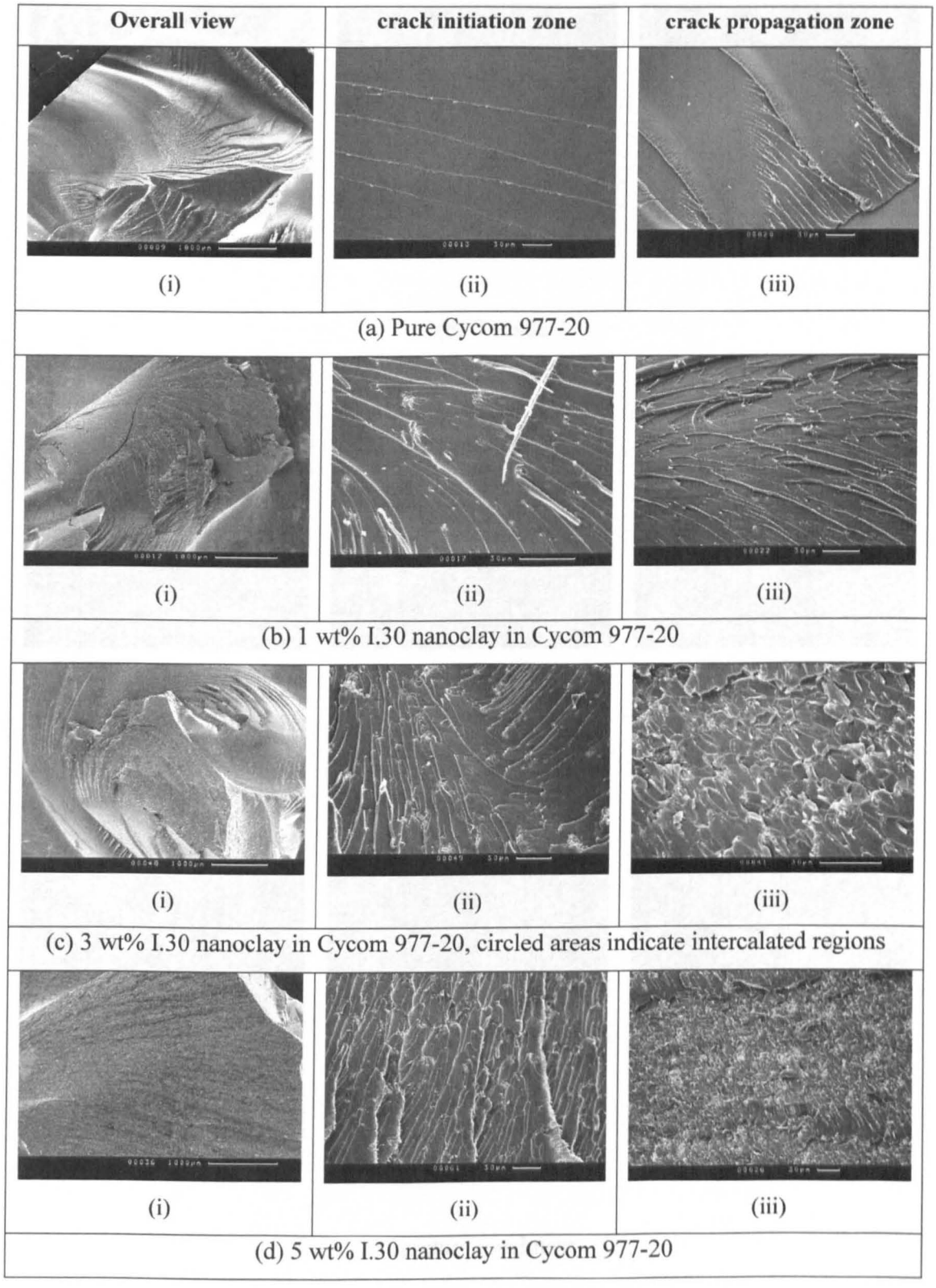

Figure 7.15: SEM examination on fracture surface of cubic shape specimens of clay/977 system, prepared using mechanical stirring technique, after compression.

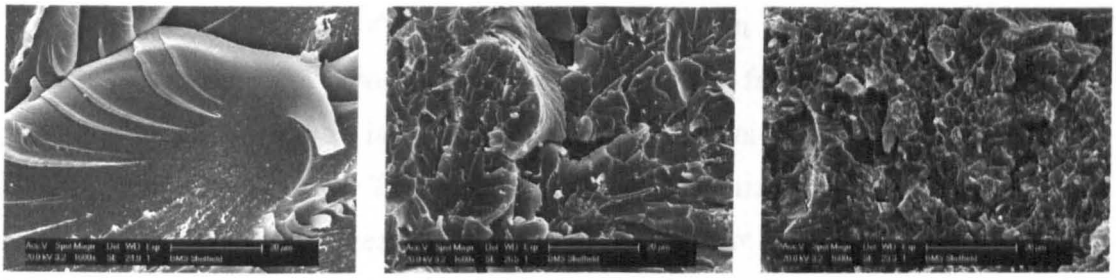

(i) Pure Cycom 977-20 (ii) 1 wt% I.30 nanoclay (iii) 5 wt% I.30 nanoclay

(a) Tensile

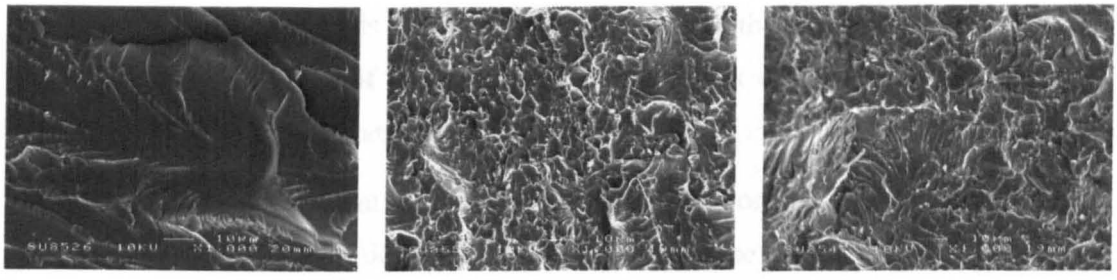

(i) Pure Cycom 977-20 (ii) 1 wt% I.30 nanoclay (iii) 5 wt% I.30 nanoclay

(b) Flexural

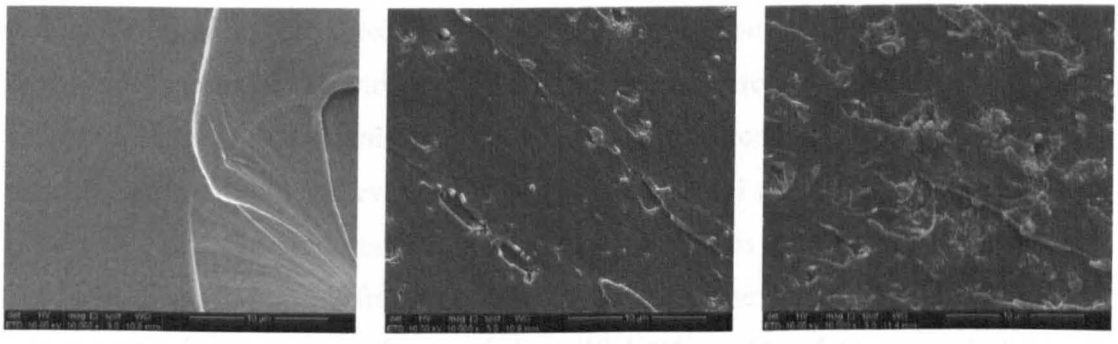

(i) Pure Cycom 977-20 (ii) 1 wt% I.30 nanoclay (iii) 5 wt% I.30 nanoclay

(c) Fracture toughness

Figure 7.16: SEM examination on fracture surface of (a) tensile, (b) flexural and (c) fracture toughness specimens of pure and nanoclay-modified Cycom 977-20 polymers.

The fracture surface of pure Epikote 828 is shown in Figure 7.11a where the direction of crack propagation is from left to right. The fracture surface is relatively smooth and glassy, which is typical of a brittle material where there is no plastic deformation during fracture. The observations on crack initiation and propagation zones agree well with the low measured toughness of the pure polymer, where K_{1C}=0.67 MPa.m$^{1/2}$ and G_{1C}=152.73 J/m^2. The addition of nanosilica, CNT and nanoclay obviously roughened the fracture surface of the Epikote 828 as shown in Figures 7.11-7.14. The fracture surface of nanomodified polymers demonstrates large-scale plastic deformation of the matrix and crack deflection mechanisms. This contributes to a higher fracture energy and a tougher system compared to neat polymer. Of course, the degree of toughening effect depends on the type and amount of the nanofillers, the degree of distribution or exfoliation of the nanofillers in the matrix or quality of the fabricated nanocomposites and filler/matrix interfacial adhesion.

Figure 7.11 shows that an increase in nanosilica content causes an increase in surface roughness. The addition of nanosilica improved the matrix plasticity behaviour which led to shear yielding of the matrix mechanism and the formation of shear bands. This explains the increasing in K_{IC} and G_{IC} of the epoxy with increasing in nanosilica content as shown in Figure 7.9. The toughening effect can obviously be seen in Figure 7.11d where the addition of 25 wt% nanosilica contributes to a large plastic deformation of the matrix and hence agrees well with the enhancement of about 163% in fracture energy compared to pure epoxy. Figure 7.12b shows that the crack path deflection is the major mechanismthat contributes to a higher fracture toughness of CNT/828 nanocomposite. This mechanism occurs when the crack front approaches the CNT rich regions and it is tilted and even twisted out of its original plane. This alters the stress state near crack tip, produces non-planar cracks, increases fracture surface roughness and consumes additional fracture energy. Therefore the addition of CNT causes improvement in fracture toughness of about 60-100% compared to the neat epoxy as shown in Figure 7.9b. The crack path deflection mechanism can be seen clearly on high magnification SEM images as shown in Figure 7.13 where the clusters of 10 nm multiwalled CNTs can clearly be observed under 80000x magnification.

For the clay/828 system, the increased surface roughness, as shown in Figure 7.12c-d, implies that the path of the crack tip is distorted because of the clay platelets, hence, making crack propagation more difficult. The crack deflection and plastic deformation of the matrix as observed on the fracture surfaces were responsible for the

increased in fracture energy for about 16-60% by adding I.28 nanoclay into the Epikote 828, as shown in Figure 7.9b. However, at high nanoclay content, the clusters of intercalated regions (nanoclay rich regions), as shown in Figure 7.14, limit the toughening capability of the nanoclay. The weak interfacial adhesion between agglomerated nanoclay and the matrix allowed the cracks to easily pass through them. Moreover some microvoids and matrix cracking can also be observed on the fracture surface, see Figure 7.12c-d. This contribute to a slightly lower fracture toughness compared to low content clay nanocomposite system, see Figure 7.9.

Examination of the fracture surface of pure Cycom 977-20 specimen after compression, Figure 7.15a, showed a relatively smooth and glassy surface (brittle-like failure) compared to those of the nanoclay-modified polymer which demonstrate a crack deflection mechanism and micro-rough fracture surface, as shown in Figure 7.15b-d. The surface roughness increases with increasing clay content. Therefore, the formation of a large number of micro-cracks and the increase in the fracture surface area due to crack deflection can be considered as the major toughening mechanisms in the clay/977 system. The crack deflection toughening is created when the crack front approaches an exfoliated or intercalated rich region. It is deflected out of its original plane and produced non-planar cracks. A large number of microcracks and large fracture surface areas, as shown in Figure 7.15b-d, consumes additional fracture energy, and hence, contribute to a tougher system. However, as shown in Figure 7.9 the presence of intercalated structure nanoclay in the epoxy reduced the toughening effect. Thus, the nanocomposite with 3 and 5 wt% nanoclay has a lower K_{IC} and G_{IC} values compared to that of the nanocomposite with 1 wt% nanoclay.

The topography of the fracture surfaces of clay/977 system after tensile, flexural and fracture toughness tests were also observed under SEM. Figure 7.16 shows that nanoclay gave a similar effect on the fracture morphology of tensile, flexural and fracture toughness specimens as have been discussed previously on compression specimens. The addition of nanoclay into the epoxy increased the surface roughness of failed specimens. Figure 7.16a shows the presence of numerous dimples on the fracture surface of the nanomodified system, and the dimple density increases with nanoclay content. The formation of large number of dimples contributes to an increase in the fracture surface areas and thus much of the fracture energy is likely to dissipate, thus contributing to a tougher system. Figure 7.16a also shows that for the nanocomposites system, the clay contributes to the formation of the dimples where a cluster of clay

particles can be found in the middle of the dimples. This shows that the cluster of intercalated structure clay induces high-localised stress concentrations in the specimen that is loaded in tension. This may initiate premature failure if the filler/matrix interface is weak and thus leads to low fracture toughness at high clay content. This is the reason why the fracture toughness of nanocomposites with 3 and 5 wt% nanoclay was less than the fully exfoliated nanocomposite (1 wt% nanoclay) as shown in Figure 7.9. A similar fracture mechanism was found on the fracture surface of flexural specimens as shown in Figure 7.16b. In bending, the specimens are subjected to a combination of tension and compression stresses. The pure and nanomodified epoxy are more likely to fail in tension rather than in compression because the epoxy has very low tensile failure strain. Therefore the fracture surface of neat and nanomodifed systems shows the formation of dimples. The fracture surface areas increase with increasing clay content.

Figure 7.16c shows the fracture surface of neat and nanomodified epoxy of SENB specimens loaded in three-point bending. The fracture surface of the neat epoxy shows a brittle failure with very smooth surface areas, while the addition of nanoclay roughened the surface with the formation of secondary cracks. The surface roughness increases with increasing clay content and the major toughening mechanisms is by the formation of micro-cracks via crack deflection. Figure 7.16c(iii) shows evidence of micro-voids and clusters of nanoclay rich region in the matrix and nanoparticle debonding occurred at high clay content. This limits the toughening benefit of large surface areas offered by the nanoparticles due to a weak filler/matrix interfacial bonding.

7.3 Effect of nanosilica on the compressive properties of HTS40/828 laminates

7.3.1 Physical properties

In the previous section, it was shown that nanomodified epoxy with uniformly dispersed silica nanospheres enhanced the compressive, tensile, flexural and fracture toughness properties with no significant reduction in thermal properties of the Epikote 828. The study was then extended to the fabrication of CFRP laminates using the 5, 13 and 25 wt% nanosilica-modified Epikote 828 and HTS40 carbon fibres. A conventional technique, using dry filament winding, resin impregnation and vacuum bagging, was

employed to fabricate a series of nanosilica-modified HTS40/828 laminates. The TGA results confirmed that the nanosilica contents in the HTS40/828 laminate were 3, 7 and 13 vol.%. It is well known that density is one of the most important characteristics in composite design. The density of the unmodified system is 1.45 g/cm^3 while the addition of 13 vol.% nanosilica slightly increased the density of the HTS40/828 laminate to 1.53 g/cm^3. The measured density of commercial system HTS40/977-2 was 1.54 g/cm^3. Therefore this value is similar to 13%si/HTS40/828 system.

The fabricated laminate has average V_f = 42%, low fibre waviness distribution (average ϕ_0 = 2.5°) and less than 1% void content. This implies that the fabrication technique, which was employed in the current work, successfully produced good quality laminates. The fibre volume fraction (V_f = 42%) measured by image analysis was proven using the TGA technique. In addition, the TGA results showed that the addition of nanosilica improved the thermal stability of the laminate. The presence of nanosilica also results in a narrow fibre angle distribution in the HTS40/828 laminate. For instance, for the unmodified system, 90% of fibre volume fraction within ±2° to the 0°-fibre direction while ±1.5° fibre misalignment was recorded for 13%si/HTS40/828 system. This suggests that the nanomodified resin contributes to a better fibre alignment in the laminate. It provides a better thermal stability hence reduces the fibre waviness caused by fibre/resin thermal mismatched during curing.

7.3.2 In-plane shear properties

The addition of nanosilica enhanced the in-plane shear stress-strain response of the HTS40/828 laminate. This is desirable since raising the elastic and plastic tangent shear modulus leads to a higher compressive strength of the composite. The 0.5% offset technique was introduced to determine the in-plane shear yield stress. The $[\pm 45]_{2s}$ laminate failed prematurely in tension due to a reduced gauge length. Therefore, the overall in-plane shear stress-strain response was also plotted, using an equation given in [7], to determine the in-plane elastic and plastic moduli and shear yield and ultimate stresses. For instance, the addition of 13 vol.% nanosilica improved the in-plane shear elastic modulus, plastic modulus, yield stress and strength by 49%, 34%, 40% and 39%, respectively. The in-plane shear properties were incorporated into several analytical models in order to study the effect of nanosilica on compressive properties of UD HTS40/828 laminate.

7.3.3 Compressive properties

The degree of reinforcement provided by a very well dispersed nanosilica in the epoxy was evaluated using compression tests on the UD laminate. The valid measurement of the compressive response of CFRP has always presented difficulties [161]. This is because the compression testing is sensitive to various factors such as Euler buckling and specimen designs, type of test fixtures and applied loads to the specimens, specimen misalignment in the test fixture, bending/stretching coupling in the laminate and local stress concentrations near the end tab [161,184]. For example, the experimentally measured compressive strength data presented in [4-6] were concluded as invalid due to premature failure of the specimens. The UD laminates were tested using a short-block compression fixture. The test specimens failed by longitudinal splitting, crushing and end-brooming at the load introduction end.

In the current work, the specimen failed within the gauge length. This was identified as transverse shear failure mode according to ASTM D3410. This implies that the compression tests, using the ICSTM test fixture, were successful. The results showed that the addition of nanosilica improved the compressive properties of the HTS40/828 laminate. The post failure examination on the fracture surface of the unmodified and nanomodified composites showed that individual fibres failed due to micro-bending, where tension and compression regions can be clearly identified on the fracture surface. The optical micrographs also showed that the kink band zones were formed after the fibres break. Therefore, based on these failure mechanisms, the compressive strength of UD laminates was predicted using fibre microbuckling and fibre kinking models.

Figure 7.17 shows the predicted compressive strength of UD laminates using three different models. The compressive strength of unmodified and nanomodified-HTS40/828 systems was predicted using initial fibre misalignment angle ϕ_0 of 2°, while for HTS40/977-2 system used ϕ_0 = 1°. These values were chosen based on the fibre angle distribution plots, as discussed in Chapter 6 Section 6.2.1, where 90-95% fibres lie within these angles with respect to the 0°-fibre axis.

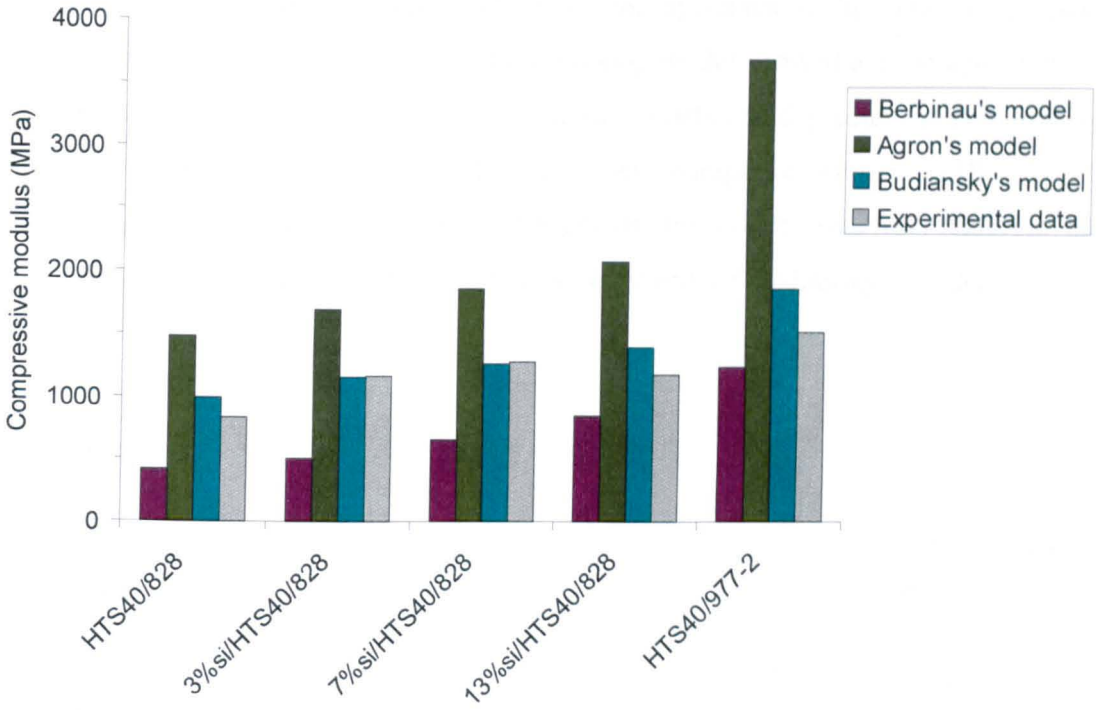

Figure 7.17: Comparison of predicted and measured compressive strength of the UD HTS40/828 and HTS40/977-2 CFRP composites. The compressive strength of unmodified and nanomodified HTS40/828 laminate was predicted using $\phi_0 = 2^\circ$, while $\phi_0 = 1^\circ$ was used for HTS40/977-2 system (based on experimental result).

Figure 7.17 shows that all models predicted enhancement in the compressive strength of HTS40/828 system by the inclusion of silica nanoparticles. The degree of reinforcement depends on various parameters such as initial fibre misalignment angle, in-plane shear elastic and plastic moduli, shear yield and ultimate stresses and fibre volume fraction. However if all of these parameters were considered in the prediction model, Berbinau's model underestimated the actual compressive strength. This is because the predicted value corresponds to the critical stress at which fibre instability or microbuckling initiates and not necessarily the final failure stress of the whole laminate caused by both fibre microbuckling (damage initiation) and plastic kinking (damage propagation mechanism). For instance, the compressive strength of HTS40/828 laminate, which was predicted using Berbinau's model, was 610 MPa at $\phi_0 = 1^\circ$ and 417 MPa at $\phi_0 = 2^\circ$. These values fall within the material's softening region observed in the compressive stress-strain curve as shown in Figure 7.18. Therefore, for the current system, the buckled fibres continue to support load and final failure occurs when the

fibre kink band zone has propagated across the specimen width. The compressive strength predicted using Budiansky's fibre kinking model showed a good agreement to the measured value. For $\phi_0 = 1^\circ$, none of these models could predict the compressive strength of the thermoplastic-toughened CFRP composite system HTS40/977-2. However, the predicted compressive strength of this system was very close to the measured value of 1505 MPa if $\phi_0 = 1.5^\circ$ was employed the Budiansky's model.

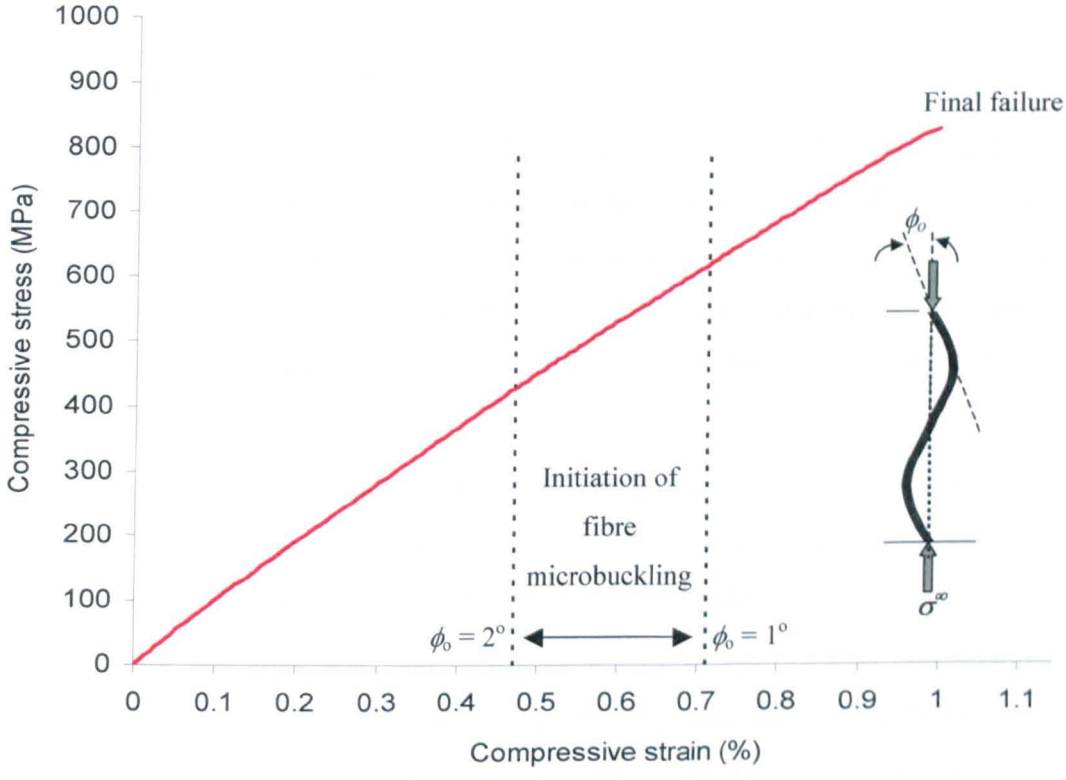

Figure 7.18: A typical measured compressive stress-strain response of a UD HTS40/828 composite laminate. Berbinau's model predicted that the fibre instability was triggered at 0.47% compressive strain if the initial fibre misalignment angle in the laminate is 2°. Triggering of fibre instability (microbuckling) depends on initial fibre waviness and this results in material softening.

Chapter 8

Conclusions and suggestions for future work

8.1 Concluding remarks

The compressive strength of UD CFRP composites is primarily influenced by the properties of the matrix and fibre alignment in the laminate [7]. Therefore, this study is aimed at enhancing the compressive properties by introducing nanofiller into the matrix. In order to achieve this, a series of nanomodified resins using silica, CNT and clay nanofillers, were evaluated. Based on the thermal and mechanical tests results, a number of conclusions are drawn.

- Stiffer resins were successfully developed using nanosilica, CNT and nanoclay. The elastic modulus of the epoxy polymer (measured in compression, tension and bending) was increased with increasing nanofiller content.
- Nanosilica was homogeneously dispersed in Epikote 828 polymer. The addition of nanosilica improves the compressive, tensile, flexural, fracture toughness, thermal stability and dimensional stability of the epoxy polymer. The major toughening mechanisms involved the formation of crack deflection, micro-cracks and plastic yielding as revealed by SEM micrographs.
- At low CNT content, a good quality of nanocomposite was fabricated however, at high CNT content (>0.5 wt%) the TEM micrographs showed evidence of some CNT entanglement. CNT moderately improved the compressive and tensile properties of the epoxy polymer, however it gave significant improvement in flexural properties and fracture toughness.
- The presence of I.28 nanoclay slightly improved the elastic modulus of the Epikote 828, however the nanocomposite failed prematurely when it was loaded in compression, tension and 3-point bending. The TEM micrographs revealed the

presence of nanovoids and clusters of intercalated nanoclay in the nanocomposite. Limitations in processing time and high nanoresin viscosity contributed to a low quality nanocomposite. Despite all weaknesses in mechanical performance, I.28 nanoclay significantly improved the thermal and dimensional stabilities of the epoxy polymer.

- At low content, the I.30 nanoclay was successfully exfoliated in Cycom 977-20 resin by using a 3-roll mill machine. However, at high clay content (>3 wt%), clusters of intercalated nanoclay were found in the polymer due to processing difficulties. The addition of nanoclay improved the dimensional stability, thermal stability, compressive and tensile properties of the polymer. However, in bending, no improvement in strength and failure strain was recorded. The degree of reinforcement in fracture toughness was also dependent on the microstructure of the nanocomposite. At low clay content, exfoliated structure nanocomposite substantially improved the fracture toughness (K_{IC} and G_{IC}), however this toughening effect was reduced as the clay content increased.

Unlike conventional toughening systems using micron-sized fillers and agglomerated nanofillers, nanosilica improved the stiffness and strength without sacrificing toughness, failure strain and thermal properties of the Epikote 828. These interesting properties rendered this type of nanoresin as a suitable candidate for the fabrication of CFRP composite. Therefore the study was extended to investigate the effect of nanosilica on the compressive properties of HTS40/828 laminate. Based on the physical, thermal and mechanical tests that have been conducted, a number of conclusions are drawn.

- The 3, 7 and 13 vol.% nanosilica-modified HTS40/828 composite laminates were successfully fabricated using a conventional technique (dry filament winding, wet resin impregnation and vacuum bagging). A good quality laminate (such as V_f=42 vol% and narrow fibre waviness distribution) was revealed by TGA and image analysis.
- The in-plane shear properties of the HTS40/828 composite, such as elastic modulus, yield stress and shear strength, were increased with increasing nanosilica content.

- The presence of nanosilica significantly improved the compressive modulus and strength without sacrificing the failure strain of the laminate provided that the nanosilica content was less than 13 vol.%.
- The SEM and optical micrographs showed that the failure of the UD laminate was due to fibre microbuckling and kinking mechanisms. Therefore, the UD compressive strength was predicted using several analytical models based on these failure mechanisms. The predicted strength using Budiansky's model showed a good agreement to the experimental results. However, a conservative prediction was made by Berbinau's model, where the model provides a good indication of the initiation of fibre microbuckling in the composite during compression.
- The experimental results showed that the compressive modulus of 7 and 13 vol% nanosilica-filled HTS40/828 was comparable to that of the commercial CFRP composite system HTS40/977-2. As predicted using Budiansky's model, the compressive strength of 13%si/HTS40/828 was 1392 MPa. This suggests that the performance of this newly developed system could be even better than that of the commercial system provided an improved fabrication method (commercial type) is employed.

Based on the systematic experimental investigation and results that have been discussed in the previous chapters, it can be concluded that a nanomodified CFRP system (developed using appropriate treated-nanofiller and epoxy resin) is a promising advanced material that can be used in modern FRP structures to improve damage tolerance and damage resistance properties. A large number of opportunities for further study have arisen based on various topics which have been investigated in this thesis. These are briefly listed in the following section.

8.2 Recommendations for future work

The work performed during this project demonstrated that a properly treated-nanosilica dispersed in CFRP composite enhanced the compressive and in-plane shear properties. However, in order to compete with commercially available systems, the other properties must be studied further. The tensile, bending, fracture toughness and thermal properties of the nanomodified laminates must be further investigated. In addition, the performance of the CFRP composite materials is usually characterised by their damage resistance and damage tolerance. Damage resistance is the resistance of a material to damage from impact, while damage tolerance is the ability of a material or structure to perform safely after damage. These properties are often measured using the compression after impact (CAI) and the open hole compression (OHC) tests. Therefore, there is a strong need to investigate the effect of nanosilica on these two properties. In addition, hygrothermal effect and fatigue performance of the nanomodified-CFRP systems also need further examination.

Even though DGEBA type epoxies (such as Epikote 828) have widely been used for various applications, high performance resins (which have high thermal properties such as Cycom 977 series) are usually selected for the development of advanced systems and structures such as aerospace and high-end automotive. A preliminary work has been conducted to disperse a similar type of nanosilica into commercial resin Cycom 977-20. TEM micrographs showed a homogeneous dispersion of nanosilica in the epoxy. Therefore, this work should be extended to investigate the reinforcement effect of nanosilica on the properties of the high performance resin (Cycom 977-20).

With many industries looking to lower cost and high quality composites, higher volume manufacturing and fabrication methods, such as prepreg, autoclave and resin transfer moulding, are becoming of increasing interest. A conventional lab-scale technique was employed in this study yielded CFRP laminates with a 42% volume fraction. Therefore, a better fabrication method such as resin transfer moulding or prepreg technique must be further explored.

CNT is one of the most versatile nanofillers that currently used to improve electrical and thermal properties of polymers. It has high elastic modulus (1000GPa) and strength (11-200GPa) [61,86]. However, the full potential of reinforcement offered by this type of nanofiller is always limited by improper treatment of the CNT's wall, selection on the resin system and dispersion of CNT in the matrix. These limit the

capability of transferring load between filler and the matrix. Therefore, further investigation should be conducted to improve the system. This is a promising nanoresin for CFRP system in order to improve bending, fracture toughness, electrical and thermal properties.

Clay/epoxy nanocomposites exhibit good thermal and dimensional stability. This low cost nanofillers has high elastic modulus and provide enormous surface areas when properly distributed in the resins. In this study, it enhanced the mechanical and thermal properties of Cycom 977-20. However, limitation in processing time due to the presence of hardener during milling limits the degree of dispersion. Hence, TEM micrographs revealed the high-density clay nanoplatelets distributed in the matrix. Therefore, further improvement in the fabrication process is still required.

References

[1] **Soutis, C.** Fibre reinforced composites in aircraft construction. *Progress in Aerospace Sciences*, 2005, **41**(2), 143-151.

[2] **Mallick, P.K.** *Fiber-Reinforced Composites.* (Marcel Dekker Inc, 1988).

[3] **Soutis, C. and Fleck, N.A.** Static compression failure of carbon fibre T800/924C composite plate with a single hole. *Journal of Composite Materials*, 1990, **24**, 241-256.

[4] **Cano, R.J. and Dow, M.B.** *Properties of five toughened matrix composite materials.* (NASA Langley research centre, technical paper 3254, 1992).

[5] **Smith, D.L. and Dow, M.B.** *Properties of three graphite/toughened resin composites.* (NASA Langley research centre, technical paper 3102, 1991).

[6] **Dow, M.B. and Smith, D.L.** *Properties of two composite materials made of toughened epoxy resin and high strain graphite fibre.* (NASA Langley research centre, technical paper 2826, 1988).

[7] **Jumahat, A., Soutis, C., Jones, F.R. and Hodzic, A.** Fracture mechanisms and failure analysis of carbon fibre/toughened epoxy composites subjected to compressive loading. *Composite structures*, 2010, **92**(2), 295-305.

[8] **Kaw, A.K.** *Mechanics of composite materials.* (CRC Press, 1997).

[9] **Jones, F.R.** *Handbook of polymer-fibre composites.* (Longman scientific & technical, 1994).

[10] **Jang, B.Z.** *Advanced polymer composites: principles and applications.* (ASM International, 1994).

[11] **Yokozeki, T., Aoki, Y. and Ogasawara, T.** Experimental characterization of strength and damage resistance properties of thin-ply carbon fiber/toughened epoxy laminates. *Composite Structures*, 2008, **82**(3), 382-389.

[12] **Sihn, S., Kim, R.Y., Kawabe, K. and Tsai, S.W.** Experimental studies of thin-ply laminated composites. *Composites Science and Technology*, 2007, **67**(6), 996-1008.

[13] **Mouritz, A.P., Leong, K.H. and Herszberg, I.** A review of the effect of stitching on the in-plane mechanical properties of fibre-reinforced polymer composites. *Composites Part A: Applied Science and Manufacturing*, 1997, **28**(12), 979-991.

[14] **Farley, G.L., Smith, B.T. and Maiden, J.** Compression Response of Thick Layer Composite Laminates with Through-the-Thickness Reinforcement. *Journal of Reinforced Plastics and Composites*, 1992, **11**(7), 787-810.

[15] **Reeder, J.R.** Stitching vs. a Toughened Matrix: Compression Strength Effects. *Journal of Composite Materials*, 1995, **29**(18), 2464-2487.

[16] **Vlasveld, D.P.N., Daud, W., Bersee, H.E.N. and Picken, S.J.** Continuous fibre composites with a nanocomposite matrix: improvement of flexural and compressive strength at elevated temperatures. *Composites Part A: Applied Science and Manufacturing*, 2007, **38**, 730-738.

[17] **Vlasveld, D.P.N., Bersee, H.E.N. and Picken, S.J.** Nanocomposite matrix for increased fibre composite strength. *Polymer*, 2005, **46**, 10269-10278.

[18] **Parlevliet, P.P., Bersee, H.E.N. and Beukers, A.** Residual stresses in thermoplastic composites – a study of the literature Part III: Effect of thermal residual stresses. *Composites Part A: Applied Science and Manufacturing*, 2007, **38**, 1581-1596.

[19] **Recker, H.G., Hartness, T., Folda, T., Tesch, H., Weber, T. and Boyd, J.D.** *Toughened thermosetting structural materials.* (United States Patent, 5605745, 1997).

[20] **Babayan, E.P. and Nguyen, H.X.** *Epoxy matrix containing amine hardener and micropulverized polyimide.* (United States Patent, 5310825, 1994).

[21] **Buyny, R.A. and Olesen, K.A.** *Toughened resin systems for composite applications.* (United States Patent, 5248711, 1993).

[22] **Cytec Engineered Materials Inc.** *Cycom 977-2 Toughened epoxy resin technical datasheet.* (www.cytec.com)

[23] **Cytec Engineered Materials Inc.** *Cycom 977-20 RTM with priform technology soluble fibre co-woven textile technical datasheet.* (www.cytec.com)

[24] **LoFaro, C., Abusafieh, A., Webb, W.E. and Doyle, M.** *Resin soluble thermoplastic veil for composite materials.* (United States Patent, US 2006/0252334 A1, 2006).

[25] **Mimura, K., Ito, H. and Fujioka, H.** Toughening of epoxy resin modified with in situ polymerized thermoplastic polymers. *Polymer*, 2001, **149**, 9223-9233.

[26] **Cardwell, B.J. and Yee, A.F.** Toughening of epoxies through thermoplastic crack bridging. *Journal of Materials Science*, 1998, **33**, 5473-5484.

[27] **Kinloch, A.J. and Yuen, M.L.** Thermoplastic-toughened epoxy polymers. *Journal of Materials Science*, 1994, **29**, 3781-3790.

[28] **Pearson, R.A. and Yee, A.F.** Toughening mechanisms in thermoplastic-modified epoxies: 1. Modification using poly(phenylene oxide). *Polymer*, 1993, **34**, 3658-3670.

[29] **McGrail, P.T.** Polyaromatics. *Polymer International*, 1996, **41**, 103-121.

[30] **Bucknall, C.B. and Partridge, I.K.** Phase separation in epoxy resins containing polyethersulphone. *Polymer*, 1983, **24**(5), 639-644.

[31] **Evans, R.E. and Hirschbuehler, K.R.** *Thermoplastic interleafed resin matrix composites with improved impact strength and toughness.* (United States Patent, 4604319, 1986).

[32] **Carter, J.T., Faro, C.L., Maskell, R.K. and McGrail, P.T.** *Flexible polymer element as toughening agent in prepregs.* (United States Patent, US 2004/0041128 A1, 2004).

[33] **Recker, H.G., Altsaedt, V., Tesch, H. and Weber, T.** *Toughened, fibre-reinforced thermosetting resin matrix prepregs and composites made therefrom.* (United States Patent, 5627222, 1997).

[34] **Gawin, I.** *Damage tolerant composites containing infusible particles.* (United States Patent, 4863787, 1989).

[35] **Nguyen, F.N. and Natsume, N.** *Toughened fibre reinforced polymer compsite with core-shell particles.* (United States Patent, US 2010/0280151 A1, 2010).

[36] **Bagheri, R. and Pearson, R.A.** Role of particle cavitation in rubber-toughened epoxies: II. Inter-particle distance. *Polymer*, 2000, **41**, 269-276.

[37] **Lu, R., Plummer, C.J.G., Cantwell, W.J. and Kausch, H.H.** Toughening mechanisms in modified epoxy resins with different crosslink densities. *Polymer Bulletin*, 1996, **37**, 399-406.

[38] **Bagheri, R. and Pearson, R.A.** The use of microvoids to toughened polymers. *Polymer*, 1995, **36**(25), 4883-4885.

[39] **Frohlich, J., Kautz, H., Thomann, R., Frey, H. and Mulhaupt, R.** Reactive core/shell type hyperbranched blockcopolyethers as new liquid rubbers for epoxy toughening. *Polymer*, 2004, **45**, 2155-2164.

[40] **Day, R.J., Lovell, P.A. and Wazzan, A.A.** Toughened carbon/epoxy composites made by using core/shell particles. *Composites Science and Technology*, 2001, **61**, 41-56.

[41] **Lewis, T.B. and Nielsen, L.E.** Dynamic mechanical properties of particulate-filled composites. *Journal of applied polymer science*, 1970, **14**(6), 1449-1471.

[42] **Nielsen, L.E. and Landel, R.F.** *Mechanical properties of polymers and composites.* (Marcel Dekker Inc, 1994).

[43] **McGrath, L.M., Parnas, R.S., King, S.H., Schroeder, J.L., Fischer, D.A. and Lenhart, J.L.** Investigation of the thermal, mechanical and fracture properties of alumina-epoxy composites. *Polymer*, 2008, **49**, 999-1014.

[44] **Lee, J. and Yee, A.F.** Inorganic particle toughening II: toughening mechanisms of glass bead filled epoxies. *Journal of Materials Science*, 2001, **36**, 7-20.

[45] **Budiansky, B.** Micromechanics. *Computers and Structures*, 1983, **16**(1-4), 3-12.

[46] **Berbinau, P., Soutis, C. and Guz, I.A.** Compressive failure of 0° unidirectional carbon-fibre-reinforced plastic (CFRP) laminates by fibre microbuckling. *Composites Science and Technology*, 1999, **59**, 1451-1455.

[47] **Mackinley, C.P.** *Compressive failure of CFRP laminates containing pin-loaded holes.* (Imperial College of Science Technology and medicine, PhD thesis, 2000)

[48] **Rosen, B.W.** Mechanics of composite strengthening, In: Fibre composite materials. *Proceedings of the American Society for Metals*, pp. 574-586 (American Society for Metals, USA, 1965).

[49] **Argon, A.S.** *Fracture of composites, In: Treatise of material science and technology.* (Academic Press, 1972)

[50] **Berbinau, P., Soutis, C., Goutas, P. and Curtis, P.T.** Effect of off-axis ply orientation on 0°-fibre microbuckling. *Composites Part A: Applied Science and Manufacturing*, 1999, 30, 1197–1207.

[51] **Soutis, C.** Measurement of the static compressive strength of carbon-fibre/epoxy laminates. *Composites Science and Technology*, 1991, **42**, 373-392.

[52] **Agarwal, B.D., Brout L.J. and Chandrashekhara, K.** *Analysis and Performance of Fiber Composites*. (John Wiley & Sons, 2006).

[53] **Hahn, H.T. and Williams, J.G.** Compression failure mechanism in unidirectional composites. *Composite materials: testing and design (seventh conference) ASTM STP 893*, pp. 115-139 (American Society for Testing and Materials, Philadelphia, 1986).

[54] **Budiansky, B. and Fleck, N.A.** Compressive kinking of fibre composites: a topical review. *Applied mechanics review*, 1994, **47**(6), 246-270.

[55] **Budiansky, B. and Fleck, N.A.** Compressive failure of fibre composites. *J. Mech. Phys. Solids*, 1993, **41**(1), 183-211.

[56] **Koo, J.H.** *Polymer nanocomposites processing, characterization and applications.* (McGraw Hill, 2006).

[57] **Pinnavaia, T.J. and Beall, G.W.** *Polymer-clay nanocomposites*. (John Wiley & sons, 2000).

[58] **Friedrich, K., Fakirov, S. and Zhang, Z.** *Polymer composites from nano- to macro-scale*. (Springer, 2005).

[59] **Zhou, G.** *Preparation, structure, and properties of advanced polymer composites with long fibers and nanoparticles.* (The Ohio State University, PhD thesis, 2007).

[60] **Thostenson, E.T., Li, C. & Chou, T.W.** Review: nanocomposites in context. *Composites Science and Technology*, 2005, 65, 491-516.

[61] **Hussain, F., Hojjati, M., Okamoto, M. and Gorga, R.E.** Review article: Polymer-matrix nanocomposites, processing, manufacturing, and application: An overview. *Journal of Composite Materials*, 2006, 40(17), 1511-1575.

[62] **Zheng, Y., Ning, R. and Zheng, Y.** Study of SiO_2 nanoparticles on the improved performance of epoxy and fibre composites. *Journal of Reinforced Plastics and Composites*, 2005, 24(3), 223-233.

[63] **Chen, C., Justice, R.S., Schaefer, D.W. and Baur, J.W.** Highly dispersed nanosilica-epoxy resins with enhanced mechanical properties. *Polymer*, 2008, 49, 3805-3815.

[64] **Battistella, M., Cascione, M., Fiedler, B., Wichmann, M.H.G., Quaresimin, M. and Schulte, K.** Fracture behaviour of fumed silica/epoxy nanocomposites. *Composites Part A: Applied Science and Manufacturing*, 2008, 39, 1851-1858.

[65] **Liu, S., Zhang, H., Zhang, Z., Zhang, T. and Sprenger, S.** Tailoring the mechanical performance of epoxy resin by various nanoparticles. *Polymers & Polymer Composites*, 2008, **16**(8), 471-477.

[66] **www.hanse-chemie.com.** Hanse chemie AG, Charlottenburger Str. 9, 21502 Geesthacht, Germany.

[67] **www.nanoresins.ag.** Nanoresins AG, Charlottenburger Str. 9, 21502 Geesthacht, Germany.

[68] **Zhang, H., Zhang, Z., Friedrich, K. and Eger, C.** Property improvements of in situ epoxy nanocomposites with reduced interparticle distance at high nanosilica content. *Acta Materialia*, 2006, **54**, 1833-1842.

[69] **Deng, S. and Friedrich, K.** Fracture behaviours of epoxy nanocomposites with nano-silica at low and elevated temperatures. *Journal of Materials Science*, 2007, **42**, 2766-2774.

[70] **Zhang, H., Tang, L.C., Zhang, Z., Friedrich, K. and Sprenger, S.** Fracture behaviour of in situ silica nanoparticle-filled epoxy at different temperatures. *Polymer*, 2008, **49**, 3816-3825.

[71] **Blackman, B.R.K., Kinloch, A.J., Lee, J.S., Taylor, A.C., Agarwal, R., Schueneman, G. and Sprenger, S.** The fracture and fatigue behaviour of nano-modified epoxy polymers. *Journal of Materials Science Letters*, 2007, **42**, 7049-7051.

[72] **Kinloch, A.J., Mohammed, R., Taylor, A., Eger, C., Sprenger, S. and Egan, D.** The effect of silica nano particles and rubber particles on the toughness of multiphase thermosetting epoxy polymers. *Journal of Materials Science*, 2005, **40**(18), 5083-5086.

[73] **Johnsen, B.B., Kinloch, A.J., Mohammed, R.D., Taylor, A.C. and Sprenger, S.** Toughening mechanisms of nanoparticle-modified epoxy polymers. *Polymer*, 2007, **48**, 530-541.

[74] **Kinloch, A.J., Johnsen, B.B., Mohammed, R.D., Taylor, A.C. and Sprenger, S.** Toughening mechanisms in novel nano-silica epoxy polymers. *Proceedings of the 5th Australasian Congress on Applied Mechanics* (Australia, 2007).

[75] **Rosso, P., Ye, L., Friedrich, K. and Sprenger, S.** A toughened epoxy resin by silica nanoparticle reinforcement. *Journal of Applied Polymer Science*, 2006, **100**, 1849-1855.

[76] **Rosso, P. and Ye, L.** Epoxy/silica nanocomposites: Nanoparticle-induced cure kinetics and microstructure. *Macromolecular Rapid Communications*, 2007, **28**, 121-126.

[77] **Ma, J., Mo, M.S., Du, X.S., Rosso, P., Friedrich, K. and Kuan, H.C.** Effect of inorganic nanoparticles on mechanical property, fracture toughness and toughening mechanism of two epoxy systems. *Polymer*, 2008, **49**, 3510-3523.

[78] **Kinloch, A.J., Mohammed, R., Taylor, A.C., Sprenger, S. and Egan, D.** The interlaminar toughness of carbon-fibre reinforced plastic composites using 'hybrid-toughened' matrices. *Journal of Materials Science*, 2006, **41**, 5043-5046.

[79] **Kinloch, A.J., Masania, K., Taylor, A.C. and Sprenger, S.** The fracture of naosilica and rubber toughened epoxy fibre composites. *Composites & Polycon 2009 conference* (American Composites Manufacturers Association, USA, 2009).

[80] **Manjunatha, C.M., Taylor, A.C., Kinloch, A.J. and Sprenger, S.** The tensile fatigue behaviour of a silica nanoparticle-modified glass fibre reinforced epoxy composite. *Composites Science and Technology*, 2010, **70**, 193-199.

[81] **Manjunatha, C.M., Taylor, A.C., Kinloch, A.J. and Sprenger, S.** The effect of rubber micro-particles and silica nano-particles on the tensile fatigue behaviour of a glass-fibre epoxy composite. *Journal of Materials Science*, 2009, **44**, 342-345.

[82] **Hsieh, T.H., Kinloch, A.J., Masania, K., Lee, J.S., Taylor, A.C. and Sprenger, S.** The toughness of epoxy polymers and fibre composites modified with rubber microparticles and silica nanoparticles. *Journal of Materials Science*, 2010, **45**, 1193-1210.

[83] **Kinloch, A.J., Masania, K., Taylor, A.C., Sprenger, S and Egan, D.** The fracture of glass-fibre-reinforced epoxy composites using nanoparticle-modified matrices. *Journal of Materials Science*, 2008, **43**, 1151-1154.

[84] **Uddin, M.F. and Sun, C.T.** Strength of unidirectional glass/epoxy composite with silica nanoparticle-enhanced matrix. *Composites Science and Technology*, 2008, **68**(7-8), 1637-1643.

[85] **Thostenson, E.T., Ren, Z. and Chou, T.-W.** Advances in the science and technology of carbon nanotubes and their composites: a review. *Composites Science and Technology*, 2001, **61**(13), 1899-1912.

[86] **Yu, M.F., Lourie, O. Dyer, M.J., Moloni, K., Kelly, T.F. and Ruoff, R.S.** Strength and breaking mechanism of multiwalled carbon nanotubes under tensile load. *Science*, 2000, **287**(5453), 637–640.

[87] **Wong, E.W., Sheehan, P.E. and Lieber, C.M.** Nanobeam Mechanics: Elasticity, Strength, and Toughness of Nanorods and Nanotubes. *Science*, 1997, **277**(5334), 1971-1975.

[88] **Yokozeki, T., Iwahori, Y., Ishiwata, S. and Enomoto, K.** Mechanical properties of CFRP laminates manufactured from unidirectional prepregs using CSCNT-dispersed epoxy. *Composites Part A-Applied Science and Manufacturing*, 2007, **38**(10), 2121-2130.

[89] **Yokozeki, T., Iwahori, Y. and Ishiwata, S.** Matrix cracking behaviors in carbon fiber/epoxy laminates filled with cup-stacked carbon nanotubes (CSCNTs). *Composites Part A-Applied Science and Manufacturing*, 2007, **38**(3), 917-924.

[90] **Rice, B.P., Gibson, T. And Lafdi, K.** Development of Multifunctional advanced composites using a VGNF enhanced matrix. *Proceedings of the 49th Int. SAMPE symposium and exhibition* (Society for the Advancement of Material and Process Engineering, USA, 2004).

[91] **Merkulov, V.I., Lowndes, D.H., Wei, Y.Y. and Eres, G.** Pattern growth of individual and multiple vertically aligned carbon nanofibers. *Applied Physics Letters*, 2000, **76**(24), 3555-3557.

[92] **Kim, J.A., Seong, D.G., Kang, T.J. and Youn, J.R.** Effects of surface modification on rheological and mechanical properties of CNT/epoxy composites. *Carbon*, 2006, **44**(10), 1898-1905.

[93] **Tseng, C.H., Wang, C.C. and Chen, C.Y.** Functionalizing carbon nanotubes by plasma modification for the preparation of covalent-integrated epoxy composites. *Chemistry of Materials*, 2007, **19**(2), 308-315.

[94] **Wang, S.R., Liang, Z.Y., Liu, T., Wang, B. and Zhang, C.** Effective amino-functionalization of carbon nanotubes for reinforcing epoxy polymer composites. *Nanotechnology*, 2006, **17**(6), 1551-1557.

[95] **Shen, J.F., Huang, W.S., Wu, L.P., Hu, Y.Z. and Ye, M.X.** Thermo-physical properties of epoxy nanocomposites reinforced with amino-functionalized multi-walled carbon nanotubes. *Composites Part A-Applied Science and Manufacturing*, 2007, **38**, 1331-1336.

[96] **Quaresimin, M. and Varley, R.J.** Understanding the effect of nano-modifier addition upon the properties of fibre reinforced laminates. *Composites Sciences and Technology*, 2008, **68**, 718-726.

[97] **Zhou, Y., Pervin, F., Jeelani, S. and Mallick, P.K.** Improvement in mechanical properties of carbon fabric-epoxy composite using carbon nanofibres. *Journal of Materials Processing Technology*, 2008, **198**, 445-453.

[98] **Arai, M., Noro, Y., Sugimoto, K. and Endo, M.** Mode I and mode II interlaminar fracture toughness of CFRP laminates toughened by carbon nanofibre interlayer. *Composites Science and Technology*, 2008, **68**, 516-525.

[99] **Li, Y., Hori, N., Arai, M., Hu, N., Liu, Y. and Fukunaga, H.** Improvement of interlaminar mechanical properties of CFRP laminates using VGNF. *Composites Part A: Applied Science and Manufacturing*, 2009, **40**, 2004-2012.

[100] **Kostopoulos, V., Tsotra, P., Karapappas, P., Tsantzalis, S., Vavouliotis, A., Loutas, T.H., Paipetis, A., Friedrich, K. and Tanimoto, T.** Mode I interlaminar fracture of CNF or/and PZT doped CFRPs via acoustic emission monitoring. *Composites Science and Technology*, 2007, **67**, 822-828.

[101] **Tsantzalis, S., Karapappas, P., Vavouliotis, A., Tsotra, P., Kostopoulos, V., Tanimoto, T. and Friedrich, K.** On the improvement of toughness of CFRPs with resin doped with CNF and PZT particles. *Composites Part A: Applied Science and Manufacturing*, 2007, **38**, 1159-1162.

[102] **Tsantzalis, S., Karapappas, P., Vavouliotis, A., Tsotra, P., Paipetis, A., Kostopoulos, V. and Friedrich, K.** Enhancement of the mechanical performance of an epoxy resin and fibre reinforced epoxy resin composites. *Composites Part A: Applied Science and Manufacturing*, 2007, **38**, 1076-1081.

[103] **Yokozeki, T., Iwahori, Y., Ishibashi, M., Yanagisawa, T., Imai, K., Arai, M., Takahashi, T. and Enomoto, K.** Fracture toughness improvement of CFRP laminates by dispersion of cup-stacked carbon nanotubes. *Composites Science and Technology*, 2009, **69**, 2268-2273.

[104] **Choi, Y.K., Gotoh, Y., Sugimoto, K., Song, S.M., Yanagisawa, T. and Endo, M.** Processing and characterization of epoxy nanocomposites reinforced by cup-stacked carbon nanotubes. *Polymer*, 2005, **46**, 11489-11498.

[105] **Qiu, J.J., Zhang, C., Wang, B. and Liang, R.** Carbon nanotube integrated multifunctional multiscale composites. *Nanotechnology*, 2007, **18**(27).

[106] **Fan, Z., Santare, M.H. and Advani, S.G.** Interlaminar shear strength of glass fibre reinforced epoxy composites enhanced with multi-walled carbon nanotubes. *Composites Part A: Applied Science and Manufacturing*, 2008, **39**, 540-554.

[107] **Gojny, F.H., Wichmann, M.H.G., Kopke, U., Fiedler, B. and Schulte, K.** Carbon nanotube-reinforced epoxy-composites: enhanced stiffness and fracture toughness at low nanotube content. *Composites Science and Technology*, 2004, **64**(15), 2363-2371.

[108] **Gojny, F.H., Wichmann, M.H.G., Fiedler, B., Bauhofer, W. and Schulte, K.** Influence of nano-modification on the mechanical and electrical properties of conventional fibre-reinforced composites. *Composites Part A: Applied Science and Manufacturing*, 2005, **36**, 1525-1535.

[109] **Wichmann, M.H.G., Sumfleth, J., Gojny, F.H., Quaresimin, M., Fiedler, B. and Schulte, K.** Glass-fibre-reinforced composites with enhanced mechanical and

electrical properties – Benefits and limitations of a nanoparticle modified matrix. *Engineering Fracture Mechanics*, 2006, **73**, 2346-2359.

[110] **Cho, J., Daniel, I.M. and Dikin, D.A.** Effects of block copolymer dispersant and nanotube length on reinforcement of carbon/epoxy composites. *Composites Part A: Applied Science and Manufacturing*, 2008, **39**, 1844-1850.

[111] **Cho, J. and Daniel, I.M.** Reinforcement of carbon/epoxy composites with multi-wall carbon nanotubes and dispersion enhancing block copolymers. *Scripta Materialia*, 2008, **58**, 533-536.

[112] **Khabashesku, V.N., Zhu, J., Peng, H., Barrera, E.V. and Margrave, M.L.** *Fabrication of carbon nanotube reinforced epoxy polymer composites using functionalized carbon nanotubes.* (United States Patent, US2006/0166003 A1, 2006).

[113] **Kostopoulos, V., Baltopoulos, A., Karapappas, P., Vavouliotis, A. and Paipetis, A.** Impact and after-impact properties of carbon fibre reinforced composites enhanced with multi-wall carbon nanotubes. *Composites Science and Technology*, 2010, **70**, 553-563.

[114] **Garcia, E.J., Wardle, B.L., John Hart, A. and Yamamoto, N.** Fabrication and multifunctional properties of a hybrid laminate with aligned carbon nanotubes grown In Situ. *Composites Science and Technology*, 2008, **68**(9), 2034-2041.

[115] **Abot, J.L., Song, Y., Schulz, M.J. and Shanov, V.N.** Novel carbon nanotube array-reinforced laminated composite materials with higher interlaminar elastic properties. *Composites Science and Technology*, 2008, **68**, 2755-2760.

[116] **Thostenson, E.T., Li, W.Z., Wang, D.Z., Ren, Z.F. and Chou, T.W.** Carbon nanotubes/carbon fibre hybrid multiscale composites. *Journal of Applied Physics*, 2002, **91**(9), 6034-6037.

[117] **Yasmin, A., Luo, J.J., Abot, J.L. and Daniel, I.M.** Mechanical and thermal behavior of clay/epoxy nanocomposites. *Composites Science and Technology*, 2006, **66**, 2415–2422.

[118] **Liu, W., Hoa, S.V. and Pugh, M.** Organoclay-modified high performance epoxy nanocomposites. *Composites Science and Technology*, 2005, **65**, 307-316.

[119] **Tsai, J.L., Kuo, J.C. and Hsu, S.M.** Organoclay effect on transverse compressive strength of glass/epoxy nanocomposites. *Journal of Materials Science*, 2006, **41**, 7406-7412.

[120] **Xidas, P.I. and Triantafyllidis, K.S.** Effect of the type of alkylammonium ion clay modifier on the structure and thermal/mechanical properties of glassy and rubbery epoxy-clay nanocomposites. *European Polymer Journal*, 2010, **46**, 404-417.

[121] **Kinloch, A.J. and Taylor, A.C.** The mechanical properties and fracture behaviour of epoxy-inorganic micro- and nano-composites. *Journal of Materials Science*, 2006, **41**, 3271-3297.

[122] **Haque, A., Shamsuzzoha, M., Hussain, F. and Dean, D.** S2-Glass/Epoxy Polymer Nanocomposites: Manufacturing, Structures, Thermal and Mechanical Properties. *Journal of Composite Materials*, 2003, **37**(20), 1821-1837.

[123] **Lin, L.-Y., Lee, J.-H., Hong, C.-E., Yoo, G.-H. and Advani, S.G.** Preparation and characterization of layered silicate/glass fiber/epoxy hybrid nanocomposites via

vacuum-assisted resin transfer molding (VARTM). *Composites Science and Technology*, 2006, **66**(13), 2116-2125.

[124] **Subramaniyan, A.K. and Sun, C.T.** Enhancing compressive strength of unidirectional polymeric composites using nanoclay. *Composites Part A: Applied Science and Manufacturing*, 2006, **37**(12), 2257-2268.

[125] **Subramaniyan, A.K. and Sun, C.T.** Interlaminar Fracture Behavior of Nanoclay Reinforced Glass Fiber Composites. *Journal of Composite Materials*, 2008, **42**(20), 2111-2122.

[126] **Tsai, J.-L., Kuo, J.-C. and Hsu, S.-M.** Organoclay effect on transverse compressive strength of glass/epoxy nanocomposites. *Journal of Materials Science*, 2006, **41**(22), 7406-7412.

[127] **Kornmann, X., Rees, M., Thomann, Y., Necola, A., Barbezat, M. and Thomann, R.** Epoxy-layered silicate nanocomposites as matrix in glass fibre-reinforced composites. *Composites Science and Technology*, 2005, **65**(14), 2259-2268.

[128] **Hamidi, Y.K., Aktas, L. and Altan, M.C.** Effect of Nanoclay Content on Void Morphology in Resin Transfer Molded Composites. *Journal of Thermoplastic Composite Materials*, 2008, **21**(2), 141-163.

[129] **Bozkurt, E., Kaya, E. and Tanoglu, M.** Mechanical and thermal behavior of non-crimp glass fiber reinforced layered clay/epoxy nanocomposites. *Composites Science and Technology*, 2007, **67**(15-16), 3394-3403.

[130] **Karaki, T., Killgore, J.P. and Seferis, J.C.** Characterization of fatigue behaviour of polynanomeric matrix composites. *Proceedings of the 49th Int. SAMPE symposium and exhibition* (Society for the Advancement of Material and Process Engineering, USA, 2004).

[131] **Timmerman, J.F., Hayes, B.S. and Seferis, J.C.** Nanoclay reinforcement effects on the cryogenic microcracking of carbon fibre/epoxy composites. *Composites Science and Technology*, 2002, **62**, 1249-1258.

[132] **Becker, O., Varley, R.J. and Simon, G.P.** Use of layered silicates to supplementarily toughen high performance epoxy-carbon fibre composites. *Journal of Materials Science*, 2003, **22**, 1411-1414.

[133] **Xu, Y. and Hoa, S.V.** Mechanical properties of carbon fiber reinforced epoxy/clay nanocomposites. *Composites Science and Technology*, 2008, **68**(3-4), 854-861.

[134] **Dean, D., Obore, A.M., Richmond, S. and Nyairo, E.** Multiscale fiber-reinforced nanocomposites: Synthesis, processing and properties. *Composites Science and Technology*, 2006, **66**(13), 2135-2142.

[135] **Chowdhury, F.H., Hosur, M.V. and Jeelani, S.** Studies on the flexural and thermomechanical properties of woven carbon/nanoclay-epoxy laminates. *Materials Science and Engineering: A*, 2006, **421**(1-2), 298-306.

[136] **Hosur, M.V., Islam, M.M. and Jeelani, S.** Processing and performance of nanophased braided carbon/epoxy composites. *Materials Science and Engineering: B*, 2010, **168**(1-3), 22-29.

[137] **Hosur, M.V., Chowdhury, F. and Jeelani, S.** Low-velocity impact response and ultrasonic NDE of woven carbon/epoxy-nanoclay nanocomposites. *Journal of Composite Materials*, 2007, **41**(18), 2195-2212.

[138] **Chowdhury, F., Hosur, M. and Jeelani, S.** Investigations on the thermal and flexural properties of plain weave carbon/epoxy-nanoclay composites by hand-layup technique. *Journal of Materials Science*, 2007, **42**(8), 2690-2700.

[139] **Zhou, Y., Pervin, F., Rangari, V.K. and Jeelani, S.** Influence of montmorillonite clay on the thermal and mechanical properties of conventional carbon fiber reinforced composites. *Journal of Materials Processing Technology*, 2007, **191**(1-3), 347-351.

[140] **Siddiqui, N.A., Woo, R.S.C., Kim, J.-K., Leung, C.C.K. and Munir, A.** Mode I interlaminar fracture behavior and mechanical properties of CFRPs with nanoclay-filled epoxy matrix. *Composites Part A: Applied Science and Manufacturing*, 2007, **38**(2), 449-460.

[141] **Khan, S.U., Iqbal, K., Munir, A. and Kim, J.-K.** Quasi-static and impact fracture behaviors of CFRPs with nanoclay-filled epoxy matrix. *Composites Part A: Applied Science and Manufacturing*, **42**(3), 253-264.

[142] **Khan, S.U., Munir, A., Hussain, R. and Kim, J.-K.** Fatigue damage behaviors of carbon fiber-reinforced epoxy composites containing nanoclay. *Composites Science and Technology*, **70**(14), 2077-2085.

[143] **Iqbal, K., Khan, S.-U., Munir, A. and Kim, J.-K.** Impact damage resistance of CFRP with nanoclay-filled epoxy matrix. *Composites Science and Technology*, 2009, **69**(11-12), 1949-1957.

[144] **Sabo, J., Strait, L.H., Strauch, E.C., Koudela, K.L. and Giannetti, W.B.** Processing and characterization of thick laminated composites. *In: Composites Materials, Mechanics and Processing, Proceedings of the American Society for Composites*, pp. 574-586 (CRC Press, USA, 1994).

[145] **Pethrick, R.A., Hollins, E.A., McEwan, L., MacKinnon, A.J., Hayward, D., Cannon, I.A., Jenkins, S.D. and McGrail, P.T.** Dielectric, mechanical and structural, and water absorption properties of a thermoplastic-modified epoxy resin: poly(ether sulfone)–amine cured epoxy resin. *Macromolecules*, 1996, **29**(15), 5208-5214.

[146] **Di Pasquale, G., Motta, O. and Recca, A.** New high-performance thermoplastic toughened epoxy thermosets. *Polymer*, 1997, **38**(17), 4345-4348.

[147] **Akay, M. and Cracknell, J.G.** Epoxy resin-polyethersulphone blends. *Journal of Applied Polymer Science*, 1994, **52**(5), 663-688.

[148] ASTM Standard E1131. Standard test method for compositional analysis by thermogravimetry. *Book of Standards Volume 14.02*, pp. 394-398 (American Society for Testing and Materials (ASTM) International, USA, 1998).

[149] ASTM Standard D792. Standard test methods for density and specific gravity (relative density) of plastics by displacement. *Book of Standards Volume 08.01*, pp. 159-163 (ASTM International, USA, 1998).

[150] ASTM Standard D3171-99. Standard test methods for constituent content of composite materials. *ASTM Book of Standards Volume 15.03*, pp. 119-127 (ASTM International, USA, 1998).

[151] British Standard ISO 11359-2:1999. Plastics–thermomechanical analysis (TMA)–Part 2: Determination of coefficient of linear thermal expansion and glass transition temperature.

[152] British Standard ISO 11357-2:1999. Plastic–Differencial scanning calorimetry (DSC)–Part 1: Determination of glass transition temperature.

[153] **Yurgartis, S.W.** Measurement of small angle fiber misalignments in continuous fiber composites. *Composites Science and Technology*, 1987, **30**, 279-293.

[154] **Behzadi, S. and Jones, F.R.** The effect of temperature on stress transfer between a broken fibre and the adjacent fibres in unidirectional fibre composites. *Composites Science and Technology*, 2008, **68**, 2690-2696.

[155] ASTM Standard D695-96. Standard test method for compressive properties of rigid plastics. *Book of Standards Volume 8.01*, pp. 78-84. (ASTM International, USA, 1998).

[156] **Kalidindi, S.R., Abusafieh, A. and EI-Danaf, E.** Accurate Characterization of Machine Compliance for Simple Compression Testing. *Experimental Mechanics*, 1997, **37**(2), 210-215.

[157] British Standard ISO 604:2003. Plastics–Determination of compressive properties.

[158] British Standard BS EN ISO 527-1 and -2:1996. Plastics–Determination of tensile properties – Part 1: General principles and – Part 2: test conditions for moulding and extrusion plastics.

[159] British Standard BS EN ISO 178:2003. Plastics–Determination of flexural properties.

[160] British Standard BS EN ISO 13586:2000. Plastics–Determination of fracture toughness (G_{IC} and K_{IC}) – Linear elastic fracture mechanics (LEFM) approach.

[161] **Soutis, C.** Compression testing of pultruded carbon fiber-epoxy cylindrical rods. *Journal of Material Science*, 2000, **35**(14), 3441-3446.

[162] **Xie, M. and Adams, D.F.** Effect of Loading Method on Compression Testing of Composite Materials. *Journal of Composite Materials*, 1995, **29**(12), 1581-1600.

[163] **Lee, J. and Soutis, C.** A study on the compressive strength of thick carbon fibre–epoxy laminates. *Composites Science and Technology*, 2007, **67**, 2015-2026.

[164] ASTM Standard D3410/D3410M-95. Standard test method for compressive properties of polymer matrix composite materials with unsupported gage section by shear loading. *Book of Standards Volume 15.03*, pp. 129-144 (ASTM International, USA, 1998).

[165] **Lee, J.H.** *Compressive behaviour of composite laminates before and after low velocity impact.* (University of London, PhD thesis, 2003).

[166] **Curtis, P.T.** CRAG test methods for the measurement of the engineering properties of fibre reinforced plastics. *Royal Aircraft Establishment (RAE) Technical Report 85099* (Defence Evaluation Research Agency, Farnborough UK, 1985).

[167] ASTM Standard D3518/D3518M-94. Standard test method for in-plane shear response of polymer matrix composite materials by tensile test of a ±45° laminate. *Book of Standards Volume 15.03*, pp. 152-157 (ASTM International, USA, 1998).

[168] ASTM Standard D3039/D3039M-00. Standard test method for tensile properties of polymer matrix composite materials. *Book of Standards Volume 15.03*, pp. 106-117 (ASTM International, USA, 1998).

[169] **Ahmed, S. and Jones, F.R.** A review of particulate reinforcement theories for polymer composites. *Journal of Materials Science*, 1990, **25**, 4933-4942.

[170] **Hill, R.** Theory of mechanical properties of fibre-strengthened materials: I. Elastic behaviour. *Journal of the Mechanics and Physics of Solids*, 1964, **12**(4), 199-212.

[171] **Halpin, J.C. and Kardos, J.L.** The Halpin-Tsai equations: a review. *Polymer Engineering and Science*, 1976, **16**(5), 344-352.

[172] **Nielsen, L.E.** Mechanical properties of particulate-filled systems. *Journal of composite materials*, 1967, **1**, 100-119.

[173] **Van Es, M., Xiqiao, F., Van Turnhout, J. and Van der Giessen, E.** *Specialty Polymer Additives: Principles and Applications*. Editors: Al-Malaika, S., Golovoy, A. and Wilkie, C.A. (Blackwell Science, 2001).

[174] **Fornes, T.D. and Paul, D.R.** Modeling properties of nylon 6/clay nanocomposites using composite theories. *Polymer*, 2003, **44**, 4993–5013.

[175] **Luo, J.J. and Daniel, I.M.** Characterization and modeling of mechanical behaviour of polymer/clay nanocomposites. *Composites Science and Technology*, 2003, **63**, 1607–1616.

[176] **Halpin, J.C. and Pagano, N.J.** The laminate approximation for randomly oriented fibrous composites. *Journal of Composite Materials*, 1969, **3**, 720-724.

[177] **Mori, T. and Tanaka, K.** Average stress in matrix and average elastic energy of materials with misfitting inclusions. *Acta Metallurgica*, 1973, **21**(5), 571-574.

[178] **Wang, J. and Pyrz, R.** Prediction of the overall moduli of layered silicate-reinforced nanocomposites-part I: basic theory and formulas. *Composites Science and Technology*, 2004, **64**, 925-934.

[179] **Hull, D.** *An Introduction to Composite Materials*. (Cambridge University Press, 1981).

[180] **Jochum, Ch., Grandidier, J.C. and Smaali, M.A.** Experimental study of long T300 carbon fibre undulations during the curing of LY556 epoxy resin. *Composites Science and Technology*, 2007, **67**, 2633-2642.

[181] **Agag, T., Koga, T. and Takeichi, T.** Studies on thermal and mechanical properties of polyimide-clay nanocomposites. *Polymer*, 2001, **42**, 3399-3408.

[182] **Liu, T., Tjiu, W.C., Tong, Y., He, C., Goh, S.S. and Chung, T.S.** Morphology and fracture behaviour of intercalated epoxy/clay nanocomposites. *Journal of Applied Polymer Science*, 2004, **94**, 1236-1244.

[183] **Wang, K., Chen, L., Wu, J., Toh, M.L., He, C. and Yee, A.F.** Epoxy nanocomposites with highly exfoliated clay: mechanical properties and fracture mechanisms. *Macromolecules*, 2005, **38**, 788-800.

[184] **Lee, J. and Soutis, C.** Thickness effect on the compressive strength of T800/924C carbon fibre-epoxy laminates. *Composites Part A: Applied Science and Manufacturing*, 2005, **36**, 213-227.

Appendix A: Mechanical test results of nanomodified-epoxy polymers

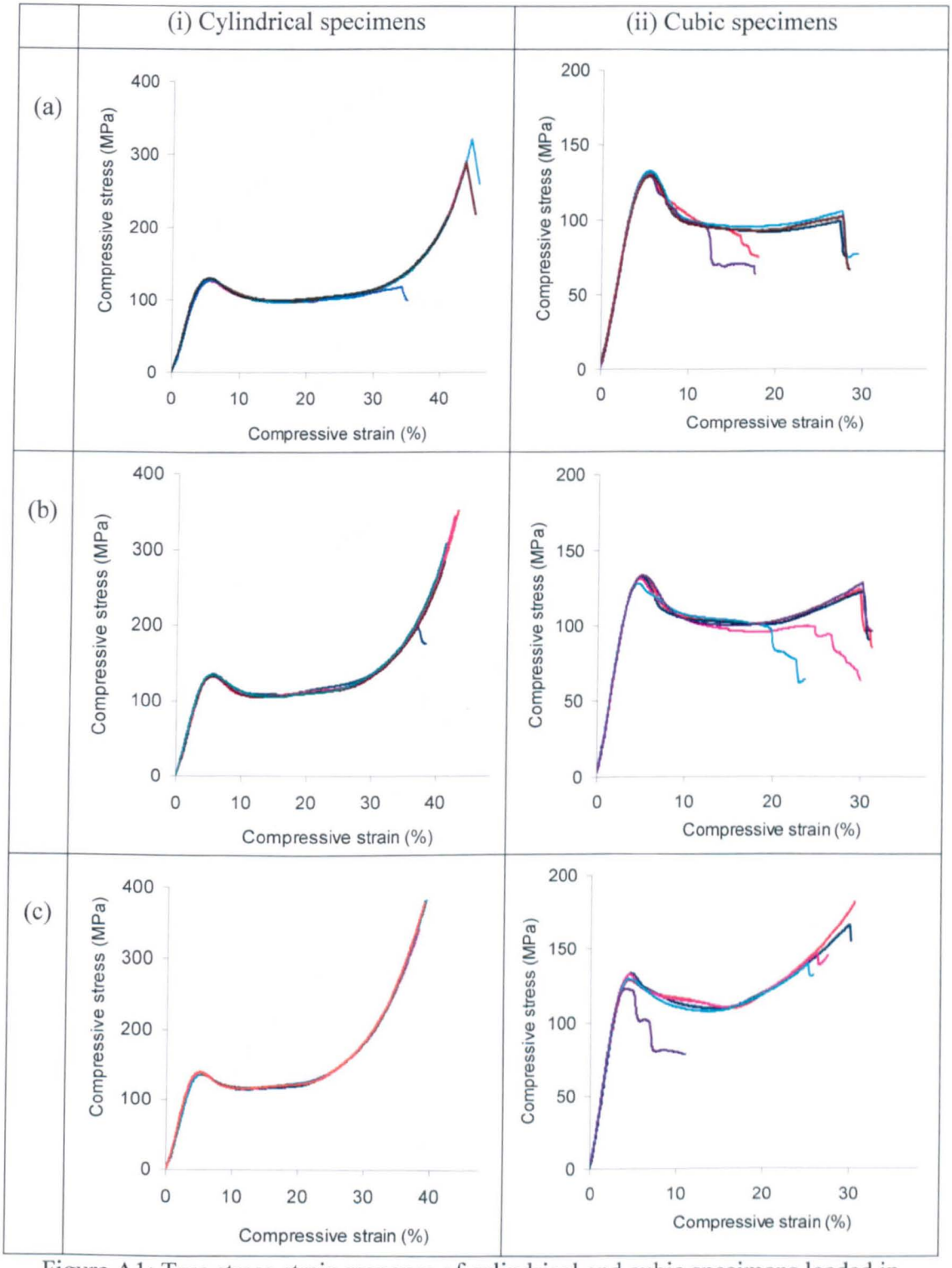

Figure A1: True stress-strain response of cylindrical and cubic specimens loaded in compression for three different systems; (a) 5 wt%, (b) 13 wt% and (c) 25 wt% nanosilica-filled Epikote 828. Five specimens were tested for each system.

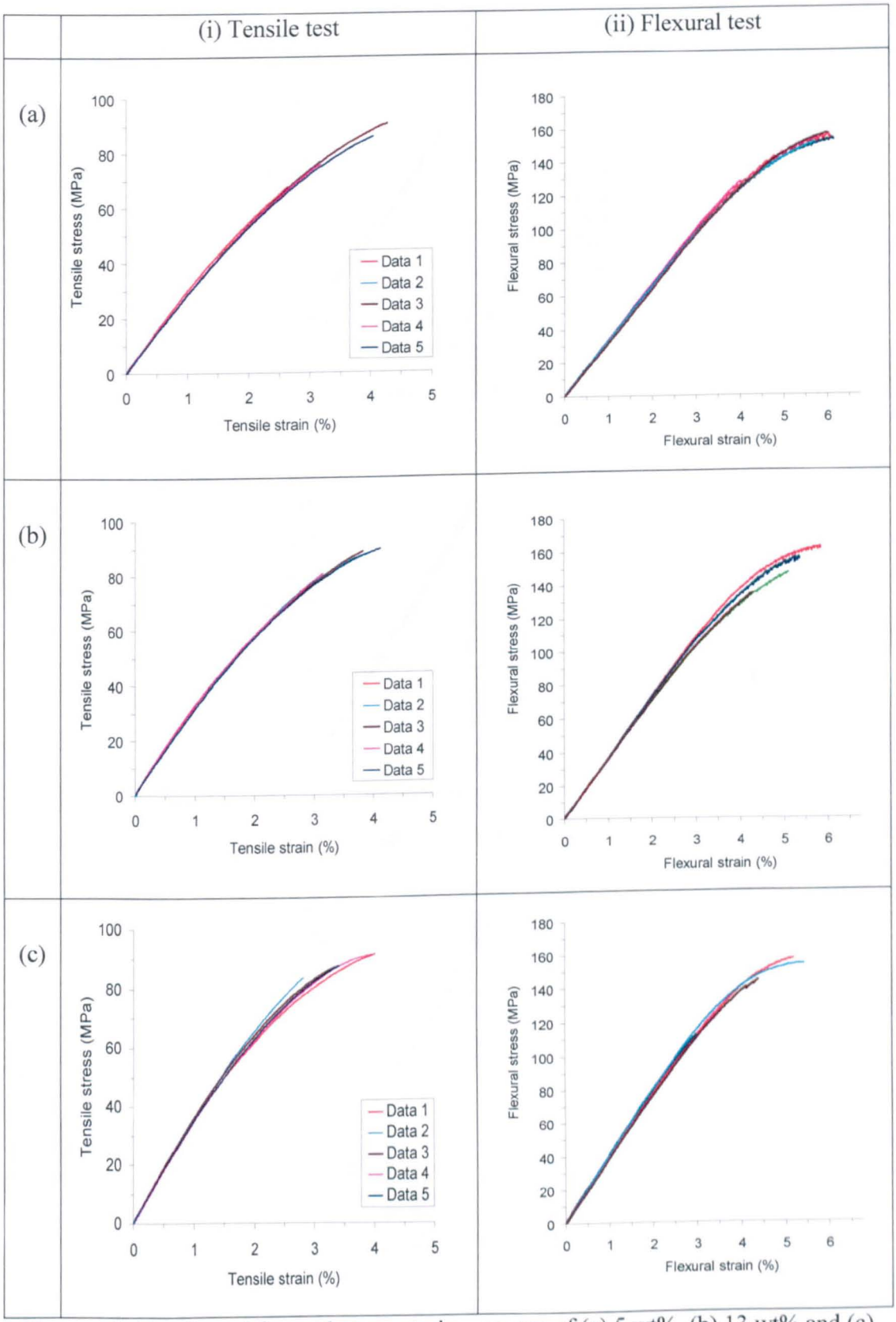

Figure A2: Tensile and flexural stress-strain response of (a) 5 wt%, (b) 13 wt% and (c) 25 wt% nanosilica-filled Epikote 828. Five specimens were tested for each system.

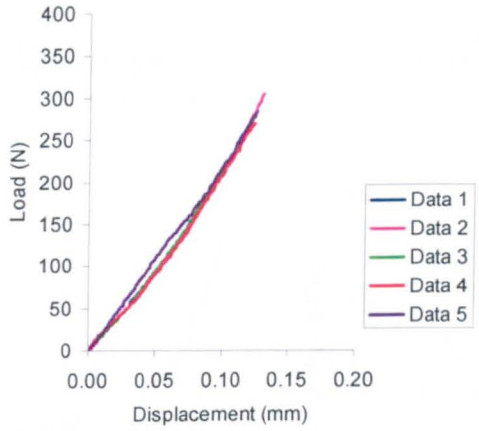

(a) 5 wt% si

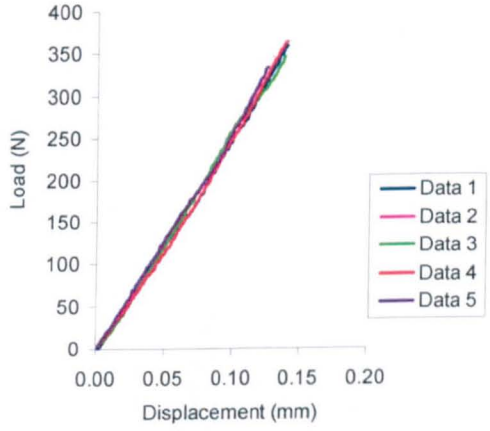

(b) 13 wt% si

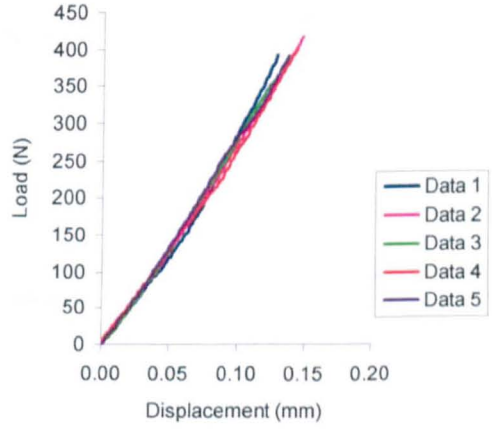

(c) 25 wt% si

Figure A3: Load-displacement curves of compact-tension specimens loaded in tension for three different systems; (a) 5 wt%, (b) 13 wt% and (c) 25 wt% nanosilica-filled Epikote 828 for the measurement of fracture toughness.

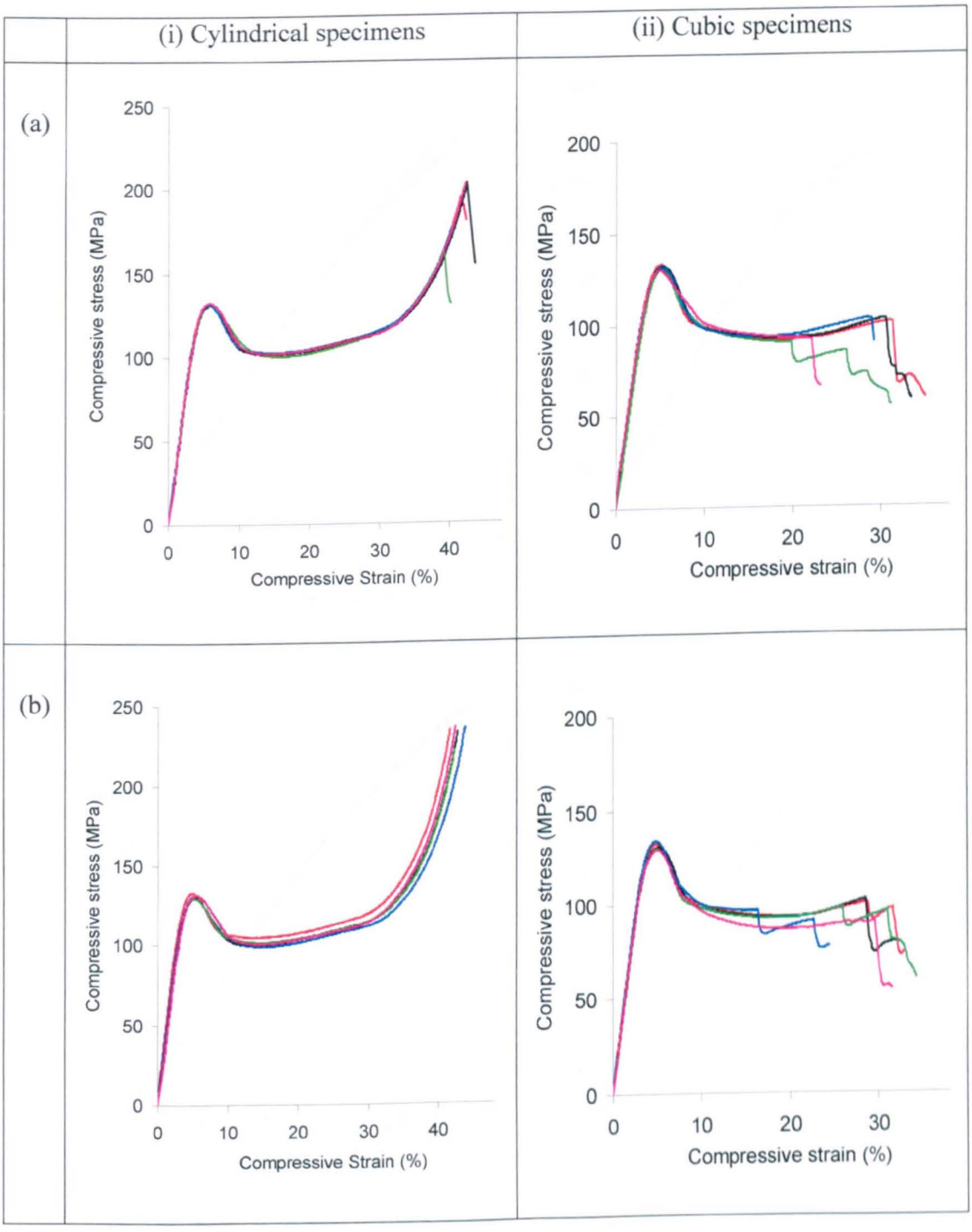

Figure A4: True stress-strain response of cylindrical and cubic specimens loaded in compression for two different systems; (a) 0.5 wt% and (b) 1 wt% multiwalled CNT-filled Epikote 828. Five specimens were tested for each system.

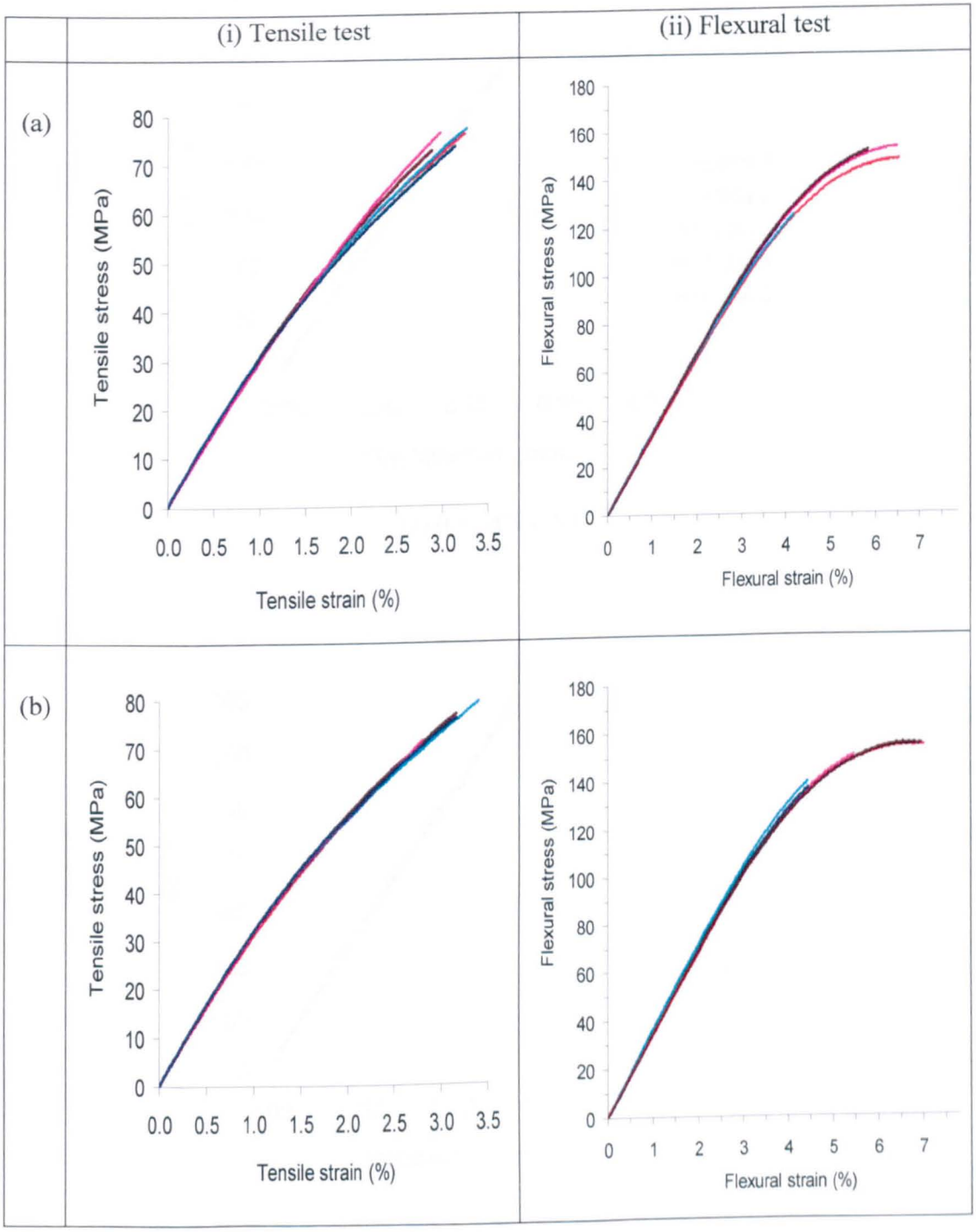

Figure A5: Tensile and flexural stress-strain response of (a) 0.5 wt% and (b) 1 wt% multiwalled CNT-filled Epikote 828. Five specimens were tested for each system.

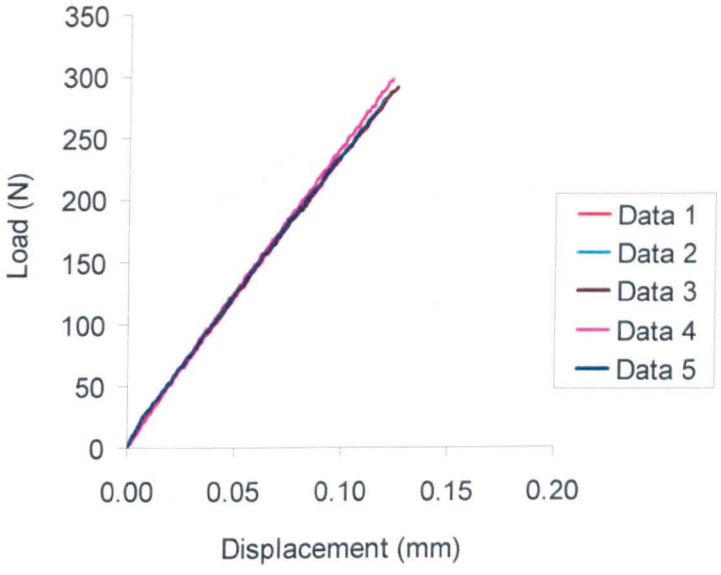

(a) 0.5 wt% CNT

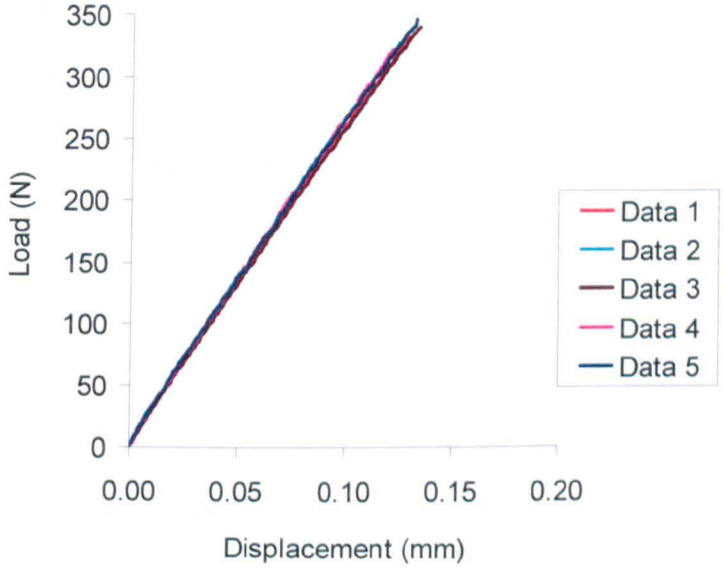

(b) 1 wt% CNT

Figure A6: Load-displacement curves of compact-tension specimens loaded in tension for two different systems; (a) 0.5 wt% and (b) 1 wt% multiwalled CNT-filled Epikote 828 for the measurement of fracture toughness.

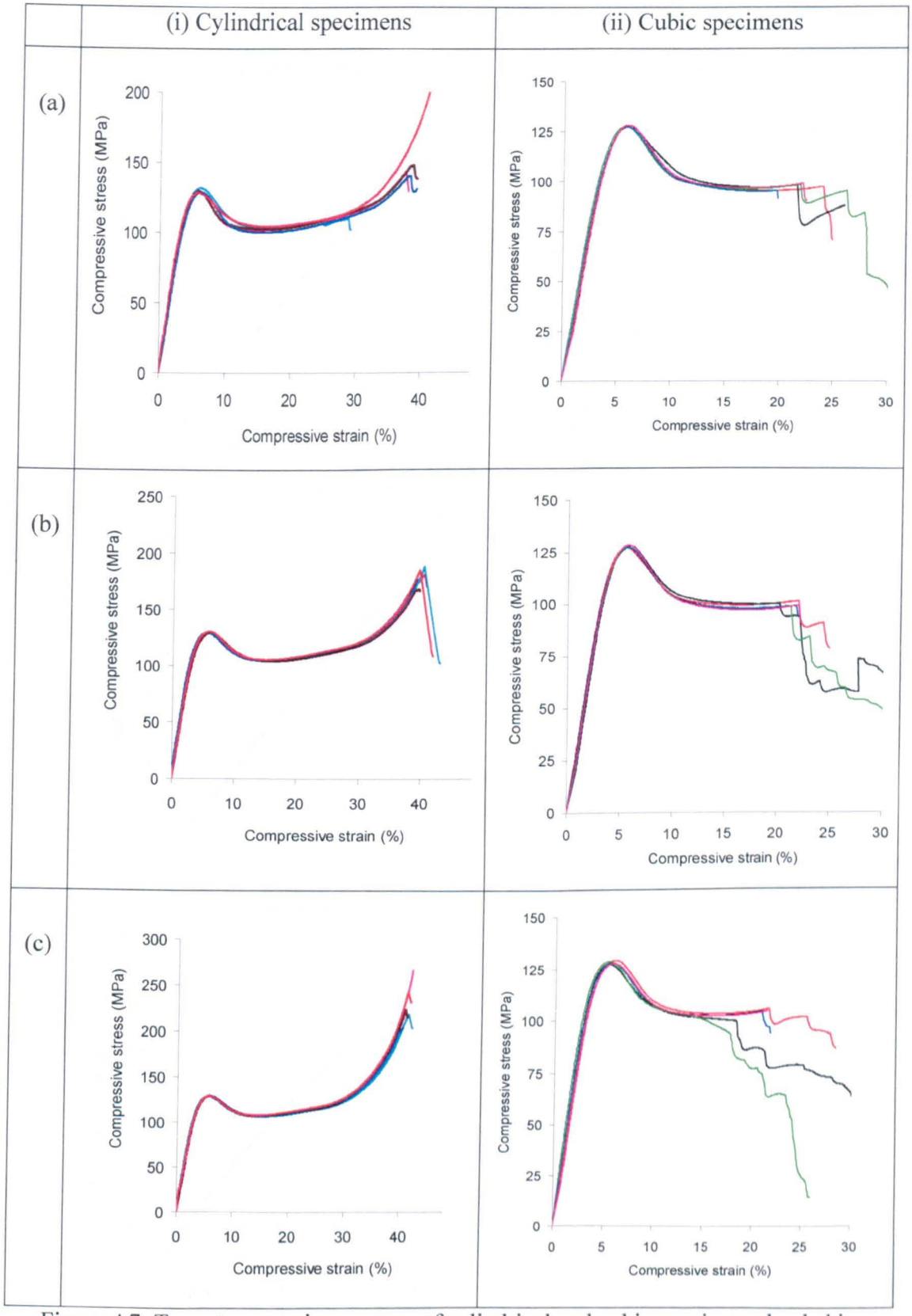

Figure A7: True stress-strain response of cylindrical and cubic specimens loaded in compression for three different systems; (a) 1 wt%, (b) 3 wt% and (c) 5 wt% I.28 nanoclay-filled Epikote 828. Five specimens were tested for each system.

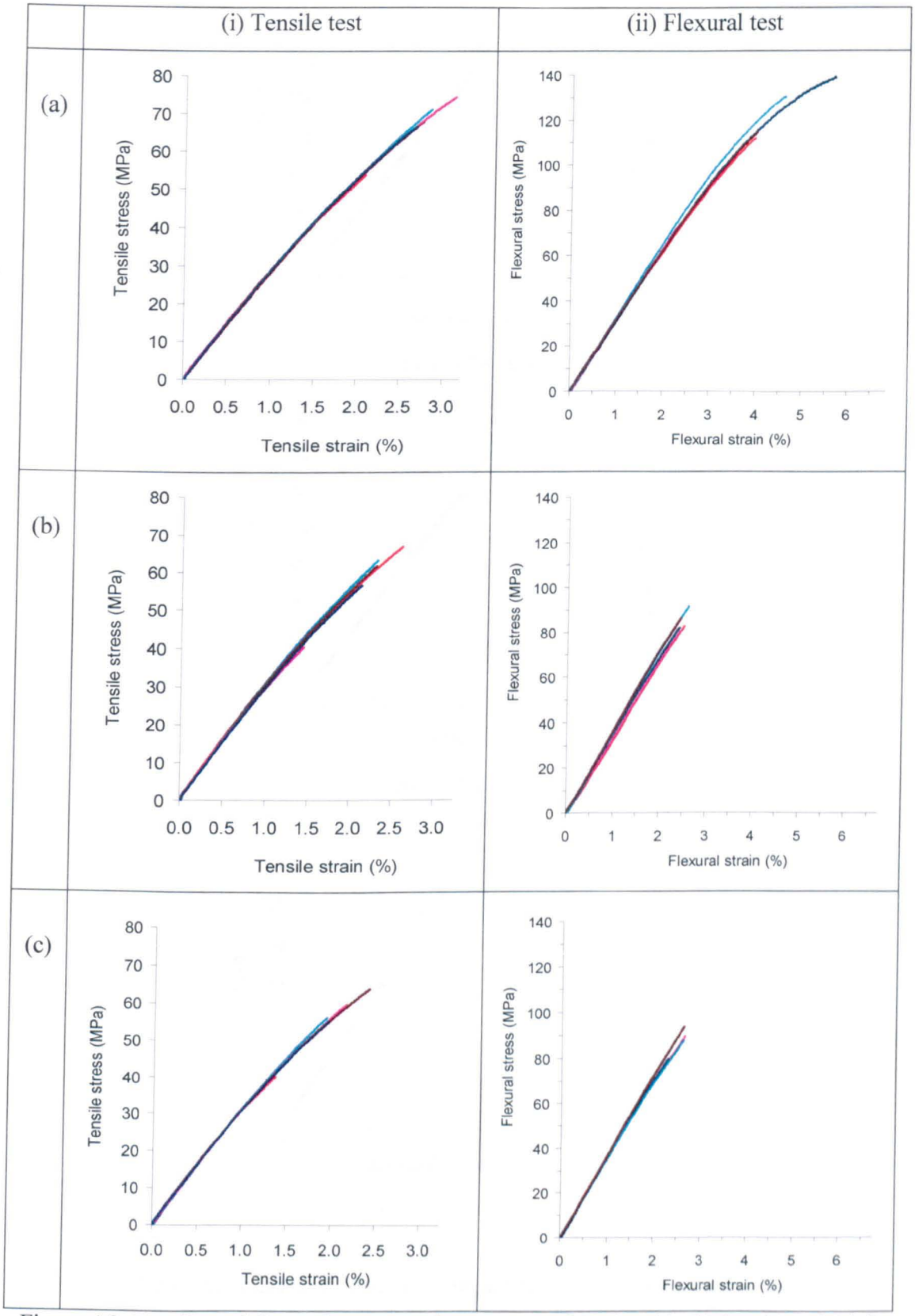

Figure A8: Tensile and flexural stress-strain response of (a) 1 wt%, (b) 3 wt% and (c) 5 wt% I.28 nanoclay-filled Epikote 828. Five specimens were tested for each system.

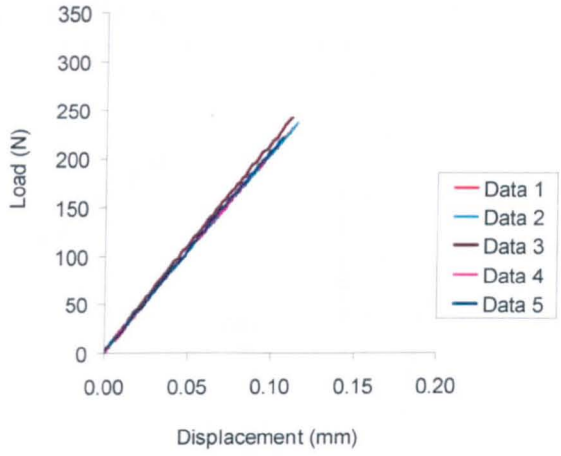

(a) 1 wt% clay

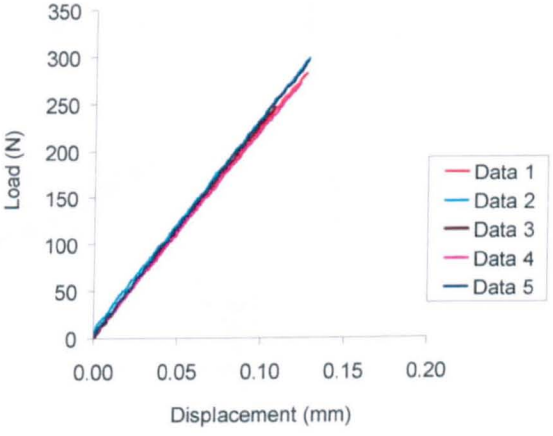

(b) 3 wt% clay

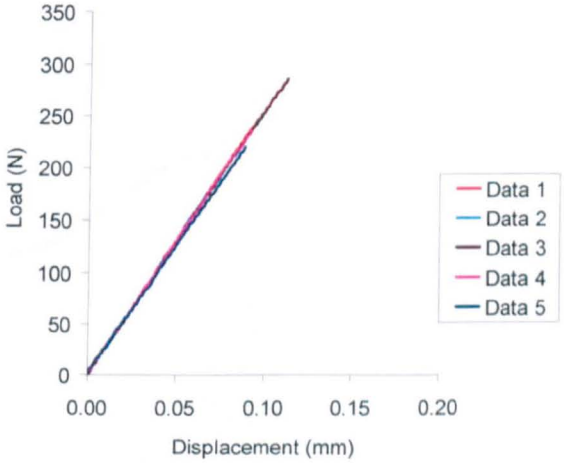

(c) 5 wt% clay

Figure A9: Load-displacement curves of compact-tension specimens loaded in tension for three different systems; (a) 1 wt%, (b) 3 wt% and (c) 5 wt% I.28 nanoclay-filled Epikote 828 for the measurement of fracture toughness.

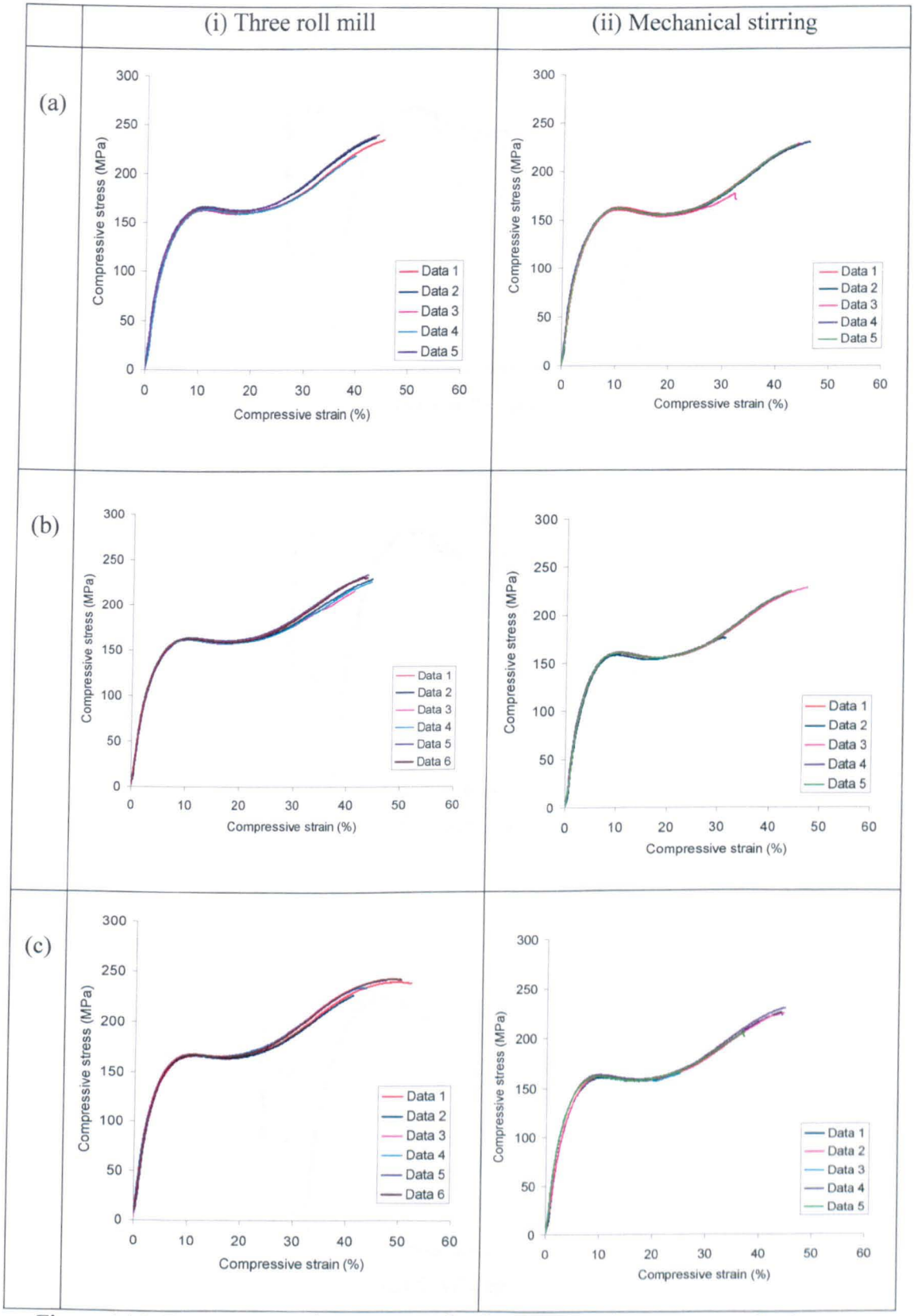

Figure A10: True stress-strain response of cylindrical specimens prepared using two different methods, (i) 3-roll mill and (ii) mechanical stirring, loaded in compression for three different systems (a) 1 wt%, (b) 3 wt% and (c) 5 wt% I.30 nanoclay/977-20.

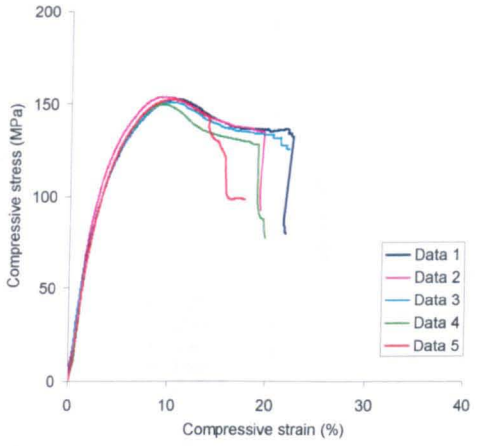

(a) 1 wt% clay

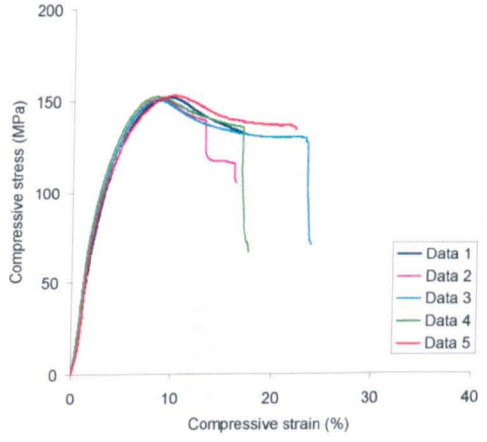

(b) 3 wt% clay

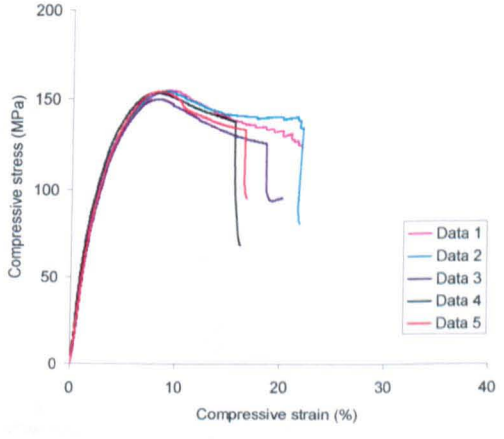

(c) 5 wt% clay

Figure A11: True stress-strain response of cubic specimens loaded in compression for three different systems (a) 1 wt%, (b) 3 wt% and (c) 5 wt% I.30 nanoclay-filled Cycom 977-20

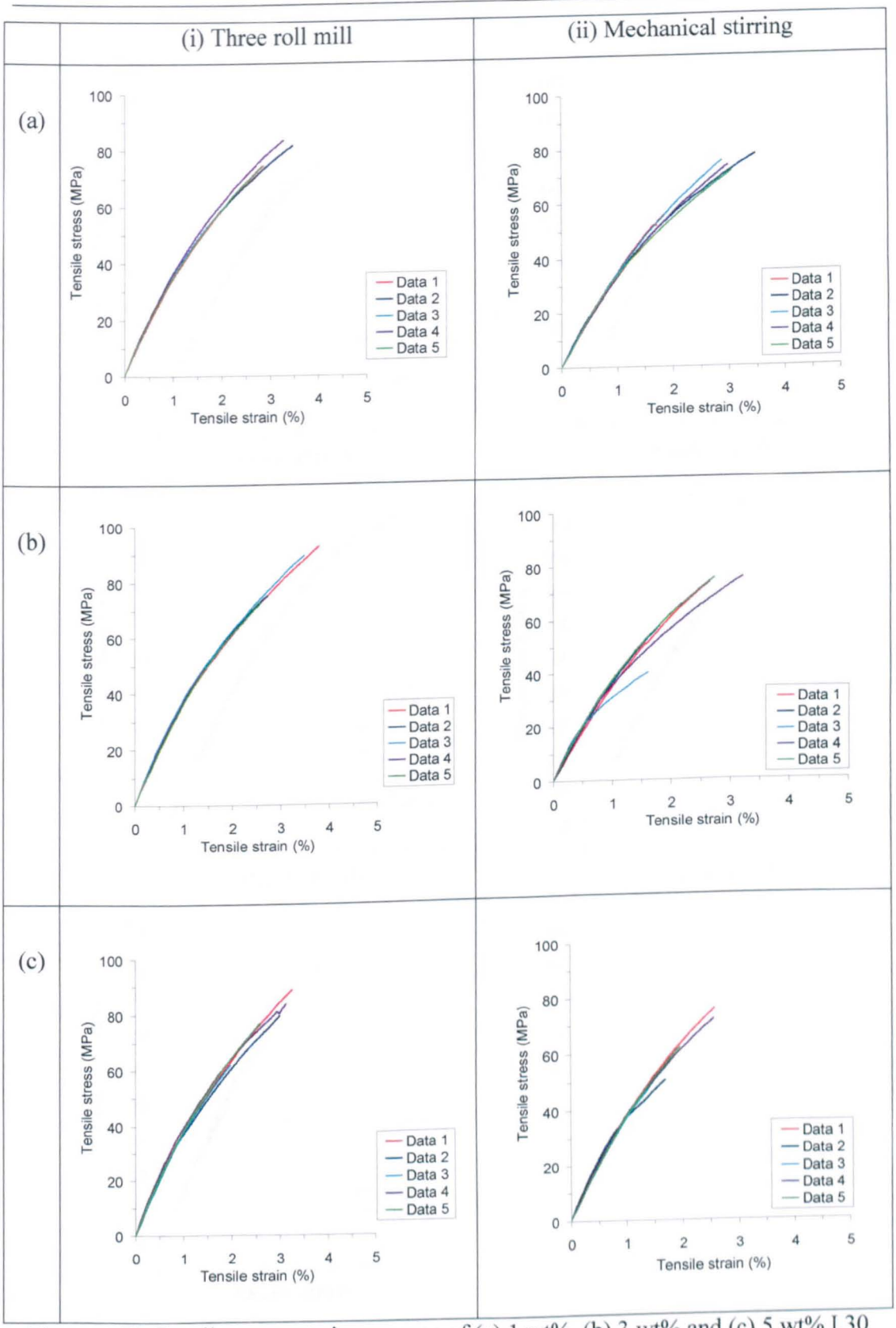

Figure A12: Tensile stress-strain response of (a) 1 wt%, (b) 3 wt% and (c) 5 wt% I.30 nanoclay-filled Cycom 977-20 which were prepared using two different methods; (i) 3-roll mill and (ii) mechanical stirring.

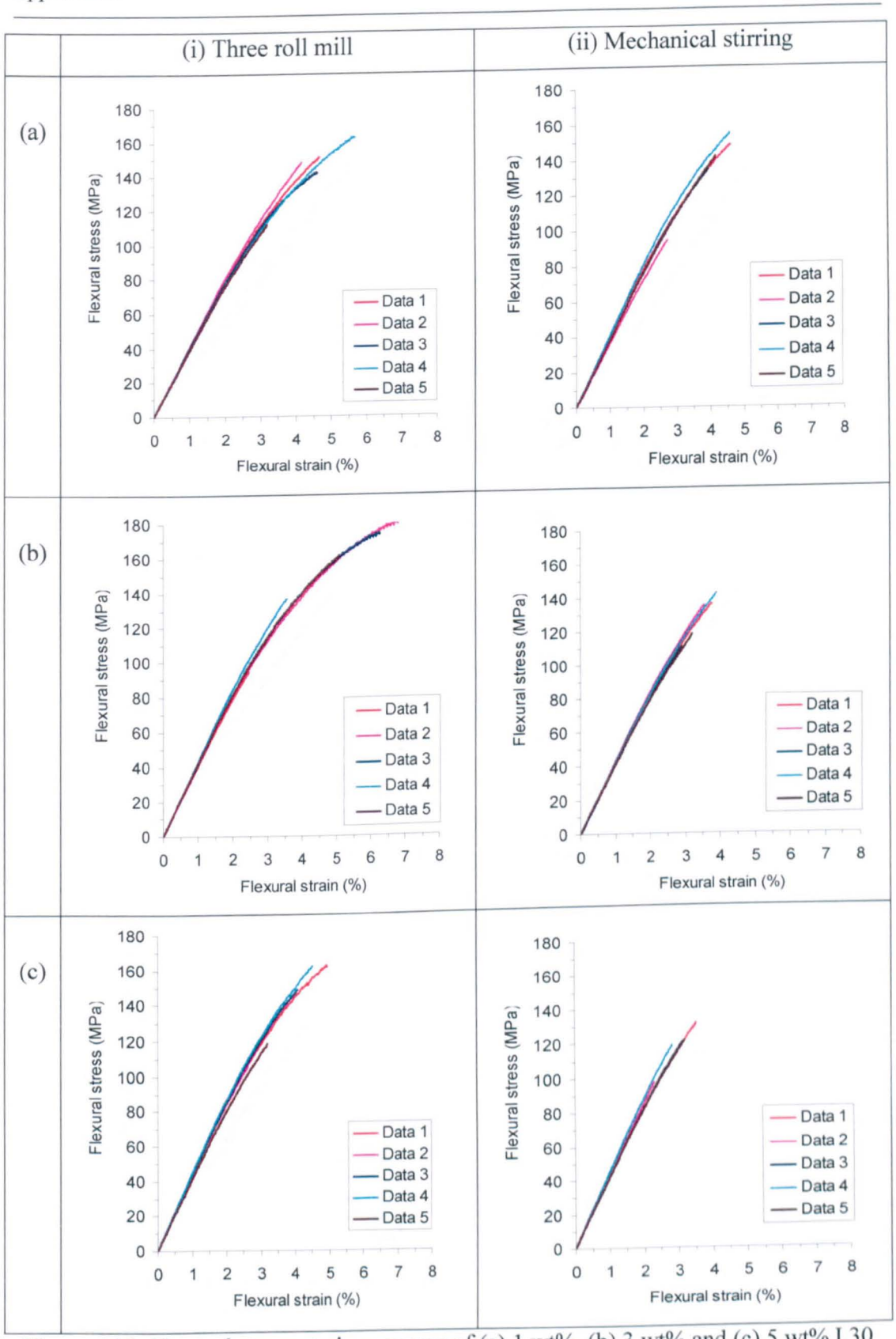

Figure A13: Flexural stress-strain response of (a) 1 wt%, (b) 3 wt% and (c) 5 wt% I.30 nanoclay-filled Cycom 977-20 which were prepared using two different methods; (i) 3-roll mill and (ii) mechanical stirring.

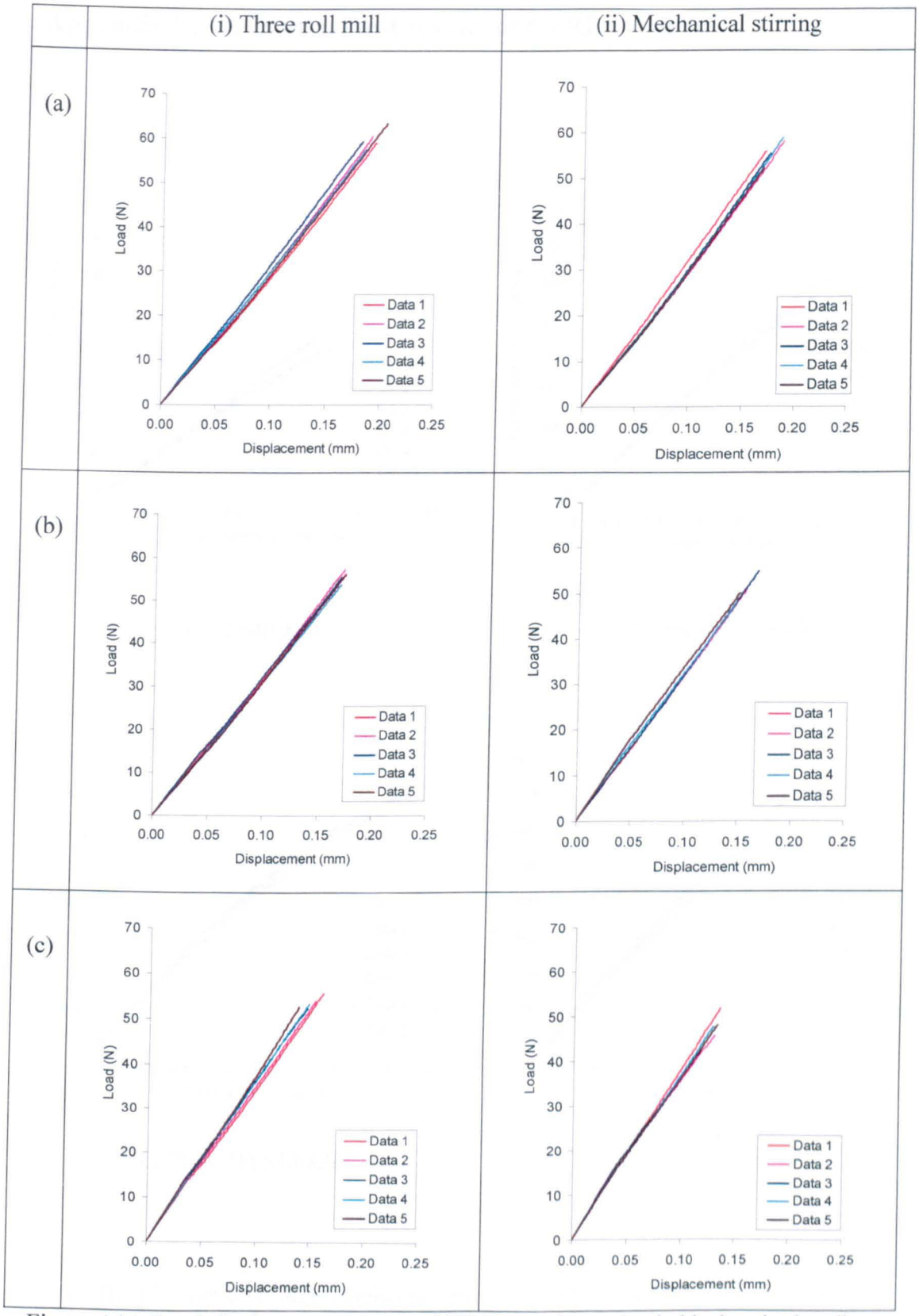

Figure A14: Load-displacement curves of SENB specimens loaded in 3-point bending for three different systems; (a) 1 wt%, (b) 3 wt% and (c) 5 wt% I.30 nanoclay-filled Cycom 977-20 which were prepared using (i) 3-roll mill and (ii) mechanical stirring.

Appendix B: Mechanical test results of CFRP composites

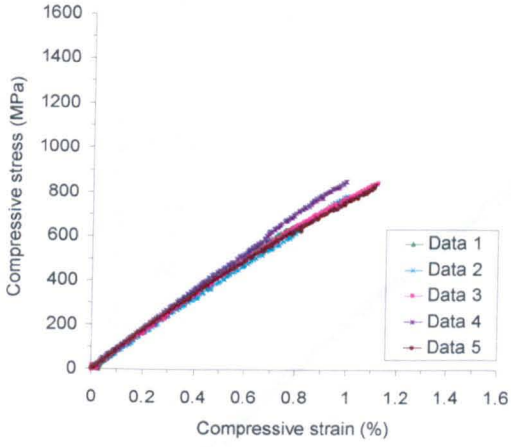

(a) HTS40/828

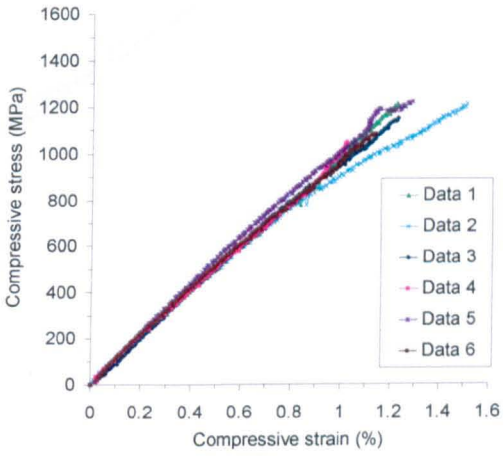

(b) 3%si/ HTS40/828

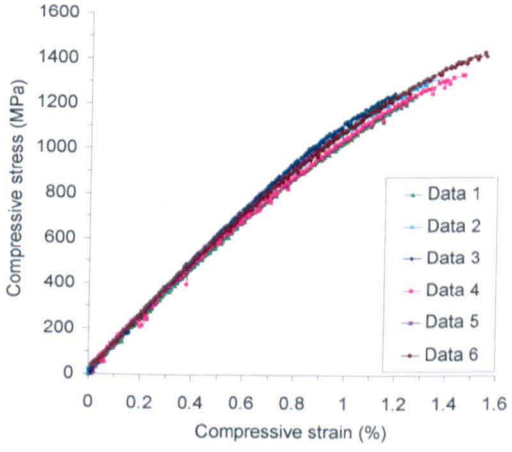

(c) 7%si/ HTS40/828

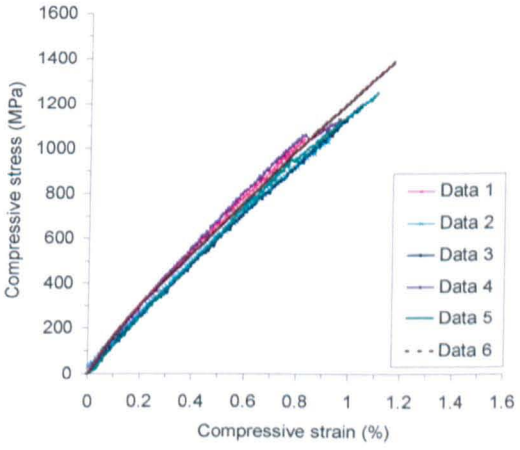

(d) 13%si/ HTS40/828

Figure B1: Compressive stress-strain response of (a) HTS40/828 CFRP composite and its nanomodified system with three different nanosilica contents: (b) 3 vol%, (c) 7 vol% and (d) 13 vol%.

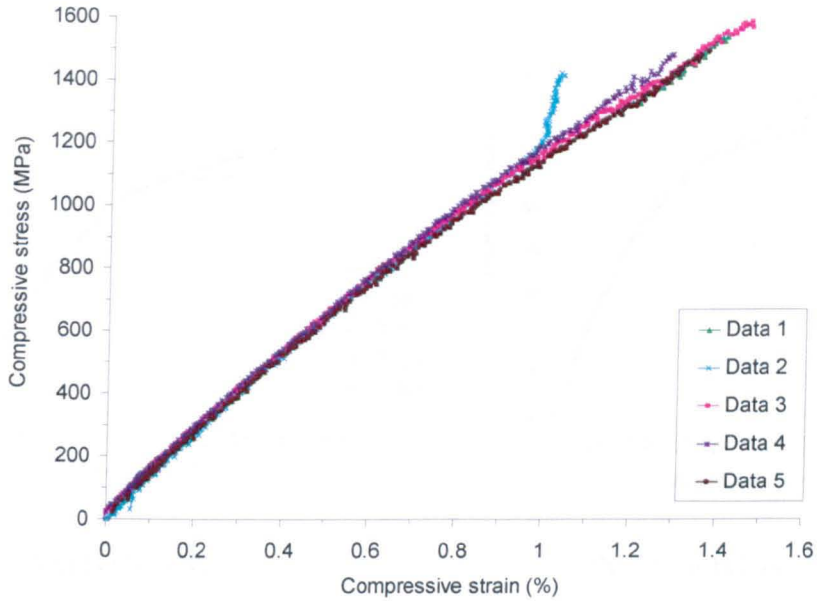

Figure B2: Compressive stress-strain response of HTS40/977-2 CFRP composite which was fabricated using Autoclave.

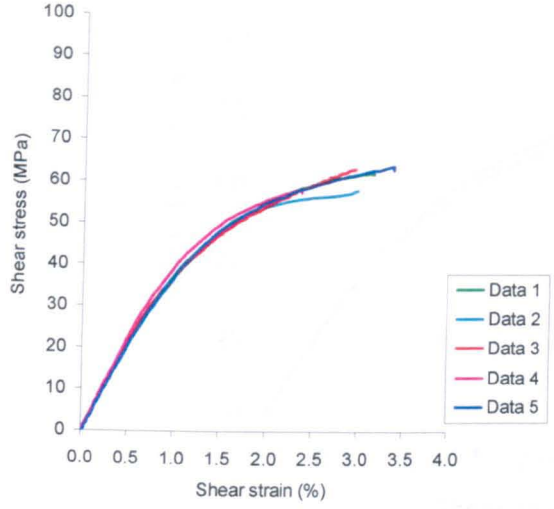

(a) HTS40/828

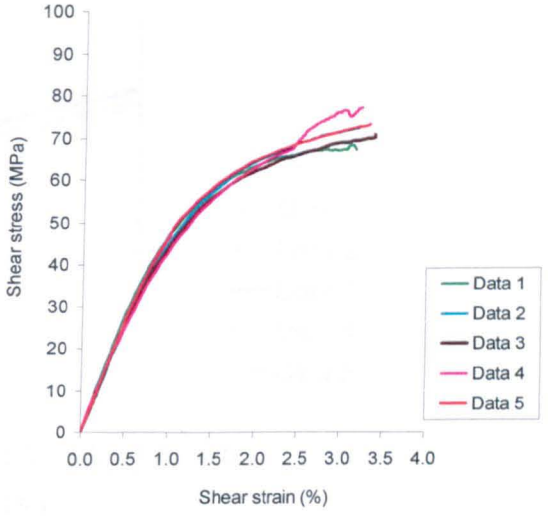

(b) 3%si/ HTS40/828

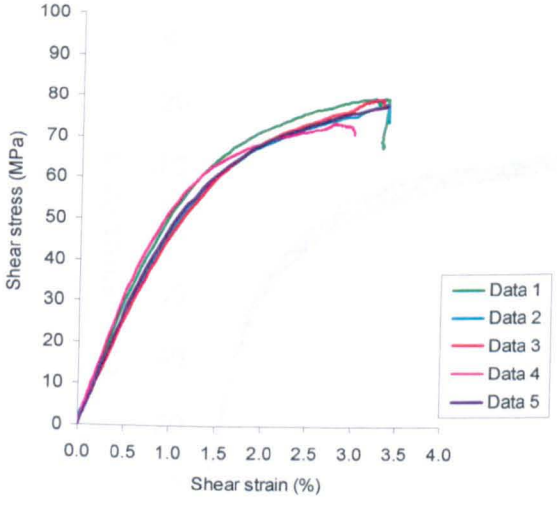

(c) 7%si/ HTS40/828

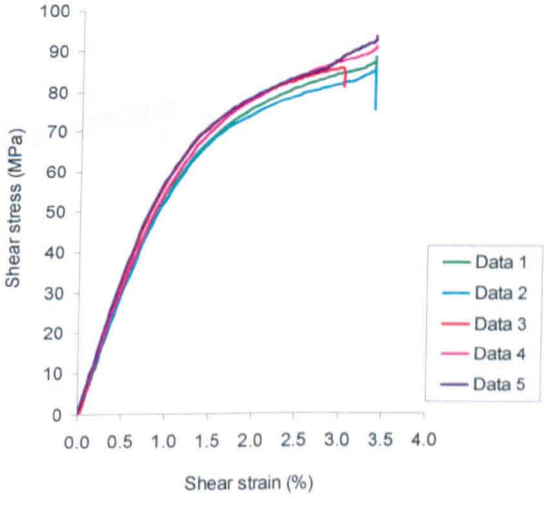

(d) 13%si/ HTS40/828

Figure B3: In plane shear stress-strain response of (a) HTS40/828 CFRP composite and its nanomodified system with three different nanosilica contents: (b) 3 vol%, (c) 7 vol% and (d) 13 vol%.

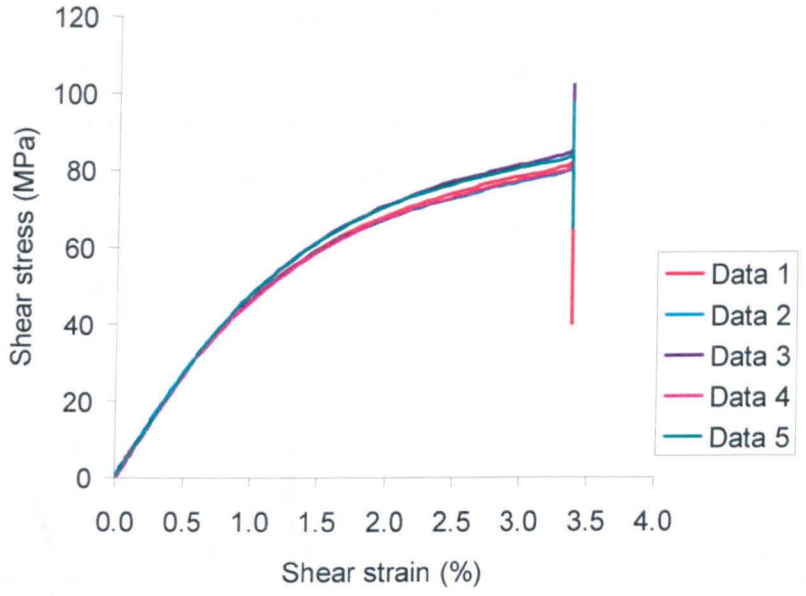

(a)

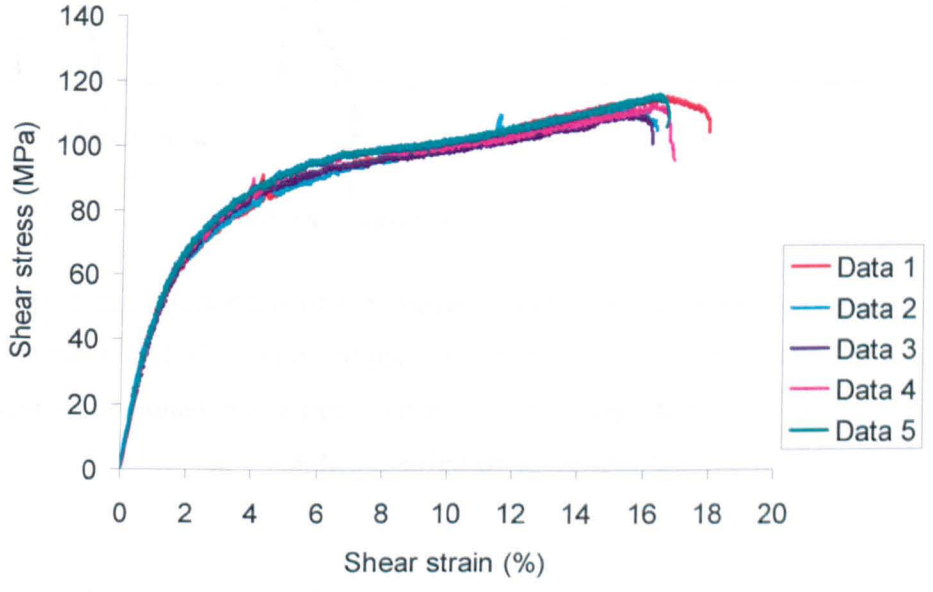

(b)

Figure B4: In-plane shear stress-strain response of HTS40/977-2 CFRP composite with two different gauge lengths: (a) 50 mm and (b) 100 mm.

Appendix C: Berbinau's Fibre Microbuckling Model [46]

The fibre microbuckling model was developed by Berbinau *et al.* [46] based on the assumption of fibre acts as an Euler slender column supported by a non-linear matrix. Based on the fact that carbon fibres in the 0^{o} UD laminates are not perfectly aligned with the loading direction, (up to 5^{o} fibre misalignment; mainly due to the thermal mismatch), therefore Berbinau *et al.* [46] modelled the initial fibre waviness by a sin function $v_0(x)$ as shown in Figure C1a.

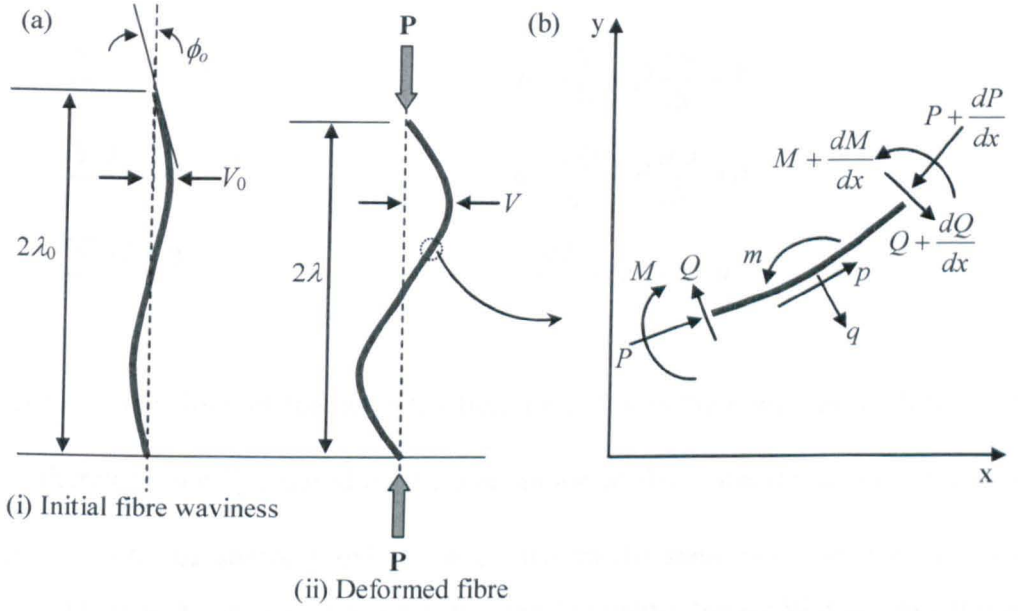

Figure C1: (a) A schematic of fibre microbuckling [46] (b) Free body diagram for a fibre element [53]. P = Axial compressive force, Q = Transverse shear, M = Bending moment, p = Applied distributed axial force, q = Applied distributed transverse force, m = Applied distributed bending moment.

A sine function $v_0(x)$ is characterised by its amplitude V_0 and its half-wavelength λ_0 as follows:

$$v_0(x) = V_0 \sin\left(\frac{\pi x}{\lambda_0}\right) \tag{C1}$$

Figure C1a shows when the compressive load is applied the misaligned fibre deform into a new sine function $v(x)$ of amplitude V and half-wavelength λ. The function $v(x)$ is given by:

$$v(x) = V \sin\left(\frac{\pi x}{\lambda}\right) \tag{C2}$$

Figure C1b shows a free body diagram of an infinitesimal element of a deformed fibre. Assume that a small deflection and the initial fibre axis to be along the x-axis, the equilibrium equations can be written [53] as follows:

$$\sum F_{axial} = 0 \qquad p - \frac{dP}{dx} + Q\frac{d\omega}{dx} = 0 \tag{C3}$$

$$\sum F_{transverse} = 0 \qquad q + \frac{dQ}{dx} + P\frac{d\omega}{dx} = 0 \tag{C4}$$

$$\sum M = 0 \qquad \frac{dM}{dx} - Q + m = 0 \tag{C5}$$

where ω is the slope of the deflected fibre axis. If v is the transverse deflection of the fibre therefore $\omega = \frac{dv}{dx}$. Based on the assumption of fibres buckle in-phase (fibres kink in-phase with one another) and all fibres deform the same way therefore $p = q = 0$. Other than that, a constant axial force P is used to reduce the equilibrium conditions for the transverse forces and bending moments into the following equilibrium equation:

$$\frac{d^2M}{dx^2} + P\frac{d^2v}{dx^2} + \frac{dm}{dx} = 0 \tag{C6}$$

Noting that,

$$\frac{d^2(v - v_0)}{dx^2} = \frac{M}{E_f I_f} \tag{C7}$$

where E_f and I_f are the elasticity modulus and the second moment of area of the fibre respectively. The compressive load P applied to the fibre is related to the global stress σ_0 on the 0^o-ply by the following equation:

$$\sigma_0 = \frac{PV_f}{A_f} \tag{C8}$$

where V_f is the fibre volume fraction of the composite. The equation of applied distributed bending moment m is given by:

$$m = -A_f \tau(\gamma) \tag{C9}$$

Then

$$\frac{dm}{dx} = -A_f \frac{d\tau(\gamma)}{d\gamma}\frac{d\gamma}{dx} = -A_f G(\gamma)\frac{d\gamma}{dx} \tag{C10}$$

Since the shear strain γ can be approximated by $\gamma \approx \frac{d(v-v_0)}{dx}$, therefore

$$\frac{dm}{dx} = -A_f G(\gamma)\frac{d^2(v-v_0)}{dx^2} \tag{C11}$$

where A_f is the cross section area of the fibre, $G(\gamma)$ is the composite shear modulus in a function of the shear strain, τ and γ are the composite shear stress and strain, respectively. Based on the non-linear behaviour of in-plane shear stress-strain response, Jumahat et al. [7] proposed the equation of elasto-plastic shear modulus as follows:

$$G_{12}^{ep}(\gamma) = G_{12}^{e}\exp\left(-\frac{G_{12}^{e}\gamma}{\tau_y}\right) + G_{12}^{p}\exp\left(-\frac{G_{12}^{p}\gamma}{\tau_{ult}-\tau_y}\right) \tag{C12}$$

where G_{12}^{e} is the elastic shear modulus (tangent at 0.1-0.5% shear strain) and G_{12}^{p} is the plastic shear modulus (calculate tangent at yield point). τ_y and τ_{ult} are the yield and ultimate shear stress, respectively. Substitute Equations (C7), (C8), (C11) and (C12) into equation (C6) hence the equation becomes:

$$E_f I_f \frac{d^4(v-v_0)}{dx^4} + \frac{A_f\sigma_0}{V_f}\frac{d^2v}{dx^2} - A_f G_{12}^{ep}(\gamma)\frac{d^2(v-v_0)}{dx^2} = 0 \tag{C13}$$